Cláudia Raquel da Silva Nóbrega

Licenciatura em Biologia Molecular e Genética e
Mestrado em Microbiologia Aplicada

Biochemical and physiological insights into bacterial cytochrome *c* peroxidases from *Escherichia coli* and *Neisseria gonorrhoeae*

Dissertação para obtenção do Grau de Doutor em
Bioquímica, especialidade em Bioquímica Física

Orientador: Doutora Sofia Rocha Pauleta,
Investigadora Principal da Faculdade de Ciências e Tecnologia
da Universidade Nova de Lisboa

Co-orientador: Doutor Bart Devreese,
Professor da Universidade de Ghent, Bélgica

Júri:

Presidente: Doutora Maria João Lobo dos Reis Madeira Crispim Romão

Arguentes: Doutor Arsénio do Carmo Sales Mendes Fialho

Doutor Carlos Alberto Gomes Salgueiro

Vogais: Doutor João Paulo dos Santos Gomes

Doutora Maria João Lobo dos Reis Madeira Crispim Romão

Doutora Sofia Rocha Pauleta

FACULDADE DE CIÊNCIAS E TECNOLOGIA
UNIVERSIDADE NOVA DE LISBOA

Setembro 2017

2017

Biochemical and physiological insights into bacterial cytochrome *c* peroxidases from *Escherichia coli* and *Neisseria gonorrhoeae*

Cláudia Nóbrega

Cláudia Raquel da Silva Nóbrega

Licenciatura em Biologia Molecular e Genética e
Mestrado em Microbiologia Aplicada

Biochemical and physiological insights into bacterial cytochrome *c* peroxidases from *Escherichia coli* and *Neisseria gonorrhoeae*

Dissertação para obtenção do Grau de Doutor em
Bioquímica, especialidade em Bioquímica Física

Orientador: Doutora Sofia Rocha Pauleta,
Investigadora Principal da Faculdade de Ciências e Tecnologia
da Universidade Nova de Lisboa

Co-orientador: Doutor Bart Devreese,
Professor da Universidade de Ghent, Bélgica.

Júri:

Presidente: Doutora Maria João Lobo dos Reis Madeira Crispim Romão

Arguentes: Doutor Arsénio do Carmo Sales Mendes Fialho

Doutor Carlos Alberto Gomes Salgueiro

Vogais: Doutor João Paulo dos Santos Gomes

Doutora Maria João Lobo dos Reis Madeira Crispim Romão

Doutora Sofia Rocha Pauleta

Setembro 2017

Biochemical and physiological insights into bacterial cytochrome *c* peroxidases from *Escherichia coli* and *Neisseria gonorrhoeae*

Setembro 2017

Acknowledgments

I would like to express my sincere gratitude to all the people that made this thesis possible. All of them provided a valuable contribution to this journey and I can just hope that I may meet them again, someday.

First of all, I would like to thank my supervisors. To my advisor Doctor Sofia Pauleta I have to thank for the opportunity to work in this project, for all that she taught me, her support, the time spent and much more, throughout all these years. I thank my co-advisor Prof. Bart Devreese for all the help with mass spectrometry analysis and for the uplifting and positive emails he has sent when I needed anything, always kind and available.

I would like to show my appreciation to Prof. Isabel Moura and Prof. José Moura for allowing me to work in their labs and for sharing their knowledge and books.

I thank to my collaborators from the X-Tal group, the crystallography group from UCIBIO, REQUIMTE. To Prof. Maria João Romão, who kindly received me in her lab and for providing new insightful ideas. To Doctor Ana Luísa Carvalho and Lina Juknaite for teaching me and helping me in all the crystallization experiments, but above all for never giving up and encouraging me to keep trying. I would also like to express my gratitude to the rest of the group, which was always available to help me and guide me.

I thank to all my colleagues, the present and the past ones, for their advice, guidance, knowledge, help, inspiring discussions, friendship and innumerous special memories. I would like to express my gratitude especially to Cíntia Carreira, for being my PhD partner and a trusted friend. Words cannot describe how fortunate I am to have met her and how much she inspired me to be a better scientist.

I thank Bernardo, my partner in life, for always, always, always, supporting me during my PhD thesis and for not complaining for all the long hours I made him wait before going home or for making him "wake up too early" to go to the lab.

I am grateful to my brother, who inspired me to pursue a PhD and has always been available whenever I needed him.

Agradeço aos meus pais que sempre me apoiaram, me motivaram a fazer o meu melhor e demonstraram interesse em tudo o que eu faço.

Finally, I would like to thank for the financial support provided by UCIBIO, REQUIMTE and Fundação para a Ciência e Tecnologia (PTDC/BIA-PRO/109796/2009 and SFRH/BD/87878/2012).

Abstract

Bacteria display an array of enzymes to detoxify reactive oxygen species that cause cell damage and death, such as the bacterial cytochrome *c* peroxidase (BCCP) that reduces H_2O_2 to water in the periplasm. The BCCPs studied up-to-date are soluble dihemic enzymes from non-pathogenic bacteria. This thesis focus on the trihemic BCCP from *Escherichia coli* (YhjA), and the dihemic BCCP from the obligate human pathogen *Neisseria gonorrhoeae* (*Ng*BCCP). These two enzymes are membrane anchored thus, soluble recombinant proteins of their conserved globular domains were produced, purified and characterized biochemically and spectroscopically.

Recombinant *Ng*BCCP, a 38 kDa protein, forms a homodimer in the presence of calcium ions. It contains a high-potential E heme (+310 mV, pH 7.5) and a low-potential P heme (-190 mV/-300 mV, pH 7.5), the active site, with a unique high-spin EPR signal at low temperatures in the mixed-valence active form. *Ng*BCCP has catalytic activity with $ABTS^{2-}$ (synthetic electron donor) and a Lipid-modified Azurin (LAz) as electron donors (low K_M values 4.0 and 0.4 µM H_2O_2, respectively) which was dependent on reductive activation and calcium ions, and optimum at physiological pH (7.0) and temperature (37 ºC). LAz, identified as *Ng*BCCP physiological electron donor, was capable of activating the enzyme. The *Ng*BCCP/LAz electron transfer complex has a low binding affinity (micromolar range), and the interaction is dynamic and of a hydrophobic nature according to NMR, docking and preliminary calorimetry studies.

The peroxidase activity was inhibited by exogenous ligands bound at the active site, such as azide, cyanide and imidazole, as demonstrated by spectroscopic, kinetic and structural analysis. The structure of *Ng*BCCP was determined for the mixed-valenced and azide-inhibited form, and a catalytic mechanism for BCCPs was proposed based on the structural analysis of *Ng*BCCP active site.

The recombinant YhjA, a 50 kDa monomer, has a C-terminal domain homologous to dihemic BCCPs and a N-terminal (NT) domain. This domain was characterized for the first time, demonstrating that NT heme is His63/Met125 coordinated. The reduction potentials of P, NT and E hemes were determined: –170 mV, +133 mV and +210 mV, at pH 7.5, respectively. YhjA has quinol peroxidase activity *in vitro* (millimolar range K_M values) using hydroquinone and menadiol (menaquinol analogue), as electron donors. Calcium ions were needed for maximum activity but not reductive activation, as P heme is always high-spin penta-coordinated. This property allowed to detect the formation of an intermediate radical species upon incubation with H_2O_2. Real Time PCR data showed that YhjA was expressed under anaerobic conditions, which agrees with the use of menaquinol in those conditions. Hence it was suggested a role in H_2O_2 detoxification when transitioning from anaerobic to aerobic environments.

Keywords: bacterial peroxidases, oxidative stress response, *Neisseria gonorrhoeae*, *Escherichia coli*, electron transfer complex, catalytic mechanism.

Resumo

As bactérias dispõem de um conjunto de enzimas que removem as espécies reactivas de oxigénio que causam danos e morte celular, tais como a peroxidase de citocromo *c* bacteriana (BCCP) que reduz H_2O_2 a água no periplasma. As BCCPs estudadas até à data são enzimas di-hémicas solúveis de bactérias não patogénicas. Esta tese foca-se na BCCP tri-hémica de *Escherichia coli* (YhjA), e na BCCP di-hémica da bactéria patogénica *Neisseria gonorrhoeae* (*Ng*BCCP). Estas duas enzimas estão ancoradas à membrana pelo que, proteínas recombinantes solúveis do domínio globular foram produzidas, purificadas e caracterizadas bioquimicamente e espectroscopicamente.

A *Ng*BCCP recombinante, uma proteína de 38 kDa, forma um homodímero na presença de iões de cálcio. Esta proteína contém o hemo E de alto potencial (+310 mV, pH 7.5) e o hemo P de baixo potencial (-190 mV/-300 mV, pH 7.5), o centro activo, que apresenta um sinal de spin alto único no espectro de EPR da forma de valência mista, a baixas temperaturas. A *Ng*BCCP tem actividade catalítica com $ABTS^{2-}$ (dador de electrões sintético) e a azurina modificada por lípidos (LAz), como dadores de electrões (valores de K_M de 4.0 e 0.4 µM H_2O_2, respectivamente). A actividade da *Ng*BCCP é dependente de activação por redução e de iões de cálcio, e é óptima a valores de pH (7.0) e temperatura (37 ºC) fisiológicos. A LAz, identificada como o dador de electrões fisiológico de *Ng*BCCP, é capaz de activar esta enzima. O complexo de transferência electrónica *Ng*BCCP/LAz tem uma afinidade de ligação baixa (na ordem de micromolar) e tem uma interação dinâmica e de natureza hidrofóbica de acordo com os dados de NMR, "*docking*" e estudos preliminares de calorimetria.

A análise espectroscópica, ensaios cinéticos e análise estrutural demonstraram que a actividade da *Ng*BCCP é inibida pela ligação de ligandos exógenos ao centro activo, tais como a azida, cianeto e imidazol. A estrutura da *Ng*BCCP foi determinada na forma de valência mista e na forma inibida com azida, e um mecanismo catalítico para as BCCPs foi proposto com base na análise estrutural do centro activo da *Ng*BCCP.

A YhjA recombinante, um monómero de 50 kDa, tem um domínio C-terminal homólogo às BCCPs di-hémicas e um domínio N-terminal (NT). Este domínio foi caracterizado pela primeira vez, demonstrando que o hemo NT é coordenado pela His63 e Met125. Os potenciais de redução dos hemos P, NT e E foram determinados: –170 mV, +133 mV e +210 mV, a pH 7.5, respectivamente. A YhjA tem actividade de peroxidase de quinol *in vitro* (valores de K_M na ordem de milimolar) usando hidroquinona e menadiol (análogo do menaquinol) como dadores de electrões. Os iões de cálcio são necessários para a actividade máxima mas a activação por redução não é pois o hemo P está sempre na forma penta-coordenada de spin alto. Esta propriedade permitiu a detecção da formação de uma espécie radical intermediária após incubação com H_2O_2. Os dados de PCR em tempo real demonstraram que a YhjA é expressa em condições anaeróbias, o que está de acordo com

a utilização do menaquinol nessas condições. Com base nestes dados, foi sugerido um papel na destoxificação do H_2O_2 durante a transição de ambientes anaeróbios para ambientes aeróbios.

Palavras-chave: Peroxidases bacterianas, resposta ao "*stress*" oxidativo, *Neisseria gonorrhoeae*, *Escherichia coli*, complexo de transferência electrónica, mecanismo catalítico

Table of contents

Figure Index

Table Index

List of Abbreviations

5c – penta-coordinated

6c – hexa-coordinated

ABTS – 2,2'-azino-bis(3-ethylbenzothiazoline-6-sulphonic acid)

ASA – Accessible surface area

Asc – Sodium ascorbate

BCCP – Bacterial cytochrome *c* peroxidase

BSA – Bovine serum albumin

CCP – Cytochrome *c* peroxidase

c.f.u. – colony-forming unit

CT – C-terminal

DAD – Diaminodurol

DSC – Differential scanning calorimetry

DTT – Dithiothreitol

$E^{o\prime}$ – Standard reduction potential at specified pH value

ED – Electron donor

EDTA – 2,2',2",2"'-(Ethane-1,2-diyldinitrilo)-tetraacetic acid

EGTA – Ethylene glycol-bis(2-aminoethylether)-*N,N,N',N'*-tetraacetic acid

EPR – Electron paramagnetic resonance

ET – Electron transfer

FMN – Flavin mononucleotide

HALS – Highly axial low-spin

HEPES – 4-(2-hydroxyethyl)-1-piperazineethanesulfonic acid

HS – High-spin

IR – Infrared

ITC – Isothermal titration calorimetry

LAz – Lipid-modified Azurin

LB – Luria-Bertani

LS – Low-spin

MCD – Magnetic circular dichroism

MES – 2-(N-morpholino)ethanesulfonic acid

*Ng*BCCP – *Neisseria gonorrhoeae* bacterial cytochrome *c* peroxidase

NIR – Near infrared

NMR – Nuclear magnetic resonance

NT – N-terminal

PCR – Polymerase chain reaction

*q*PCR – Quantitative real time polymerase chain reaction

QPO – Quinol peroxidase

RMSD – Root mean square deviation

ROS – Reactive oxygen species

SHE – Standard hydrogen electrode

SOD – Superoxide dismutase

UV – Ultraviolet

WT – Wild type

YhjA – *Escherichia coli* bacterial cytochrome *c* peroxidase

Chapter 1

Introduction

1 Introduction

1.1 Metalloproteins containing heme redox centers – cytochromes

1.1.1 Cytochromes role in biological systems

In biological systems, oxidation-reduction reactions play an important role in many processes, such as respiration or photosynthesis. These reactions are possible due to a variety of proteins, most of them containing metal cofactors, the metalloproteins. These proteins contain a variety of metal centers, such as hemes, iron-sulfur clusters, copper centers and molybdenum centers. Moreover, one or more identical or different redox centers can be found in the same polypeptide chain, allowing the protein to perform a wide variety of functions, such as enzymatic catalysis and signal transduction.

Cytochromes are a major class of heme containing proteins, found in all organisms, which were first discovered by Charles A. MacMunn in 1886 and then rediscovered in 1925 by David Keilin that named them and identified their function in cell respiration [1, 2]. Nature evolved hemes to carry out diverse processes, such as electron transfer (ET), in cellular pathways that allow important processes, such as energy production [3], substrate oxidation [4], oxygen sensing [5], signaling (apoptosis in eukaryotic cells [6]), oxygen transport and storage [7].

These proteins can be found in the periplasmic space of Gram-negative bacteria, anchored to or inserted in the cytoplasmic membranes of Gram-positive bacteria and overall, associated to the membranes of all organisms (*e.g.* membranes of eukaryotic organelles, such as the mitochondria).

1.1.2 Heme types and properties

Cytochromes can be named according to their heme types. Hemes were classified as *a, b, c, d, f* and *o*, according to their distinct UV-visible spectra when the heme iron in the ferrous state is coordinated with pyridine (pyridine hemochrome). The distinctive feature that distinguishes the heme types is the wavelength of the α band [8].

A heme is a tetrapyrrole macrocyclic ligand, the protoporphyrin IX, which can have different peripheral β-pyrrolic substituents (Figure 1.1) [2] and thus, different spectroscopic properties.

Heme *b*, which is also named protoheme IX, is the most abundant heme group [9]. It has methyl groups at positions 1, 3, 5 and 8, vinyl groups at positions 2 and 4 and propionates at positions 6 and 7 of the macrocycle.

Hemes *a, c* and *d* are protoheme derivatives [10, 11]. In order to synthesize heme *a*, the heme *a* synthase (HAS) converts the vinyl group at position 2 into a hydroxyethylfarnesyl side chain (constituting heme *o*) and the methyl group at position 8 is oxidized to a formyl group [12]. In heme *d*, two cis-hydroxyl groups are inserted at positions 5 and 6. Additionally, in heme d_1 the vinyl groups at positions 2 and 4 are replaced by two ketone groups, and two acetate groups are added to positions 1 and 3 [13].

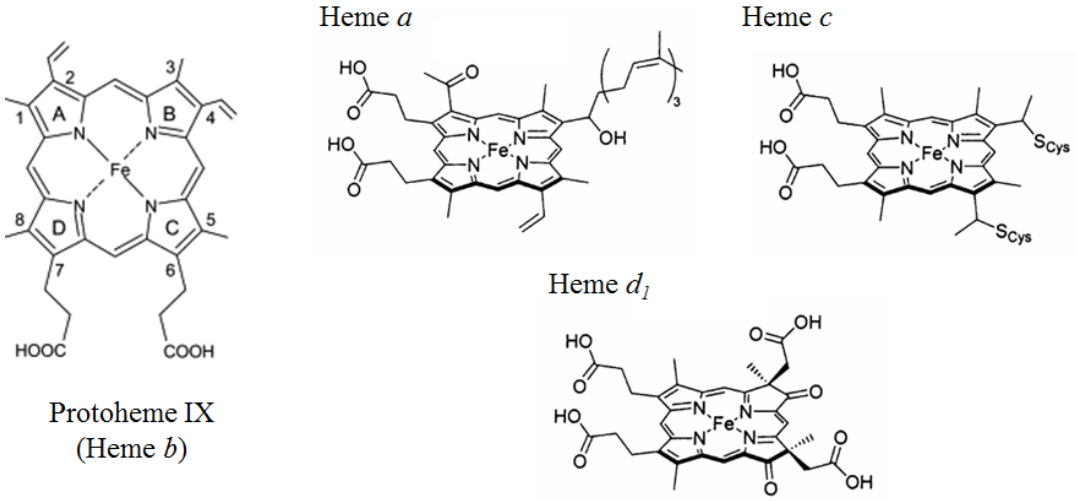

Figure 1.1 – Chemical structures of heme *b* (protoheme IX) and *a*, *c* and d_1 (protoheme derivatives). Adapted from Reedy and Gibney [2].

Heme *c* is similar to heme *b* but instead of vinyl groups it is covalently bound to two cysteines in the polypeptide chain by thioether bonds. This process is performed by specialized enzymatic machinery, encoded by the *ccm* operon [14], which attaches the heme to the two cysteine residues of the conserved $C(X)_{2\text{-}4}CH$ sequence motif found in cytochrome *c* and cytochrome *f*. Heme *f* is identical to heme *c* but its unique distal ligand, an amine group from a tyrosine, confers different spectroscopic properties [15].

The CXXCH sequence is the most common *c*-type heme binding-motif but there are slightly different motifs, such as CXXXCH in dihemic cytochrome c_{552} from *Pseudomonas stutzeri* [16], $C(X)_4CH$ found in tetrahemic cytochromes c_3 [17] and $C(X)_{15}CH$ motif in the multiheme *c*-type cytochrome MccA from *Wolinella succinogenes* [18]. The conserved histidine residue in these motifs is the proximal heme ligand in both *c*- and *f*-type hemes. However, the cytochrome *c* nitrite reductase (NrfA) from *Escherichia coli* is an exception as it has a CXXCK motif with a lysine residue as proximal ligand [19].

Hemes are bound to the polypeptide chain through the axial coordination to the heme iron, hydrophobic interactions with the heme macrocycle, polar interactions with the propionate groups and in the case of *c*/*f*-type hemes, the thioether bonds with the cysteine residues.

The most common axial ligands are histidine and methionine residues, though not exclusively, as other residues can play this role in some rare cases [15, 20], as mentioned before for cytochrome *f* and NfrA. The second axial ligand can be absent, which is the case of cytochrome *c'* [21]. Changes in heme coordination result in distinct redox properties and spectroscopic features.

Furthermore, cytochromes in nature can have just a single heme, multiple hemes of the same type (*e.g.* bacterial cytochrome *c* peroxidases can have two or three *c*-type hemes [22]), more than one heme type (*e.g. cytochrome* cd_1, a nitrite reductase [23]) or heme and non-heme cofactors in the same

polypeptide chain (*e.g.* cytochrome bo_3, a heme-copper terminal oxidase [24]). These few examples illustrate the role of *c*-type cytochromes in enzymatic reactions, such as reduction of hydrogen peroxide and reduction of nitrite in the denitrification pathway. The wide variety of cytochromes are involved in different functions besides ET, such as catalyzing redox reactions and sensing. Therefore, these proteins are often applied in biosensors, due to their unique properties in order to detect a particular analyte that can be important in environmental monitoring or pharmaceutical industry (*e.g.* cytochrome P450, also known as CYP biosensors [25]).

1.1.3 Class classification and properties of *c*-type cytochromes

C-type cytochromes are present in biological processes such as respiratory chains [26], denitrification pathways (cytochrome cd_1 nitrite reductase [27]), ROS detoxification systems (cytochrome *c* peroxidases [22]) and dissimilatory metal reduction (multi-heme "nanowires" [28]).

This family of cytochromes has been extensively studied to understand their ET mechanisms, identify the axial ligands, the role played by the hemes in their spectroscopic and biochemical properties. This has been accomplished by extensive biochemical characterization, protein engineering and by comparison of the increasing number of *c*-type cytochrome structures available in the databases.

With such diversity it is necessary, for ease of understanding, to divide *c*-type cytochromes into different classes according to their properties and functions. According to Ambler system [29], *c*-type cytochromes can be divided into four classes considering the identity of the axial ligands, number of hemes, reduction potentials and protein sequence/folding.

Class I *c*-type cytochrome include small soluble low-spin proteins with a classical cytochrome fold. The classical cytochrome fold consists of five α-helices arranged in a characteristic tertiary structure with a N-terminal conserved CXXCH motif and a C-terminal loop carrying the distal axial ligand [30]. An example of a class I *c*-type structure is presented in Figure 1.2.

In class II *c*-type cytochromes is found the high-spin heme containing cytochrome *c'* that lacks the distal axial ligand. It is only coordinated by the proximal histidine residue. Cytochromes from class III are multiheme proteins with low reduction potentials (-380 mV to -20 mV) [3]. These cytochromes can harbor up to twelve or sixteen *c*-type hemes in only one polypeptide chain, as observed in a cytochrome *c* from *Geobacter sulfurreducens* (GSU1996 [28]) and *Desulfovibrio vulgaris* Hildenborough (HmcA [31]), respectively.

The last class, class IV, comprises proteins with higher molecular weight that contain other prosthetic groups besides *c*-type hemes.

Although there is a separation into four classes, each class itself is widely diverse and includes several sub-classes, which will not be further explored here.

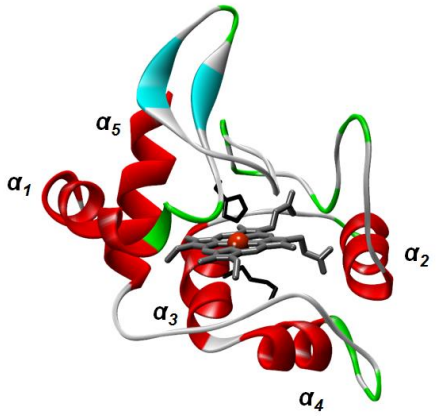

Figure 1.2 – Example of class I *c*-type cytochrome. X-ray structure of *Rhodobacter capsulatus* cytochrome c_2 colored according to secondary structure. It has the typical five α-helices with a histidine and methionine as axial ligands (in black) coordinating the iron center (red sphere) from the *c*-type heme (in grey). This structure was retrieved from PDB (ID:1C2R) and rendered in Discovery Studio Visualizer.

Regarding the reduction potentials reported for *c*-type cytochromes, they cover a wide range from - 390 mV to + 450 mV, even with similar axial ligands because the heme environment, heme distortion and the overall geometry can affect this property [3, 32]. For instance, the distal axial ligand can change the reduction potential, with His/Met coordinated hemes typically having higher redox potentials than bis-His coordinated hemes [32].

1.1.4 Spectroscopic properties of *c*-type cytochromes

Spectroscopy is the study of the interaction of electromagnetic radiation with matter. Through the observation of this interaction, where radiation is absorbed, emitted or scattered, spectroscopic techniques have proven to be essential to obtain important information regarding *c*-type cytochromes: type of heme, identity of the axial ligand, spin-state and oxidation state [33].

The electromagnetic spectrum goes from the low-energy radio waves to the high energy γ-ray radiation. The division of the spectrum into the various named regions (such as X-ray, microwave, visible, ultraviolet) does not imply any fundamental differences but it is useful to indicate that different spectroscopic techniques are used. These region boundaries, which should not be regarded as such, can be delimited by a given wavelength, frequency or energy value.

The spectroscopic properties of the heme are provided by its iron (Fe) atom. Iron is a transition metal that is typically in one of two oxidation states, ferrous state (Fe^{2+}, $[Ar]3d^6$) or ferric state (Fe^{3+}, $[Ar]3d^5$). In some catalytic cycles, such as the ones from catalases and peroxidases, an intermediary Fe^{4+} is formed [34, 35].

It is the distribution of the electrons on the five 3d (t_{2g} and e_g) orbitals (Figure 1.3) that determines the spin state and the electronic properties of the iron. These depend on the type of ligands and in the

case of transition metal complexes, the phenomena observed can be mainly explained by the crystal field theory.

The porphyrin ring is a strong ligand allowing small energy differences, attributed to the axial ligands, to cause the spin-state to change. Furthermore, the axial ligands and the protein folding can cause distortion of the octahedral crystal field and deviations of the iron from the heme plane. All these changes are responsible for the unique properties of the heme in different systems [33].

A few spectroscopic techniques will be introduced (the ones used in this thesis) with emphasis on the information that they can provide on the *c*-type heme characterization.

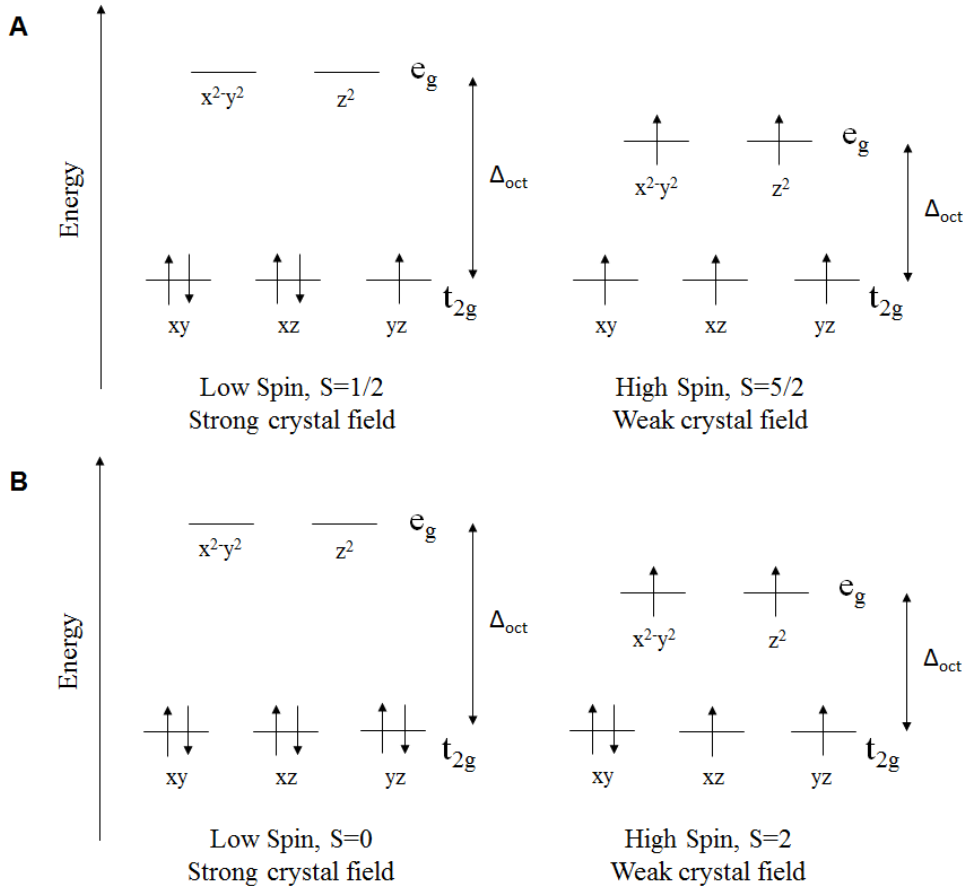

Figure 1.3 – Electrons distributed in the 3d orbitals in an octahedral geometry, like the one observed for heme iron: Fe^{3+} (A) and Fe^{2+} (B).

1.1.4.1 UV-visible spectroscopy

The most commonly used spectroscopic technique is absorption spectroscopy. Absorption is measured by monitoring the amount of radiation that is transmitted through the material. Common types of spectroscopy involving absorption are ultraviolet-visible (UV-visible) or infrared (IR) spectroscopies.

The absorption spectra is different for each type of heme and for the same type it has specific features that can be correlated to the oxidation state and spin-state (usually with further support from other spectroscopic techniques). The Figure 1.4 shows a typical UV-visible spectra of a *c*-type cytochrome.

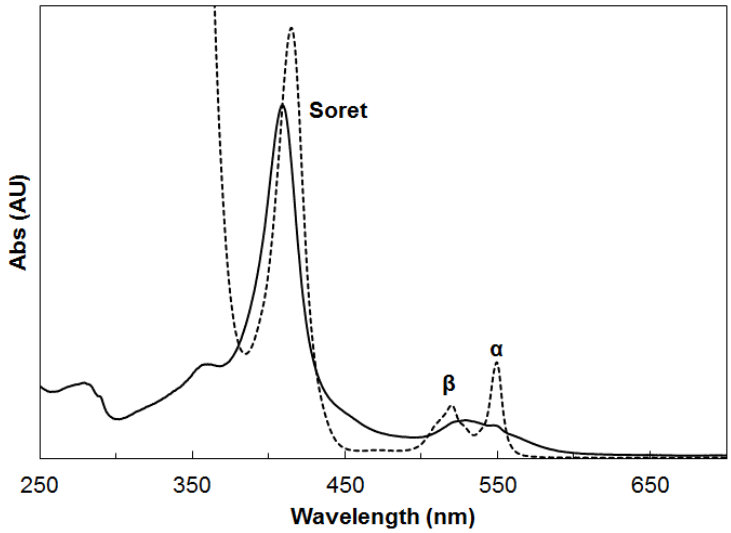

Figure 1.4 – Absorption spectra of horse heart cytochrome *c* in the ferric state (solid line) and in the ferrous state (dotted line).

These spectra are the result of different electronic transitions: the $\pi \rightarrow \pi^*$, *d-d* and charge-transfer transitions.

The $\pi \rightarrow \pi^*$ transitions give rise to intense bands in the UV-visible spectra, the Soret and the α and β bands (which appear only in the ferrous state), being the first more intense than the remaining ones and correspond to the excitation of electrons from bonding (π) and antibonding (π^*) molecular orbitals, on the porphyrin ring. The shift in the Soret band and the different α band wavelength positions for different types of hemes result from the diversity in porphyrin ring substituents and from the electronic state of the iron. The *d-d* transitions produce weak absorption bands in the 800 – 860 nm region which are not usually observed [36]. Charge-transfer transitions for the low-spin ferric heme are observed at 1200 nm and 1500 nm. These bands in the near IR (NIR) region of the spectra can be used to identify axial ligands [37].

Another absorption band that provides information on the axial ligand is the band around 695 nm. This band has been reported in *c*-type cytochromes to be associated with a methionine as distal axial ligand and it is only observed in the oxidized state [38]. The high-spin feature of ferric heme arises approximately from 600 to 640 nm and was described in cytochrome *c'*, which is penta-coordinated, with no distal axial ligands. This feature is also found in bacterial cytochrome *c* peroxidases P heme [21, 39].

1.1.4.2 Electron Paramagnetic Resonance

Electron paramagnetic resonance (EPR) is a spectroscopic technique, which is only informative when there are paramagnetic centers in the molecule of interest. Although this is a limitation of the technique it grants great specificity.

Metalloproteins often contain metal centers that are paramagnetic in some functional state, hence EPR spectroscopy can be a powerful tool in their study.

An important parameter given by EPR experiments is the *g* factor, which is specific to a paramagnetic center with a certain structure. EPR spectra are generally presented as the first order derivative of the absorption spectra and it is from that spectra that *g* values are obtained. EPR signal magnitude is proportional to the difference in species population by varying the magnetic field at a defined frequency. The majority of the EPR spectrometers hold the frequency constant either at 1-2 GHz (L-Band), 2-4 GHz (S-Band), 8-10 GHz (X-Band), 35 GHz (Q-Band) or 65 GHz (W-Band). The most commonly used is the X-band EPR spectrometer.

In an EPR experiment the unpaired electrons not only respond to a magnetic field (B_0) but also to local magnetic fields derived from its environment, the nuclei closer to those electrons. The latter depends on the orientation of the nuclei towards the magnetic field. It is possible to calculate the *g* factor using the following equations:

$$\Delta E = h.v = g\mu_B B_0 \qquad (1.1)$$

$$g = \frac{h.v}{\mu_B B_0} \qquad (1.2)$$

where ΔE is the difference in energy between the two spin states, called Zeeman energy (*e.g.* S = +1/2, S = -1/2), h is Planck's constant (6.626 x 10^{-34} J.s^{-1}), v is the frequency of radiation, μB the Bohr magneton (9.274 x 10^{-24} J.T^{-1}) and B_0 the external magnetic field (Tesla). The same equation can be applied to unpaired electrons and the *g* factor.

In an isotropic system there is only one *g* value. When there is anisotropy the signal divides into three signals that represent the three Cartesian coordinates, g_x, g_y and g_z. According to the values taken for each signal it is possible to determine the system geometry using crystal field theory.

Hemes typically display an anisotropic signal derived from the ferric form. Low-spin Fe^{2+} is EPR silent since it has no unpaired electrons (Figure 1.3B). As discussed previously there can be a high-spin heme species or a low-spin species, according to the distribution of the electrons on the *d* orbitals. The low-spin species show different EPR signals dependent on the relative energy differences between the t_{2g} orbitals. Those differences can be described by two components: the rhombic distortion (V) in the heme plane and the axial distortion (Δ) of the octahedral ligand field,

described previously [40]. These factors can be calculated through the following equations using a spin orbit coupling constant ξ [41]:

$$\frac{V}{\xi} = \frac{E_{yz}}{\xi} - \frac{E_{xz}}{\xi} = \frac{g_x}{g_z + g_y} + \frac{g_y}{g_z - g_x} \qquad (1.3)$$

$$\frac{\Delta}{\xi} = \frac{E_{yz}}{\xi} - \frac{E_{xz}}{\xi} - \frac{V}{2\xi} = \frac{g_x}{g_z + g_y} + \frac{g_z}{g_y - g_x} - \frac{V}{2\xi} \qquad (1.4)$$

This theory applies not only to *c*-type cytochromes but also to other types of hemes. In low-spin hemes g_x is typically very broad and with low intensity, and thus it is difficult to observe in the EPR spectrum. Therefore, a general rule for low-spin hemes is that $g_x^2 + g_y^2 + g_z^2 = 16$ [42].

By calculating all these parameters for hemoglobin A and various cytochromes, Blumberg and Peisach designed what they called the "Truth Diagram", which allowed to identify the axial ligands of low-spin hemes [43].

In some cases a highly axial low-spin (HALS) signal arises from EPR low-spin hemes, which have a large *g* max ≥ 3.2 at cryogenic temperatures. These type of signals, however, do not fit the "truth diagram" ligand field parameters [40], hence complementary techniques are needed to address the axial ligands identity, such as NIR, magnetic circular dichroism (MCD), nuclear magnetic resonance (NMR) or ultimately, if possible, to solve the protein structure by heteronuclear NMR or X-ray crystallography.

There are other spectroscopic techniques that can also provide important information on *c*-type cytochromes, such as Mössbauer and resonance Raman (RR) spectroscopies which allow the identification of the oxidation state and spin state of the heme. RR spectroscopy also gives information on the axial ligand (though usually other techniques are preferred) and on the distortion of the porphyrin ring (*e.g.*, if it is planar, domed, saddled) by measuring the pyrrole tilt angle [33]. In fact, many of these techniques will be mentioned when addressing bacterial peroxidases (Section 1.3) as these were important to understand their activation and catalytic mechanism.

1.2 Oxidative stress systems

1.2.1 Reactive oxygen species and bacterial defense mechanisms

The first living microorganisms evolved in a world without oxygen. With the oxygenation of the planet's atmosphere a new challenge is presented to the wide variety of existing microorganisms.

Oxygen is a reactive molecule which can cross the biological membranes due to its small, non-polar nature. The ability to deal with this new molecule divided the organisms in either strict anaerobes that survive in the few habitats without oxygen, microaerophiles that tolerate low levels of oxygen in the environment or aerobes that can survive in oxygenated environments.

However, molecular oxygen itself cannot react with most biomolecules, such as amino acids, carbohydrates, nucleic acids and lipids, essential for life. The toxic molecules are the intermediates of the reduction of molecular oxygen to water [44], which are known as the reactive oxygen species (ROS) namely: superoxide (O_2^-), hydrogen peroxide (H_2O_2) and hydroxyl radical ($HO^\bullet$) (Figure 1.5).

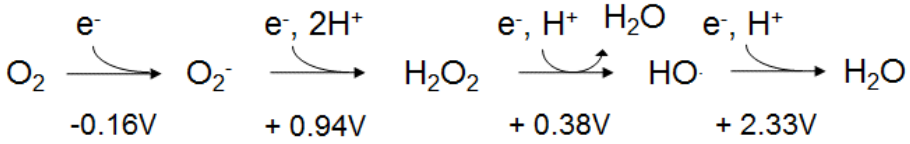

Figure 1.5 – Stepwise reduction by one-electron transfer of molecular oxygen to superoxide, hydrogen peroxide, hydroxyl radical and water. The reduction potentials indicated are *vs.* SHE, at pH 7.0. Scheme adapted from Mishra and Imlay [45].

It should be noted that molecular oxygen has an even number of electrons in which two are unpaired, making it difficult to accept one electron at a time (the first reaction in Figure 1.5 should be thermodynamically unfavorable) [46]. However, molecular oxygen can receive electrons from good electron donors, such as quinones, flavins and metal redox centers. Electron carriers in the respiratory chains are rich in these type of cofactors and were shown as one of the intracellular sources of O_2^- and H_2O_2 [47-49]. Even without respiratory enzymes it was found that both these ROS could arise from the autoxidation of non-respiratory flavoproteins *in vitro.* So the levels of ROS will depend on the amount of these autooxidizable enzymes in the cell and on the oxygen concentration in the environment (more oxygen leads to more successful encounters) [50].

A source of the hydroxyl radical is the Fenton reaction (1.5), where ferrous iron transfers an electron to H_2O_2 as follows:

$$Fe^{2+} + H_2O_2 \rightarrow FeO^{2+} + OH^- + H^+ \rightarrow Fe^{3+} + OH^- + HO^\bullet \quad (1.5)$$

The iron that catalyzes this reaction is “free iron”, which means that it is not incorporated into enzymes or iron-storage proteins, but it is iron that is presumably ligated to metabolites and to the surfaces of biomolecules. The $HO^\bullet$ produced in this reaction, is considered highly toxic as it can directly damage most biomolecules and it is therefore, linked to protein carbonylation, lipid peroxidation and DNA damage [51]. Other sources of ROS are extracellular, such as the host immune system or other microorganisms. These molecules are able to cause serious damage to the cell components [52] thus, to survive in oxygenated environments, microorganisms developed strategies to detoxify the cells from these compounds.

These strategies include specialized enzymes, such as superoxide dismutases (1.6), catalases (1.7) and peroxidases (1.8) that perform the following general reactions:

$$O_2^- + O_2^- + 2\ H^+ \rightarrow H_2O_2 + O_2 \quad (1.6)$$

$$H_2O_2 + H_2O_2 \rightarrow O_2 + 2H_2O \quad (1.7)$$

$$RH_2 + H_2O_2 \rightarrow R + 2H_2O \quad (1.8)$$

E. coli is the main bacterial model to study oxidative stress. It is a facultative anaerobe with several scavenging enzymes that respond to distinct stress signals in the cell. Therefore, it will be referenced several times as an example of what is known in oxidative stress molecular systems.

In the following sections it will be presented an overview on those enzymes and respective regulators in bacterial systems. However, it should be noted that many of these enzymes have an eukaryotic homologue, while others are unique to prokaryotic organisms. A better understanding of the oxidative stress scavengers and regulators is crucial to comprehend the role of bacterial cytochrome *c* peroxidases, the focus of this thesis.

1.2.2 Oxidative stress regulators – OxyR, PerR and SoxRS

Microorganisms typically present a low basal expression of the enzymes that help them detoxify ROS at low levels. However, when ROS levels increase this exerts an oxidative stress. This stress is sensed by specific protein sensors that are transcription factors, regulating gene expression. These regulators are found in a wide range of bacteria reflecting their positive selection and important physiological role [53].

OxyR is one of these regulators, a protein with two cysteine residues that is usually inactive and downregulating its own expression. When the H_2O_2 levels in the cytoplasm rise up to 200 nM it is enough to form a disulfide bond between the cysteines, activating OxyR, which then promotes the transcription of several genes related to oxidative stress (some of them will be described below) [53-55]. The disulfide bonds are re-reduced by glutathione, which in turn is reduced by glutathione reductase, inactivating OxyR (Figure 1.6). The expression of the glutathione reductase (GSH) and glutaredoxin (Grx1) genes is under control of OxyR, therefore the response is self-regulated [56].

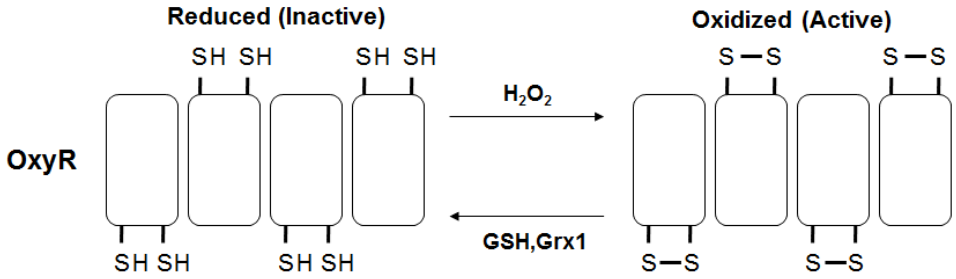

Figure 1.6 – Schematic representation of the reduction/oxidation mechanism of the OxyR transcription regulator in *E. coli*. The reduced inactive form is oxidized by hydrogen peroxide forming disulphide bonds between the cysteines. This active oxidized form induces the expression of several genes of the OxyR regulon, many involved in ROS detoxification. The oxidized form is reduced by the glutathione reductase/glutaredoxin system. Scheme adapted from Chiang and Schellhorn [53].

Besides H_2O_2, this protein also senses another type of stress, nitrosative stress, which leads to the activation of OxyR by S-nitrosylation followed by the expression of genes that allow the cell to adapt to reactive nitrogen species. This shows that OxyR can process different signals with distinct transcriptional responses [57, 58].

In Gram-positive bacteria there is an alternative mechanism to OxyR, the PerR. *Bacillus subtilis* PerR in its active form has two metal centers, zinc and iron. The zinc stabilizes the homodimeric protein form and the Fe^{2+} is necessary for the protein to acquire the correct conformation and bind DNA [59, 60]. H_2O_2 is able to oxidize one of the histidines coordinating the iron atom, inactivating PerR that no longer binds DNA. This leads to the transcription of oxidative stress related genes. PerR not only senses H_2O_2 as it seems to be important in transitioning from anaerobic to aerobic environments by sensing O_2. [60, 61].

OxyR and PerR are two of the systems that sense H_2O_2 but O^{2-} can also increase in certain conditions. For instance, bacteria can induce production of O^{2-} in the cytoplasm of other bacteria by secreting redox-cycling organic compounds [62].

For sensing O^{2-}, bacteria have the SoxRS system, which consists of two components. SoxR is a homodimer with a [2Fe-2S] cluster in each subunit, which becomes oxidized when exposed to redox-cycling compounds or O^{2-} [63-65]. In both oxidation states, the protein binds the upstream *soxS* gene but only the oxidized form induces its expression. SoxS induces the expression of several genes that include systems that deal with these redox-cycling compounds and O^{2-}, which is catalyzed by superoxide dismutases [66]. In some microorganisms (such as *Pseudomonas aeruginosa* that lacks SoxS) SoxR can directly affect the transcription levels of oxidative stress related genes [67, 68].

In sum, these oxidative stress sensors prevent the toxic effects of ROS by inducing the expression of genes that encode detoxifying enzymes.

1.2.3 Superoxide dismutases

Superoxide dismutases (SODs) are metalloenzymes capable of promoting the dismutation of O^{2-} to O_2 and H_2O_2 (an endogenous source of hydrogen peroxide, which will be scavenged by catalases and peroxidases). These enzymes are ubiquitous in both prokaryotes and eukaryotes. Superoxide cannot cross the membranes so SODs need to be located where O^{2-} is formed, in the cytoplasm, during aerobic growth.

Nevertheless, some pathogenic bacteria, such as strains of *Brucella, Haemophilus, Legionella, Mycobacterium* and *Nocardia*, secrete SODs suggesting also a role in neutralizing ROS secreted by the host immune system or other exogenous sources [69].

In *E. coli* alone there are three types of SODs: two cytoplasmatic SODs with iron or manganese cofactors (FeSOD and MnSOD) and a periplasmatic SOD with a copper-zinc center (CuZnSOD)

(Figure 1.7). SODs are typically dimers and in each subunit there is a single atom constituting its active site. In CuZnSOD each subunit contains an atom of each metal, the copper atom being cyclically reduced and oxidized, with the zinc atom probably conferring structural stability to the active site [70].

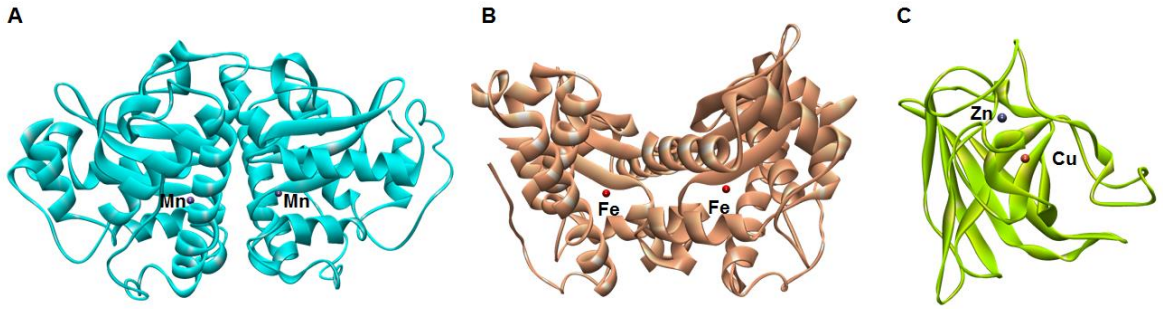

Figure 1.7 – Molecular structure of *E. coli* superoxide dismutases: (A) MnSOD, (B) FeSOD and (C) CuZnSOD. The dimeric form of each structure is represented except for CuZnSOD where the assymetric unit comprised only one of the subunits. Figure prepared with PDB IDs: 3K9S, 1ISA and 1ESO, respectively.

FeSOD and MnSOD are encoded by *sodA* and *sodB*, respectively, and are both regulated in response to iron levels. FeSOD is expressed when there are high levels of iron and when iron levels decrease the Fur repressor that is blocking MnSOD synthesis (and a MntH manganese importer) is deactivated. This allows MnSOD transcription, as well as the sRNA RyhB that triggers the degradation of FeSOD transcript. This system, depending on the cofactor availability, controls which SOD is activated [71, 72]. MnSOD expression can also be stimulated by the SoxRS system, which is active in the presence of exogenous superoxide sources [73].

CuZnSOD encoded by *sodC* was believed to be only present in eukaryotes. However, it is present in some bacterial species (*E. coli* and *Neisseria meningitidis* are two examples [74, 75]) and compared to eukaryotic CuZnSODs, the prokaryotic form appears to be highly resistant to hydrogen peroxide, which is one of the products of its enzymatic activity [76]. In *E. coli* CuZnSOD is repressed by FNR (fumarate and nitrate reduction regulatory protein, a transcription factor activated under anaerobiosis) under anaerobic conditions and induced in the stationary phase by RpoS [70].

In the absence of SOD activity in *E. coli*, a variety of oxygen-dependent phenotypic alterations occur. One of such effects is a high rate of spontaneous mutagenesis [77], which shows the importance of SOD activity in preventing oxygen-dependent DNA damage. Cytoplasmic SODs in fact, are able to maintain O^{2-} at sub-nanomolar concentrations [78].

1.2.4 Catalases

Catalases, as well as peroxidases, have an important role in scavenging H_2O_2. These cytoplasmic enzymes catalyze the dismutation of H_2O_2 to molecular oxygen and water and are found in most bacterial species, with a few exceptions (enterococci, streptococci and leuconostocs [45]).

These enzymes can be divided into three families: two are heme catalases and one is a manganese catalase (a protein family found only in some bacteria, as for instance *Lactobacillus plantarum* [79]). All catalases catalyze the dismutation reaction of H_2O_2 but one family of heme catalases has also peroxidase activity, called bifunctional catalases or catalase-peroxidases. The bifunctional catalases are only found in prokaryotes and eukaryotes, with the exception of plants and animals. Heme monofunctional catalases are widespread among various organisms, prokaryotes and eukaryotes [80]. The dismutation reaction of H_2O_2, common to both heme catalases, requires two molecules of H_2O_2.

$$\text{Por-Fe}^{3+} + H_2O_2 \rightarrow \text{(Compound I) Por}^{+}\text{-Fe}^{4+}\text{=O} \qquad (1.9)$$

$$\text{(Compound I) Por}^{+}\text{-Fe}^{4+}\text{=O} + H_2O_2 \rightarrow \text{Por-Fe}^{3+} + H_2O + O_2 \qquad (1.10)$$

In the first step of the reaction (1.9) a Por-Fe^{3+} reduces H_2O_2 forming a Por^{+}-Fe^{4+}=O radical intermediate (an oxoferryl species commonly known as compound I, with a porphyrin cation radical [34]). In the second step (1.10), compound I oxidizes another molecule of H_2O_2 releasing O_2 and H_2O and returning to the initial Por-Fe^{3+}.

This highly reactive Compound I is a potential problem within the cell when the levels of H_2O_2 decrease. In monofunctional catalases, it was shown that NADPH can be used to revert Compound I to the Por-Fe^{3+} initial state [81].

The bifunctional catalases have a low peroxidatic activity, thus it receives electrons from exogenous electron donors (R) to reduce Compound I (from reaction in 1.9) to Compound II (Por^{+}-Fe^{4+}=OH) and then back to Por-Fe^{3+}:

$$\text{(Compound I) Por}^{+}\text{-Fe}^{4+}\text{=O} + RH \rightarrow \text{(Compound II) Por-Fe}^{4+}\text{-OH} + R \qquad (1.11)$$

$$\text{(Compound II) Por-Fe}^{4+}\text{-OH} + RH \rightarrow \text{Por-Fe}^{3+} + H_2O + R \qquad (1.12)$$

However, this activity represents only about 1 % of the catalytic activity of bifunctional catalases.

The K_M values of both bifunctional (3.5 - 8 mM) and monofunctional (40 - 600 mM) are in the millimolar ranges although physiological concentrations of H_2O_2 are in the micromolar range, well below the K_M of both types of catalases [82]. Therefore, in physiological conditions catalases would play the major role in detoxifying the cell from H_2O_2 when its concentrations drastically increase.

In *E. coli* there are two catalases, the bifunctional catalase KatG and the monofunctional catalase KatE (Figure 1.8). The *katG* gene is induced by OxyR in the presence of ROS or at lower levels in the exponential phase. The genes encoding most bifunctional catalases are usually induced by oxidative stress through regulatory systems, such as OxyR [55] or PerR [83]. The *katE* gene is overexpressed in the stationary phase, induced by the stationary phase sigma factor RpoS [84].

Bacteria usually have more than one catalase isoenzyme and there are even cases in which bifunctional catalases are secreted to the periplasm in pathogenic bacteria (these bacteria also contain cytoplasmic catalases), such as KatP in *E. coli O157:H7* [85]. Nevertheless, it is not clear why both

catalases, with distinct expression patterns, are needed when a *E. coli* catalase mutant, in the absence of oxidative stress is phenotypically similar to the wild-type [45].

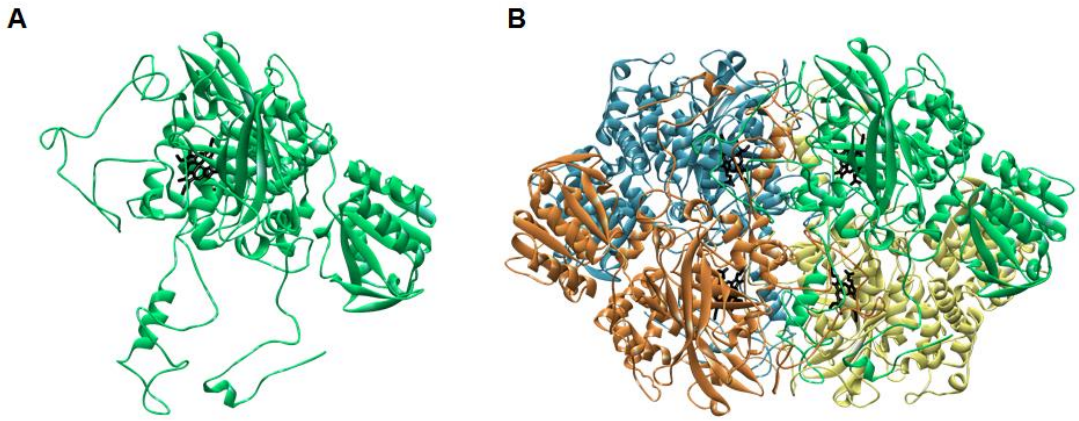

Figure 1.8 – Molecular structure of *E. coli* KatE (A) monomer and (B) tetramer. The structure is colored by chain, each one with a single *d*-type heme (black). Figure prepared with PDB ID:4BFL.

1.2.5 Reduction of hydrogen peroxide

Prokaryotes have several enzymes with peroxidase activity, capable of reducing H_2O_2 to water. In the presence of low-level H_2O_2 stress, the peroxidases are better scavengers compared to catalases, but just as long as there is enough reductant. Peroxidases may not have enough catabolic substrates, for instance during starvation periods, and they can saturate at slightly higher H_2O_2 concentrations (micromolar range). In those scenarios, the catalases present an advantage to the cells.

Some of these enzymes are thiol-based peroxidases, such as alkylhydroperoxide reductase (Ahp), bacterioferritin comigratory protein (BCP), thiol peroxidase (Tpx) (all three from the peroxiredoxin family), and glutathione peroxidase (Gpx) [86]. Others non thiol-based peroxidases include bacterial cytochrome *c* peroxidase and rubrerythrin [45].

These peroxidases differ in their substrate specificity, localization, metal requirements and protein stability. For this reason some bacteria (such as *E. coli*) have in their cells more than one of these enzymes, which enables them to cope with oxidative stress from various sources and different environments.

1.2.5.1 Thiol-based peroxidases

Alkylhydroperoxide reductase (**Ahp)** consists of two cytoplasmic proteins: AhpC is the catalytic subunit containing two conserved cysteine residues, which forms a dimer, and AhpF, a flavoprotein dimer with NADH:disulfide oxidoreductase activity [87]. The *ahpCF* expression is regulated by OxyR. Ahp receives electrons from NADH in order to reduce H_2O_2 (concentrations < 20 µM). Moreover,

reduction of H_2O_2 leads to the oxidation of AhpC. This oxidized AhpC dimer forms a decameric complex (pentamer of dimers), which is reduced by AhpF.

This enzyme is present in several bacteria but its importance as peroxidase became clear as an Ahp and KatG/KatE *E. coli* triple mutant was not able to scavenge H_2O_2 and the cells continuously released H_2O_2 to the medium [88]. This showed that although *E. coli* has several other peroxidases, these three enzymes are the main scavengers that maintain the low levels of hydrogen peroxide, and that allow to successfully grow under aerobic conditions.

Bacterioferritin comigratory protein (**BCP)** is another thiol-based peroxidase with a conserved N-terminal cysteine. The physiological electron donor is unknown but the thioredoxin system (Figure 1.9) is proposed as a likely candidate [89]. Recombinant BCP was shown to react with *t*-butylhydroperoxide and linoleic hydroperoxide, besides H_2O_2 [90]. In other microorganisms, such as *Campylobacter jejuni* and *Helicobacter pylori*, BCP mutants show sensitivity to cumene hydroperoxide or to aerated conditions but no sensitivity to H_2O_2 [91, 92]. This hints to a role as organic hydroperoxidase, which would explain why an *E. coli* Ahp^-Kat^- mutant cell suspension, when incubated with 1.5 µM H_2O_2 does not reduce hydrogen peroxide [88], thus presenting no peroxidase activity *in vivo*, even though BCP is produced in exponentially growing cells [45]. There is also no evidence of *bcp* responding to hydrogen peroxide as this gene is not regulated by either OxyR or PerR.

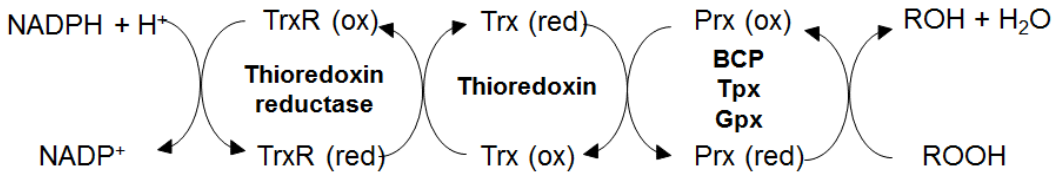

Figure 1.9 – Proposed mechanism for the thiol-based reductases (Prx): BCP, Tpx and Gpx. These enzymes use thioredoxin (Trx) and thioredoxin reductase (TrxR) as electron donors, to reduce peroxides (ROOH). Adapted from Mishra and Imlay [45].

Thiol peroxidase (**Tpx)** is a cytoplasmatic enzyme dependent on two conserved cysteine residues [91, 93, 94] and it is proposed to use thioredoxin as direct electron donor [95, 96] (Figure 1.9). *E. coli* Tpx shows peroxidase activity *in vitro* with H_2O_2, *t*-butylhydroperoxide, cumene hydroperoxide and linoleic acid hydroperoxide, using dithiothreitol as electron donor. However, as observed for BCP, an *E. coli tpx* null mutant did not display a different phenotype when grown under aerobic conditions, only a slight sensitivity to organic hydroperoxides [94], hinting to a role as an organic hydroperoxidase.

Organic hydroperoxidases main function is to detoxify the cells from organic hydroperoxides, which can damage the membranes, affecting their integrity and fluidity. These organic hydroperoxides can have two sources: one is the oxidation of linoleic acid and arachidonic acid by lipoxygenases or

cyclooxygenases. The other is the reaction between polyunsaturated fatty acids and free radicals, also known as lipid peroxidation. Lipid peroxidation in bacteria is not well documented due to the absence of polyunsaturated fatty acids that are more susceptible to oxidation. However, this phenomenon has been described in bacteria [97, 98] and in some cases it was demonstrated the uptake of exogenous polyunsaturated fatty acids from host organisms or the ability to produce them in some marine bacteria [99]. Therefore, although the focus is on hydrogen peroxide reducing enzymes, the role of hydroperoxidases (as suggested for BCP and Tpx) is crucial for cell survival.

Glutathione peroxidase (Gpx) is a thiol-based peroxidase with the ability to reduce hydroperoxides using glutathione as electron donor. This enzyme was first discovered in eukaryotes with a selenocysteine as peroxidatic residue [100]. The bacterial enzyme, found by sequence homology in *E. coli* is BtuE [101] and it has a cysteine instead of selenocysteine. *E. coli* BtuE has peroxidase activity *in vitro* with *t*-butylhydroperoxide, linoleic hydroperoxide and H_2O_2. However, *btuE* expression is not induced by H_2O_2, and even when it is overexpressed it does not confer significant peroxidase activity in a *E. coli* strain lacking Ahp and catalases, as BCP [45].
Gpx, besides using glutathione, as BCP and Tpx, also uses thioredoxin [102] explaining how this bacterial enzyme can exist in a system that lacks the glutathione biosynthetic pathway (Figure 1.9).

Overall BCP, Tpx and Gpx showed peroxidase activity *in vitro*, but no clear indication that this was their role *in vivo*. Also depending on the microorganism they have shown different affinities for the substrates previously discussed. For instance, in *C. jejuni* a *bcp* mutant showed lower cell-viability upon aeration and sensitivity to cumene hydroperoxide [91], and in *Enterococcus faecalis* a *tpx* mutant is sensitive to exogenous H_2O_2 and cumene hydroperoxide, but not to aeration [103].

1.2.5.2 Rubrerythrin

Rubrerythrin is an example of an enzyme which has non thiol-based peroxidase activity and that is widely distributed in anaerobic and microaerophilic bacteria. It has two metal centers: a rubredoxin-type iron center [$Fe(Cys)_4$] and a di-iron site with a µ-oxo bridge [104]. The di-iron center is oxidized by H_2O_2 (forming water) and to complete the cycle it requires two consecutive electrons from the rubredoxin site that *in vivo* would receive electrons from a rubredoxin protein (Figure 1.10).

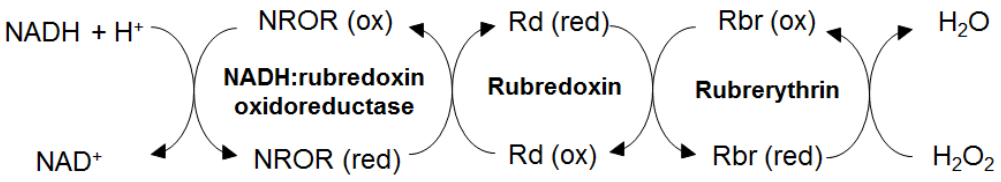

Figure 1.10 – Proposed electron transfer mechanism to rubrerythrin (Rbr) to reduce hydrogen peroxide. The NADH:rubredoxin oxidoreductase (NROR) reduces rubredoxin (Rd) which reduces Rbr. Adapted from Mishra and Imlay [45].

In some bacteria there is a reverse form of rubrerythrin (the position of the two domains is reversed) whose expression is regulated by PerR, suggesting a role for these enzymes in scavenging H_2O_2. *In vivo* and *in vitro* studies with the reverse rubrerythrin from *Clostridium acetobutylicum* showed that it had peroxidase and oxidase activity. Furthermore, a *C. acetobutylicum* strain overproducing this protein had higher tolerance to H_2O_2 and O_2 [105, 106].

1.2.5.3 Bacterial cytochrome c peroxidases

Bacterial cytochrome *c* peroxidases (BCCPs) constitute a family of enzymes that catalyze the reduction of H_2O_2 to water using *c*-type heme cofactors. Classical BCCPs contain two *c*-type hemes and are homodimers located in the periplasm [107, 108].

The eukaryotic counterpart, cytochrome *c* peroxidase (CCP), contains one *b*-type heme and accepts electrons from a small redox protein, cytochrome *c* (Figure 1.11). One of the most well characterized peroxidases in the literature is eukaryotic. It was the first CCP to be discovered, isolated from *Saccharomyces cerevisiae*, and it is located in the inter-membrane space of mitochondria [109].

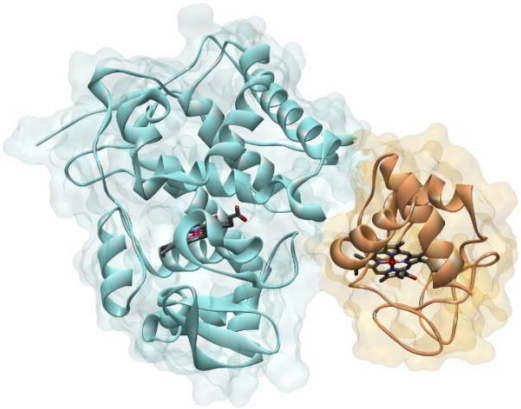

Figure 1.11 – Molecular structure of the co-crystallized *S. cerevisiae* CCP and cytochrome *c*. This structure allowed to determine the primary interface region of this redox pair and the electron transfer pathway [110]. The hemes are colored by atom color. Figure prepared with PDB ID: 2PCB.

Another well-studied eukaryotic peroxidase is the one isolated from horseradish (HRP), which has several isoenzymes, being isoenzyme C the most abundant and studied [111, 112]. There are other heme containing peroxidases in eukaryotes, such as ascorbate peroxidase (APX, isolated from chloroplasts [113]) and lignin peroxidases (LiP, found in fungi [114]).

The study of these various peroxidases, although significantly different from bacterial peroxidases, was essential to understand many of the BCCPs characteristics, such as spectroscopic and kinetic properties and their catalytic mechanism.

The BCCPs are a unique family of peroxidases that will be described in the following section. It will be discussed in more detail the structural and biochemical properties of these enzymes, the currently accepted catalytic mechanism and some of the questions that remain to be answered.

1.3 Bacterial Cytochrome *c* Peroxidases

1.3.1 Gene distribution, regulation and peroxidase location

The *ccp* gene that encodes the BCCP is ubiquitous, found in many bacteria, some of them pathogenic species, such as the ones from *Neisseria* and *Salmonella* genus. Some bacteria species have more than one *ccp* homologous gene such as *Geobacter sulfurreducens*, where a MacA enzyme was reported as a second BCCP [115], and *C. jejuni* that has in its genome two putative genes encoding for BCCPs [116].

Gene expression is regulated by one or two main transcription regulators, FNR and OxyR. FNR (fumarate and nitrate reduction regulatory protein) is a global regulator of anaerobic gene expression and is essential for bacteria when switching from aerobic to anaerobic conditions[117]. BCCPs regulated by FNR can be found in *Neisseria gonorrhoeae* [118, 119] (Figure 1.12A), *Pseudomonas aeruginosa* [120] and *Pseudomonas stutzeri* [121]. OxyR, an oxidative stress regulator, regulates the expression of the BCCP in *Shewanella oneidensis* [122]. In *E. coli* the expression of *yhjA*, the gene encoding a putative BCCP is proposed to be regulated by both OxyR and FNR [123] (Figure 1.12B).

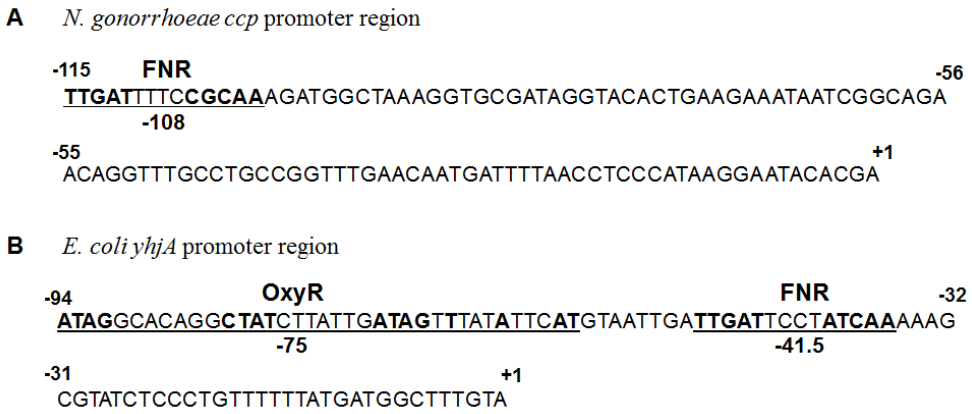

Figure 1.12 – Nucleotide sequence of the promoter region of (A) *N. gonorrhoeae ccp* gene [119] and (B) *E. coli yhjA* gene [123]. The putative FNR and OxyR binding sites are underlined and the nucleotides in bold match their consensus sequences.

In Gram-negative bacteria it was demonstrated that BCCP is located in the periplasmic space [107]. These enzymes are typically not found in Gram-positive bacteria and archaea species (with a few exceptions) [22].

The first BCCP to be biochemically characterized was isolated from *P. aeruginosa* [124, 125]. Since then this enzyme has been isolated from many different Gram-negative bacteria such as: *Paracoccus pantotrophus* [107] , *Nitrosomonas europaea* [126], *Rhodobacter capsulatus* [127], *Methyloccocus capsulatus* Bath [128], *P. stutzeri* [129], *Marinobacter hydrocarbonoclasticus* [130], *N. gonorrhoeae* [118], *S. oneidensis* [131] and *G. sulfurreducens* [115, 132] (Table 1.1).

Table 1.1 – Summary of the biochemical properties of BCCPs studied up-to-date.

Species name	Electron donor ([ED]) [a]	K_M H_2O_2 (μM)	K_M ED [b] (μM)	k_{cat} (s^{-1})	pK [c]	Reduction potential (mV *vs.* SHE) E heme	Reduction potential (mV *vs.* SHE) P heme	Ref.
Geobacter sulfurreducens CcpA	$ABTS^{2-}$ (3 mM) [d]	6.2	-	15.5	6.8; 9.1	-	-	*132, 133*
Geobacter sulfurreducens MacA	$ABTS^{2-}$ (3 mM) [d]	38.5	-	0.46	-	-	- 241	*115*
Marinobacter hydrocarbonoclasticus	cytochrome c_{552} (38 μM)	-	122	2033	-	-	-	*130*
Methylococcus capsulatus	cytochrome c_{555} (9 μM)	0.5	-	7.1	-	+ 432	- 254	*128*
Nitrosomonas europaea	horse heart cytochrome *c* [d]	-	-	3	6.5; 8.4	+ 450	- 260	*126, 134, 135*
Paracoccus pantotrophus	cytochrome c_{550} (23 μM)	-	13	1417	7.0	+ 226	- 200	*136-139*
	pseudoazurin	-	>50	-				
Pseudomonas aeruginosa	cytochrome c_{551} (13 μM)	6	88	143	4.4; 7.0; 10.0	+ 320	-330	*124, 140-144*
	azurin (40 μM)	11	120	196				
Pseudomonas stutzeri	cytochrome c_{551} (7 μM)	1.8	>50	88.3	-	-	-	*129*
Rhodobacter capsulatus	cytochrome c_2 (6 μM)	33	60	1060	-	+ 270	- 190 / -310	*127, 145*
Shewanella oneidensis	cytochrome c_5 (4 μM)	0.3	-	73	6.4;8.8 [e]	-	-	*131, 146*

[a] Concentrations in parenthesis are the ones used to calculate the kinetic parameters presented (K_M and k_{cat}).

[b] K_M values for the electron donor are an estimative, as the concentrations used are below this value, except for cytochrome c_{550} from *P. pantotrophus*.

[c] pK values determined by steady-state kinetics or protein-film voltammetry.

[d] In the absence of a physiological electron donor, the synthetic electron donor $ABTS^{2-}$ or the reduced horse heart cytochrome *c* were used.

[e] These values were determined for a H81G BCCP mutant.

1.3.2 Physiological role of bacterial peroxidases

All the previously discussed catalases and peroxidases (such as Ahp, KatG, KatE) are cytoplasmatic enzymes. BCCPs are the only peroxidases located in the periplasm and this suggested that their role *in vivo* is to protect the cells from exogenous hydrogen peroxide or the one produced in the ET chain in the inner membrane (Figure 1.13). In particular, the pathogenic bacteria encounter exogenous peroxides during oxidative burst by macrophages and tissue inflammation.

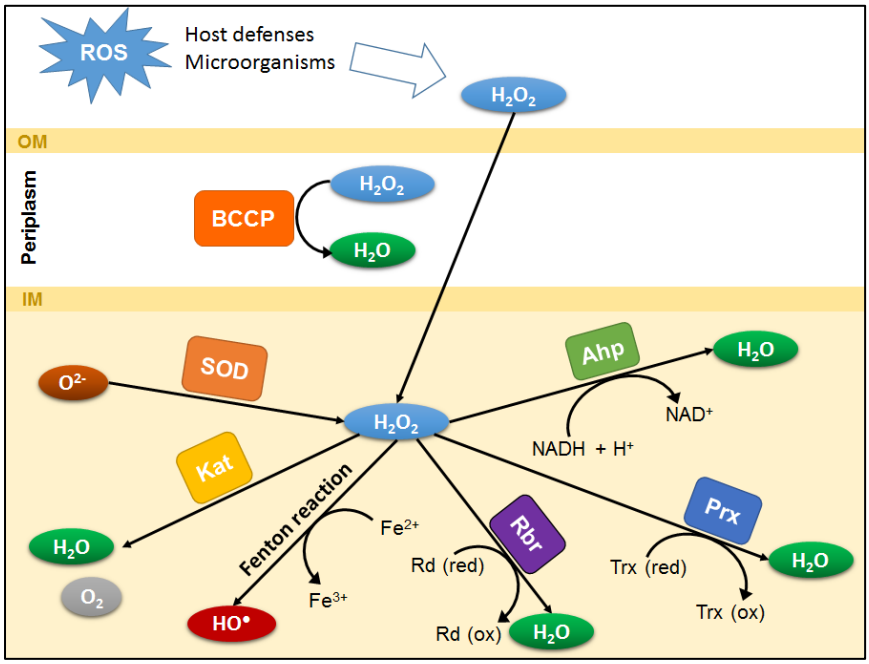

Figure 1.13 – Schematic representation of the oxidative stress responses in a Gram-negative bacteria. The proteins and reactions represented might not occur at the same time in one single organism. BCCP is the only enzyme with peroxidase activity in the periplasm. SOD – Superoxide dismutases; Kat – Catalases; Ahp – Alkylhydroperoxide reductase; Prx – thiol-based peroxidases (BCP, Tpx, Gpx); Trx – thioredoxin; Rbr – rubrerythrin; Rd – Rubredoxin; OM – Outer membrane; IM – Inner membrane.

The most recent works have been focused on BCCPs from bacteria involved in dissimilatory metal-reduction, such as *S. oneidensis* and *G. sulfurreducens*. In the first, BCCP plays a role as hydrogen peroxide scavenger as a *S. oneidensis ccp* mutant resulted in significant loss of the cells peroxidase activity [147]. The second is a micro-aerotolerant bacteria that, as mentioned, has two *ccp* genes that encode CcpA[132] and MacA [115]. MacA is an example of a BCCP that has peroxidase activity but it also has the ability to channel electrons to a soluble trihemic cytochrome PpcA, suggesting a double role for this enzyme in the periplasm of this bacterium [115].

In pathogenic bacteria such as *N. gonorrhoeae*, a *katA* and *ccp* double mutant was much more sensitive to hydrogen peroxide in disc diffusion assays, than a *katA* mutant alone. However, a *ccp* single mutant was not much more sensitive than the wild-type [118]. Nevertheless, it has been reported that this BCCP plays a crucial role during infection [148].

In *C. jejuni*, deletion of each of the two putative *ccp* genes, encoding DocA and Cjj0382, showed that these strains had a 10^5-fold and 50-fold reduction in colonization of chick cecum, respectively. This suggested a different role for the BCCPs in this bacterium during colonization, while its catalase (KatA), seemed to be responsible for hydrogen peroxide resistance.

It seems that BCCPs play a role as hydrogen peroxide scavengers and in virulence as this enzyme is important in colonization settings, specially in pathogenic bacteria.

1.3.3 Bacterial cytochrome *c* peroxidase phylogenetic groups

The bacterial peroxidases are a wide group of enzymes that contain *c*-type hemes as cofactors. The classical BCCPs have a core scaffold that is constituted by two domains, each binding a *c*-type heme, and are soluble proteins in the periplasm (Figure 1.14A). However, there are other types of dihemic BCCPs that are anchored to the inner-membrane by a transmembrane helix or to the outer-membrane by a lipid-modified residue, such as the ones from *Deinococus radiodurans* (Figure 1.14B) and *N. gonorrhoeae* [118] (Figure 1.14C), respectively.

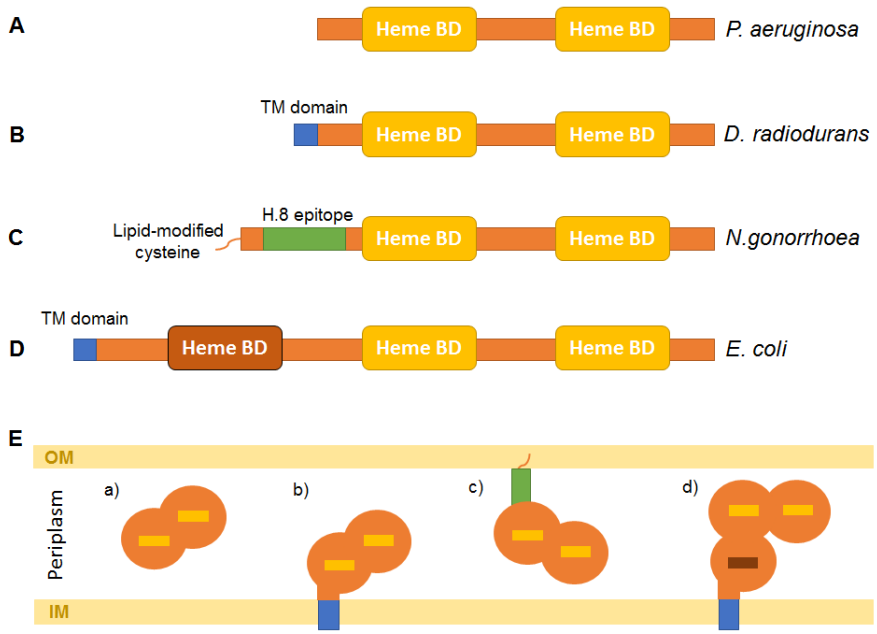

Figure 1.14 – Schematic representation of the BCCPs primary sequence (A-D) and of their respective location in the periplasm (E). (A) The *P. aeruginosa* BCCP is soluble in the periplasm and has two *c*-type heme binding domains (Heme BD). (B) The putative *D. radiodurans* BCCP has a transmembrane (TM) domain predicted as a transmembrane helix that anchors the enzyme to the inner membrane (IM). (C) The *N. gonorrhoeae* BCCP is bound to the outer membrane (OM) by a lipid-modified cysteine and has a linker region (named H.8 epitope) that confers flexibility within the periplasm. (D) The *E. coli* BCCP has three heme binding domains, two of them homologous to the other BCCPs and an extra N-terminal heme binding domain. Similar to *D. radiodurans* it has a transmembrane helix that anchors the enzyme to the IM. (E) The putative structure of each BCCP type is represented by the various heme domains (orange circles) with respective heme (yellow bars).

Another group of BCCPs with three *c*-type hemes, initially identified by phylogenetic analysis of BCCPs primary sequences [22], has not yet been significantly explored. Two heme domains are homologous to the dihemic BCCPs and a third N-terminal heme domain is completely new (Figure 1.14D). These trihemic BCCPs are also anchored to the membrane by a transmembrane helix [149]. There are only a few studies in trihemic BCCPs from *Aggregatibacter actinomycetemcomitans* [149-152] and *Zymomonas mobilis* [153] that have quinol peroxidase activity, which means they use the quinol pool reductive power to reduce hydrogen peroxide. Other trihemic enzymes can be found in pathogenic bacteria, such as *Salmonella typhimurium* and *Yersinia pestis* [22]. There is still much to learn about this type of bacterial peroxidases, which include *E. coli* BCCP YhjA. This enzyme was one of the BCCPs studied in this thesis, therefore, further information regarding this group will be addressed in a separate chapter dedicated to YhjA (Chapter 5).

There are other groups of BCCPs or BCCP-like proteins, such as the orthologous MauG proteins and the extracellular rubber oxygenase RoxA from *Xanthomonas* sp. These proteins have two *c*-type hemes and share structural similarities, but do not have the same physiological role.

The MauG proteins can be found in many Gram-negative bacteria that use methylammonium as a carbon and nitrogen source. These proteins are involved in the formation of tryptophan-tryptophylquinone (TTQ), a co-factor of methylamine dehydrogenase (MADH). MauG forms TTQ by binding and activating oxygen, and linking two tryptophan residues of MADH. These enzymes, although having high sequence homology and structural similarity to BCCP, present little peroxidase activity suggesting common ancestral gene for MauG and BCCP [154, 155].

The RoxA, a 75 kDa protein secreted by *Xanthomonas* sp., is a dioxygenase that catalyzes the slow cleavage of cis-1,4-polyisoprene, present in the latex milk from rubber trees, to 12-oxo-4,8-dimethyl-trideca-4,8-diene-1-al [156]. The majority of the protein structure consists in unstructured loop regions explaining the high molecular mass compared to BCCP, which is typically about 35 kDa. RoxA has low sequence homology but a portion of its core structure surrounding the heme domains, is similar to BCCP structure suggesting that they are evolutionary related enzymes [157].

1.3.4 Classical bacterial peroxidases - Characterization of *c*-type hemes

In early studies it became clear that BCCPs have a high potential heme capable of receiving electrons from sodium ascorbate or small electron donor proteins, named the electron transfer heme (E heme) [158, 159] and a low-potential heme, which could only bind exogenous substrates when E heme was reduced, named the peroxidatic heme (P heme).

It was possible to assign the axial ligands of each heme using NIR-MCD at cryogenic temperatures. BCCPs are isolated with both hemes in the oxidized state. In this oxidized state, the P heme has features of a low-spin bis-histidine coordinated heme and E heme, of a low-spin histidine-methionine

coordinated heme. At room temperature, E heme showed also high-spin features suggesting a high/low-spin equilibrium that was attributed to a weak methionine-iron bond. When E heme is reduced (mixed-valence state) the P heme becomes penta-coordinated and therefore, high-spin (featuring bands between 700-1300 nm) [160, 161]. In the visible spectra of mixed-valence BCCPs there are two characteristic bands of this penta-coordinated ferric heme, one at 350-380 nm and another less intense charge-transfer band at 600-640 nm that is also found in the visible spectrum of the penta-coordinated cytochrome *c'* [21]. This mixed-valence state is the BCCP active form.

The reduction potential of each heme varies greatly among BCCPs (see all values in Table 1.1). For E heme between + 226 mV (*P. pantotrophus* BCCP [137]) to + 450 mV (*N. europaea* BCCP [126]), while P heme reduction potential ranges from - 150 mV (*P. pantotrophus* BCCP [137]) to - 330 mV (*P. aeruginosa* BCCP [140]).

1.3.5 The activation mechanism

To achieve maximum catalytic activity BCCPs require calcium ions and reductive activation, with the exception of *N. europaea* and *M. capsulatus* BCCPs. Reductive activation refers to reduction of E heme with consequent formation of the penta-coordinated P heme.

The importance of calcium ions was first studied in *P. pantotrophus* BCCP since without excess calcium ions, the mixed-valence state enzyme had little catalytic activity [138, 162]. In fact, in *P. pantotrophus* and *P. stutzeri* BCCP, removal of calcium ions by EGTA led not only to an inactive enzyme but also to the disappearance of the P heme high-spin bands at 380 nm and 630 nm in the visible spectrum [129, 138, 162]. This led to the conclusion that calcium ions were essential to form the penta-coordinated P heme in the mixed-valence active form (Figure 1.15).

Furthermore, ultracentrifugation, differential scanning calorimetry (DSC) and chromatographic techniques demonstrated that BCCPs in solution are in a monomer-dimer equilibrium and that addition of calcium ions or a higher ionic strength in *P. pantotrophus* BCCP led to homodimerization [162-164] (Figure 1.15B). *P. stutzeri* BCCP was purified as a dimer and addition of calcium ions led to the formation of a tetramer, while removal of calcium ions by EGTA led to a monomeric population in solution (Figure 1.15C). This is the only case where a tetramer was reported.

Hence the active form of BCCP requires calcium ions, is dimeric and the P heme is high-spin, penta-coordinated. Analysis of the activation mechanism of *P. stutzeri* BCCP by mediated cyclic voltammetry (using its redox partner, cytochrome c_{551}) showed that the activation process is fast as there was no difference in results when using the oxidized or the mixed-valence states of the enzyme [165].

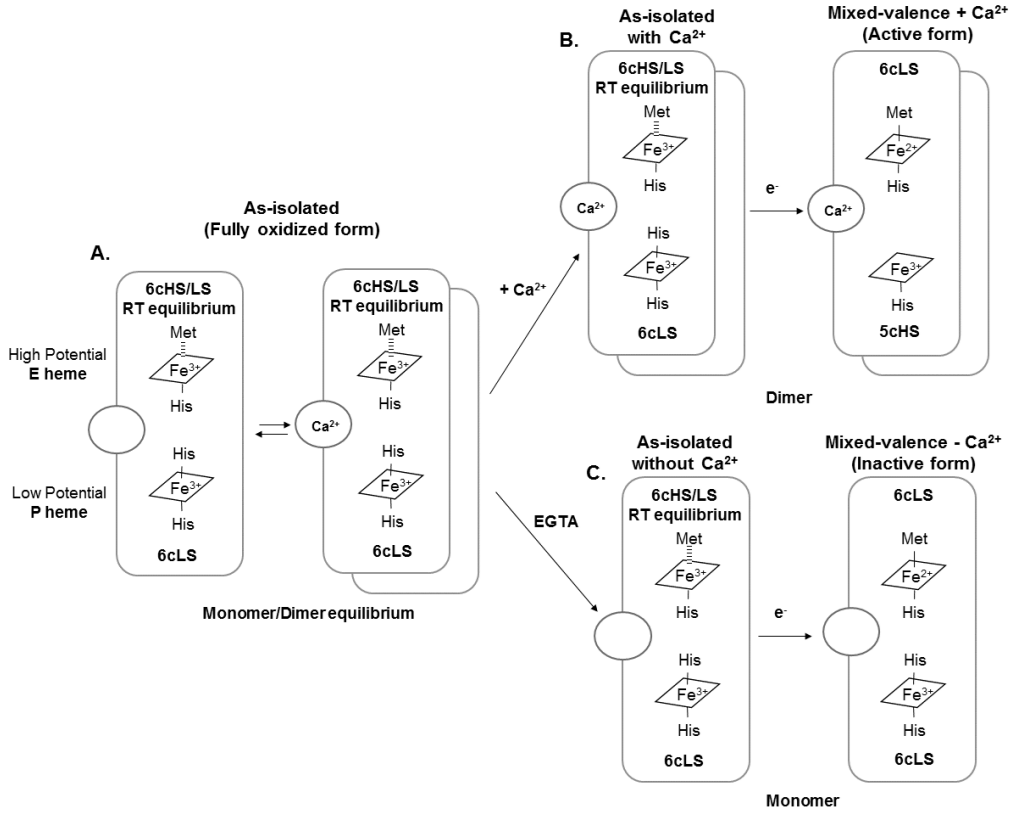

Figure 1.15 – Activation mechanism of BCCPs. (A) The as-isolated BCCP has a His/Met hexa-coordinated E heme in a high/low-spin (6cHS/LS) equilibrium at room temperature (RT) due to a loosely bound methionine residue (dashed line). The low potential P heme is hexa-coordinated and low-spin (6cLS) with two axial histidine ligands. Typically it is in a monomer-dimer equilibrium and becomes fully dimeric in the presence of calcium ions. (B) When E heme is reduced by a small redox protein or a reducing agent, such as sodium ascorbate, if there are calcium ions, the P heme becomes penta-coordinated, high spin (5cHS), and this is the mixed-valence active form (C) Removal of calcium ions by a calcium chelator such as EGTA, induces monomerization of BCCP. In the mixed-valence state the P heme continues to be 6cLS and the enzyme is inactive.

1.3.5.1 The calcium binding site

Although it was known that calcium ions were essential for dimerization and for activation, prior to the crystallographic structures it was not clear how many calcium ions existed per protein nor the location of the calcium binding site. The early data from *P. pantotrophus* BCCP suggested the existence of two calcium binding sites [162], one with higher affinity (site I, K_D = 1.2 µM) and usually fully occupied, and the other with lower affinity (site II, K_D = 0.52 mM) and empty/partially occupied in the oxidized state. It was proposed that calcium in site II was required for the activation of the enzyme and for enzyme activity. The *P. aeruginosa* BCCP is purified with calcium tightly bound to the protein (K_D = 0.3 nM), which is sufficient to acquire a fully active, dimeric form of the enzyme [124, 166]. For this reason there was no biochemical studies on the role of calcium ions on the activation of this enzyme until recently, when the mixed-valence structure was solved by Echalier and co-workers showing that as calcium ions were removed the enzyme became inactive [166].

Therefore, the enzyme from *P. pantotrophus* needed additional calcium ions, which were lost throughout the purification process, probably due to a low binding affinity. In the case of *P. stutzeri* BCCP and *P. aeruginosa* BCCP, these two enzymes have high calcium affinity and therefore, it is not lost even when EDTA was used in the preparation of the spheroplasts [129, 141]. This demonstrates that this property is not identical in all BCCPs.

When the first crystallographic structures were published, it was found that BCCPs bind one calcium ion per monomer between the two heme domains (Figure 1.16) [108, 167, 168]. In these structures the calcium atom is coordinated by four water molecules and three conserved residues: the amide oxygen from Asn79 side-chain and the carbonyls from Thr256 and Pro258 (*P. aeruginosa* numbering) [108].

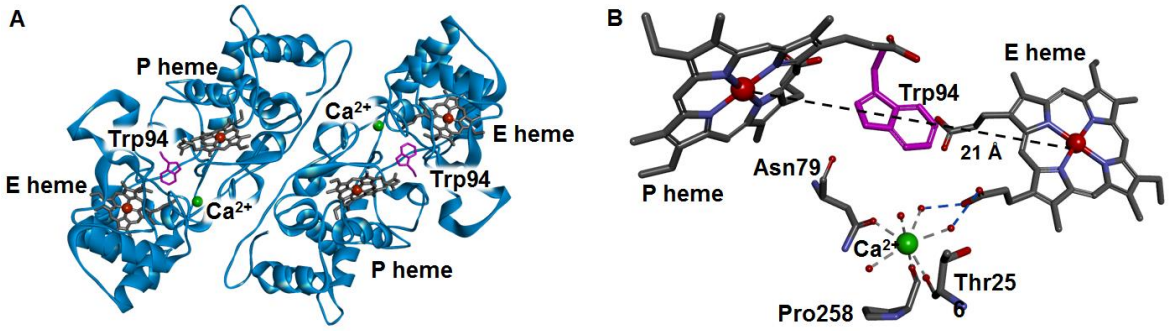

Figure 1.16 – (A) Crystallographic structure of *P. aeruginosa* BCCP in the mixed-valence state. The asymmetric unit is a homodimer. Each monomer has two hemes, E heme and P heme, a calcium atom (green sphere) between the two heme domains and the conserved tryptophan (purple). (B) The calcium binding site is coordinated by four water molecules and the oxygens from carboxyl group from Thr256 and Pro258, and from the side chain of Asn79. Two of the waters are coordinated by the propionate group A from E heme. Figure prepared with PDB ID: 2VHD.

There was a particular case in which *M. hydrocarbonoclasticus* BCCP was crystallized without calcium, at low, non-physiological pH (4.0). Although both hemes were reduced after exposure to synchrotron radiation, they were hexa-coordinated (named form IN) and the position of the conserved Trp94 changed. This conserved tryptophan residue (Trp 94) with the indole ring positioned between the propionate groups of each heme (a shorter distance of ≈10 Å than the 21 Å Fe-Fe distance) was proposed to act as a bridge between the two redox centers [108]. Point mutations in this tryptophan in *P. aeruginosa* and *R. capsulatus* BCCPs abolished their catalytic activity [169, 170], supporting the role of this tryptophan in the ET pathway between the two hemes. Therefore the tryptophan position should also be conserved. Another structure at pH 5.3 was suggested as the activated form (form OUT) but it could not be reduced by sodium ascorbate. When it was later compared to other mixed-valence structures acquired at physiological pH values (*P. pantotrophus* BCCP) [171] it was clear that these conformations were not relevant for the enzyme, as they were acquired in non-physiological conditions [172], but they indicated that P heme was penta-coordinated.

1.3.5.2 Spectroscopic and structural changes in the activation mechanism

The formation of the high-spin penta-coordinated P heme during activation was thoroughly characterized by various spectroscopic techniques besides the previously mentioned MCD and UV-visible, such as ^{1}H NMR [137, 173], Mössbauer [174] Resonance Raman [175-177] and EPR [126, 129, 160, 166]. A unique property of this high-spin P heme was that it became low-spin at cryogenic temperatures. However, this low-spin species was not the same as the low-spin P heme signal in the oxidized state even though the EPR spectroscopic properties were consistent with a bis-His ligation [137, 161]. In the EPR spectra, the low-spin signal from P heme in the mixed-valence state was also sensitive to the presence or absence of calcium ions. For instance, in *P. aeruginosa* BCCP, in the absence of calcium ions the *g* values were 2.96, 2.26 and 1.49, while in the presence of calcium ions the *g* values changed to 2.86, 2.36 and 1.53 [166]. The first set of *g* values corresponded to the bis-His coordination and the second to a different sixth distal ligand. Similar pairs of *g* values are found in the EPR spectra of BCCPs [35, 115, 126, 129, 131, 137]. The nature of this P heme ligand was not certain until the first mixed-valence BCCP crystallographic structure was solved, for *P. pantotrophus* BCCP, showing a water molecule bound to the P heme. Thus, although water is typically a weak ligand, it acts as a strong ligand at cryogenic temperatures, as proposed by Echalier *et al.* [171] (Figure 1.17C).

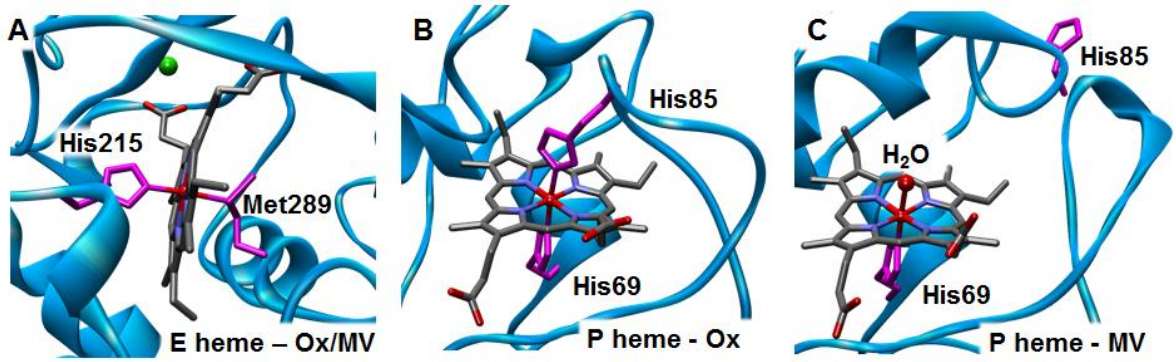

Figure 1.17 – Molecular structure of (A) E heme and (B) P heme in the oxidized (Ox) state and (C) P heme in mixed-valence (MV) state in *P. pantrotrophus* BCCP. The heme axial ligands are shown in purple. Figure prepared with PDB ID: 2C1U and 2C1V for the oxidized and mixed-valence structures, respectively.

The first BCCP crystallographic structures were all in the oxidized state [108, 169] therefore the mixed-valence structures not only clarified the identity of the sixth ligand, but they were crucial to understand how the reduction of one heme, the E heme, triggered the removal of the P heme distal ligand, since these two hemes are located in distinct protein domains.

Structural comparison between the oxidized and mixed-valence states of the BCCPs from *P. pantotrophus* and *P. aeruginosa* revealed the activation mechanism. When E heme receives an electron, changes occur at the D propionate group (the authors suggested the uptake of a proton at

the propionate group) that triggers the movement of loop regions, mainly a loop (described in *P. pantotrophus* BCCP as region 105-132) between the two heme domains that moves to the dimer interface leading to the loss of the P heme distal histidine ligand (located in this loop) [171]. Conformational changes in *P. pantotrophus* BCCP during activation were further addressed using resonance Raman spectroscopy which showed changes in P heme environment, which became high-spin in the presence of calcium, while the E heme suffered little change. These changes created a strong saddling deformation (out-of-plane distortion) of the P heme, which was also observed in other peroxidases and in the BCCPs crystallographic structures [175, 176].

The functional and structural data of the oxidized/mixed-valence *P. aeruginosa* BCCP further confirmed that this was only possible if there was one calcium ion per protein [166, 171]. Furthermore, in the mixed-valence state of this BCCP, the loop carrying the P heme histidine ligand (His71) at the dimer interface, stabilizes the dimer by a π-stacking interaction between the tryptophan side chain and the peptide bond of a glycine in the opposite monomer (Gly72-Trp73 residues in *P. aeruginosa* BCCP X-ray structure [166], Figure 1.18). This tryptophan is conserved in most BCCPs described up-to-date.

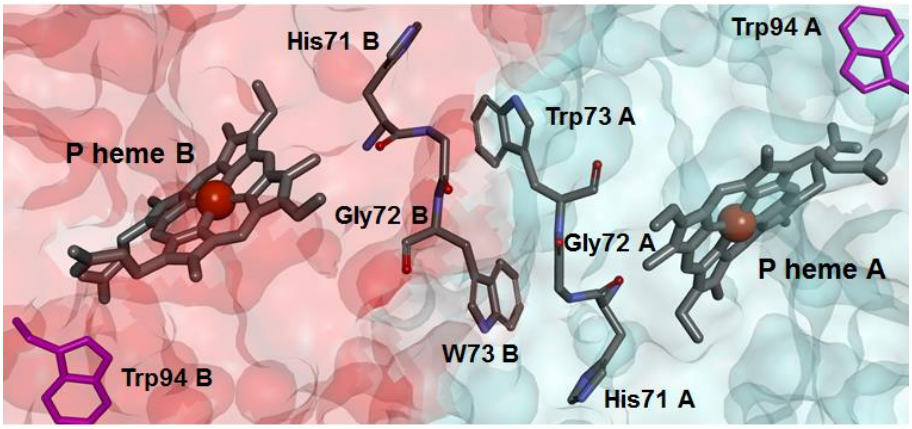

Figure 1.18 – Dimer interface of *P. aeruginosa* BCCP. A π-stacking interaction between the tryptophan (Trp73) and the glycine (Gly72) of the opposite monomer stabilizes the loop that carries the P heme histidine distal ligand (His71). The surfaces of chain A and B are colored in blue and red, respectively. Figure prepared with PDB ID: 2VHD.

Dimerization was considered to be essential for activity, however, a recent study with a *S. oneidensis* BCCP mutant unable to form a dimer, proved that in the monomeric mixed-valence form this enzyme was active. However, the lifetime of the activated form diminished compared to the wild-type [178]. Therefore, dimerization might have a role in stabilizing the conformation of the active form, mainly of the loop with the P-heme distal histidine ligand, reason why all described BCCPs are homodimers.

1.3.6 The catalytic mechanism

BCCPs catalyze the reduction of hydrogen peroxide to water. To perform a complete catalytic cycle, two consecutive electron transfers delivered by a small redox protein to E heme, are needed to reduce one molecule of hydrogen peroxide at the P heme, the active site (1.13) and to return the enzyme to the active form (1.14) releasing a total of two water molecules, as follows:

$$e^- + H_2O_2 + Fe^{3+} \rightarrow H_2O + Fe^{4+}{=}O \qquad (1.13)$$

$$Fe^{4+}{=}O + e^- + 2H^+ \rightarrow H_2O + Fe^{3+} \qquad (1.14)$$

Figure 1.19 shows a model of the as-isolated fully oxidized form and mixed-valence active form of a BCCP, its mechanism and intermediary species.

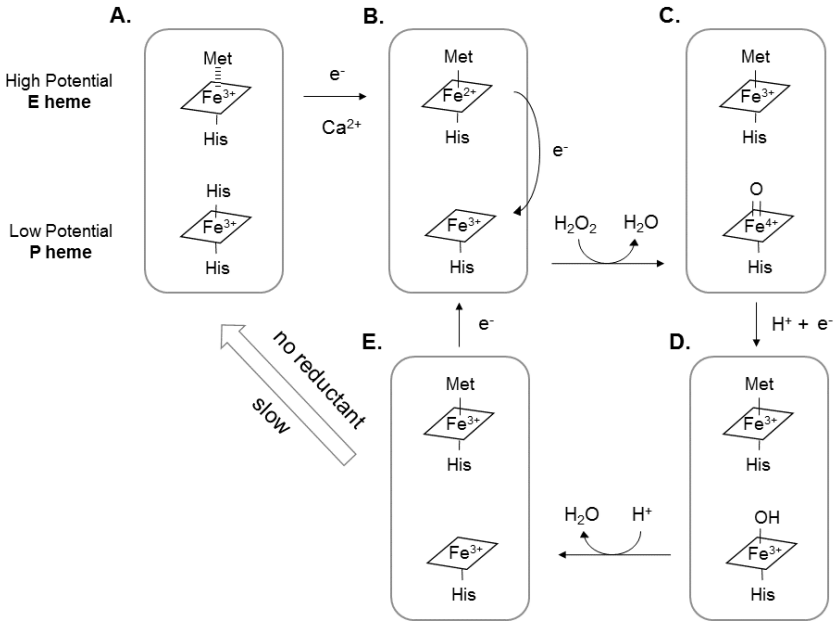

Figure 1.19 – Schematic representation of the bacterial cytochrome *c* peroxidases (BCCPs) E and P hemes redox state, axial ligands and the intermediary species formed during its catalytic cycle. For ease of representation only one monomer of the BCCP is represented. (A) The as-isolated BCCP is fully oxidized and inactive. (B) The electrons are delivered by a small redox protein to E heme, which becomes reduced leading to conformational changes that remove the distal histidine ligand in P heme. (C) E heme transfers one electron to P heme, the active site, which reduces hydrogen peroxide, releasing a water molecule and one oxygen remains bound, forming a Fe^{4+}-oxo intermediary species (compound I). (D) One electron from the electron donor and one proton forms the Fe^{3+}-OH (compound II) and (E) addition of another proton releases a second water molecule. If there is reductive power the cycle continues to (B), otherwise it slowly reverts to (A). The dashed methionine bond in the as-isolated state is representative of the E heme high/low-spin equilibrium at room temperature. Adapted from Pettigrew *et al.* [179].

The reduction of H_2O_2 requires two electrons, one electron from the ferrous E heme and one from P heme, which becomes Fe^{4+} releasing a water molecule. The remaining oxygen from the H_2O_2 forms a Fe^{4+}-oxo species (oxoferryl, Figure 1.19C). Evidence of this species (compound I) was first described in rapid mixing and freezing MCD and EPR experiments in *P. aeruginosa* BCCP [35, 180].

The spectra showed features similar to the equivalent oxoferryl species in eukaryotic monohemic peroxidases (horseradish and yeast peroxidases).

Furthermore, the data was consistent with both hemes iron being Fe^{3+} afterwards, as shown in Figure 1.19D, E. The formation of this oxoferryl species involves an intermediate protein radical species, as described for a *P. aeruginosa* BCCP mutant (H71G) that lacked the P heme histidine distal ligand in the oxidized state. When the oxidized BCCP mutant was mixed with excess hydrogen peroxide, there was a shift in the Soret band consistent with formation of a protein radical. This was similar to what was observed in the visible spectra of horseradish peroxidase, for a tryptophan radical species, further confirmed by EPR [181]. The authors proposed a "charge hopping" mechanism in the process of intra-molecular electron transfer and that a possible candidate for this radical was the tryptophan residue between the heme domains [170, 182].

The reduction of the oxoferryl species by one electron (donated by the small redox protein) is proposed to be coupled to two proton transfers, the first forms Fe^{3+}-OH (Figure 1.19D) and the second releases a water molecule (Figure 1.19E). At this stage, the protein is in an equivalent redox state to the inactive as-isolated protein, however P heme is still penta-coordinated. As long as there is sufficient reducing power, the BCCP does not decay back to the as-isolated state, since this is a slow process [179]. This inactivation was proposed as a defense mechanism, as it does not allow hydrogen peroxide to bind if there are insufficient electrons to reduce it to water and also avoiding damage to the active site [179].

In the catalytic cycle, the proton donors are proposed to be the conserved residues in the P heme cavity, Gln118 and Glu128 (other conserved residues are Phe107, Pro122 and Met 129, *P. pantotrophus* X-ray structure numbering, Figure 1.20) as they are in close proximity to the P heme iron. In fact, mutation of the conserved glutamine, glutamate and methionine residues in *R. capsulatus* BCCP results in an inactive enzyme. Mutation of the phenylalanine residue also inactivates a *S. oneidensis* BCCP [146].

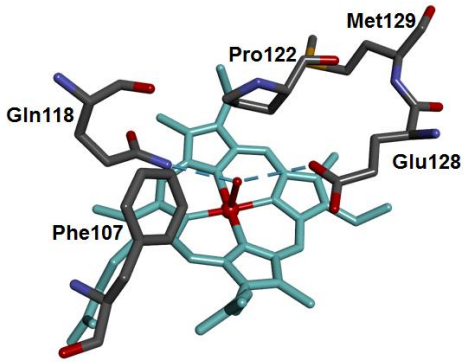

Figure 1.20 – The P heme cavity of *P. pantotrophus* BCCP has five highly conserved residues: Phe107, Gln118, Pro122, Glu128 and Met129. Two of these residues, Gln118 and Glu128, are within hydrogen bond distance from the water molecule coordinating the P heme (dashed lines). Figure prepared with PDB ID: 2C1V.

The peroxidatic activity is pH dependent and typically has two p*Ka* values, one 6-7 and another between 8-10 (see Table 1.1). A lower p*Ka* value of 4.4, in *P. aeruginosa* BCCP was associated to an acid group involved in the formation of Compound I [143]. This suggests that at these pH values, the protonation state of key residues changes. One of such residues can be the glutamate, which is in close proximity to the iron center.

Another important step in this catalytic cycle is the heterolytic cleavage of the peroxide O-O bond that leads to the formation of the intermediate oxoferryl species. In eukaryotic peroxidases, the distal histidine ligand is essential for this role, but in the BCCPs active form this residue is too distant from the P heme cavity. It was suggested that, similarly to the chloroperoxidases, BCCP uses the conserved glutamate as the catalytic residue [167].

So far, regarding BCCPs catalytic mechanism, there is no structural evidence of this hydrogen peroxide intermediary species and X-ray crystallographic structures do not give information regarding the protonation stages. Nevertheless, this information could be obtained using neutron cryo-crystallography as described for the yeast CCP, which not only showed the formation of the oxoferryl species, but also the protonation state of the distal histidine and other important residues in the heme cavity [183], allowing to infer possible catalytic pathways.

The steady-state kinetics of BCCPs showed the maximum catalytic activity of the active form can be achieved with concentrations of hydrogen peroxide in the micromolar range (usually K_M values < 40 µM H_2O_2, see Table 1.1) and high turnover numbers (e.g. 1060 s^{-1} for *R. capsulatus* BCCP/cytochrome c_2 redox pair [127]). The lowest K_M value reported up to date is for the tag-free *S. oneidensis* BCCP/cytochrome c_5 physiological redox pair, in unsaturated conditions, with a K_M of 0.3 µM H_2O_2 [131].

Regarding the catalytic mechanism and more specifically its intermediary species, there is still little information. Nevertheless, kinetic assays and comparison of the P heme biochemical and structural properties (active center) of multiple enzymes have proven essential to the understanding of this mechanism.

1.3.6.1 Nitrosomonas europaea BCCP – a different catalytic mechanism?

N. europaea BCCP was the first reported bacterial peroxidase to not require reductive activation for maximum activity [126]. This trait was only found in one more BCCP, the one isolated from *M. capsulatus* Bath [128].

The crystallographic structure of *N. europaea* BCCP was the first available structure of an active form of the enzyme, in which P heme was penta-coordinated (high-spin) [167]. Although the protein was oxidized, later on it was clear that this oxidized BCCP structure was identical to the mixed-valence structure of other BCCPs and it did not need an additional reduction step of the E heme to be active.

Furthermore, *N. europaea* BCCP showed all the typical features of other BCCPs: similar calcium binding-site, E and P hemes, a tryptophan between the two hemes and other structural similarities. This suggested a similar enzymatic mechanism. Nevertheless, an apparently different intermediary Fe^{4+}-oxo species was detected when adding hydrogen peroxide to the oxidized *N. europaea* BCCP. Rapid changes in the Soret region of the visible spectra were consistent with the formation of a Fe^{4+}-oxo radical species (Fe^{4+}=O $R^{+\cdot}$) [126]. This radical was proposed to be a porphyrin π cation radical [134], instead of the tryptophan radical, as described before.

Catalytic protein film voltammetry showed a high-potential E_{cat} (+ 540 mV), unique to *N. europaea* BCCP, which was assigned to an active species at the P heme that is dependent on pH and represents an one electron proton-coupled process [135], such as the one proposed in Figure 1.19 between (C) and (D). The major difference in this BCCP, according to the authors, is that the E heme does not store the electron for the catalytic reaction in the P heme, as hydrogen peroxide binds to the oxidized BCCP forming the Fe^{4+}=O $R^{+\cdot}$ without requiring a reduced E heme [134, 135]. However, it should be noted that the E heme domain, the electron transfer domain, remains conserved and that overall *N. europaea* BCCP is identical to the activated forms of all other classical BCCPs.

In fact, a recent work comparing a *S. oneidensis* BCCP H81G (histidine following the P heme distal histidine ligand His80) with *N. europaea* BCCP, using the same technique, showed a similar pH dependence and that the rate-limiting step of the first enzyme also involves a proton-coupled single electron reduction of a high valent iron species (centered approximately at + 450 mV) at the P heme [146]. The *S. oneidensis* BCCP H81G mutant showed that the loop in which the P heme histidine ligand is located, shifts during the rate limiting step. In the absence of His81, the catalytic intermediary of this BCCP had the same electron stoichiometry and pH dependence as *N. europaea* BCCP. Therefore, the intermediates between these two BCCPs had more similarities than originally believed.

In sum, although *N. europaea* BCCP does not require reductive activation, there is no clear indication that the catalytic mechanism is significantly different nor that *in vivo* the electron pathway does not pass through E heme. These intermediate species appear to be similar in other BCCPs, but besides *P. aeruginosa* BCCP H71G mutant, they have not been demonstrated because P heme is only accessible in the mixed-valence state, where such a species would be rapidly reduced by E heme.

1.3.7 Electron donors – small redox proteins

The small redox proteins that donate electrons to the BCCPs are either monoheme cytochrome *c* proteins or type 1 copper proteins, such as azurins or pseudoazurins [139, 158, 159].

Heteronuclear NMR and docking studies with *P. pantotrophus* BCCP and the cytochrome *c* or pseudoazurin electron donors showed that these two small redox proteins interact at the same site, at E heme, which has a hydrophobic surface surrounded by charged residues [159, 184]. These

protein-protein interactions can be electrostatic as described for *P. pantotrophus* [184] and for *R. capsulatus* BCCP/cytochrome c_2 pair[185]. The cytochrome c_2 has an interaction surface with charged lysines that when lost, disrupts the interaction with BCCP [185]. A ring of lysines has also been described in *P. pantotrophus* pseudoazurin, surrounding a hydrophobic patch containing the ET site. The ET complex can have a hydrophobic character, as for *M. hydrocarbonoclasticus* BCCP/cytochrome c_{552}, in which the activity remains unchanged throughout a wide range of ionic strengths [130].

A small interface, weak and fast interactions, are essential to achieve the high catalytic turnovers described previously. Other characteristics, such as pre-orientation and lateral mobility (the electron donor probes the surface of the BCCP) are also important aspects for the formation of a productive ET complex [179]. All these properties will be discussed in detail in Chapter 4, which is focused on the *N. gonorrhoeae* BCCP physiological electron donor.

1.4 Objectives

From the numerous BCCPs studied up until now, none of them were isolated from pathogenic bacteria. Pathogenic bacteria have to withstand the host immune defenses, such as the oxidative burst and a BCCP, located in the periplasm, in this scenario would be crucial for bacterial survival. Also, throughout the introduction, it became clear that most data and knowledge of BCCPs is from dihemic soluble enzymes. Hence, in this thesis, the main objective was to characterize two BCCPs: the globular domain of the membrane-anchored bacterial peroxidase from the obligate pathogenic bacterial species *N. gonorrhoeae* (*Ng*BCCP) and the trihemic BCCP from the ubiquitous bacterial species *E. coli* (YhjA).

It is of great interest to know if this association to the membrane translates into differences in the properties of their globular domains and if the pathogenic origin has led to distinct biochemical and kinetic properties. Also the potential as therapeutic target was to be assessed by inhibition studies, since *N. gonorrhoeae* in particular, still presents a serious threat to human health (Chapter 3).

Relative to *Ng*BCCP, we aimed to demonstrate the role of the neisserial lipid-modified azurin (LAz) as its physiological electron donor. The study of this *Ng*BCCP/LAz electron transfer pair, its interaction and kinetic parameters, constituted the second main objective (Chapter 4).

As very little is known about trihemic enzymes, the main points of interest regarding YhjA were to identify its physiological role *in vivo* and the biochemical characterization of YhjA and its domains, specifically the uncharacterized N-terminal domain (Chapter 5).

As a whole, the goal of this thesis is to gain further knowledge on BCCPs by studying enzymes that have unique features.

Chapter 2

Materials and Methods

2 Materials and Methods

2.1 Chemicals and solutions

Unless otherwise stated, all reagents were of analytical or higher grade and were purchased from Sigma-Aldrich and Fluka. Solutions were prepared in bi-distilled water or Milli-Q water when mentioned. EGTA solutions (ethylene glycol-bis(β-aminoethyl ether)-N,N,N′,N′-tetraacetic acid) were prepared by addition of 1 M NaOH to bring the pH to 8.0.

2.2 Bioinformatic analysis

2.2.1 Sequence analysis

All the analyzed protein sequences were obtained from the Protein database in NCBI (http://www.ncbi.nlm.nih.gov/protein) and the DNA sequences, that were translated, were deposited in the GenBank (http://www.ncbi.nlm.nih.gov/genbank). Multi-sequence alignments were performed using the software Mega6.06 [186] with ClustalW [187]. The secondary structure and transmembrane helices were predicted with Jpred 4 (http://www.compbio.dundee.ac.uk/jpred/) [188] and TMHMM 2.0 (http://www.cbs.dtu.dk/services/TMHMM-2.0/) [189], respectively. Jalview 2.9.0 software was used for sequence representation and consensus analysis [190].

2.2.2 Protein structure and surface analysis

All structures were analyzed and their images prepared on BIOVIA Discovery Studio Visualizer 4.5 except when otherwise stated in the text. Comparison of protein structures and determination of RMSD was performed using SuperPose (http://wishart.biology.ualberta.ca/SuperPose/) [191]. PDB files of superimposed crystallographic structures were created in Chimera 1.10.2.

The dimer interfaces were analyzed in PDBePISA ('Protein interfaces, surfaces and assemblies' service PISA at the European Bioinformatics Institute; http://www.ebi.ac.uk/pdbe/prot_int/pistart.html) [192].

The protein electrostatic surface was analized using Adaptive Poisson-Boltzmann Solver (APBS [193, 194]). The PDB files were treated in PDB2PQR [195] (http://nbcr-222.ucsd.edu/pdb2pqr_2.1.1/) which applies a forcefield (AMBER), assigns charges and radius parameters, optimizes hydrogen bonding networks and assigns protonation states according to pH (7.0) using PROPKA. The final PQR file from PDB2PQR was used as input in the APBS (http://www.poissonboltzmann.org/) to determine electrostatic properties using default parameters. The solvent accessible surface was colored according to electrostatic potential in Chimera, from – 5 to + 5 kT/e (red to blue). The hydrophobic surface was rendered in BIOVIA Discovery Studio Visualizer 4.5, colored from non-hydrophobic residues in green, to hydrophobic residues in mangenta (-3 to + 3: color scale green-white-mangenta).

2.3 Cloning and protein production

2.3.1 *N. gonorrhoeae* cytochrome *c* peroxidase

N. gonorrhoeae bacterial cytochrome *c* peroxidase (*Ng*BCCP) encoding gene (DNA sequence from *N. gonorrhoeae* FA 1090) was synthesized *in vitro* and codon optimized for heterologous expression in *E. coli* and cloned in an *Eco*RV digested pUC57 by NZYtech. In the gene sequence, the regions encoding the signal peptide and H8.epitope segments in the N-terminus of the protein were excluded, in order to obtain a soluble protein. Using this pUC57 as template, the gene was amplified with primers that added a *Nco*I (Forward: CAATGCCATGGGCGAAGATCAGGACCTGCTGAAAC) and a *Xho*I (Reverse: CCAGCTCGAGTTTGTTGTCCGGTTTGCTTT) restriction sites (underlined), for cloning into a pET22b (+) plasmid, named thereafter pET22-*Ng*BCCP. The thermocycling program was the following: 5 min at 95 ºC, 35 cycles of 45 s at 95 ºC, 48 s at 56 ºC and 90 s at 72 ºC, finishing with 10 min at 72 ºC (High-Fidelity Taq, Fermentas). The plasmid pET22b confers ampicillin resistance and adds a signal peptide (*pelB*) to the N-terminus of the cloned gene, to direct the encoding protein to the periplasm, and a C-terminal His-tag to aid in the purification. Therefore, this cloning strategy introduced a Met-Gly at the N-terminus (after cleavage of signal peptide) and a Leu-Glu-6His (HisTag) at the C-terminus.

E. coli strains TOP10 (Invitrogen) and BL21(DE3) (Novagen) were used for plasmid propagation and protein production, respectively. For protein production, *E. coli* BL21(DE3) was co-transformed with pET22-*Ng*BCCP and pEC86 (harboring the ccm genes to produce all the machinery for *c*-type heme biosynthesis and maturation [196], and confers chloramphenicol resistance).

For protein production, four to five colonies of the co-transformed *E. coli* BL21(DE3) with pEC86/pET22-*Ng*BCCP were added to 50 mL of Luria-Bertani (LB) medium (10 g tryptone, 10 g NaCl and 5 g yeast extract per liter) supplemented with 100 $\mu g.mL^{-1}$ ampicillin and 30 $\mu g.mL^{-1}$ chloramphenicol and grown overnight at 210 rpm, 37 ºC. Fresh LB medium, also supplemented with ampicillin and chloramphenicol, was inoculated with 2 % of pre-inoculum. Cultures were incubated under orbital shaking at 37 ºC, 210 rpm until an $O.D._{600nm}$ of 1.5 was reached. At this point, cells were collected by centrifugation at 3500 *g*, 6 ºC, 20 min, and resuspended in half the volume of fresh LB medium containing the same antibiotics (adapted from Fernandes *et al.* [197]). After incubating for 1 h at 37 ºC, 120 rpm, to stabilize the cells, *Ng*BCCP expression was induced at 30 ºC with 0.5 mM IPTG, during 18 h. At the end of the growth, the cells were harvested at 7500 *g*, 6 ºC, 10 min, and resuspended in 50 mM Tris-HCl, pH 7.6 containing protease inhibitors (cOmplete™, Mini, EDTA-free, Protease Inhibitor Cocktail Tablets, Roche).

2.3.2 *N. gonorrhoeae* Lipid-modified azurin

The DNA sequence from *N. gonorrhoeae* FA 1090 encoding the Lipid-modified azurin (LAz) was synthesized without the N-terminal signal peptide and H8.epitope regions leaving only the soluble region which comprises residues 56 to 183 in the amino acid sequence. To the N-terminal of this synthetic sequence it as added the signal peptide from *P. pantotrophus* pseudoazurin [139] (22 residues, plus two other, AT, for correct signal peptide processing) to direct LAz to the periplasm of *E. coli*. This gene was cloned into pET21-c (Novagen) using *Nde*I and *Xho*I restriction sites included in the synthetic sequence.

A new construct was prepared using the previous construct as template, in which the N-terminal signal peptide from pseudoazurin was substituted by *pelB* from pET22b (+) plasmid. The gene was amplified (as described in Section 2.3.1) with primers that added a *Nco*I (Forward: CAATGCCATGGGTAACTGCGCCGCAA) and a *Xho*I (Reverse: CCAGCTCGAGTCAGTCAACCAGGGTAACTTTACCG) restriction sites (underlined), for cloning into a pET22b (+) plasmid. The stop codon (TCA) after the *Xho*I restriction site excludes the His-tag sequence (in pET22b) from the construct. The thermocycling program was the following: 5 min at 95 ºC, 35 cycles of 45 s at 95 ºC, 48 s at 58 ºC and 90 s at 72 ºC, finishing with 10 min at 72 ºC. Both constructs were used for LAz production as follows.

Heterologous production was carried out in *E. coli* BL21 (DE3) (Novagen) grown in LB or M9 minimum media (1.0 $g.L^{-1}$ NH_4Cl, 3.0 $g.L^{-1}$ KH_2PO_4, 6.0 $g.L^{-1}$ $Na_2HPO_4.7H_2O$, 0.5 $g.L^{-1}$ NaCl, 1.2 % glucose, 1 mM $MgSO_4$, 0.01 $mg.mL^{-1}$ thiamine, 18.5 µM $FeCl_3.6H_2O$ and 0.1 mM $CaCl_2.2H_2O$) supplemented with 100 $\mu g.mL^{-1}$ ampicillin and 0.5 mM $CuSO_4$ (LB media) or 0.01 mM $CuSO_4$.(M9 minimum media). ^{15}N labeled LAz was produced in M9 minimum medium that contained 1 $g.L^{-1}$ $^{15}NH_4Cl$ as the sole nitrogen source.

The transformed *E. coli* BL21 (DE3) cells with pET21-LAz/pET22-LAz were grown at 37 ºC, at 210 rpm, to an $O.D._{600nm}$ of 0.4–0.6. Gene transcription was induced with 0.5 mM IPTG for 7 h at 16 ºC and 180 rpm. The cells were harvested by centrifugation at 7500 *g*, at 6 ºC for 10 min, and the pellet was resuspended in 50 mM Tris–HCl at pH 7.6, containing protease inhibitors (cOmplete™, Mini, EDTA-free, Protease Inhibitor Cocktail Tablets, Roche).

2.3.3 *E. coli* YhjA and its domains

Using *E. coli* K-12 genomic DNA as template, *yhjA* gene was amplified and cloned into a pET22b (+) vector without the region encoding for the N-terminal transmembrane domain to obtain a soluble protein (amino acid residues 42-465). Two other clones were prepared, one containing only the N-terminal domain (NT; consisting of the N-terminal *c*-type heme binding domain with residues 42-155) and the other the C-terminal domain (CT; conserved classical bacterial peroxidase domain with two *c*-type heme binding sites comprising the residues 171-465). These DNA sequences were

amplified with *Nco*I (N-terminal) and *Xho*I (C-terminal) restriction sites (as described in Section 2.3.1) and cloned into pET22b (+) vectors (primers in Table 2.1) that confers ampicillin resistance. Two different YhjA constructs were prepared: StrepII_YhjA and YhjA_6His. In the first, a N-terminal StrepII-tag with a TEV protease cleavage site for tag removal after purification was added to YhjA. YhjA_6His, CT and NT domains were cloned with a His-tag at the C-terminus, which also adds two additional residues (LEHHHHHH).

Table 2.1 – Sequence of oligonucleotides used for cloning. The restriction sites are underlined, the StrepII-tag sequence is in the grey box and the sequence of the TEV cleavage site in bold. The His-tag sequence is included in the pET22b (+) vector.

Protein	Primer	Primer Sequence (5'-3')
StrepII YhjA	Forward	CAATGCCATGGCTTGGTCTCATCCGCAGTTT**GAAAAAGAAA ACCTGTATTTTCAG**TCTGCTGTCAGTGAAAATAATAAGG
	Reverse	CCAGCTCGAGTTGTTTATCCTGCATATACGGC
YhjA_6His	Forward	CAATGCCATGGCTTCTGCTGTCAGTGAAAATAATAAGG
	Reverse	CCAGCTCGAGTTGTTTATCCTGCATATACGGC
N-terminal	Forward	CAATGCCATGGCTTCTGCTGTCAGTGAAAATAATAAGG
	Reverse	CCAGCTCGAGGCGCTGTTTTGCAATCC
C-terminal	Forward	CAATGCCATGGCTAATGAACCGGTGCAGCC
	Reverse	CCAGCTCGAGTTGTTTATCCTGCATATACGGC

E. coli strains TOP10 (Invitrogen) and BL21(DE3)/pEC86 (Novagen) were used for plasmid propagation and protein production, respectively. For protein production, all constructs were co-transformed with pEC86, that harbors the *ccm* operon in order to produce all the machinery for *c*-type heme biosynthesis and maturation [14]. This plasmid confers chloramphenicol resistance. The protein production was performed as described for *Ng*BCCP (Section 2.3.1) except for the induction temperature that was 25 ºC instead of 30 ºC.

2.3.4 TEV protease production

Rosetta-Gami (DE3) *E. coli* cells (Novagen) were transformed with the pRK793 plasmid that contains the TEV protease S219V mutant with an N-terminal His-tag. Expression was performed as described by Tropea, Cherry and Waugh [198]. Cells were grown in LB media supplemented with 100 µg.mL^{-1} ampicillin and 30 µg.mL^{-1} chloramphenicol up to an O.D.$_{600nm}$ of 0.5, at 210 rpm, 37 ºC. At this point, protein production was induced by adding 1 mM IPTG and the temperature was reduced to 30 ºC. 4 h after induction the cells were harvested by centrifugation at 7500 *g*, 6 ºC, for 10 min. The pellet was resuspended in 10 mL of 50 mM sodium phosphate buffer, pH 8.0, 100 mM NaCl, 10 % glycerol and 25 mM imidazole, per gram of cells.

2.4 Protein purification

2.4.1 Purification of recombinant *Ng*BCCP

The periplasmic fraction containing the protein was obtained by 5 freeze-thaw cycles and separated from spheroplasts and cell debris by centrifugation at 48000 *g*, 6 ºC, 15 min. Purification was performed in two chromatographic steps. The first step was an affinity chromatography using a 5 mL HisTrap column (GE Healthcare) equilibrated with 20 mM Tris-HCl, pH 7.6 and 500 mM NaCl. The periplasmic fraction was loaded into the HisTrap column and the unbound proteins were eluted with 5 column volumes of equilibration buffer, and an imidazole step gradient was applied from 0 to 500 mM, in equilibration buffer. *Ng*BCCP was eluted with an imidazole concentration between 100-200 mM. The fractions containing *Ng*BCCP were concentrated over a 5 kDa membrane VivaCell70 (Sartorius) and buffer was exchanged to 50 mM Tris-HCl, pH 7.6 with a desalting PD-10 column (GE Healthcare) equilibrated in the same buffer. In the second purification step, this fraction was applied onto a gel filtration chromatographic column (HiLoad Superdex 200 16/600, GE Healthcare) equilibrated with 50 mM Tris-HCl, pH 7.6 and 150 mM NaCl.

All fractions with A_{402nm}/A_{278nm} above 4.0 were considered pure and combined. The final *Ng*BCCP fraction was concentrated and the buffer exchanged to 20 mM HEPES pH 7.5 using a desalting PD-10 column. A 12.5 % Tris-Tricine SDS-PAGE stained for protein (Coomassie blue) and heme content [107] was also used throughout the purification to verify protein purity of the intermediate and final fractions (Figure 2.1). The final protein sample had a purity ratio (A_{402nm}/A_{278nm}) of 4.2. *Ng*BCCP was stored in small aliquots at - 80 ºC, until further use.

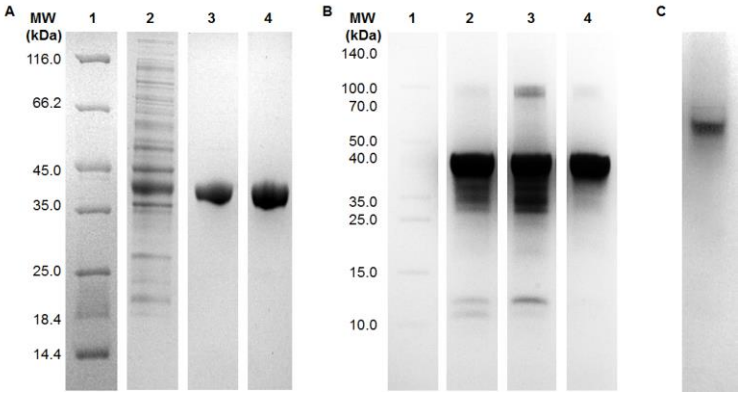

Figure 2.1 – SDS-PAGE of the intermediate purification fractions and the purified *Ng*BCCP in a 12.5 % Tris-Tricine gel stained by (A) Coomassie blue and (B) and heme stained. (Lane 1 - Protein Marker; Lane 2 – periplasmatic extract; Lane 3 – HisTrap final fraction; Lane 4 - purified *Ng*BCCP). (C) Coomassie blue stained PAGE of purified *Ng*BCCP in a 10 % Tris-Tricine gel.

2.4.2 Purification of recombinant LAz

The periplasmic extract was obtained by 5 freeze–thaw cycles, and separated from the whole cell by centrifugation at 48,000 *g*, 6 º C, 15 min. This soluble extract was diluted 5 times with cold distilled

water and loaded onto a DE52 (Whatman) column equilibrated with 10 mM Tris–HCl, pH 7.6. The unbound proteins were eluted with 10 mM Tris–HCl, pH 7.6 and LAz was eluted with a gradient between 0 and 500 mM NaCl in 10 mM Tris–HCl, pH 7.6. The fractions containing LAz were combined and concentrated over a 5 kDa membrane using a Vivacell70 (Sartorius) and loaded onto a HiLoad Superdex 75 16/600 column (GE Heathcare) equilibrated with 50 mM Tris–HCl, 150 mM NaCl, pH 7.6. The fractions purity was assessed by a 15 % Tris-Tricine SDS-PAGE (Figure 2.2 shows gel of final fraction) and the A_{625nm}/A_{278nm} of the oxidized sample.

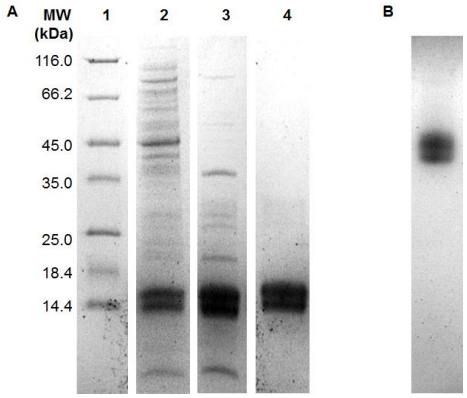

Figure 2.2 – (A) SDS-PAGE of the intermediate purification fractions and the purified LAz in a 15 % Tris-Tricine gel and (B) PAGE of purified LAz in a 10 % Tris-Tricine gel, stained by Coomassie blue (Lane 1 - Protein Marker; Lane 2 – periplasmatic extract; Lane 3 – DE-52 final fraction; Lane 4 - purified LAz).

The fractions were combined, concentrated and the buffer exchanged to 20 mM Tris-HCl, pH 7.6 in a PD-10 desalting column (GE Healthcare). The maximum A_{625nm}/A_{278nm} ratio for the pure sample was 1.0. Protein was stored in small aliquots at – 80 ºC.

2.4.3 Purification of recombinant YhjA and subdomains

The periplasmic fraction was obtained by 5 freeze-thaw cycles and separated from spheroplasts and cell debris by centrifugation at 48000 *g*, 6 ºC, 15 min. Purification of each protein was performed in two chromatographic steps.

In StrepII_YhjA purification the first step was an affinity chromatography using a 5 mL StrepTrap column (GE Healthcare) equilibrated with 100 mM Tris-HCl, pH 7.6 and 500 mM NaCl. After loading the periplasmic fraction, the unbound proteins were eluted with 5 column volumes of equilibration buffer, and afterwards YhjA was eluted with 2.5 mM *d*-desthiobiotin. The fractions containing YhjA were concentrated over a 5 kDa membrane VivaCell70 (Sartorius) and buffer was exchanged to 50 mM Tris-HCl, pH 7.6 and 150 mM NaCl in a desalting PD-10 column (GE Healthcare). In the second purification step this fraction was applied onto a gel filtration chromatographic column (HiLoad Superdex 75 16/600, GE Healthcare) equilibrated with 50 mM Tris-HCl, pH 7.6 and 150 mM NaCl. The fractions purity was assessed in a 12.5 % Tris-Tricine

SDS-PAGE stained for protein (Coomassie blue) and heme content [107]. The fractions were combined, concentrated and desalted using a PD-10 column equilibrated in 20 mM HEPES pH 7.5. The final sample had a purity ratio (A_{407nm}/A_{280nm}) of 3.2.

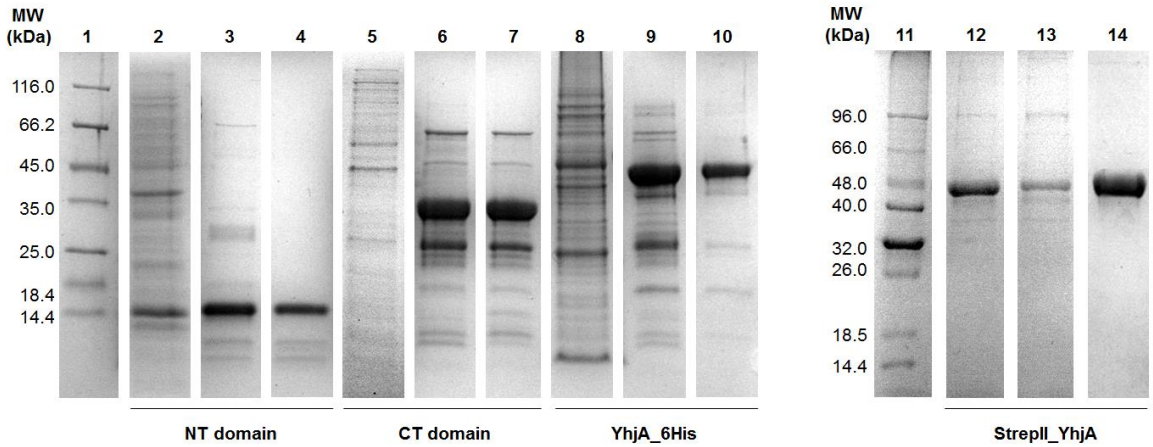

Figure 2.3 – Coomassie blue stained SDS-PAGE of the intermediate purification fractions and the purified protein samples of the NT domain (2-4), CT domain (5-7), YhjA_6His (8-9) and StrepII_YhjA (12-14) in a 12.5 % Tris-Tricine gel (Lanes 1 and 11 - Protein Markers; Lanes 2, 5, 8 and 12 – periplasmatic extracts; Lanes 3, 6 and 9 – HisTrap final fractions; Lane 13 – StrepTrap final fraction; Lanes 4, 7, 10, 14 - purified proteins).

For YhjA_6His, NT and CT domains, the periplasmic fraction was loaded into a 5 mL HisTrap column (GE Healthcare) equilibrated with 20 mM Tris-HCl, pH 7.6 and 500 mM NaCl. The unbound proteins were eluted with 5 column volumes of equilibration buffer, and afterwards an imidazole step gradient was applied from 0 to 500 mM in equilibration buffer. Both proteins were eluted with 100-200 mM imidazole. The fractions were concentrated over a 5 kDa membrane VivaSpin4 (Sartorius) and the buffer exchanged to 20 mM Tris-HCl, pH 7.6 with a desalting NAP-5 column (GE Healthcare). This fraction was injected onto a 1 mL Resource Q (GE Healthcare) equilibrated with 20 mM Tris-HCl, pH 7.6. An ionic strength gradient between 0 and 500 mM was applied and proteins eluted with 100-150 mM NaCl. The protein purity was assessed by SDS-PAGE and by A_{409nm}/A_{280nm} (purity ratio). The final protein samples had a purity ratio of 2.0 and 2.6 for NT domain and YhjA, respectively. The CT domain final sample had many contaminant proteins and a purity ratio < 1.0.

The proteins were stored in small aliquots at - 80 ºC, until further use.

2.4.4 TEV protease purification

TEV purification was performed as described by Tropea, Cherry and Waugh[198] with a few modifications. 1 mM β-mercapthoethanol was added to the lysis buffer (50 mM sodium phosphate buffer pH 8.0, 100 mM NaCl, 10 % glycerol and 25 mM imidazole) and the cells were lysed by passing 3 times in a French Press at 20000 psi. The first purification step used a 5 mL HisTrap column

(GE Healthcare) equilibrated in the lysis buffer and the protein was eluted with 200 mM imidazole in equilibration buffer. The second purification step used a Superdex 75 10/300 GL (GE Healthcare) equilibrated with 25 mM sodium phosphate buffer, pH 8.0, 200 mM NaCl, 10 % glycerol, 2 mM EDTA and 1 mM DTT. The pure protein (Figure 2.4) was stored at - 80 ºC, at a final concentration of 1 mg.mL^{-1} in the same equilibration buffer with added DTT to a final concentration of 10 mM.

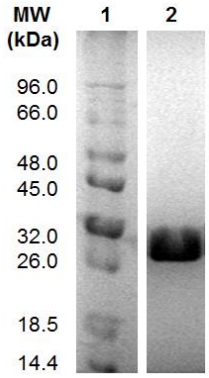

Figure 2.4 – Coomassie blue stained SDS PAGE of purified TEV (29 kDa) in a 12.5 % Tris-Tricine gel. (Lane 1 - Protein Marker; Lane 2 – purified TEV).

2.5 Digestion of YhjA Strep-Tag using TEV protease

The digestion of Strep-tagged YhjA (Figure 2.5) was performed overnight (20 h), at 4 ºC in 50 mM Tris-HCl, pH 8.0, containing 1 mM DTT, 5 mM sodium citrate, 200 mM NaCl and TEV:YhjA in the proportion of 1:20 (mg/mg). In order to remove uncut YhjA, the digest was injected into a 5 mL StrepTrap column followed by a 5 mL HisTrap column (to remove TEV protease), both equilibrated with 50 mM Tris-HCl, pH 8.0, 500 mM NaCl.

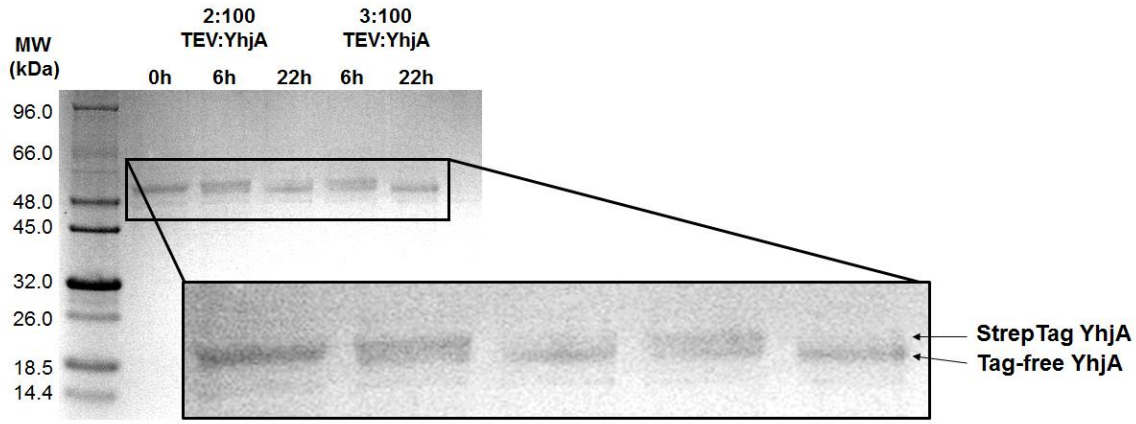

Figure 2.5 – Digestion test with different ratios of TEV:YhjA and incubations times at 4 ºC (6 h and 22 h). The result was assessed in a 12.5 % tricine SDS-PAGE stained with Coomassie Blue. The Tag-free YhjA has a slightly lower molecular weight. Digestion was mostly complete in a ratio of 3:100 (mg/mg). Final ratio was 1:20 TEV:YhjA (mg/mg) to guarantee full digestion.

The final protein was concentrated and the buffer exchanged to 20 mM HEPES, pH 7.5. 12.5 % Tris-Tricine SDS-PAGE showed a single band with smaller molecular mass (than the uncut protein, Figure 2.5) and size-exclusion chromatography (Superdex 200 10/300 GL, GE Healthcare) showed one single protein peak. This tag-free YhjA was mainly used in the kinetic assays and molecular mass determination.

2.6 Biochemical characterization

2.6.1 Molecular mass determination

The apparent molecular weight of all proteins was estimated by molecular size-exclusion chromatography, with a Superdex 200 10/300 GL (GE Healthcare, used for *Ng*BCCP, YhjA and its domains) a Superdex 75 10/300 GL (used for LAz). The columns were equilibrated with 50 mM Tris-HCl, pH 7.6, 150 mM NaCl with or without 2 mM $CaCl_2$, or 2 mM EGTA, to assess calcium ions dependence of apparent molecular weight. In order to assess the influence of ionic strength, the column was equilibrated with 50 mM Tris-HCl, pH 7.6, with or without 500 mM NaCl. Calibration curves were prepared using the Molecular Weight Gel Filtration Calibration Kits (GE Healthcare) according to the manufacturer instructions. Protein samples were pre-incubated in the respective equilibration buffer in each run. The protein apparent molecular weight was calculated from the partition coefficient K_{av} of the calibration protein standards according to the following equation:

$$K_{av} = \frac{V_e - V_o}{V_c - V_o} \qquad (2.1)$$

where V_o is the column void volume determined by injecting blue dextran at 0.1 mg.mL^{-1}, V_e the elution volume and V_c the geometric column volume (both 24 mL). These K_{av} values were plotted in function of log molecular weight.

The molecular mass was determined by electrospray ionization mass spectrometry (ESI-MS) on a Waters Synapt G1 HDMS mass spectrometer, by the group of Prof. Bart Devreese, L-ProBE, Ghent University, Belgium. They have also determined the N-terminal sequence.

2.6.2 Spectroscopic characterization

2.6.2.1 UV-visible spectroscopy

The UV-visible spectra were recorded on a Shimadzu UV-1800 spectrophotometer, connected to a computer, using 1 cm quartz cuvette.

LAz spectra were acquired for a 30 µM LAz solution in 20 mM phosphate buffer pH 7.0. The fully reduced form of LAz was obtained with 1 mM sodium ascorbate (Asc, 100 mM stock solution prepared in H_2O) and 5 µM diaminodurol (DAD, 5 mM stock solution prepared in 20 % ethanol).

For the oxidized LAz spectrum one or two grains of potassium ferricyanide were added to the cuvette solution.

*Ng*BCCP, YhjA and NT domain spectra were acquired for a 2 μM protein solution in 10 mM HEPES pH 7.5.

The reduced NT domain spectrum was obtained with a solution of sodium dithionite (a 100 mM stock solution in 100 mM HEPES pH 7.5) to a final concentration of 1 mM.

The BCCP (*Ng*BCCP or YhjA) in the mixed-valence state was obtained by reduction with a solution of Asc/DAD with a final concentration of 1 mM and 5 μM, respectively. In order to determine the effect of calcium ions in the visible spectrum of the mixed-valence state, a $CaCl_2$ solution (100 mM stock solution prepared in Milli-Q water) was added to a final concentration of 1 mM.

The calcium role in the enzyme, was evaluated by treating the mixed-valence protein sample with EGTA to a final concentration of 1 mM. UV-visible spectra were collected in an Agilent Diode Array over a period of 20 min. The calcium depleted enzyme (prepared as described) was titrated with small volumes of a stock solution of 100 mM $CaCl_2$ (prepared in 10 mM HEPES pH 7.5) until no changes were observed. Spectra were collected 1 min after each addition since no further differences were observed over longer periods of time. The concentration of free calcium ions at each titration point was calculated considering the EGTA binding affinity of 21 nM (for a pH of 7.5, temperature of 25 ºC). The ratio of bound/unbound protein was plotted as a function of log[free Ca^{2+}] and the data was fitted to the following sigmoid function consistent with a single binding site, where K_D is the dissociation constant and *h* the Hill slope (> 0):

$$Bound/Unbound = \frac{1}{10^{(logK_D - \log[Ca^{2+}]).h}} \qquad (2.2)$$

For the *Ng*BCCP inhibition studies, the UV-visible spectra of approximately 2 μM mixed-valence *Ng*BCCP solutions (in 10 mM HEPES pH 7.5 and 1 mM $CaCl_2$) were recorded in the presence of increasing concentrations of inhibitor, such as cyanide (0-95 μM), azide (0-225 mM) and imidazole (0-190 mM) sodium salts prepared in Milli-Q water (imidazole pH was adjusted to 7.5). The difference in the Soret band, at specific wavelengths, (ΔA) was plotted as a function of inhibitor concentration *i* and data was simulated with the following binding-model, where *Bmax* is the maximum difference at which all protein molecules are bound to inhibitor and k_{app} is the apparent dissociation constant:

$$\Delta A = \frac{B_{max}.i}{k_{app} + i} \qquad (2.3)$$

2.6.2.2 EPR spectroscopy

The X-band EPR (9.65 GHz) spectra were recorded on a Bruker EMX 6/1 spectrometer equipped with a dual-mode rectangular cavity (Bruker model ER4116DM) and the samples were cooled with an Oxford Instruments ESR900 continuous liquid helium flow cryostat, fitted with a temperature controller, at 10 K. The *Ng*BCCP and YhjA/NT samples for EPR were at 0.2 mM and 0.3 mM, respectively, in 20 mM HEPES buffer, pH 7.5. Samples were reduced with a solution of Asc/DAD, to a final concentration of 1 mM and 5 μM, respectively, followed by addition of a $CaCl_2$ solution to a final concentration of 2 mM.

Experimental conditions for spectra acquisition were: 10 K, 5 Gpp of modulation of amplitude, 1 x 10^5 receiver gain, 3 scans and 20 mW (*Ng*BCCP and NT) or 2 mW (YhjA) of microwave power. The spectra simulations were performed using WINEPR SimFonia software version 1.2 (Bruker).

2.6.3 Protein quantification – modified Lowry

Protein concentration of each purified sample was estimated using the modified Lowry method [199] using horse heart cytochrome *c* or BSA as protein standards. BSA was only used when quantifying LAz protein samples.

In short, 400 μL of Biuret reagent [199] were added to 100 μL protein sample and incubated for 10 min at room temperature. Then 3.5 mL of 2.3 % Na_2CO_3 and 100 μL of Folin-Ciocalteau reagent were added in this order, mixed and incubated for 30 min at room temperature, after which the absorbance was measured at 750 nm. Protein concentration was calculated using a protein standard calibration curve (0 – 0.3 $mg.mL^{-1}$ of protein).

2.6.4 Heme and copper quantification – determination of molar extinction coefficients

The molar extinction coefficients of each protein were calculated based on the concentration of their cofactor. For hemic proteins the heme content was determined by the pyridine hemochrome assay [8]. In short, 100 μL of 2 M NaOH, 250 μL pyridine and 10 μL sodium dithionite 500 mM were added in this order to 640 μL of a 2-3 μM protein solution, to a final volume of 1 mL. The solution was quickly mixed and the absorbance measured at 550 nm, the peak for *c*-type hemes (ε_{550nm} = 29.1 $mM^{-1}cm^{-1}$). This method was also used to confirm the presence of heme *c* as all proteins showed a maximum at 550 nm characteristic for this type of heme. The molar extinction coefficients were calculated considering the number of hemes per protein in each purified protein.

LAz molar extinction coefficients were calculated based on copper content (1:1, Cu:protein). The copper concentration was determined with a modified version of the method of Hanna *et al.*[200]. This method quantifies the amount of Cu^I based on the formation of a complex between Cu^I and

2,2′-biquinoline in acetic acid. A sample of LAz or a standard solution of copper acetate (100 µL) was reduced by adding 300 µL of 20 mM sodium ascorbate (prepared in 0.1 M sodium phosphate buffer, pH 6.0) and incubated for 30 min at room temperature. 600 µL of a 2,2′-biquinoline solution (0.5 $mg.mL^{-1}$) prepared in glacial acetic acid was added to that solution, and the solution was incubated for 10 min. Finally, the absorbance at 546 nm was measured and the concentration of Cu^{I} determined from the $copper^{II}$ acetate calibration curve (0-24 µM).

2.6.5 Differential scanning calorimetry

In the differential scanning calorimetry (DSC) experiments, the NanoDSC instrument (TA Instruments) was loaded with degassed buffers (baselines and reference cell) and protein solution (approximately 20 µM protein in the sample cell). Each protein sample passed through a desalting NAP-5 column (GE Healthcare) equilibrated in the appropriate buffer (10 mM HEPES pH 7.5, with or without 2 mM $CaCl_2$, or 2 mM EGTA or 1 mM sodium ascorbate/5 µM DAD and 2 mM $CaCl_2$) and then diluted to the desirable concentration in the same buffer. The temperature was raised from 10 to 100 ºC at a scan rate of 1 $ºC.min^{-1}$. The thermograms were analyzed with NanoAnalyze software from TA instruments using a non-two state model to simulate the data and obtain the melting temperature (T_m), the calorimetric (ΔH) and van't Hoff (ΔH_v) enthalpies. The corresponding baseline was subtracted from each sample scan.

2.6.6 Potentiometric redox titrations

Potentiometric redox titrations were performed under anoxic conditions (argon atmosphere inside a Mbraun anaerobic chamber), at 25 ºC, by measuring the absorbance changes of a 8 µM *Ng*BCCP (fully oxidized) in 100 mM HEPES, pH 7.5, and 2 µM of each mediator (reduction potentials for each mediator at pH 7.0 [201]: diaminodurol + 260 mV, 1,2-naphthoquinone + 180 mV, phenazine methosulfate + 80 mV, phenazine ethosulfate + 55 mV, phenazine - 125 mV, 2-hydroxy-1,4-naphthoquinone -145 mV, flavin mononucleotide - 205 mV and neutral red - 325 mV), with or without 2 mM $CaCl_2$, or with 2 mM EGTA.

The YhjA and NT domain titrations were performed with a 6 µM protein sample (fully oxidized) in 100 mM HEPES, pH 7.5, 2 mM $CaCl_2$ and 2 µM of each mediator.

The reduction potential was monitored using a Pt pin electrode in combination with an Ag^{+}/AgCl reference (Crison), and the potential, with reference to the standard hydrogen electrode, was obtained by adding 210 mV.

The electrode was calibrated before each assay with fresh iron solutions. A 100 mM stock solution of 0.5 mM ammonium iron (II) sulphate was sequentially added to a solution of 0.1 M sodium acetate pH 5.0, 0.5 mM ammonium iron (III) sulphate and 10 mM EDTA, to a final concentration of 0.2 mM and 0.5 mM. The potential difference between these two concentrations should be about 23 mV,

according to the Nernst equation for transfer of one single electron, and the final potential + 108 mV (corrected for standard hydrogen electrode). The difference between this theoretical value and the actual value given by the potentiometer was subtracted to all data points.

Reductive titration was carried out by stepwise additions of small volumes of 0.1 - 100 mM sodium ascorbate, or 0.1 - 100 mM sodium dithionite, prepared in 100 mM HEPES pH 7.5, while the oxidative titration was carried out by addition of 0.1 - 100 mM potassium ferricyanide prepared in the same buffer. The spectra were scanned from 350 nm to 900 nm, using a TIDAS diode array spectrophotometer connected to an external computer.

The absorbance at 554 nm was monitored and used to calculate a [oxidized]/[reduced] protein ratio for each acquired spectrum. This [ox]/[red] was plotted as a function of the measured reduction potential at each titration point. The reduction potentials were then obtained from the simulation of the titration curves based on the Nernst equation considering one (NT), two (*Ng*BCCP) or three (YhjA) independent redox centers.

The following scheme (Figure 2.6) and equations are represented for the most complex scenario with three independent redox centers that can be simplified to either two or one redox centers.

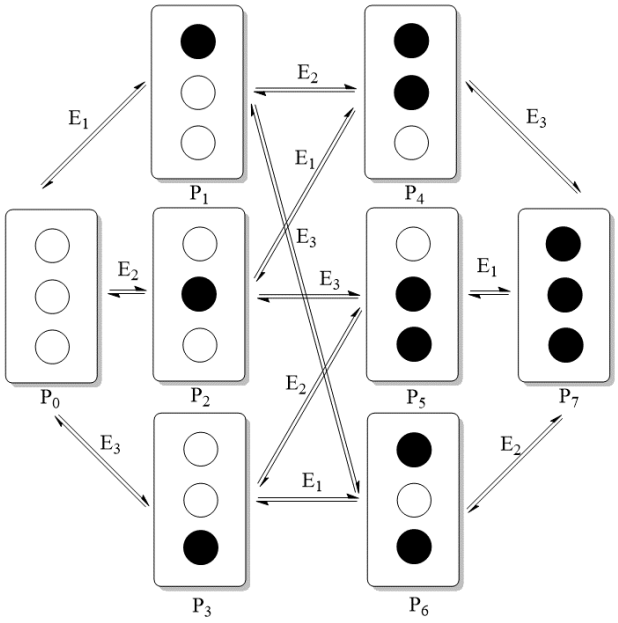

Figure 2.6 – Model of the potentiometric titration of a protein with three independent redox centers that are either oxidized (open circles) or reduced (closed circles). This scheme shows all the possible redox states (P_n) and the reduction potential (E_i) of each redox center *i*.

The Nernst equation (2.4) allows to calculate the reduction potential of each center *i* considering a single electron transfer for each of the redox equilibriums represented in Figure 2.6:

$$E = E_i^0 + 59 \log\left(\frac{P_{ox}}{P_{red}}\right) \qquad (2.4)$$

The Nernst equations for each equilibrium can be rewritten for instance in function of P_0. Equation 2.5 describes that the sum of all states equals one at a given potential (E). This can then be reformulated to have a global equation that allows to calculate P_0 and then the remaining states for any reduction potential considering the three redox centers midpoint potentials E_i.

$$P_0 + P_1 + P_2 + P_3 + P_4 + P_5 + P_6 + P_7 = 1 \quad \Leftrightarrow$$

$$\Leftrightarrow P_0 + \frac{P_0}{10^{\left(\frac{E-E_1}{59}\right)}} + \frac{P_0}{10^{\left(\frac{E-E_2}{59}\right)}} + \frac{P_0}{10^{\left(\frac{E-E_3}{59}\right)}} + \frac{P_0}{10^{\left(\frac{E-E_1}{59}\right)}.10^{\left(\frac{E-E_2}{59}\right)}} + \frac{P_0}{10^{\left(\frac{E-E_2}{59}\right)}.10^{\left(\frac{E-E_3}{59}\right)}} + \frac{P_0}{10^{\left(\frac{E-E_1}{59}\right)}.10^{\left(\frac{E-E_3}{59}\right)}} + \frac{P_0}{10^{\left(\frac{E-E_1}{59}\right)}.10^{\left(\frac{E-E_2}{59}\right)}.10^{\left(\frac{E-E_3}{59}\right)}} = 1 \qquad (2.5)$$

From these P_n values, the [ox]/[red] data was simulated for any given potential considering the total (corrected by a factor ε_n) of each protein state (Equation 2.6):

$$\left[ox\right]/_{\left[red\right]} = P_0\varepsilon_0 + P_1\varepsilon_1 + P_2\varepsilon_2 + P_3\varepsilon_3 + P_4\varepsilon_4 + P_5\varepsilon_5 + P_6\varepsilon_6 + P_7\varepsilon_7 \qquad (2.6)$$

2.7 Steady-state kinetics

2.7.1 *Ng*BCCP kinetic assays with $ABTS^{2-}$

The specific activity of *Ng*BCCP using 2,2'-azino-di-(3-ethyl-benzthiazoline-6-sulphonic acid ($ABTS^{2-}$, from Sigma) as electron donor was determined by monitoring the increase in absorbance at 420 nm (ε_{420nm} = 36 $mM^{-1}cm^{-1}$) over time, as a result of $ABTS^{2-}$ oxidation [202] in the presence of substrate H_2O_2, in an Agilent Diode Array. The assay was performed at 25 ºC in 10 mM HEPES pH 7.0, 10 mM NaCl and 1 mM $CaCl_2$, containing 3 mM $ABTS^{2-}$, 100 µM H_2O_2, and initiated with 10 nM pre-activated *Ng*BCCP (Figure 2.7). *Ng*BCCP was pre-activated for all kinetic assays (as otherwise stated) in 5 µM enzyme stocks in 10 mM HEPES, 10 mM NaCl, pH 7.5, 0.2 mM sodium ascorbate, 5 µM DAD, 1 mM $CaCl_2$, during 30 min, at room temperature, and then used directly in the assay.

In the assay for the Michaelis-Menten curve, H_2O_2 concentration ranged between 0.01 and 1 mM. The temperature was varied from 15 ºC to 50 ºC, in order to assess the temperature dependence of the catalytic activity. The pH dependence assay was performed in the same conditions as above at distinct pH values, varying the buffer at a concentration of 10 mM, (MES buffer with pH values from 5.5 to 6.5, HEPES buffer with pH values from 6.5 to 8.0 and Bis-Tris-Propane buffer with pH values from 8.0 to 9.5).

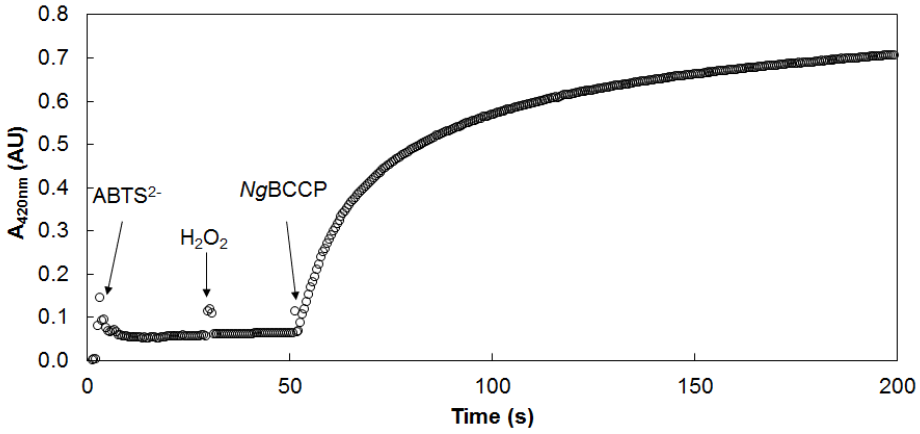

Figure 2.7 – Kinetic trace of peroxidatic activity of the pre-activated *Ng*BCCP using 3 mM $ABTS^{2-}$ as electron donor and 100 µM H_2O_2 in 10 mM HEPES, pH 7.5, 10 mM NaCl, 1 mM $CaCl_2$, at 25 ºC.

The observed initial rates, v_{obs}, were determined in the first seconds of the re-oxidation curve, to which $ABTS^{2-}$ auto-oxidation rates were subtracted to determine the real initial rates (initial velocity, $v_0 = \Delta[ABTS^{2-}].s^{-1}$). Those rates were fitted to a Michaelis-Menten curve (Equation 2.7) to estimate K_M and V_{max}.

$$v = \frac{V_{max}[S]}{K_M + [S]} \qquad (2.7)$$

The turnover number, k_{cat}, given by $k_{cat} = V_{max}/[NgBCCP]$, was estimated using the enzyme concentration in the assay. The pH dependence of the catalytic activity was simulated using Equation 2.8, considering a di-acid-basic event:

$$v = \frac{v_{high1} + v_{low1}.10^{(pKa_1 - pH)}}{1 + 10^{(pKa_1 - pH)}} . \frac{v_{high2} + v_{low2}.10^{(pKa_2 - pH)}}{1 + 10^{(pKa_2 - pH)}} \qquad (2.8)$$

in which the initial rate, v, is given as a function of pH considering two pK_a values. The values v_{high} and v_{low} are the average initial rate at high and low pH, respectively, for each acid-base equilibrium (for either pKa_1 or pKa_2). The amount of $ABTS^{2-}$ consumed during the first 100 s as a function of the pH, was simulated using Equation 2.9 [203]:

$$\Delta[ABTS_{ox}] = \frac{\Delta[ABTS_{ox}]_{max}}{1 + 10^{(pka_1 - pH)} + 10^{(pH - pKa_2)}} \qquad (2.9)$$

Temperature dependence of the reaction was evaluated by fitting the data from Arrhenius and Eyring plot to their respective equations 2.10 and 2.11:

$$\ln(v_0) = \ln(A) - \frac{E_a}{R} . \frac{1}{T} \qquad (2.10)$$

$$\ln\left(\frac{v_0}{T}\right) = \frac{-\Delta H^{\ddagger}}{R} . \frac{1}{T} + ln\left(\frac{k_B}{h}\right) + \frac{\Delta S^{\ddagger}}{R} \qquad (2.11)$$

In Arrhenius equation (2.10) E_a is the activation energy, R is the gas constant (8.314 J.mol^{-1}.K^{-1}), T is the absolute temperature in Kelvin and v_0 is the rate determined experimentally. Ln(A) is given by the y-intercept and the slope equals $-E_a/R$. In Eyring equation (2.11) $\Delta H^{\ddagger}$ is the enthalphy of activation, $\Delta S^{\ddagger}$ is the entropy of activation, k_B is the Boltzmann's constant (1.381 x 10^{-23} J.K^{-1}) and h is Planck's constant (6.626 x 10^{-34} J.s). The y-intercept gives the $\ln(k_B/h)+(\Delta S^{\ddagger}/R)$ and the slope is equal to $-(\Delta H^{\ddagger}/R)$. Given the enthalpy and entropy of activation it is possible to calculate the Gibbs energy of activation ($\Delta G^{\ddagger}$) according to the following equation:

$$\Delta G^{\ddagger} = \Delta H^{\ddagger} - T\Delta S^{\ddagger} \qquad (2.12)$$

For steady-state kinetics with inhibitors various concentrations of sodium cyanide (0-70 µM), sodium azide (0-100 mM) and imidazole (0-170 mM) were tested at three H_2O_2 concentrations: 10, 25 and 100 µM. As in the previous kinetic assays, the reaction was initiated with 10 nM pre-activated *Ng*BCCP added to a reaction mixture containing 10 mM HEPES pH 7.5, 10 mM NaCl, 1 mM $CaCl_2$, 3 mM $ABTS^{2-}$, inhibitor and H_2O_2.

The *ki* for competitive inhibition (2.13) and mixed-inhibition (2.14) were determined according to the following equations:

$$K_{M.app} = \frac{K_M}{1 + {}^{i}/_{ki}} \qquad (2.13)$$

$$v_{max.app} = \frac{V_{max}}{1 + {}^{i}/_{\alpha ki}} \qquad (2.14)$$

where $K_{M\ app}$ and $v_{max\ app}$ are determined from the Michaelis-Menten equation at each concentration i of inhibitor. V_{max} and K_M are the values determined without any inhibitor and α was estimated from Dixon and Cornish-Bowden plots, which give apparent *ki* and *ki'* since $\alpha ki = ki'$. Although the Cornish-Bowden plot gives a good estimative of *ki*, the above equations were used to calculate the *ki* for each inhibitor concentration, separately. The final *ki* reported is an average of these values.

All the errors of these values were calculated following the error propagation rules [204].

2.7.2 *Ng*BCCP kinetics assays with LAz

The peroxidatic activity of *Ng*BCCP using reduced LAz as electron donor was determined by monitoring the increase in absorbance at 625 nm (ε_{625nm} = 5.1 mM^{-1}cm^{-1}) over time, as a result of LAz oxidation [205] in the presence of substrate, in an Agilent Diode Array.

LAz was reduced with 1 mM sodium ascorbate and 5 µM DAD for 30 min at room temperature, which were removed using a desalting column, NAP-5 (GE Healthcare), equilibrated with 10 mM MES, pH 6.0, 10 mM NaCl and 1 mM $CaCl_2$. The final concentration of reduced LAz was determined by oxidizing a diluted LAz sample with potassium ferrycyanide and measuring the absorbance at 625 nm (ε_{625nm} = 5.1 mM^{-1}cm^{-1}).

The assay was performed at 25 ºC in the same buffer, containing 10 µM reduced LAz, 100 µM H_2O_2, and initiated with 10 nM pre-activated *Ng*BCCP (in all the assays, as otherwise stated). In the end, a small aliquot of potassium ferricyanide solution was added to fully oxidize LAz and confirm that all electron donor was oxidized in the assay (Figure 2.8). In the assay for the Michaelis-Menten curve, H_2O_2 concentration ranged between 0.01 and 1 mM.

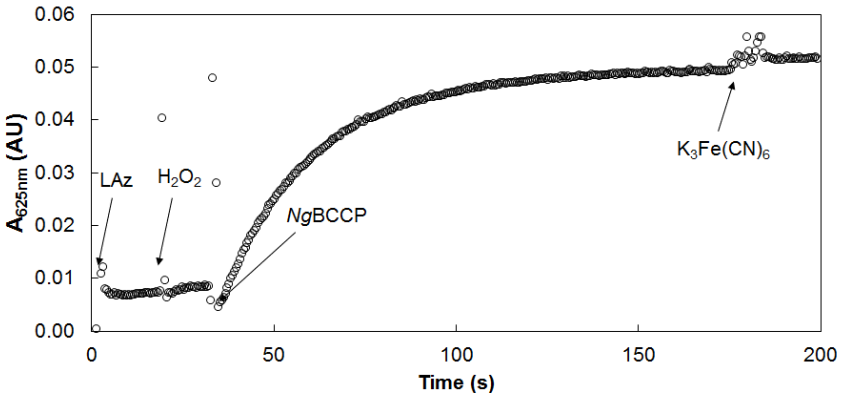

Figure 2.8 – Kinetic trace of peroxidatic activity of the pre-activated *Ng*BCCP using 10 µM LAz as electron donor and 100 µM H_2O_2 in 10 mM MES, pH 6.0, 10 mM NaCl, 1 mM $CaCl_2$, at 25 ºC.

Similarly to the assays with $ABTS^{2-}$, the temperature and pH dependence of the peroxidase activity were assessed between 15 ºC and 60 ºC and by varying the buffer at a concentration of 10 mM, (MES buffer with pH values from 5.5 to 6.5, HEPES buffer with pH values from 6.5 to 8.0 and Bis-Tris Propane buffer with pH values from 8.0 to 9.5), respectively. The ionic strength dependence of the LAz/*Ng*BCCP interaction was studied by adding NaCl to the assay buffer at different concentrations (0 – 500 mM), in 10 mM MES pH 6.0, 1 mM $CaCl_2$, 100 µM H_2O_2 and a final concentration of 10 µM reduced LAz.

In order to demonstrate *Ng*BCCP activation by LAz, 10 nM of as-isolated *Ng*BCCP was incubated with 9 µM reduced LAz in 10 mM MES, pH 6.0, 10 mM NaCl and 1 mM $CaCl_2$ for different times. The kinetic assay was initiated by adding H_2O_2 to a final concentration of 100 µM.

The observed initial rates, v_{obs}, were determined in the first seconds of the re-oxidation curve. The k_{cat}/[LAz] value was used for comparison since the electron donor is in concentrations much lower than its probable K_M. In those conditions the rate of the reaction is almost linearly proportional to the electron donor concentration.

The pH dependence kinetic data was simulated using a bell-shaped function [203] equivalent to Equation 2.9:

$$v = \frac{v_{max}}{1 + 10^{(pKa_1 - pH)} + 10^{(pH - pKa_2)}} \qquad (2.15)$$

in which the reaction rate, *v*, is given as a function of pH considering two p*Ka* values.

2.7.3 YhjA kinetic assays with $ABTS^{2-}$ and quinol electron donors

The specific peroxidatic activity of YhjA was assessed using various electron donors: (i) 2,2'-azino-di-(3-ethyl-benzthiazoline-6-sulphonic acid ($ABTS^{2-}$;) oxidation was monitored by the increase in absorbance at 420 nm (ε_{420nm} = 36 $mM^{-1}cm^{-1}$) over time [206]; (ii) hydroquinone oxidation forming benzoquinone was monitored at 260 nm (ε_{260nm} = 5.4 $mM^{-1}cm^{-1}$); (iii) duroquinol monitored at 270 nm (ε_{270nm} = 19.1 $mM^{-1}cm^{-1}$) and (iv) menadiol at 260 nm (ε_{260nm} = 16.5 $mM^{-1}cm^{-1}$). Extinction coefficients were calculated from the UV-visible spectra of que oxidized form shown in Figure 2.9.

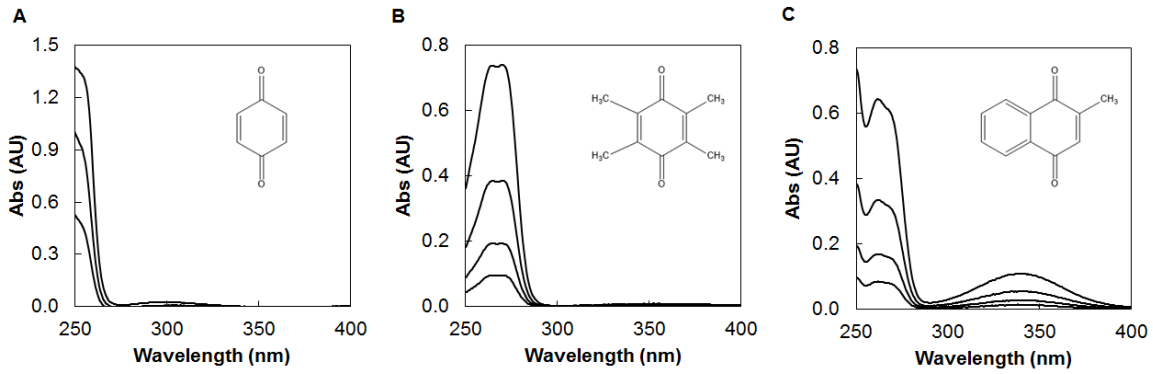

Figure 2.9 – UV-visible absorption spectra of (A) benzoquinone, (B) duroquinone and (C) menadione in 10 mM HEPES pH 7.5, 10 mM NaCl and 1 mM $CaCl_2$. The concentrations used for benzaquinone were 125, 67.5 and 31.25 µM, while for duroquinone and menadione solutions with 40, 20, 10 and 5 µM were prepared.

The reduced form of duroquinone and menadione was obtained as described by Giordani and Buc [207]: in short 70 mg of zinc powder was added to 20 mM quinone solution (in 1.7 mL ethanol with 0.18 M HCl) , and this solution was degassed and maintained on ice during the assays.

The assays were performed at 25 ºC in 10 mM HEPES pH 7.5, 10 mM NaCl and 1 mM $CaCl_2$, containing 3 mM $ABTS^{2-}$ or 100 µM quinol, 1 mM H_2O_2, and initiated with the addition of as-isolated (oxidized) YhjA (15-30 nM). In the assay for the Michaelis-Menten curve, H_2O_2 concentration ranged between 0.1 and 20 mM. The assays using duroquinol and menadiol were performed with degassed solutions under a constant flow of argon to maintain anoxic conditions.

The observed initial rates, v_{obs}, were determined in the first seconds of the re-oxidation curve, by subtracting the electron donor auto-oxidation rates to determine the real initial rates. A Michaelis-Menten curve was simulated to estimate K_M and V_{max} (Equation 2.7). The turnover number, k_{cat}, given by $k_{cat} = V_{max}/[YhjA]$, was determined using the concentration of enzyme present in the assay, as described previously for *Ng*BCCP.

In order to assess the pH dependence of the catalytic activity, the assays were performed as described above varying the buffer, at a concentration of 10 mM buffer with distinct pH values (MES buffer with pH values from 5.5 to 6.5, HEPES buffer with pH values from 6.5 to 8.0 and Bis-Tris-Propane

buffer with pH values from 8.0 to 9.5). Data was simulated using the following equation derived from a bell-shaped function described in Equation 2.15 [203]:

$$v = \frac{v_{max}}{1 + 10^{(pH-pKa)}} \qquad (2.16)$$

in which the reaction rate, *v*, is given as a function of pH considering one p*Ka* value.

2.8 *Ng*BCCP crystallographic structure

2.8.1 Crystallization of *Ng*BCCP in the mixed-valence state

Pure *Ng*BCCP in the as-isolated state (oxidized) was used for extensive screening of crystallization conditions, by vapour diffusion methods. Droplets consisted of 0.7 µL protein solution (10 or 20 mg.mL^{-1} in 20 mM HEPES pH 7.5) and 0.7 µL precipitant solution, equilibrated against 500 µL of the same precipitant reservoir solution. *Ng*BCCP was pre-incubated with 2 mM calcium chloride for some of the screens and in all the following crystallization conditions. Two preliminary conditions were found, using either Jeffamine SD2001 or pentaerythritol propoxylate (5/4 PO/OH) as precipitant, the former at 4 ºC and the later at 20 ºC.

Several crystals of as-isolated *Ng*BCCP, pre-incubated with 2 mM calcium chloride, were obtained in 0.1 M MES pH 5.5, Jeffamine SD2001 (25-27 %) and 0.1 M sodium malonate, at 4 ºC. In order to reduce multiplicity, various additives were screen using the previous base condition. The addition of 30 % 1,6-hexanediol or 0.1 M hexammine cobalt(III) trichloride, to 4 µL drops (ratio of 5:4:1 for protein:reservoir:additive solution) resulted in single crystals. Data collected from these crystals had a low resolution and showed multiplicity, therefore there is no structure solution for the as-isolated *Ng*BCCP.

In the case of pentaerythritol propoxylate as precipitant, crystals of as-isolated *Ng*BCCP, pre-incubated with calcium chloride, were obtained in 0.1 M MES, pH 6.0 or 6.5, 5/4 PO/OH (25-30 %) with or without 0.2 M NaCl, at 20 ºC.

These crystallization conditions for the as-isolated *Ng*BCCP were used as starting conditions to crystallize this enzyme in the mixed-valence state (under an anoxic environment in an anaerobic chamber), by adding sodium ascorbate and a mediator (flavin mononucleotide, FMN) to reduce the E heme.

The best crystals were obtained in 30 % 5/4 PO/OH and 0.1 M MES pH 6.0 in the presence of 2 mM $CaCl_2$, 10 mM sodium ascorbate and 0.2 mM FMN, using a 20 mg.mL^{-1} protein solution previously incubated with calcium, sodium ascorbate and FMN in the same concentrations as in the reservoir solution. Drops were prepared in a Coy Lab vinyl anaerobic chamber (2 % hydrogen, 98 % argon atmosphere) using the sitting drop vapour-diffusion method and kept in an incubator at 30 ºC for seven days. Afterwards, crystallization plates were removed from the anaerobic chamber to 20 ºC

for crystal cryo-cooling in liquid nitrogen. For cryopreservation, the harvesting solution (0.1 M MES pH 6.0 and 30 % 5/4 PO/OH) was supplemented with 20 % glycerol.

In order to obtain the inhibited form, the crystals were soaked in a harvesting solution with 10 mM sodium azide for 30 min, prior to cryo-cooling. Other inhibitors, namely sodium cyanide and sodium fluoride, were also attempted, although unsuccessfully. The introduction of sodium cyanide caused loss of crystal colour and subsequent disaggregation. This same effect was observed when sodium fluoride was added.

2.8.2 Data collection and processing

Data collection and processing was performed by Dr. Ana Luísa Carvalho from the Crystallography group at NOVA, X-Tal, UCIBIO, REQUIMTE, FCT-UNL, Portugal. X-ray diffraction data was collected for three *Ng*BCCP crystals in the mixed-valence state, two in the active state and a third inhibited with azide. All the statistics for the three data sets can be found Table 2.2.

Table 2.2 – Statistics of data collection and processing.

	***Ng*BCCP (active, 1.93 Å)**	***Ng*BCCP (active, 1.4 Å)**	***Ng*BCCP (inhibited, 2.3 Å)**
Source	IμS 3.0 D8 Venture, Cu Kα, UCIBIO-FCT	PXIII (X06DA), SLS	BM30, ESRF
Detector	CMOS Photon 100	PILATUS 2M-F	ADSC Q315r CCD
Wavelength (Å)	1.5418	1.0	0.979
***a* (Å)**	78.9	78.8	79.1
***b* (Å)**	88.8	89.1	89.1
***c* (Å)**	93.1	89.7	94.8
Space group	$P2_12_12_1$	$P2_12_12_1$	$P2_12_12_1$
Molecules per ASU	2 monomers	2 monomers	2 monomers
Matthews coefficient ($Å^3$.Dalton^{-1})	2.17	2.10	2.23
Resolution range (Å)	23.70 – 1.93 (1.98 – 1.93)	39.90 – 1.40 (1.42 – 1.40)	65.00 – 2.30 (2.38 – 2.30)
<I/σI>	14.1 (2.06)	11.4 (2.1)	9.2 (2.2)
Wilson B-factor	13.4	12.7	27.4
R_{merge} (%)*	15.0 (62.6)	6.8 (65.6)	11.7 (72.3)
R_{pim} (%)+	-	4.2 (44.9)	8.0 (48.7)
Half-dataset correlation CC1/2	-	0.999 (0.813)	0.995 (0.762)
Multiplicity	10 (7.8)	6.4 (5.6)	5.6 (5.6)
No. of observed reflections	588364	797508 (33769)	169921 (16295)
No. of unique reflections	61250	124619 (6083)	30270 (2907)
Completeness (%)	100 (99.9)	99.9 (99.3)	97.7 (94.9)

The first data set was collected on an in-house X-ray diffractometer (IμS 3.0 microfocus D8 Venture with copper Kα radiation), coupled to a CMOS Photon 100 detector, from a *Ng*BCCP crystal in the mixed-valence active form, to a maximum resolution of 1.9 Å.

The X-ray diffraction data from a second crystal grown in similar conditions was collected to 1.4 Å resolution at the Swiss Light Source (SLS, beamline X06DA PXIII). The final X-ray diffraction data set was collected for the azide-soaked crystal at ESRF (beamline BM30, Grenoble).

2.9 LAz/*Ng*BCCP interaction studies

2.9.1 Isothermal titration calorimetry

In the isothermal titration calorimetry (ITC) experiments the NanoITC instrument (TA instruments) was loaded with a degassed *Ng*BCCP solution. The 250 µL syringe was loaded with a degassed LAz solution. Both protein samples were previously oxidized with equimolar concentrations of potassium ferricyanide. Samples were equilibrated in the appropriate buffer solution and the excess oxidant removed in a desalting column, NAP-5 (GE Healthcare).

The syringe solution was titrated into the cell by successive injections (25 in total) of 10 µL and mixed with a stirring speed of 300 rpm. Each addition was performed with 300 s intervals. Buffer was titrated into *Ng*BCCP solution and LAz was titrated into buffer as controls for the heat of dilution. Heat changes were analyzed in the NanoAnalyze software from TA instruments.

2.9.2 Microscale thermophoresis

Microscale thermophoresis experiments were performed in Monolith NT.115 from NanoTemper Technologies. *Ng*BCCP was labeled with a fluorescent extrinsic label (NT.647) covalently attached to the protein (NHS coupling). The excess label was removed when exchanging the buffer to 10 mM Tris-HCl pH 7.6 with 2 mM $CaCl_2$. 10 µL of a concentrated LAz sample (1.5 mM in the same buffer) were diluted in 10 µL of the previous buffer with 0.2 % Tween and/or 20 $mg.mL^{-1}$ BSA. 16 serial dilutions with a dilution factor of two were prepared in low-binding tubes. To each 10 µL dilution it was added 10 µL of the labeled *Ng*BCCP solution resulting in a final concentration of 0.05 % Tween and/or 1 $mg.mL^{-1}$ BSA. The 16 samples were loaded into premium coated capillaries and the fluorescence change measured. Other capillaries were tested, such as hydrophobic and standard treated capillaries.

2.9.3 Two-dimensional NMR titration

Two-dimensional heteronuclear NMR spectra were recorded for a 0.1 mM ^{15}N labeled LAz solution in 5 mM HEPES pH 7.0, 2 mM $CaCl_2$, 10 % D_2O, 1 mM sodium ascorbate and 1 µM DAD. LAz assignment deposited under the accession number 18636 in BMRB [208] was used for data analysis.

NMR spectra were recorded for a 1:0, 1:1 and 1:2 LAz:*Ng*BCCP ratio. Both the *Ng*BCCP E heme (*Ng*BCCP in the mixed-valence state) and LAz were reduced with 1 mM sodium ascorbate.

All NMR tubes were kept under an argon stream for a few minutes and then sealed to guarantee that the concentration of oxygen was low and no oxidation of the proteins occurred during the experiments.

The assay was performed in a Bruker Avance III 600 MHz equipped with a TCI-cryoprobe at 298 K. Each spectrum had a total of 16 scans. The spectral widths are 9600 Hz for ^{1}H (16 ppm; 1024 transients) and 2400 Hz for ^{15}N (40 ppm; 128 transients). NMR spectra were processed with TOPSPIN 3.5 provided by Bruker and analyzed in CARA 1.9.0.

Chemical shifts of each resonance $\Delta\delta_{HN}$ (ppm), were calculated considering the changes in the proton $\Delta\delta_{H}$ (ppm) and nitrogen $\Delta\delta_{N}$ (ppm) according to the following equation [209]:

$$\Delta\delta_{HN} = \frac{\sqrt{\Delta\delta_H^2 + \frac{\Delta\delta_N^2}{5}}}{2} \qquad (2.17)$$

2.9.4 Dipole moment calculations

The dipole moment was determined in Chimera 1.10.2 for each protein structure. For that, hydrogens atoms were added and charges were attributed to each protein structure by using Amber. The charge of the copper atom was assigned to +1 or +2 for the reduced or oxidized protein, respectively.

The dipole vector was determined in Chimera using the "dipole.py" python script (http://plato.cgl.ucsf.edu/trac/chimera/wiki/Scripts).

2.9.5 LAz-*Ng*BCCP molecular docking simulation and complex evaluation

The docking algorithms used in this work were BiGGER [210] and ZDOCK [211, 212]. The *Ng*BCCP dimer structure was considered the target and the LAz structure the probe.

BiGGER was implemented in Chemera 3.07. A "soft dock" was performed with a complete and systematic search in space by rotating LAz around the surface of *Ng*BCCP with a translation and rotation steps of 1 Å resolution and 15 º. In the "soft dock" the side-chains are truncated allowing overlap between the structures and to ignore clashes between flexible side-chains. A maximum of 5000 solutions were selected with 150 minimum contacts. These were analyzed according to the global, hydrophobic and electrostatic scores, as well as an additional Cu-Fe (from E heme) distance score (< 20 Å). The top six cluster conformations with highest global and hydrophobic score were analyzed.

ZDOCK docking was performed in the ZDOCK web-based server 3.0.2 (http://zdock.umassmed.edu/). It is a rigid-body docking program that uses a fast Fourier transform to perform a 3D search of the spatial degrees of freedom between the two molecules. The output consists of 2000 models with a combined score based on electrostatics, shape complementarity and statistical potential terms. The five top models were analyzed.

The geometrical and physicochemical properties of each top models (six for BiGGER and five for ZDOCK) were determined according to Jones and Thornton [39] using PDBePISA [192] and ProFACE [44] for the protein-protein interface analysis, in a similar approach as Nooren and Thornton [43]. The electron transfer pathway was analyzed in PATHWAYS [213, 214].

2.10 Analysis of *yhjA* relative gene expression

2.10.1 *E. coli* K-12 strains and growth conditions

Bacterial *E. coli* K-12 strains (wild-type and *yhjA* knockout strains) were obtained from the KEIO single mutant collection [215], which were kindly provided by Doctor Karina Xavier from Instituto Gulbenkian de Ciência. The KEIO collection strains have a kanamycin resistance cassette. Cells were grown in a modified M9 minimal media (1 $g.L^{-1}$ NH_4Cl, 3 $g.L^{-1}$ KH_2PO_4, 6 $g.L^{-1}$ $Na_2HPO_4.7H_2O$, 0.4 % glycerol, 1 mM $MgSO_4$, 0.1 mM $CaCl_2$, 18.5 µM $FeCl_3$, 0.5 $g.L^{-1}$ NaCl, VM vitamins cocktail [216]) at 37 ºC, supplemented with 25 $\mu g.mL^{-1}$ of kanamycin, 5 % LB medium and an electron acceptor, either potassium fumarate (30 mM) or sodium nitrate (30 mM). Final pH was adjusted to 7.5 with 5 M KOH prior to autoclave.

Bacterial cultures were grown overnight at 210 rpm in LB media supplemented with 25 $\mu g.mL^{-1}$ kanamycin. Growth under aerobic (250 mL growth media in 500 mL conical flasks with orbital shaking at 210 rpm) and microaerobic (250 mL growth media in 500 mL conical flasks with orbital shaking at 100 rpm) conditions were inoculated with 2 % pre-inoculum. For anaerobic growths an intermediate anaerobic pre-inoculum (anaerobic bottles with 10 mL growth media) was prepared with 10 % of the overnight LB aerobic pre-inoculum. The anaerobic growths (90 mL media in anaerobic bottles) were inoculated with 10 % anaerobic pre-inoculum.

2.10.2 RNA extraction and reverse transcriptase reaction

Total RNA was extracted from samples collected at distinct time points in each growth curve to be analyzed by quantitative real time PCR (*q*PCR). Cells were centrifuged at 14000 rpm, 4 ºC for 1 min. The pellet was resuspended in 100 µL lysozyme/TE buffer (2 $mg.mL^{-1}$) and incubated at room temperature for 15 min. The lysate was then treated according to the ISOLATE II RNA Mini Kit (Bioline) protocol for bacterial RNA extraction. RNA concentration was determined at A_{260nm} using a Nanodrop 2000c spectrophotometer (Thermo Scientific). RNA purity was assessed by the A_{260nm}/A_{280nm} and A_{260nm}/A_{230nm} ratios, and samples were stored at -80 ºC until further use.

The SensiFAST™ cDNA Synthesis Kit (Bioline), which includes random hexamer primers, was used to synthesize cDNA ensuring unbiased 3' and 5' coverage and reverse transcription of all regions. The reverse transcription reaction mix consisted of 1 X TransAmp Buffer, 500 ng of total RNA and

1 µL of R.T. to a final volume of 20 µL. The reaction conditions were: 10 min at 25 ºC, 15 min at 42 ºC and 5 min at 85 ºC. cDNA was stored at - 20 ºC until further use.

2.10.3 Quantitative Real Time PCR - Quantification using Standard curves

A total of six genes (*yhjA, oxyR, fnr, ahpC, katG* and *katE*) were analyzed for their relative expression at different stages of *E. coli* growth under aerobic, microaerobic and anaerobic conditions. Gene expression was related to the ubiquitously expressed gene *16SrRNA*. This gene is expressed at similar levels during all growth stages and was therefore used as the control gene. Primers were designed for each gene using Primer3 online software [217] and *E. coli* K-12 substr. MG1655 DNA sequences as template. Table 2.3 lists all the oligonucleotides (Sigma) used. The *q*PCR was performed in a Rotor-Gene 6000 (Corbett Research) using SensiFAST™ SYBR No-ROX Kit (Bioline). The reaction mix consisted of: 500 nM of each primer, 3 µL of cDNA (100 dilution of original synthesized cDNA samples) and 1X SensiFAST SYBR® No-ROX master mix in a final volume of 12 µL. PCR efficiency was tested using genomic DNA standard curves (50 ng genomic DNA with eight serial dilutions) since it has the same number of copies for each gene.

Table 2.3 – Sequence of oligonucleotides used in *q*PCR.

Gene	Primer	Primer Sequence (5'-3')	Amplified region[a]	Base pair size
16SrRNA	Forward	CGTGTTGTGAAATGTTGGGT	1071-1160	90
	Reverse	CAGTCTCCTTTGAGTTCCCG		
yhjA	Forward	TGAAATGGCGTCGAAATCCT	807-908	102
	Reverse	CCACTGAAACCTTGCGGATA		
fnr	Forward	AATCAAAGGCGATCAGGACA	450-538	89
	Reverse	GACGGGACAGGTTGTAGATG		
oxyR	Forward	AGCACAGACCCACCAGTTA	378-487	110
	Reverse	CATCAAACAACGGCACTTCA		
ahpC	Forward	GTATGCCCGACCGAACTG	136-244	109
	Reverse	ATGCTTTGTGGGTGAAGTGA		
katG	Forward	GCTTCTACCTTCCGTGGTG	1423-1512	90
	Reverse	GGCGTTCACATCCCAGTC		
katE	Forward	GTATTCACACCTTCCGCCTG	818-922	105
	Reverse	GTGCTTCATCCCAAACGAGT		

[a] Location within gene sequence in *E. coli* K-12 substr. MG1655.

For comparison of all data points, it was essential that the efficiency was approximately 100 %. The slope for the standard curve needs to be approximately -3.32 (maximum differences of 0.1) which means that cDNA doubles after each cycle (Figure 2.10A). All genes analyzed met this criteria.
Thermocycling conditions were optimized for the best efficiency resulting in the following program: 5 min at 95 ºC, 40 cycles of 15 s at 95 ºC, 15 s at 60 ºC and 20 s at 72 ºC.

Melting curves of the PCR products were acquired by increasing the temperature from 55 ºC to 94 ºC. The melting curves showed that there was a single peak for all amplicons, therefore, the reaction was specific (Figure 2.10B).

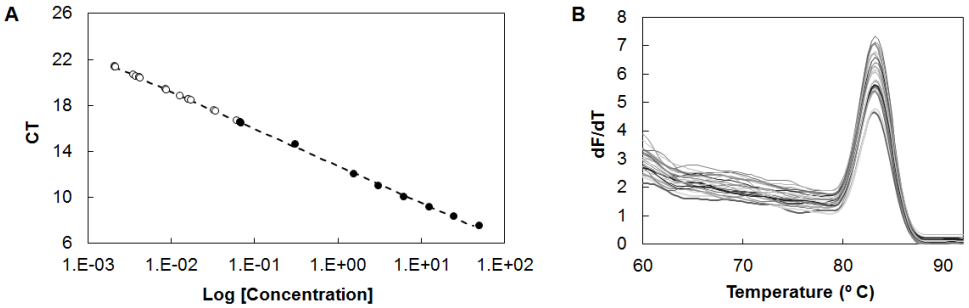

Figure 2.10 – *q*PCR data for *yhjA* gene expression in anaerobiosis. (A) PCR efficiency is approximately 1.0 with a slope of -3.2 for the DNA standard curve (closed circles) which is consistent with DNA duplicating after each cycle. (B) Melting curves show that there is one single amplicon for both DNA and cDNA samples.

For each sample there were two replicates and for each time point two to three biological replicates. Each reaction run included the standard DNA curve, a no-template control and a R.T. minus control for each growth condition (RNA sample without reverse transcriptase). The same amount of cDNA was used in each reaction for both control gene and studied genes. Therefore, it was possible to normalize the amount of target in each sample by dividing the amount of control gene (*16SrRNA*), in order to compare gene expression for all data points.

Data was compared to other results in the literature, in particular microarray data. Data was collected directly from the publication or from the EcoGene 3.0 database (http://ecogene.org).

2.11 Physiological role of YhjA in *E. coli* K-12

2.11.1 Killing assays

For the killing assays bacterial cultures of the wild-type and Δ*yhjA* mutant *E. coli* strains were grown in LB media supplemented with 25 µg.mL^{-1} of kanamycin (200 mL of each culture), at 37 ºC and 210 rpm, until an O.D.$_{600nm}$ of 0.6 was reached. Then the cultures were divided into three separate cultures (50 mL each) with 25 mM and 50 mM of H_2O_2 and a control without stress, for 30 min at 37 ºC and 110 rpm. A 1 mL culture sample was taken from each condition and centrifuged at 8000 *g* for 1 min. The cell pellet was washed and ressuspended in 1 mL of Phosphate-Buffered Saline (PBS: 8 g.L^{-1} NaCl, 0.2 g.L^{-1} KCl, 1.44 g.L^{-1} Na_2HPO_4, 0.24 g.L^{-1} KH_2PO_4, final pH adjusted to 7.4 with 1 M HCl). Plates of LB agar supplemented with kanamycin were inoculated with serial dilutions of the cell suspension in PBS. The plates were incubated at 37 ºC overnight and the amount of viable cells was calculated from the number of c.f.u. in each plate. The same assay was performed with 25 mM and 50 mM of *tert*-butyl peroxide or 1 mM cumene hydroperoxide.

2.11.2 Disc diffusion method

For disc diffusion assay bacterial cultures were grown in LB media supplemented with 25 μg.mL^{-1} kanamycin, at 37 ºC, 210 rpm, up to an O.D.$_{600nm}$ of 0.6. 200 μL of each culture was centrifuged briefly, washed with 0.9 % NaCl and resuspended to a final volume of 1 mL. This cell suspension was homogeneously spread over 1.5 % M9 agar/kanamycin plates (1 g.L^{-1} NH_4Cl, 3 g.L^{-1} KH_2PO_4, 6 g.L^{-1} $Na_2HPO_4.7H_2O$, 0.4 % glucose, 1 mM $MgSO_4$, 0.1 mM $CaCl_2$, 18.5 μM $FeCl_3$, 0.5 g.L^{-1} NaCl, VM vitamins cocktail (composition as described by Zinkevich and Beech [216]), 25 μg.mL^{-1} kanamycin, 15 g.L^{-1} agar) using a sterile cotton swab. Anaerobic plates were supplemented with 20 mM $NaNO_3$. Filter discs with a 5 mm diameter and saturated in various concentrations of cumene hydroperoxide were placed over the plate. Plates were either placed in an anaerobic box with Anaerocult A (Merck) to create an anaerobic environment, or with Anaerocult C (Merck) for microaerobic environment or outside for aerobic environment. Plates were incubated at 37 ºC for 20 h. Sensitivity was assessed by measuring the diameter of growth inhibition around the disc.

2.11.3 Membrane fraction peroxidase activity

In order to prepare the membrane fraction from *E. coli* K-12 WT and Δ*yhjA*, anaerobic flasks of 100 mL for each strain grown in fumarate supplemented modified M9 media (Section 2.10.1), were harvested in the stationary phase (16 h) by centrifugation at 7500 *g*, 6 ºC for 10 min, and the pellet cells were resuspended in 100 mM Tris-HCl pH 7.6 with protease inhibitors (cOmplete™, Mini, EDTA-free, Protease Inhibitor Cocktail Tablets, Roche). The cells were lysed 3 times in a French Press at 20000 psi. The lysate was centrifuged at 20000 *g*, 6 ºC for 15 min. The supernatant was ultracentrifuged at 200000 *g* for 1 h at 4 ºC. The membranes were washed with 100 mM Tris-HCl pH 7.6 and ultracentrifuged again during 1 h. The membranes were resuspended overnight at 4 ºC in the same buffer. In order to measure peroxidase activity a degassed solution composed of 100 mM Tris-HCl, pH 7.6, 2 mM $CaCl_2$, with 100 or 500 μM H_2O_2, and with or without 100 μM hydroquinone was prepared. The reaction was initiated with the addition of 10 μg.mL^{-1} of membrane fraction, under constant argon flow. The amount of H_2O_2 consumed over a period of 5 min (time points: 0, 0.5, 1, 2.5 and 5 min) was determined with PeroxoQuant lipid-compatible formulation kit (Pierce) according to manufacturer's instructions, using a H_2O_2 calibration curve (0-125 μM H_2O_2).

Chapter 3

Biochemical and Structural Characterization of Bacterial Cytochrome *c* Peroxidase from the Human Pathogen *Neisseria gonorrhoeae*

The work presented in this chapter is or will be published in:

"Biochemical characterization of the bacterial peroxidase from the human pathogen *Neisseria gonorrhoeae*", by Cláudia S. Nóbrega, Mariana Raposo, Gonzalez Van Driessche, Bart Devreese and Sofia R. Pauleta, J. Inorg. Biochem. 2017. Epub Mar 27;171:108-119. DOI: 10.1016/j.jinorgbio.2017.03.007.

"Structural characterization of the *Neisseria gonorrhoeae* bacterial peroxidase in the active form, in the absence and presence of an inhibitor – Insights into the catalytic cycle of bacterial peroxidases", by Cláudia S. Nóbrega, Lina Juknaite, Maria J. Romão, Ana Luisa M. Carvalho and Sofia R. Pauleta. 2017. Manuscript in preparation.

Contributions to Chapter 3:

Mariana Raposo performed the Michaelis-Menten kinetic assays for the pre-activated and as-isolated enzyme. Gonzalez Van Driessche and Bart Devreese performed all the mass spectrometry experiments. The X-ray crystallography studies were performed in collaboration with Maria J. Romão group. Lina Juknaite and Cláudia S. Nóbrega prepared the crystals. Ana Luísa Carvalho collected the crystals diffraction data and solved the X-ray structures. All the other experiments were performed by Cláudia S. Nóbrega.

3 Biochemical and Structural Characterization of Bacterial Cytochrome *c* Peroxidase from the Human Pathogen *Neisseria gonorrhoeae*

3.1 Introduction

N. gonorrhoeae is an obligate human pathogen that causes the sexually transmitted disease gonorrhea [218], that infects each year an estimate of 62 million people worldwide [219]. According to the World Health Organization (WHO reference number: WHO/RHR/11.14) a growing number of gonorrhea cases do not respond to the usual antibiotic treatment. The threat of these drug-resistant strains is increasing and new targets for gonorrhea treatment need to be assessed, such as the bacteria defenses towards the host and neighboring microorganisms.

Pathogenic microorganisms, during infection, are frequently exposed to oxidative stress due to reactive oxygen species (ROS) generated by host defense mechanisms. Some of the most common ROS found in biological systems include superoxide anion (O_2^-), hydrogen peroxide (H_2O_2) and hydroxyl radical ($HO^\bullet$) [220]. In order to cope with the oxidative stress, either endogenously or exogenously produced, *N. gonorrhoeae* has multiple enzymes that detoxify ROS or whose gene expression is induced by ROS (Figure 3.1), such as, superoxide dismutase (SodB) [221], catalase (KatA) [222], bacterioferritin (Bfr) [223], methionine sulfoxide reductase (MsrAB) [224], potential thiol-disulfide oxidoreductase (Sco) [225], peroxiredoxin (Prx) [226], glutathione reductase (Gor) [220] and bacterial cytochrome *c* peroxidase (*Ng*BCCP) [227], that catalyzes the reduction of hydrogen peroxide to water [22, 179, 227], the focus of this work.

In *N. gonorrhoeae*, the expression of *ccp* gene that encodes BCCP, is induced in environments with limiting concentrations of oxygen, as it is completely dependent on the anaerobic transcription factor FNR [119, 228]. It is well described that catalase has an important role in hydrogen peroxide detoxification, however, it is located in the cytoplasm. Therefore, BCCP can be regarded as a first defense against exogenous hydrogen peroxide, by being located in the periplasm, which explains why a *ccp/katA* mutant has increased sensitivity to hydrogen peroxide in anaerobic conditions, in comparison to a *katA* mutant [229].

In *N. gonorrhoeae*, it has been reported that this enzyme plays a crucial role during formation of biofilms and in the initial steps of infection [148], reason why a detailed study is necessary.

Previous biochemical studies on *Ng*BCCP indicated that it is a *c*-type diheme lipid-modified protein with a signal peptide cleaved by a signal peptidase II [227] and attached to the outer membrane. The globular domain of this enzyme has a high primary sequence homology with *P. aeruginosa* BCCP (48 % identity), one of the better characterized enzymes of this class.

The classical BCCP has two *c*-type hemes attached to the polypeptide chain through thioether bonds to two cysteines arranged in a -CXXCH- conserved motif and located in two different domains.

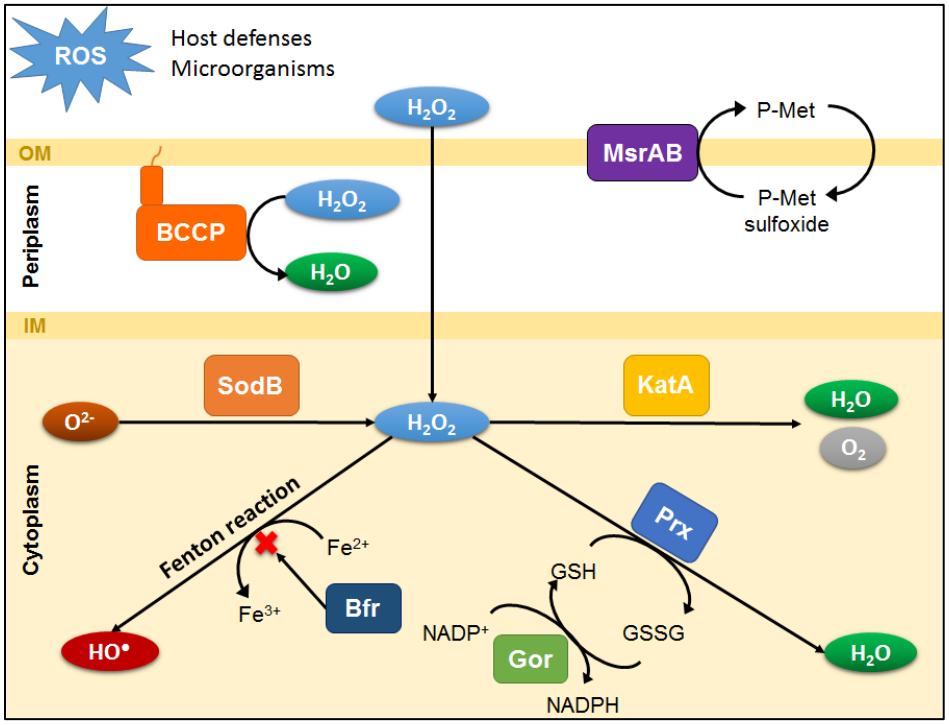

Figure 3.1 – Schematic representation of the oxidative stress responses in *N. gonorrhoeae*. *Ng*BCCP is located in the periplasm, anchored to the outer membrane. Other enzymes are located in the cytoplasm with the exception of MsrAB (methionine sulfoxide reductase) that is inserted in the outer membrane and encoded by *msrAB* gene, which expression increases when cells are exposed to H_2O_2. In the cytoplasm, peroxiredoxin (Prx) oxidizes the reduced glutathione (GSH) and reduces H_2O_2, forming GSSG, which is reduced by the glutathione reductase (Gor). Bacterioferritin binds free Fe^{2+} avoiding Fenton reactions. This bacterium has one superoxide dismutase (SodB) and one catalase (KatA). IM – Inner membrane; OM – Outer membrane.

There is a high-potential heme, in the C-terminal domain, His/Met coordinated, that acts as electron transfer center (E heme) to a low-potential heme, in the N-terminal domain, bis-His coordinated (in the fully oxidized form), where the peroxidatic reaction occurs (P heme) [108, 140, 166].

With the exception of *N. europaea* and *M. capsulatus* BCCPs [126, 128], bacterial peroxidases are inactive in the oxidized state and need reductive activation [138]. This activation mechanism consists in several conformational changes in the polypeptide chain that occur after E heme reduction. The most striking alteration is the removal of the distal axial histidine of P heme, which becomes a penta-coordinated high-spin heme (5cHS), accessible to the substrate [161, 171]. This requires that one calcium ion per monomer is bound to the polypeptide chain for complete conformational change and catalytic activity [166, 175]. Upon activation, in the presence of calcium (or higher ionic strength), BCCP is dimeric in solution [129, 163] with the formation of π-stacking interaction between the aromatic side chain of W96 and the peptide bond of G95 of each monomer (*P. aeruginosa* BCCP numbering according to the primary sequence) [166].

These enzymes typically use small redox proteins as electron donors, either *c*-type cytochromes [129, 163] or type 1 copper proteins (of the azurin or pseudoazurin sub-family) [139, 158], and

in a few organisms more than one of these small electron shuttle proteins can act as electron donors [184]. In the absence of a known electron donor, artificial electron donors, such as, 2,2'-azino-bis(3-ethylbenzothiazoline-6-sulphonic acid) ($ABTS^{2-}$) have been used to assess enzymatic activity. The turnover rates achieved are in the same order of magnitude as the ones with other electron donors found in the literature [115, 132].

There are several studies in the literature regarding binding of exogenous ligands to *c*-type cytochromes [230-232]. Those ligands can bind accessible hemes, such as the penta-coordinated P heme or disrupt the heme-protein ligand ligation. As a result they alter their properties and/or inhibit their catalytic activity. The binding affinities will depend on heme binding pocket, protein ligands and bond stability. Kinetic and spectroscopic studies with exogenous ligands have been performed in *P. aeruginosa* [125], *P. pantotrophus* [137], *R. capsulatus* [169] and *N. europaea* [126, 135] BCCPs with different ligands, such as azide, cyanide, cyanate, carbon monoxide, fluoride and imidazole. Spectroscopic data gives information regarding the dissociation constants, which can range from millimolar to micromolar concentrations reflecting the oxidation state of the hemes, coordination sphere, accessibility and heme-ligand complex formation. Kinetic studies show how effective are these ligands and what type of inhibition it is, for instance, competitive, uncompetitive or mixed-inhibition.

In the present study, the main objective was to determine if the membrane-bound peroxidase presented differences in the properties of its globular domains and if the pathogenic origin led to distinct biochemical and kinetic properties. In order to achieve this goal, *Ng*BCCP was heterologously produced in *E. coli* in a higher yield than previously reported, enabling its biochemical characterization. The *Ng*BCCP monomer-dimer equilibrium and spectroscopic properties were elucidated through the analysis of the mixed-valence *Ng*BCCP tridimensional structure. Acquisition of the protein structure in the active and inhibited form, as well as the inhibition studies presented here provides a first insight on possible inhibiting compounds for a future therapy development towards *N. gonorrhoeae* targeting *Ng*BCCP.

3.2 Results and Discussion

3.2.1 Primary Sequence Analysis

Neisseria genus includes several species that colonize the human host, such as *N. polysaccharea, N. flavescens, N. sicca, N. cinerea, N. lactamica, N. subflava, N. elongata subs. glycolitica, N. meningitidis* and *N. gonorrhoeae* [233], with only the last two being human pathogens. Supposedly, the *ccp* gene had not been identified in *N. meningitidis* however, this gene was found in newly introduced genomes of strains that were obtained by whole-genome shotgun sequencing of isolates from over 1-year period from hospital's intensive care units [234].

The analysis of the primary sequence alignment of BCCP from these *Neisseria* species indicates that they share a high percentage of identity (> 80 % identity), with most differences occurring in the N-terminal non-globular region, with a few exceptions in which the gene has an early STOP-codon, translating into a truncated non-functional BCCP.

In *Ng*BCCP primary sequence are highlighted two specific features in its N-terminal (Figure 3.2): (i) the consensus cleavage site LAA'C recognized by signal peptidase II [227]. It is proposed that Cys21 becomes a diacylglycerylcysteine, that upon cleavage is N-acylated, anchoring the enzyme to the membrane [235]; and (ii) a low complexity linker region (LCR) (black box; imperfect repeats of AAEAP), rich in alanines, that enables the enzyme to have some flexibility within the periplasm and to be ≈ 50-90 Å away from the surface of the inner leaflet of the outer membrane [236]. This feature is also present in other neisserial outer membrane attached proteins (lipid-modified azurin (LAz), outer membrane lipoprotein (Lip) and copper nitrite reductase (AniA) [205, 227, 236]).

The comparative multiple sequence alignment of *Ng*BCCP with the one of BCCPs with known tridimensional structure and of *M. capsulatus* BCCP is shown in Figure 3.2. This alignment indicates the presence of two *c*-type heme binding motifs, -CXXCH-, one at the N-terminal (P heme) and another in the C-terminal (E heme) region. The corresponding axial ligands of P heme (His115 and His131; *N. gonorrhoeae* FA 1090 BCCP numbering) and of E heme (His260 and Met336) are conserved, as well as the calcium binding residues (Asn139, Thr317 and Pro319), and the glutamine (Gln164) and glutamate (Glu174) proposed to be involved in the catalytic mechanism, the latter by promoting the cleavage of hydrogen peroxide at the O-O bond [167, 169]. Another conserved feature is the tryptophan residue (Trp154) that is proposed to be involved in the electron transfer pathway between the two hemes. This residue is located in a highly conserved region, at the interface between the two domains, with its indole ring bridging the propionates of the two hemes [108].

Besides the conserved features, *Ng*BCCP presents a few differences in residues (conversed in the other analyzed sequences) located in loop/flexible regions, which are involved in the structural changes between the oxidized and mixed-valence state (P heme domain), suggesting that this enzyme will have different biochemical properties. How these differences affect secondary structure will be further addressed in *Ng*BCCP structural analysis in Section 3.2.8.

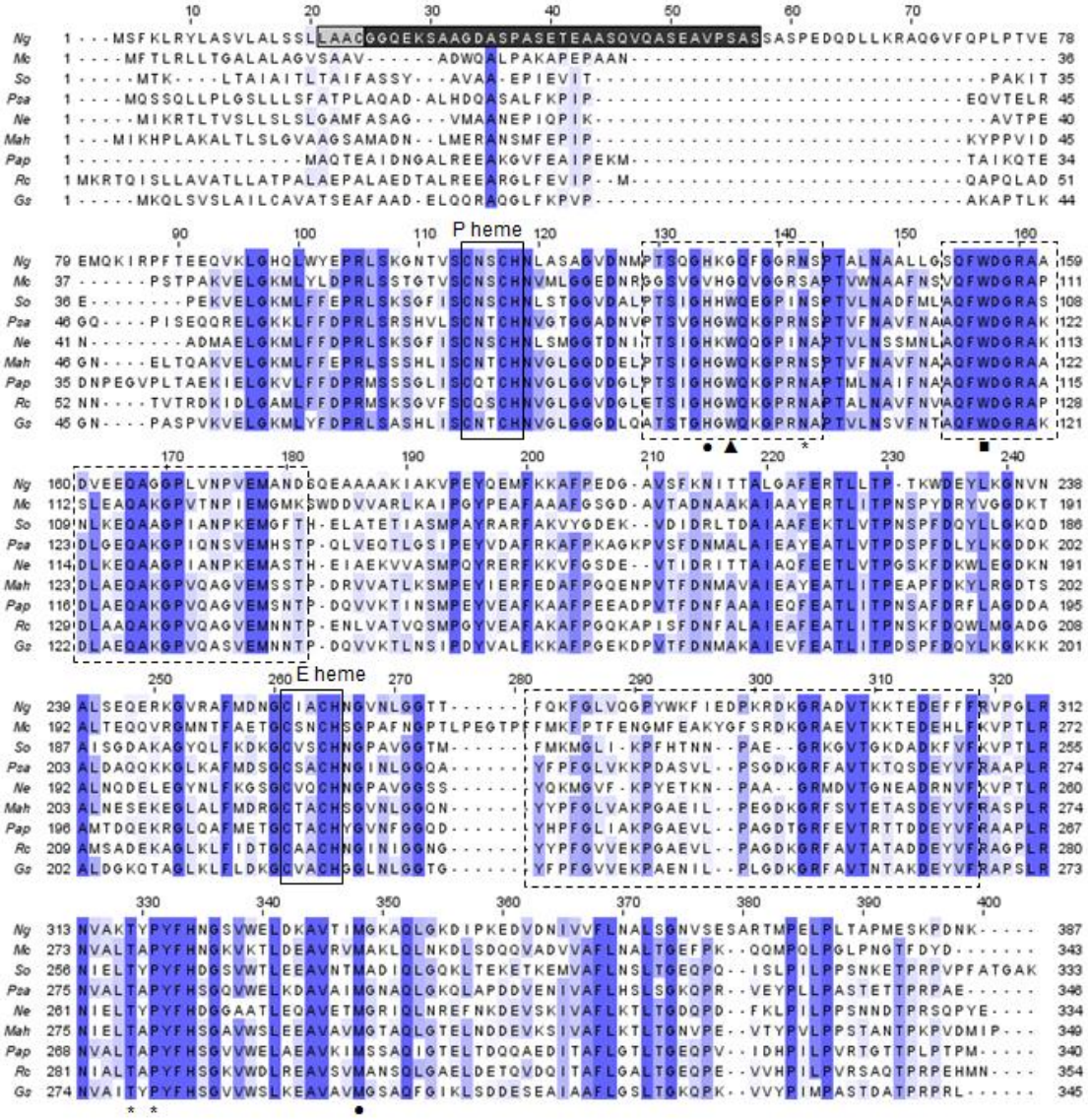

Figure 3.2 – Multiple sequence alignment of bacterial cytochrome *c* peroxidases primary sequence. *N. gonorrhoeae* FA 1090 (*Ng*; GI: 59802088), *M. capsulatus* (*Mc*; GI:53756268), *S. oneidensis* (*So*; GI:24373735), *P. aeruginosa* (*Psa*; GI:15599783), *N. europaea* (*Ne*; GI: 30180613), *M. hydrocarbonoclasticus* (*Mah*; GI:56541647), *P. pantotrophus* (*Pap*; GI:916812477), *R. capsulatus* (*Rc*; GI:940625801) and *G. sulfurreducens* (*Gs*; GI:259090277). The coloring is in accordance with percentage of identity at each position, from darker color box (100 % identity) to white box (≤ 20 % identity). The sequences are sorted by pairwise identity to *Ng*BCCP. The outlined grey box marks the *Ng*BCCP peptidase II cutting site and the black box the low complexity region with imperfect sequence repeats, only present in *Neisseria* species BCCPs. The loops and flexible regions involved in reductive activation are outlined by dashed black boxes. Some residues are marked, such as: (●) axial ligands, (*) calcium binding residues (▲) tryptophan at the dimer interface and (■) tryptophan bridging electron transfer between the two hemes.

The most striking difference is in the tryptophan residue that during activation forms a "Gly-Trp" stacking motif with a symmetry-related "Gly-Trp" pair in the neighboring monomer [166, 171] (Trp96 in *P. aeruginosa* BCCP sequence, Figure 3.2) that is conserved in all BCCPs, with the exception of the ones from *N. gonorrhoeae* and *M. capsulatus*. The formation of this stacking hydrophobic interaction

is proposed to stabilize the distal His-ligand loop that moves away from the P heme, and consequently the dimer. In fact, all BCCPs have been described to be homodimers. This small but significant change might have led to small variations in the primary sequence, which are observed for instance in *M. capsulatus*. In the *Ng*BCCP a Gln129 substituted an Ile/Val residue and Gly137 substituted a proline residue, both changes in the same loop as the distal histidine. The absence of this residue will be further discussed when analyzing the monomer-dimer equilibrium in *Ng*BCCP.

3.2.2 Heterologous production of *Neisseria gonorrhoeae* BCCP

The PCR amplified DNA fragment inserted into pET22b expression vector encoded only the conserved globular region of *Ng*BCCP (starting at Glu59, Figure 3.2), as the flexible region at the N-terminus could interfere with the stability of the enzyme. In addition, a His-tag was introduced at the C-terminus to facilitate the purification, since the amount of protein obtained is very low and a pure sample could not be obtained otherwise. This recombinant *Ng*BCCP (from now on designated as *Ng*BCCP) has 339 residues and an expected molecular mass of 38780.7 Da with two attached hemes (molecular mass of the polypeptide chain, 37547.4 Da, plus the molecular mass of two *c*-type hemes, 1233.3 Da).

*Ng*BCCP was isolated from *E. coli* periplasm and purified in two chromatographic steps, an affinity chromatography, followed by a size-exclusion chromatography. At the end, a pure enzyme fraction was obtained, as judged by its SDS-PAGE and PAGE (Figure 2.1 in Chapter 2) with a single band, which has an absorption ratio A_{402nm}/A_{278nm} of 4.2. This isolation procedure has an average yield of 8.4 mg of pure *Ng*BCCP, per liter of growth medium.

The heme/protein ratio of purified *Ng*BCCP was 1.8 ± 0.4, which indicated that there are 2 *c*-type hemes per polypeptide chain, as expected. Mass spectrometry analysis confirmed that the two hemes are covalently bound to the polypeptide chain and that the sample is pure, since *Ng*BCCP gives a single species with a molecular mass of 38780.7 ± 0.5 Da by ESI.

3.2.3 The monomer-dimer equilibrium

The monomer-dimer equilibrium was studied in solution by size-exclusion chromatography, indicating that the as-isolated *Ng*BCCP is a monomer (45 ± 2 kDa, I=200 mM) not dependent on the ionic strength (50 ± 2 kDa at I=50 mM and 44 ± 2 kDa at I=550 mM), and when treated with EGTA (42 ± 2 kDa). In the presence of calcium ions, it has an apparent molecular weight of 68 ± 2 kDa, consistent with dimer formation in solution (Figure 3.3). However, this calcium effect was only observed at enzyme concentrations above 10 μM.

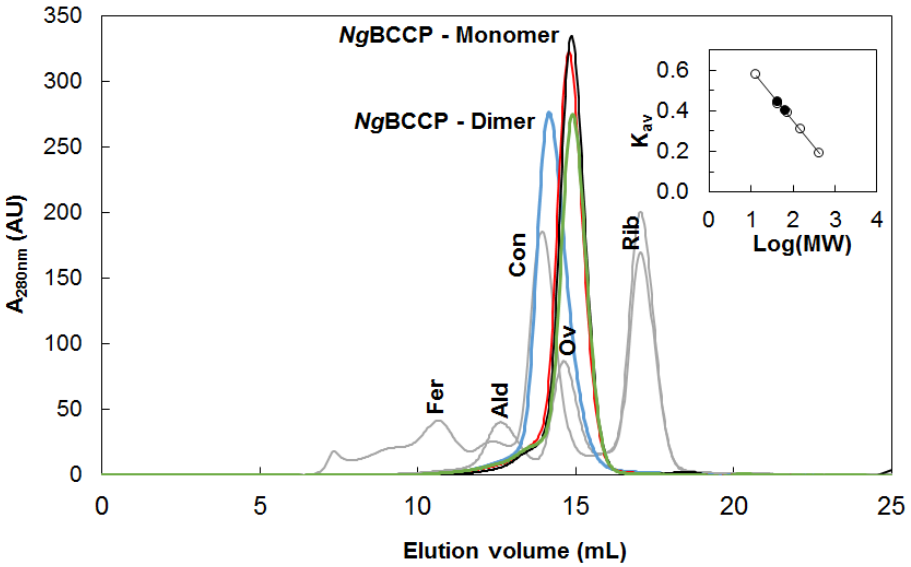

Figure 3.3 – Molecular size exclusion chromatography of as-isolated *Ng*BCCP (45 kDa, red line), at high ionic strength (44 kDa black line), with 2 mM $CaCl_2$ (68 kDa, blue line), and with 2 mM EGTA (43 kDa, green line). In grey are the elution profiles of standards proteins used to estimate the apparent molecular weight: Ferritin (Fer, 440 kDa), Aldolase (Ald, 158 kDa), Conalbumin (Con, 75 kDa), Ovalbumin (Ov, 44 kDa) and Ribonuclease A (Rib, 13.7 kDa). Concentration of *Ng*BCCP injected was 140 μM. Experimental conditions are described in Chapter 2.

Contrary to *Ng*BCCP, all other bacterial peroxidases have been reported to exhibit a monomer/dimer equilibrium in solution that is dependent on the ionic strength besides calcium ions [129, 163]. The dependence of this equilibrium on the ionic strength is an evidence of the hydrophobic nature of the dimer interface, suggesting that the dimer interface in *Ng*BCCP is less hydrophobic (the comparative analysis of *Ng*BCCP dimer interface with other bacterial peroxidases will be addressed in Section 3.2.8). This fact, together with the absence of the tryptophan residue (Gly133 in *Ng*BCCP native sequence) proposed to be essential in the stabilization of the BCCP dimer, explains the need for higher concentrations to observe dimer formation in the presence of calcium ions.

Differential scanning calorimetry was used to assess the distinct soluble states of *Ng*BCCP and study the influence of the calcium ions on those states. The thermograms obtained in the different conditions are presented in Figure 3.4, with the respective simulations.

In the presence of excess calcium ions *Ng*BCCP shows an endothermic transition, with a *Tm* of 46.9 ºC (ΔH = 823.1 kJ.mol^{-1}, ΔH_v = 752.0 kJ.mol^{-1}), that was simulated with an independent non-two state transition model (Figure 3.4, solid line), considering that *Ng*BCCP is in the dimeric state.

The thermogram of as-isolated *Ng*BCCP is broad with a thermal transition at 48.6 ºC (ΔH = 344.5 kJ.mol^{-1}, ΔH_v = 340.6 kJ.mol^{-1}) (Figure 3.4, dash-dot line). This broad peak can be attributed to the presence of a mixture of species, *Ng*BCCP with and without calcium, as well as monomers and dimers, since all solution states will behave as having distinct molecular weights.

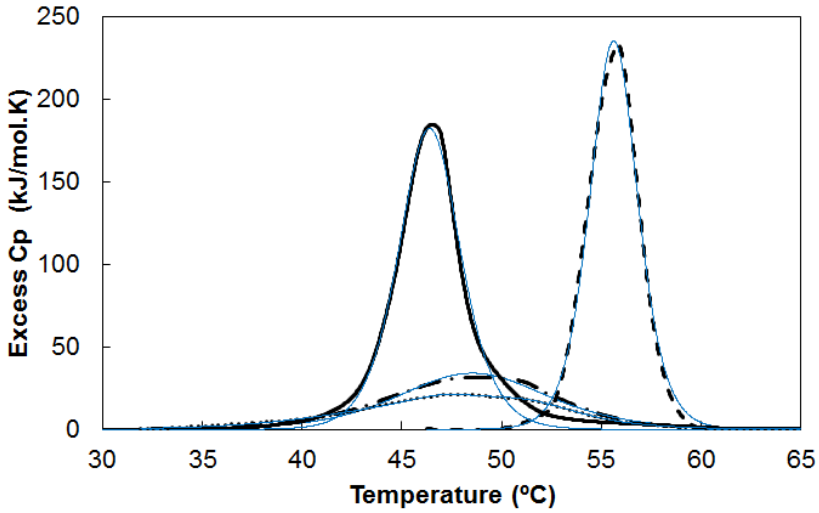

Figure 3.4 – Differential scanning calorimetry of *Ng*BCCP in different redox conditions and effect of calcium ions. *Ng*BCCP (20 µM) equilibrated in 10 mM HEPES pH 7.5 (dash-dot line), 10 mM HEPES pH 7.5 and 2 mM $CaCl_2$ (solid line), 10 mM HEPES pH 7.5 and 2 mM EGTA (dotted line), and 10 mM HEPES pH 7.5, 2 mM $CaCl_2$, 1 mM sodium ascorbate and 5 µM DAD (dashed line). The thermograms were baseline corrected and normalized for concentration. The simulations fitting the data are represented as blue lines.

To assess the effect of calcium ions, *Ng*BCCP was treated with 2 mM EGTA. The thermogram of this preparation has an even broader transition than the one of the as-isolated state (Figure 3.4, dotted line). This transition was simulated considering that *Ng*BCCP is a monomer, with a broad thermal transition occurring at 47.9 ºC, with a ΔH = 248.3 kJ.mol^{-1}. It was not possible to determine the van't Hoff enthalpy, because the data cannot be simulated with a single model as there are several overlapping intermediate species, which could not be identified.

The thermal stability of mixed-valence *Ng*BCCP in the presence of calcium ions was also assessed by DSC. The data show a shift in the endothermic transition to 55.6 ºC, an increase of around 9 ºC in comparison to the fully oxidized form (Figure 3.4, dashed line). The calorimetric enthalpy is of the same order of magnitude as the one of the as-isolated *Ng*BCCP in the presence of calcium ions (ΔH = 735.9 kJ.mol^{-1}). It was observed a strong aggregation at higher temperatures, which caused a negative ΔC_p, resulting in higher molar heat capacity. Any model used in the simulation of the data suggested a larger ΔH_v due to aggregation ($\Delta H_v > \Delta H$). This aggregation might have been caused by the presence of sodium ascorbate, but in its absence there was a mixture of higher and lower *Tm* transitions, probably due to partial oxidation of *Ng*BCCP during sample preparation prior to the DSC experiments.

These results show that in the presence of calcium ions, the thermal transition of as-isolated *Ng*BCCP becomes narrower with a higher molar heat capacity. This data was simulated considering that the enzyme is a dimer, which is consistent with the dimerization observed in the presence of calcium ions in solution. A similar result was obtained by Pettigrew *et al.* [163], though in that study it was also

observed a shift in the thermal transition towards higher values in the presence of calcium ions. The comparison of the calorimetric (ΔH) and van't Hoff (ΔH_v) enthalpies shows that in any case $\Delta H_v < \Delta H$, reflecting intermediate states for both enzymes. On the other hand, in the presence of EGTA the enzyme is proposed to exist only as a monomer consistent with the low molar heat capacity of the thermal transition, and with the monomeric form observed in solution, similarly to what was observed for *P. pantotrophus* BCCP treated with EGTA [163]. The broad transition observed in the absence of calcium ions can be explained considering that the two domains of *Ng*BCCP behave independently. This leads to the existence of distinct conformations (states) that denature as independent populations, and not as a single state. A similar interpretation was made for apocalmodulin, that has two globular lobes, for which the domains flexibility and different hydrophobicity leads to the separate unfolding of the C-terminal and N-terminal lobe [237], though in the case of *Ng*BCCP this separation is not resolved.

3.2.4 Spectroscopic characterization – UV-visible and EPR spectroscopies

The UV-visible spectrum of the as-isolated *Ng*BCCP has the usual features of an oxidized *c*-type cytochrome, with a Soret band at 402 nm (extinction coefficient of 222 ± 8 $mM^{-1}cm^{-1}$) (Figure 3.5).

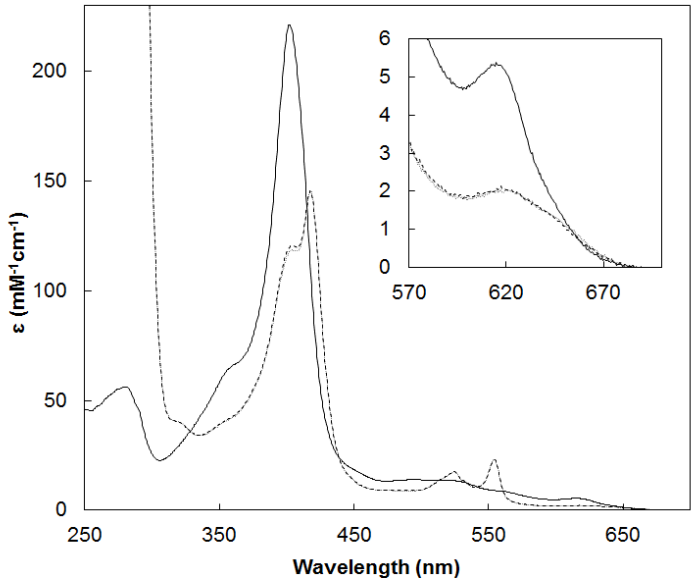

Figure 3.5 – UV-visible absorption spectra of *Ng*BCCP, in 10 mM HEPES pH 7.5. The spectrum of the as-isolated *Ng*BCCP is displayed as a solid line, the dashed and dotted lines are the spectra of the mixed-valence and mixed-valence incubated with calcium for 10 min, respectively. The inset shows the high-spin band in the visible spectra.

This spectrum has also a shoulder around 360 nm and an absorption band at 620 nm, characteristic of the presence of high-spin species. In the spectrum of the mixed-valence form, the Soret band splits into two absorption bands, one corresponding to the reduced high-potential E heme, with a maximum

at 418 nm, and the other to the low potential P heme still in the oxidized state, as a shoulder of the E heme's Soret band with an apparent maximum absorption at 402 nm. A α- and β-bands, at 554 (25.5 $mM^{-1}cm^{-1}$) and 524 nm (19.5 $mM^{-1}cm^{-1}$), respectively, become evident, consistent with E heme reduction.The analysis of these spectra indicates that the as-isolated *Ng*BCCP is mainly oxidized and the observed high-spin species can be attributed to the E heme, that has been reported to be in a low/high spin equilibrium, due to the loosely bound axial methionine ligand [160, 161] (Figure 3.6A). In the mixed-valence state, the high-spin band at 620 nm does not disappear completely indicative of the presence of a penta-coordinated high-spin heme, attributed to the P heme, as in other bacterial peroxidases, such as *P. aeruginosa* [161] and *P. stutzeri* [129], without addition of calcium ions (Figure 3.6B). Addition of calcium ions has only a small effect in the P heme's Soret band, with no additional increase in the absorption at 620 nm.

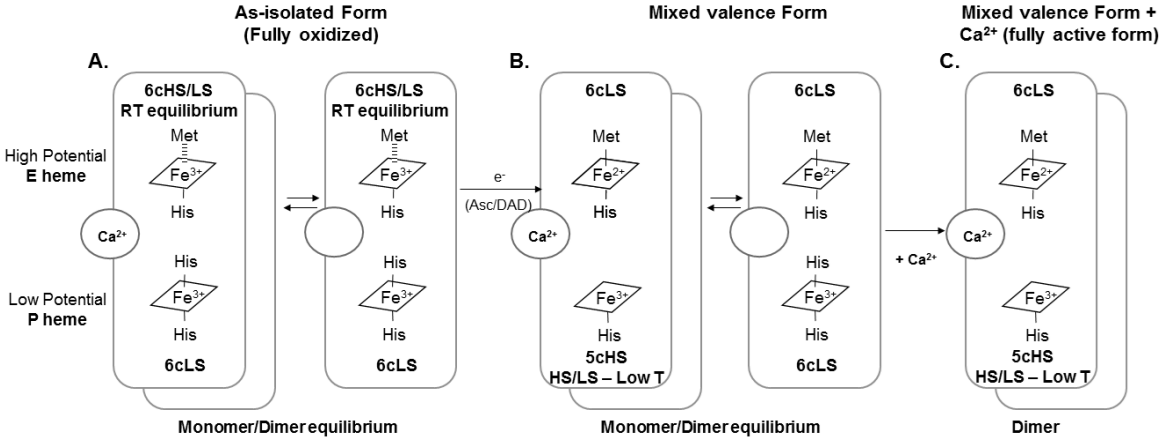

Figure 3.6 – Schematic representation of *Ng*BCCP indicating the spin-state and coordination sphere of both heme in the as-isolated fully oxidized form (A), mixed valence form without calcium ions in solution (B) and with additional calcium ions in solution (C). (A) In the fully oxidized state, ferric E heme is in a 6cHS/LS equilibrium at room temperature and the ferric P heme is 6cLS. (B) In the mixed valence form, E heme is reduced and becomes low-spin. If the calcium binding site is occupied, the reduction of E heme causes conformational changes that result in the removal of the P heme axial histidine ligand, which becomes 5cHS (active form) and HS/LS at low temperatures. In both redox states there is a monomer/dimer equilibrium due to a fraction of unoccupied calcium binding sites. Addition of calcium ions (C) promotes full dimerization and simplification of solutions states, with P heme being as 5cHS, and with some HS/LS being observed at low temperatures. 5c – penta-coordinated; 6c – hexa-coordinate; HS – high-spin; LS – low-spin.

However, addition of EGTA to the mixed-valence *Ng*BCCP leads to a decrease in the high-spin feature at 370 nm and 640 nm, accompanied by an increase in intensity of the absorption band at 402 nm (Soret band of P heme in the oxidize form, Figure 3.7A), which is an indication of the decrease in high-spin form of this heme. The decrease at 640 nm corresponds to the loss of high-spin due to calcium depletion. However, this feature is overlapped with another band that appears at 620 nm, reason why the difference spectra changes more significantly at 640 nm (this band peak is at 620 nm).

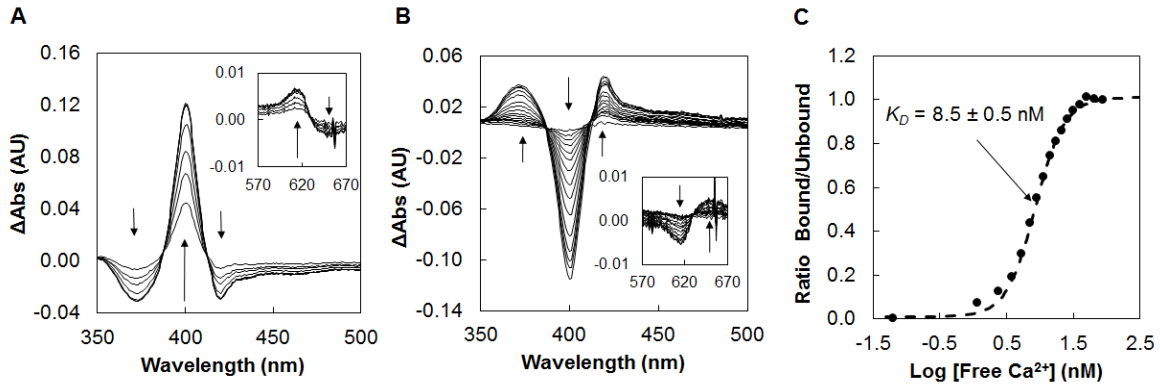

Figure 3.7 – Difference absorption spectra of *Ng*BCCP in the mixed-valence state (3 µM), in 10 mM HEPES pH 7.5, at 25 ºC, (A) upon addition of 1 mM EGTA as calcium ions are removed, and (B) after titrating calcium ions into solution, reverting the changes in *Ng*BCCP. The inset shows differences at the high-spin region of the visible spectra. Arrows indicate the direction of changes in the spectra that were acquired over time (up to 20 min) for calcium ions removal with EGTA (A), or over sequential additions of calcium ions (B). (C) The ratio of protein bound to Ca^{2+} was calculated from the absorption change at 401 nm (P heme), 10 min after each addition of 100 mM $CaCl_2$. Free Ca^{2+} was calculated considering the EGTA binding affinity at this pH value, ionic strength and temperature (K_D = 21 nM). The data was fitted considering a single calcium binding site with a K_D = 8.5 ± 0.5 nM.

The nature of this new band at 620 nm is unknown but might be due to conformational changes surrounding the P heme. As observed by DSC, *Ng*BCCP incubated with EGTA is monomeric and has more than one intermediate solution states and one of these states might affect P heme axial coordination at room temperature.

Addition of calcium ions reverted the enzyme to the original mixed-valence *Ng*BCCP (Figure 3.7B), which is consistent with having a high-spin P heme when the calcium site is occupied. *Ng*BCCP has a high affinity for calcium ions in the nanomolar range (K_D of 8.5 ± 0.5 nM, Figure 3.7C), which explains why addition of calcium ions has only a small effect on P heme high-spin features.

In Figure 3.8 is presented the EPR spectra of *Ng*BCCP in the as-isolated, mixed-valence and mixed-valence state incubated with calcium ions, with the respective simulation spectra.

In the spectrum of the as-isolated *Ng*BCCP, two low-spin and a high-spin ferric species are observed (Figure 3.8A). One of the low-spin species, with g = 3.18, is a Highly Axial Low Spin (HALS) signal, originated from the E heme with the other pair resonance not being detected in the EPR spectrum, as observed for other low-spin ferric heme proteins with a large g_{max},[40, 126]. The signals with g_z = 2.99 and g_y = 2.25 are assigned to a low-spin ferric species originated from P heme. According to the equation for low-spin hemes $g_z^2 + g_y^2 + g_x^2 = 16$ [42], there should be another signal with a g_x = 1.41, though it is most likely very broad and thus difficult to be observed. In this spectrum are also observed strong high-spin signals, with g values of 6.28, 5.56 and 1.99. This agrees with the strong absorption band observed at 620 nm in the visible spectrum of this form, at room temperature. The observation of two high-spin signals (at 6.28 and 5.56) in the EPR spectra of bacterial peroxidases has also been reported for *M. capsulatus* Bath and *P. stutzeri* as-isolated BCCPs [128, 129].

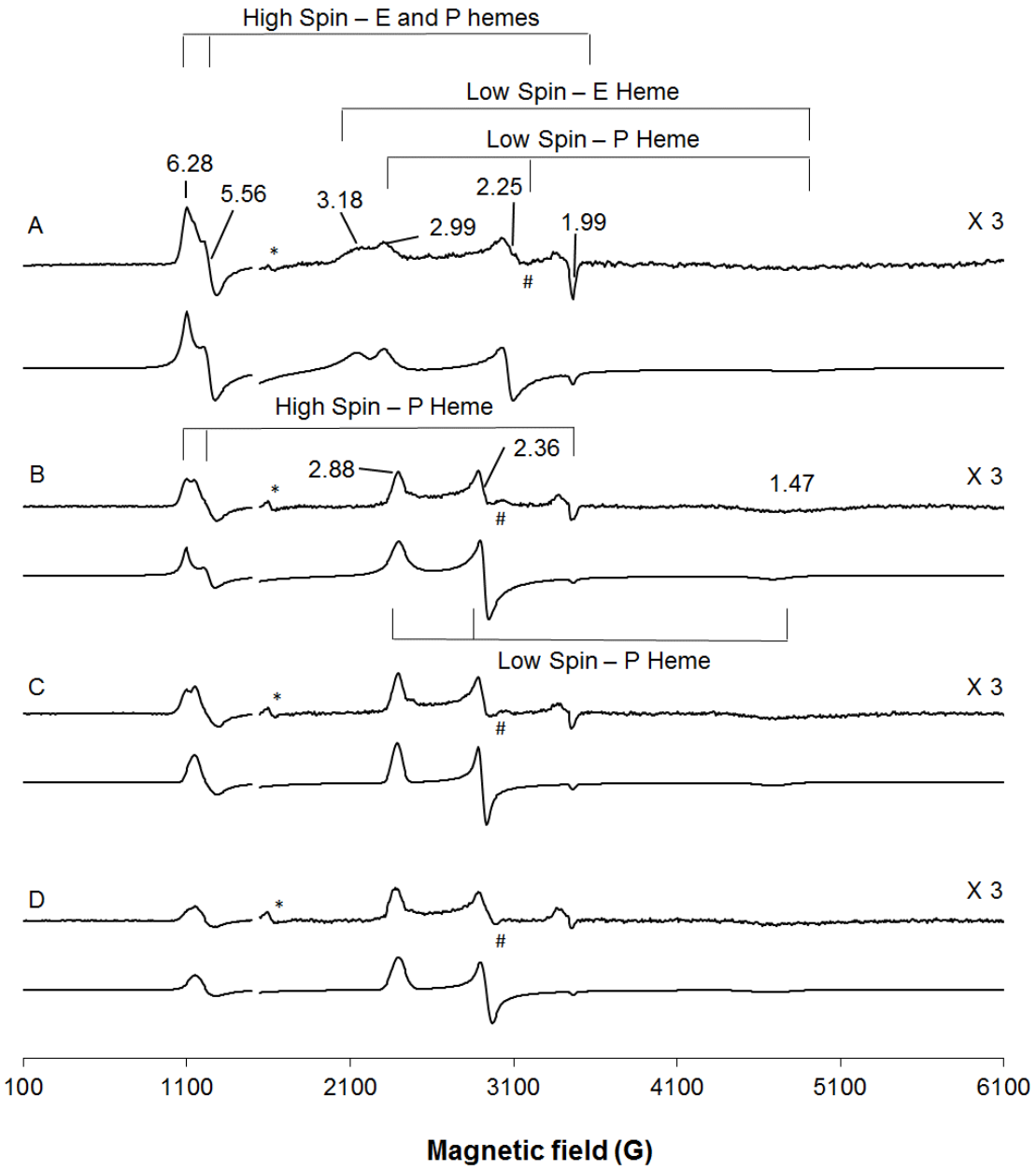

Figure 3.8 – X-band EPR spectra of 0.2 mM *Ng*BCCP and respective simulations below, in the oxidized form (A), after 1 min incubation with sodium ascorbate (B), after 30 min incubation with sodium ascorbate (C) and after 30 min incubation with 2 mM $CaCl_2$ after reduction with sodium ascorbate (D). The asterisk (*) marks the signal of free iron and the cardinal (#) is a cavity contaminant.

The spectrum in Figure 3.8B, shows that after 1 min incubation with sodium ascorbate/DAD, E heme is reduced and becomes EPR silent, which is supported by the absence of the signal at g = 3.18, the low-spin species of E heme, as well as, the disappearance of most of the $g_{\|}$ = 6.28 and $g_{\perp}$=1.99 high-spin signal, that thus can be partially attributed to this heme. This agrees with the relative amount of spin signals for the oxidized form presented in Table 3.1, where approximately 50 % corresponds to E heme (sum of the low-spin signal and high-spin signal) and the other 50 % to P heme low-spin signal. However, the high-spin species does not disappear completely when *Ng*BCCP

is reduced, similarly to what was observed in the room temperature UV-visible spectrum (Figure 3.8B). In addition, a new set of *g* values appear for a low-spin species, with g_z = 2.88, g_y =2.36 and g_x =1.47, substituting the previous signal with a g_z = 2.99 and g_y = 2.25. This change in *g* values of P heme, with the signals becoming sharper, upon reduction of E heme, has been explained by the change in coordination sphere of this heme (by loss of the distal histidine ligand, Figure 3.6B).

Table 3.1 – Relative amount of spin signal calculated by integration of the simulated high/low-spin signals of each acquired spectrum.

Heme Spin Signal	Relative amount of spin signal (%)			
	As-isolated	Ascorbate 1 min	Ascorbate 30 min	Ascorbate + Calcium
High-Spin	42	44	59	24
Low-spin E heme	13	-	-	-
Low-spin P heme	45	56	41	76

However, at cryogenic temperatures, the 5cHS species for P heme are not usually observed in the EPR spectrum [137, 174]. The presence of this low-spin species has been attributed to P heme being coordinated by a water molecule, as the sixth axial ligand in substitution of the distal histidine ligand, as observed in the X-ray structures of mixed-valence bacterial peroxidases [167], as well as in the mixed-valence *Ng*BCCP structure (see Section 3.2.8). As explained by Echalier *et al.*, although a water molecule is considered a weak ligand, the binding to P heme at cryogenic temperatures originates, in the EPR spectrum, signals with spectroscopic properties of a low-spin heme, which have been attributed to the higher energy of the Fe-water coordination at lower temperatures [171]. The observation of P heme coordination sphere change upon reduction of E heme, without added calcium ions, is an indication that in *Ng*BCCP the calcium site is almost fully occupied, enabling the conformational change of the polypeptide chain, similarly to what was observed for *P. aeruginosa* [166] and *P. stutzeri* bacterial peroxidases [129], and in agreement with the absorption spectra presented before (Figure 3.5).

After 30 min incubation with sodium ascorbate (Figure 3.8C), these signals become sharper and there is also a small decrease in the $g_{||}$ = 6.28 high-spin signal, indicating that after 1 min, the E heme was not fully reduced, and that conformational change at the P heme was also not complete. In the mixed-valence *Ng*BCCP the spin signals are solely attributed to the P heme with approximately 50 % being high-spin and the other 50 % low-spin, as presented in Table 3.1. After incubation with calcium ions (Figure 3.8D), the signal of the low-spin species becomes broader, which can be attributed to small changes in the P heme population, and/or the environment around this heme. In fact, addition of calcium ions promotes dimerization of *Ng*BCCP (Figure 3.6C; a single solution state is observed in the DSC experiments), which is expected to change the environment around the P heme (in spite of primary sequence differences, the loop close to P heme, including the P heme histidine axial ligand,

is proposed to move to the dimer interface as observed for other classical BCCPs [166], see Section 3.2.8.3). This modifies its coordination geometry, as it is observed a decrease in the relative amount of high-spin signal (59 % to 24 %) with increase of the low-spin signal (41 % to 76 %) as shown in Table 3.1.

The presence of a high-spin species in the EPR spectra of mixed-valence BCCP incubated with calcium ions is unique to *Ng*BCCP, which can be attributed to differences in the active site and also in the dimer interface. Moreover, the spectroscopic data shows that the calcium site is partially occupied, which can be explained by the nanomolar binding affinity (K_D of 8.5±0.5 nM) determined for the mixed-valence *Ng*BCCP, a higher affinity when compared with the one of *P. pantotrophus* BCCP (K_D of 2.6 µM) [162].

3.2.5 Redox titration

The oxidative and reductive titrations of *Ng*BCCP incubated with calcium ions or EGTA (to remove calcium ions) are presented in Figure 3.9.

As expected, there are two reduction potentials, corresponding to a low- and a high-potential redox center, which are titrated separately. The titration curves were simulated based on the Nernst equation and the values are listed in Table 3.2, which also lists the potentials obtained for the redox titration of the as-isolated *Ng*BCCP (these experiments were performed with the same enzyme preparation).

It should be noted that, although the midpoint potential of both hemes was determined and discussed, the oxidation-reduction equilibrium Fe^{3+}/Fe^{2+} of P heme is not relevant *in vivo*, since the catalytic mechanism of BCCP does not include the fully reduced form of the enzyme.

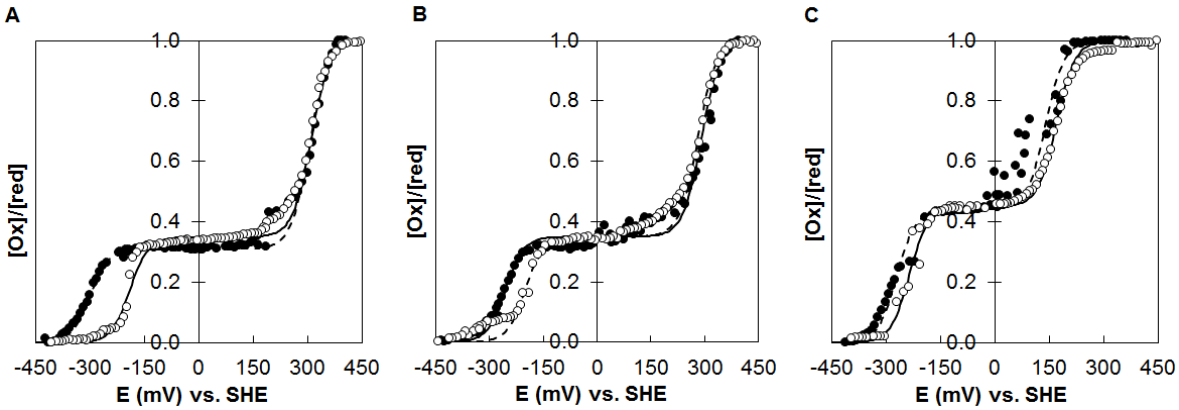

Figure 3.9 – Effect of calcium ions in the potentiometric titrations of *Ng*BCCP at pH 7.5. The reduction potentials were determined (A) in the presence of excess of calcium ions, (B) without added calcium ions and (C) in its absence, in the presence of EGTA. The reductive titration is represented by open circles and the oxidative titration by closed circles. The lines represent the simulation of the potentiometric curve using the reduction potentials listed in Table 3.2.

Table 3.2 – Reduction potential of each *Ng*BCCP heme in the reductive and oxidative direction in the presence of excess, without added (as-isolated) and in the absence of calcium ions (+ EGTA), at pH 7.5.

		Reduction Potential (mV)		
Heme	**Direction**	**+ 2 mM $CaCl_2$**	**As-isolated**	**+ 2 mM EGTA**
E heme	Reduction	310 ± 10	280 ± 10	170 ± 10
	Oxidation	305 ± 10	290 ± 10	150 ± 10
P heme	Reduction	- 190 ± 10	- 200 ± 10	- 245 ± 10
	Oxidation	- 300 ± 10	- 255 ± 10	- 270 ± 10

In the presence of excess calcium ions, the E heme of *Ng*BCCP has a reduction potential of approximately + 310 ± 10 mV, in either the reductive or oxidative titration (Figure 3.9A), showing that the reduction of E heme is reversible without hysteresis, even though its reduction is associated with considerable conformational changes in the enzyme [166]. On the other hand, the P heme, upon E heme reduction, is easier to reduce than it is oxidized, as its midpoint potential in the reductive direction (- 190 ± 10 mV) is higher than in the oxidative direction (- 300 ± 10 mV), with a hysteresis being observed.

In contrast, in the calcium depleted *Ng*BCCP (Figure 3.9C), E heme is clearly more difficult to be reduced, with a 150 mV decrease in its reduction potential (with a reduction potential of + 170 ± 10 mV), compared with the value in the presence of calcium ions. Likewise, the P heme in the reductive titration is also more difficult to be reduced, by around 60 mV, and the hysteresis effect on the oxidative titration is not as significant as the one observed before in the presence of calcium ions (Table 3.2). This lack of hysteresis can be explained by the absence of conformational change around the P heme. Thus, in the absence of calcium ions, P heme remains hexa-coordinated and low-spin regardless of the oxidation state of E heme.

In the as-isolated state, the reduction potential of E and P hemes are closer to the ones obtained for the enzyme in the presence of calcium ions (Figure 3.9B), and there is a hysteresis in the reductive and oxidative titration of P heme, similar to the one in the presence of calcium ions. This strongly suggests, as previously discussed, that the as-isolated *Ng*BCCP has the calcium site mainly occupied.

3.2.6 Steady-state kinetics with $ABTS^{2-}$

*Ng*BCCP was assayed for its peroxidatic activity using $ABTS^{2-}$ as an artificial electron donor [202]. The initial rate determined for the pre-activated enzyme in the presence of calcium ions is 0.79 ± 0.05 $ABTS^{2-}.s^{-1}$ (Figure 3.10 solid line).

*Ng*BCCP without reductive activation (as-isolated) and in the presence of calcium ions, has very little catalytic activity (0.019 ± 0.002 $ABTS^{2-}.s^{-1}$, Figure 3.10A dashed-line), that can be attributed

to a small population that is in the mixed-valence state. This is a clear indication that *Ng*BCCP requires reductive activation for catalytic activity.

In order to assess the role of calcium ions in activation, the peroxidatic activity of the pre-activated *Ng*BCCP with and without added calcium ions to the stock solution was measured, showing an initial rate of 0.70 ± 0.01 $ABTS^{2-}.s^{-1}$ and 0.68 ± 0.01 $ABTS^{2-}.s^{-1}$, respectively (Figure 3.10B). Therefore, addition of calcium ions in the stock solution has almost no effect in the initial rates. This agrees with the spectroscopic characterization, which concluded that *Ng*BCCP is purified with the calcium site partially occupied as it has a high affinity for calcium ions. The change in the high-spin species with excess calcium ions shows that calcium ions are essential for the activation and the kinetic data indicates that reductive activation is essential to attain maximum catalytic activity.

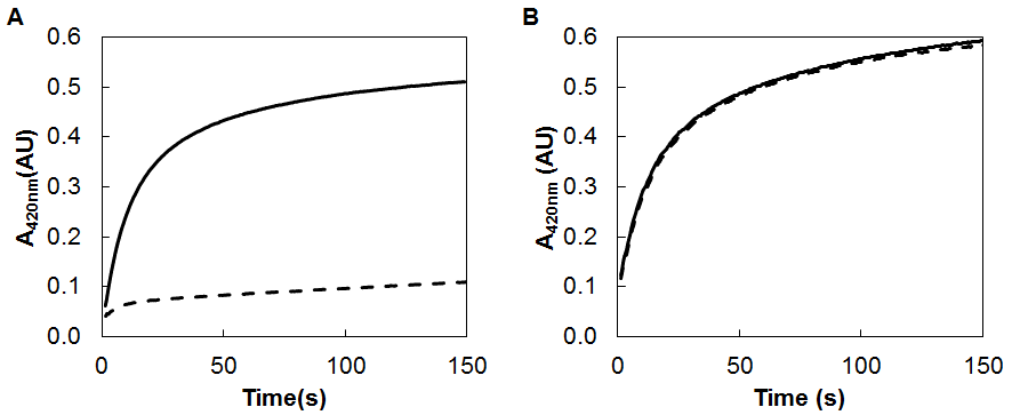

Figure 3.10 – Kinetic traces of peroxidatic activity of the (A) pre-activated *Ng*BCCP using $ABTS^{2-}$ as electron donor in the presence (solid line) of 1 mM $CaCl_2$ during the pre-activation and kinetic assay, and of the as-isolated *Ng*BCCP with 1 mM $CaCl_2$ in the kinetic assay (dashed-line). (B) Kinetic traces of pre-activated *Ng*BCCP with 1 mM $CaCl_2$ during pre-activation and the kinetic assay (solid line) and with 1 mM $CaCl_2$ only in the kinetic assay (dashed-line). The assays were performed in 10 mM HEPES, 10 mM NaCl at pH 7.0 and 25 ºC with 100 µM H_2O_2. Time zero was adjusted to the time *Ng*BCCP was added. The initial rates determined for the pre-activated *Ng*BCCP are 0.79 ± 0.05 $ABTS^{2-}.s^{-1}$ in the presence of calcium ions. The as-isolated *Ng*BCCP initial rate is 0.019 ± 0.002 $ABTS^{2-}.s^{-1}$ in the presence of calcium ions. The presence or absence of calcium ions in the pre-activation results in similar initial rates of 0.70 ± 0.01 $ABTS^{2-}.s^{-1}$ and 0.68 ± 0.01 $ABTS^{2-}.s^{-1}$, respectively.

The kinetic parameters for the catalytic activity of pre-activated *Ng*BCCP in the presence of calcium ions using $ABTS^{2-}$, as electron donor (Figure 3.11A), were a K_M of 4 ± 1 µM H_2O_2 and a turnover number of 79 ± 5 s^{-1} at pH 7.0 and 25 ºC. In comparison, the as-isolated enzyme, in the presence of calcium ions (Figure 3.11B), has a K_M = 27 ± 14 µM H_2O_2 and a turnover number of 1.9 ± 0.2 s^{-1}. This confirmed what the preliminary data suggested, that the as-isolated state has little catalytic activity, even with higher substrate concentrations.

The K_M value for the mixed-valence *Ng*BCCP is similar to *Geobacter sulfurreducens* CcpA, with K_M of 6.2 µM [132], using $ABTS^{2-}$ in the same concentration as in the present study. Other bacterial

peroxidases have K_M values in the same order of magnitude [129, 131, 169], which points out that *Ng*BCCP is an efficient hydrogen peroxide detoxifying enzyme.

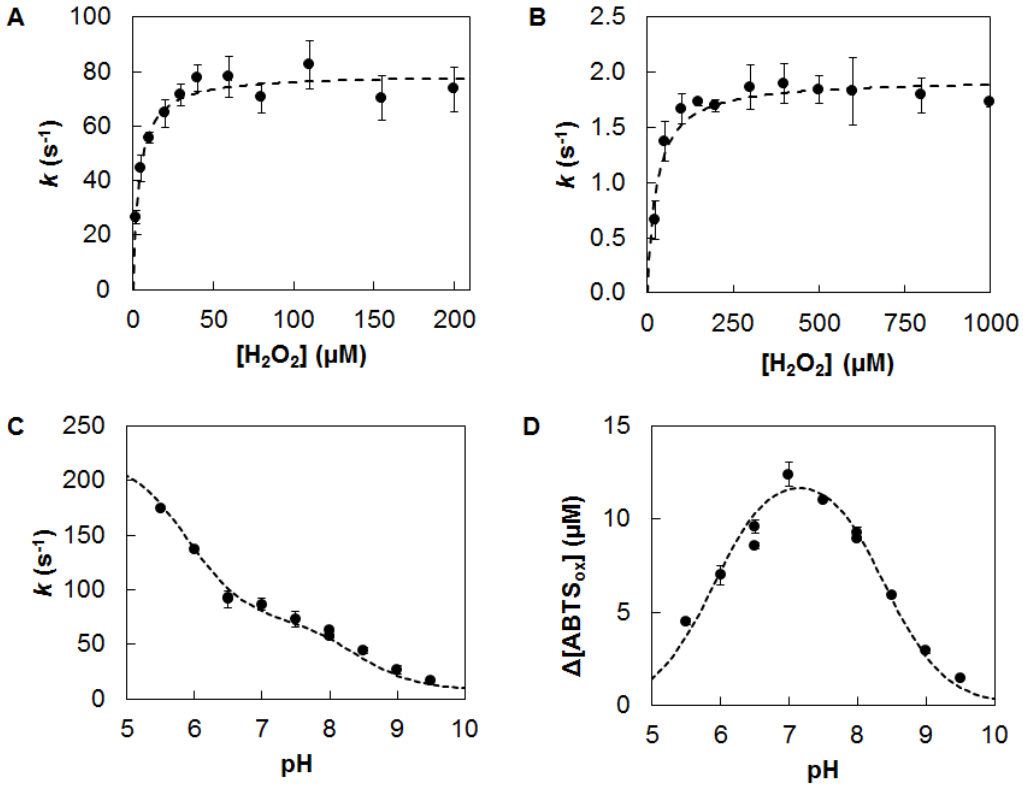

Figure 3.11 – Steady-state kinetics using $ABTS^{2-}$ as electron donor. Catalytic activity of *Ng*BCCP without (A) and with pre-activation (B). pH effect on pre-activated *Ng*BCCP catalytic activity (C) and, for each pH, the average amount of $ABTS^{2-}$ consumed in a 100 s interval starting after addition of the enzyme (D). The dashed lines represent the simulated data using Michaelis-Menten, and Equations 2.8 and 2.9 in Chapter 2 (Materials and Methods, Section 2.7.1). The parameters used in the simulation are the ones stated in the main text.

The k_{cat} of 79 s^{-1} obtained for *Ng*BCCP is similar to the one of *S. oneidensis* tag free BCCP (73 s^{-1}) in the mixed-valence state using *S. oneidensis* cytochrome c_5 as electron donor [131]. However, in that study, the electron donor is not in saturating concentrations, as well as in most of the other reported kinetic studies of BCCPs. These high turnover numbers can be attributed to the direct electron transfer of $ABTS^{2-}$ to the P heme, in addition to the usual electron transfer pathway from the E to the P heme, since $ABTS^{2-}$ is a small molecule present in excess, and such electron transfer does not require any further mechanism, such as formation of a productive encounter electron transfer complex (with recognition and electron transfer steps). Further kinetic studies with its physiological partner LAz will be presented in Chapter 4 in which this subject will be discussed.

Regarding the pH dependence, the highest catalytic rate was observed at pH 5.5 (Figure 3.11C), with a $pKa_1 = 5.9 \pm 0.1$ and a $pKa_2 = 8.4 \pm 0.1$. However, if one analyses the amount of substrate consumed after 100 s of reaction, by determining the concentration of oxidized $ABTS^{2-}$ present at that time-point, the curve has a bell-shape with an optimum pH around 7.0 and the same p*Ka* values

(pKa_1 = 5.9 ± 0.1 and pKa_2 = 8.4 ± 0.1) (Figure 3.11D). The decrease in product concentration at low and high pH is attributed to enzyme inactivation or protonation/deprotonation of catalytically relevant residues (as will be discussed in Section 3.2.8.4). At low pH values, $ABTS^{2-}$ is an efficient electron donor (high initial rates) but the changes in the protonation state of the enzyme does not favor the reaction. On the other hand, at high pH values two effects can be contributing to the decrease in activity, the lower efficiency of the electron donor and the deprotonation of important residues for catalysis, as the peroxidatic reaction requires protons.

The temperature dependence of *Ng*BCCP was assessed and maximum activity was observed at 37ºC, which is consistent with *N. gonorrhoeae* lifestyle as a human pathogen. Arrhenius and Eyring plots (Figure 3.12) were used to further analyze the effect of the temperature in the reaction rate, which shows a linear dependence, with the exceptions of the temperatures above 37 ºC, due to enzyme inactivation. Based on Arrhenius equation (Chapter 2, Section 2.7.1), it was possible to determine the activation energy, ΔE_A, associated with this reaction, which is approximately 8 ± 1 kJ/mol, and the fit of the data to the Eyring equation was used to obtain $\Delta H^{\ddagger}$ of 5 ± 1 kJ/mol and $\Delta S^{\ddagger}$ of - 0.17 ± 0.03 kJ/mol. Therefore, $\Delta G^{\ddagger}$ at room temperature is 57 ± 1 kJ/mol, which is comparable to the one estimated based on the k_{cat} at 298 K (79 s^{-1}), of 48.04 ± 0.03 kJ/mol.

The low value of the estimated entropy change indicates that there is formation of an ordered enzyme-substrate complex. Thus, the rate-limiting step of the turnover does not involve substrate binding or release, and might be the internal electron transfer from E heme to P heme.

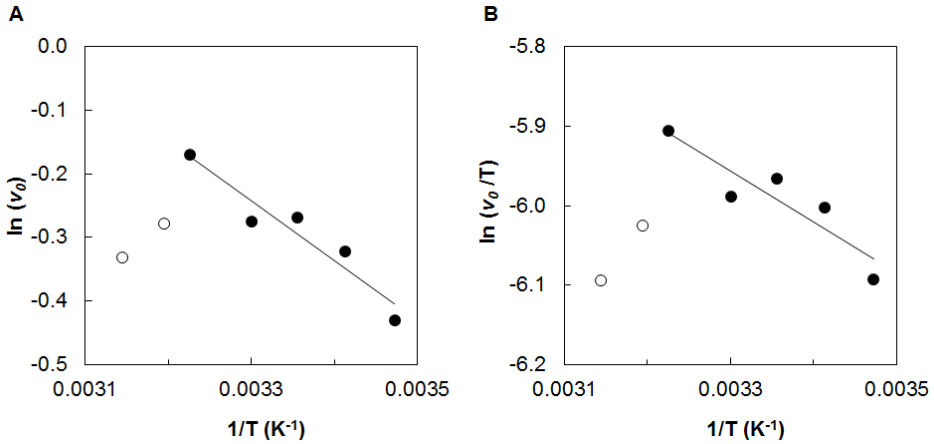

Figure 3.12 – Arrhenius plot (A) and Eyring plot (B) plot for *Ng*BCCP activity with $ABTS^{2-}$ as electron donor, in 10 mM HEPES, 10 mM NaCl and 2 mM $CaCl_2$, at pH 7.0, as a function of temperature. At temperatures above 40 ºC the plots are no longer linear due to enzyme denaturation, reason why these data were not included in the slope determination. The correlation coefficients are 0.95 and 0.91 for (A) and (B), respectively.

The kinetics with $ABTS^{2-}$ show that *Ng*BCCP is an efficient peroxidase *in vitro*, reducing H_2O_2 to H_2O, even when using this artificial electron donor. However, as observed in Figure 3.11D, the maximum difference in $ABTS^{2-}$ concentration in the assay during 100 s is 12.4 ± 0.6 µM $ABTS_{ox}$ at

pH 7.0, showing that the reaction is not complete (not all H_2O_2 was consumed), even though $ABTS^{2-}$ is in saturating concentrations. One plausible explanation is that $ABTS^{2-}$ might not be able to maintain *Ng*BCCP in the mixed-valence active form or the enzyme is inhibited over time by H_2O_2 due to Fenton reactions.

3.2.7 Inhibition Studies - Binding and Steady-state Kinetics

In order to develop inhibitors for *Ng*BCCP, three known cytochrome *c* inhibitors were tested: cyanide, imidazole and azide sodium salts. In order to assess the effect of the inhibitors, their binding was monitored by following the changes in the UV-visible spectra of the mixed-valence *Ng*BCCP upon increasing concentrations of inhibitor (Figure 3.13).

In the case of cyanide and azide the absorbance changes occurred at 395 nm, thus P heme is being affected. In order to estimate the k_{app} value, the variation of absorbance as a function of inhibitor concentration was analyzed using the equation 2.3 in Chapter 2 (Section 2.6.2). The estimated k_{app} for cyanide is 4 µM, value that is similar to what was observed for *R. capsulatus* (4 µM) and *P. pantotrophus* (5 µM) BCCPs [137, 169], but it is much lower than the one reported for *P. aeruginosa* BCCP (23 µM [238]), an indication that the P heme cavity in *Ng*BCCP is more exposed/larger than the one in *P. aeruginosa*.

Azide binds at the P heme with an estimated k_{app} of 26 mM, considering a single binding site (Figure 3.13C, D). However, at pH 6.0 the affinity is higher with an estimated k_{app} of 3.8 mM azide (not shown). Therefore, sodium azide has a low binding affinity compared to cyanide (Figure 3.13A,B). In *N. europaea* BCCP inhibition studies, it was also proposed that at higher concentrations of azide the E heme methionine was displaced [135], which was not observed in *Ng*BCCP.

The binding of imidazole has two phases. At lower concentrations of imidazole (0-100 mM), as observed by the increase at A_{407nm}, binding occurs mainly at the P heme. At higher concentrations (> 100 mM) there is a decrease at A_{421nm}, as the reduced Soret band of the E heme is also affected, (Figure 3.13E, F). In the case of *Ng*BCCP, imidazole binds to E heme in the reduced state, indicating that the methionine S-Fe bond is relatively weak and that imidazole competes and is able to dissociate the methionine from the ferrous heme at concentrations above 100 mM imidazole.

A study with cytochrome c_1 shows that binding of exogenous ligands typically results in a hyperbolic dependence on ligand concentration, but if the ligand is imidazole, the binding is more complex and involves an initial binding interaction followed by conformational change and bond formation with the heme Fe [239]. Furthermore, as demonstrated in horse heart cytochrome *c* interaction with imidazole, this molecule is able to bind low-spin *c*-type hemes in the ferrous state (a K_D = 1 M) and in the ferric state (a K_D = 72 mM). The K_D value for ferrous hemes varied greatly depending on the cytochrome, pH and temperature [231].

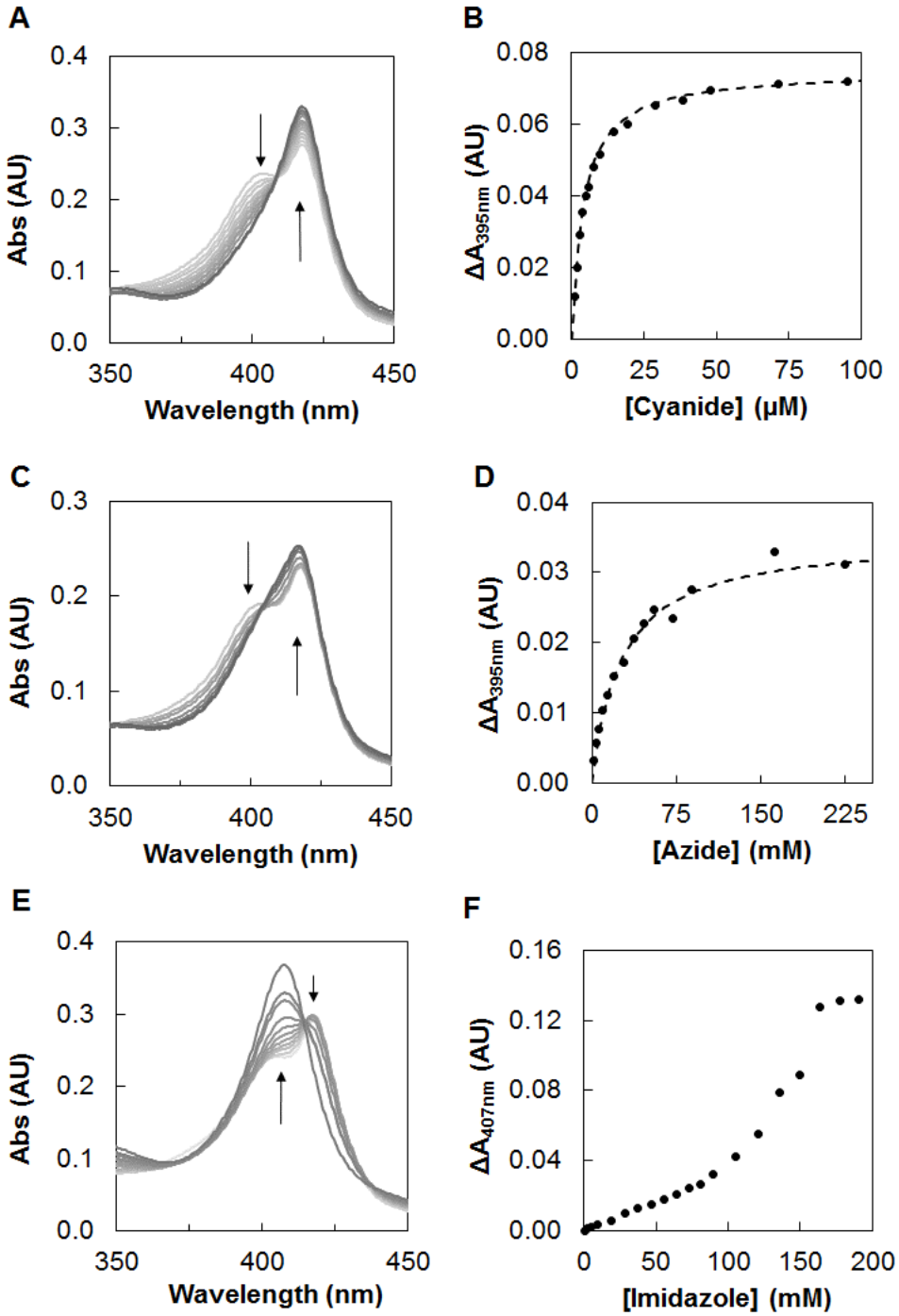

Figure 3.13 – UV-visible spectra of mixed-valence *Ng*BCCP, at pH 7.5 binding increasing amounts of cyanide (A), azide (C) and imidazole (E). The arrows indicate direction of changes in the spectra from the light grey (no inhibitor) to dark grey (maximum inhibitor concentration). The absorption difference at specific wavelengths was plotted as a function of inhibitor concentration in solution (B, cyanide; D, azide; F, imidazole). The dashed line (B, D) simulates the binding of cyanide and azide to one single binding site with a k_{app} of 4 μM and 26 mM, respectively (see equation 2.3 in Chapter 2, Section 2.6.2).

In order to determine how the binding of these inhibitors affects *Ng*BCCP activity, kinetic assays in the presence of various concentrations of inhibitor and H_2O_2 were performed, using $ABTS^{2-}$ at saturating concentrations, as the electron donor (Table 3.3).

Table 3.3 – Steady-state kinetics parameters determined for each concentration of cyanide (CN^-), azide (N_3^-) and imidazole (Im).

Cyanide				Azide				Imidazole			
[CN^-] (µM)	**K_{Mapp} (µM)**	**$V_{max\ app}$ (µM.s^{-1})**	***ki*** **(µM)**	**[N_3^-] (mM)**	**K_{Mapp} (µM)**	**$V_{max\ app}$ (µM.s^{-1})**	***ki*** **(µM)**	**[Im] (mM)**	**K_{Mapp} (µM)**	**$V_{max\ app}$ (µM.s^{-1})**	***ki*** **(µM)**
0	0.7	0.66	-	0	3.6	0.74	-	0	3.9	0.72	-
10	15.5	0.66	0.5	10	2.4	0.71	36.6	20	3.6	0.65	7.6
20	34.1	0.72	0.4	40	4.3	0.66	55.4	35	3.5	0.63	8.6
35	61.7	0.76	0.4	60	3.8	0.59	36.2	50	3.1	0.58	6.4
50	79.4	0.75	0.5	80	4.5	0.56	39.7	80	4.7	0.55	9.1
70	161.7	0.80	0.3	100	5.6	0.53	38.7	110	6.0	0.49	8.6
								140	7.4	0.48	9.8
								170	9.5	0.44	10.3

The estimated K_{Mapp} for cyanide is higher than K_M (zero inhibitor), while the $V_{max\ app} \approx V_{max}$. In the Dixon plot (Figure 3.14A) there is no intercept, therefore, no uncompetitive inhibition constant (*ki*') [240] can be calculated.

The *x*-intercept in the Cornish-Bowden plot [241] gives the estimated -*ki* (Figure 3.14B) however, an average *ki* = 0.4 ± 0.1 µM was calculated from the K_{Mapp} (Table 3.3) according to equation 2.13 in Chapter 2 (Material and Methods, Section 2.7.1). According to this data and the kinetic diagram in Figure 3.15, cyanide is a competitive inhibitor that binds preferably to the free enzyme (no uncompetitive constant, *ki'*).

In the case of azide and imidazole, the estimated K_{Mapp} is higher than K_M, which means that the apparent affinity of the substrate decreases, favoring binding of the inhibitor to the free enzyme. If $V_{max\ app}$ was similar to V_{max} then it would be a pure competitive inhibition as observed for cyanide. However, $V_{max\ app} < V_{max}$, which indicates that these inhibitors bind also to an allosteric site. In this case if K_{Mapp} was similar to K_M it would be a pure uncompetitive inhibition. The data shows the presence of a mixture of competitive and uncompetitive binding (mixed-inhibition mechanism) as shown in the kinetic diagram in Figure 3.15.

In order to determine α, the constants *ki'* and *ki* were estimated from the Dixon (Figure 3.14C,E) and Cornish-Bowden (Figure 3.14D,F) linear plots for both azide and imidazole. In the case of azide, *ki* = 41 ± 5 mM, *ki'* = 238 ± 4 mM and α = 6.4 ± 0.4, were estimated at pH 7.5 from $V_{max\ app}$ according to equation 2.14 in Chapter 2 (Section 2.7.1). Imidazole shows a lower inhibition constant with *ki* = 9 ± 4 mM and *ki'* = 350 ± 5 mM (α = 28 ± 5).

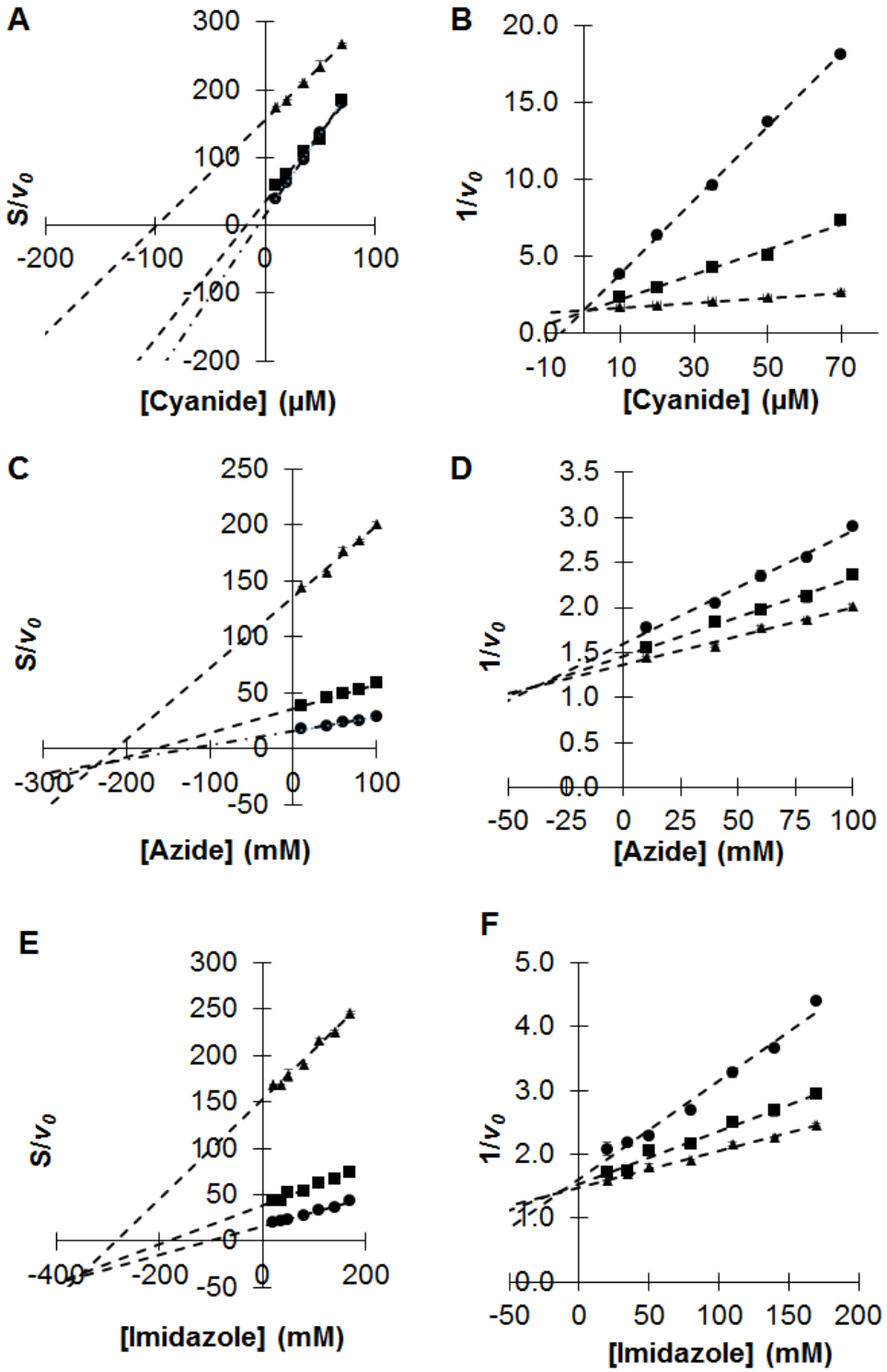

Figure 3.14 – Determination of the mixed inhibition constants according to scheme in Figure 3.15 for (A, B) cyanide, (C, D) azide and (E, F) imidazole at pH 7.5. *ki'* and *ki* estimates are given by the intercept value in plots of S/*v* (Dixon: A, C, E) or 1/*v* (Cornish-Bowden: B, D, F) respectively, against *i* at three different substrate concentrations (● 0.1 μM, ■ 25 μM and ▲ 100 μM H_2O_2). The error bars are represented for the average of duplicate measurements.

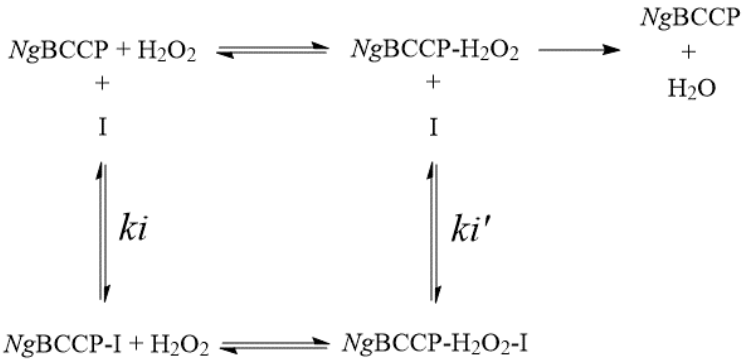

Figure 3.15 – Kinetic diagram of *Ng*BCCP activity with H_2O_2 as substrate and H_2O as final product (protons and electrons in this reaction were omitted for simplicity, see Chapter 1, Section 1.3.6 for a detailed catalytic cycle). In the presence of inhibitor (I) there is mixed-inhibition, where *ki* is the competitive inhibition constant and *ki'* the uncompetitive inhibition constant. These two constants are related by a constant α, $ki' = \alpha.ki$.

From all three inhibitors, cyanide is the most efficient with a *ki* of 0.4 µM, which is similar to the ones in BCCPs from *N. europaea* (0.153 µM, pH 7.0) and *P. aeruginosa* (7.1 µM, pH 6.0) BCCPs [125, 135]. However, in the enzyme without substrate there is no observable change at the Soret band of the P heme upon addition of 0.4 µM cyanide. One possible explanation for this lower *ki* value could be that the enzyme turnover is essential to form a cyanil radical, which is extremely reactive and is formed in the reaction of CN^- with the oxoferryl intermediate species (Fe^{4+}=O), possibly leading to irreversible inhibition of the enzyme, as proposed for the horseradish CCP [242].

The *ki* determined for azide (41 ± 5 mM at pH 7.5) is much higher than the one reported for *P. aeruginosa* BCCP (*ki* = 3.1 mM at pH 6.0 [125]). In fact, azide has a higher affinity for the *Ng*BCCP at lower pH (at pH 6.0 k_{app} = 3.8 mM) and this is due to the proportion of HN_3/N_3^- and possibly also to the protonation state at the P heme cavity, as described for yeast CCP [243]. However, at pH 6.0 the enzyme quickly loses activity and therefore it is not possible to determine a *ki* as two effects are occurring: inhibition by azide and inhibition due to pH (protonation of key residues)(data not shown). Studies of *N. europaea* BCCP using protein film voltammetry, also showed mixed-inhibition by azide at pH 7.0, with a *ki* = 4.7 mM and the *ki'* = 80 mM. This indicates that the P heme, catalytic site of that enzyme is either more accessible or has higher affinity for azide [135]. The *ki* for azide in *Ng*BCCP is in the same order of magnitude as the binding constant k_{app} previously determined for the enzyme without substrate (Figure 3.13D), indicating that inhibition is due to binding of azide to the active site, competing with hydrogen peroxide.

In the imidazole assays, contrary to what was observed for the enzyme in the absence of substrate, there is a single effect with no differences between concentrations below and above 100 mM imidazole. This indicates that interference of imidazole with the E heme does not affect the peroxidatic activity at these concentrations, probably because $ABTS^{2-}$ is able to reduce the P heme directly or the methionine displacement is not significant at the concentrations used in the kinetic

assays (about half of the *ki'*) and does not affect intramolecular electron transfer. Higher concentrations showed little activity and could not be addressed by steady-state kinetics.

Overall, for both azide and imidazole, *ki'* is much higher than *ki* (8 to 35 times, respectively) which indicates that these inhibitors bind preferably to the active site (competitive inhibition).
The low *ki* of cyanide is comparable to the one found for *N. europaea* BCCP (*ki* of 0.15 µM, pH 7.0) that shows that mixed-valence *Ng*BCCP active site is available and equally accessible to binding of exogenous ligands that are able to inhibit its catalytic activity. As previously suggested from the binding of cyanide to the free enzyme, the *Ng*BCCP active site is more accessible to cyanide than the one from *P. aeruginosa* BCCP, which has a lower binding affinity and also a higher *ki* value (7.1 µM, pH 6.0). However, there are no other examples in the literature on the effects of cyanide on the BCCPs catalytic activity for a more extensive comparison.
Azide and imidazole also bind the active site but their affinity is lower (in the millimolar range). The apparent dissociation constant for azide anion at pH 6.0 is similar to the *ki* reported for *P. aeruginosa* at pH 6.0 and *N. europaea* at pH 7.0 as mentioned, however it is not possible to determine the effect in the catalytic activity at this pH. In this case, *Ng*BCCP does not seem to have a more accessible heme pocket and this might be due to the affinity of the azide anion to specific residues at the entrance of the active site or in the heme pocket (although these ones are highly conserved), or possibly due to the larger size of the molecule and its protonation state. Computational studies would be essential to understand this effect and also to improve the affinity by creating derivative compounds of these inhibitors.

3.2.8 X-ray structures of the active and azide-inhibited *Ng*BCCP

In order to understand the spectroscopic data and the differences in the catalytic site and dimer interface it was essential to determine the tridimensional structure of *Ng*BCCP. Furthermore, a structure will also enable the design of different inhibitors in the future, through computational binding inhibition studies. The structures of the active and azide-inhibited *Ng*BCCP were determined by X-ray crystallography.

3.2.8.1 *Crystallization conditions*

i) As-isolated *Ng*BCCP

Several of the crystallization conditions tested for the as-isolated *Ng*BCCP produced crystals but these were not reproducible or showed multiplicity. Pre-incubating the enzyme with calcium chloride improved the reproducibility, as expected, since it reduces the solution states making it a more homogeneous sample and increases the stability of the enzyme.

The addition of additives to the condition containing 0.1 M MES pH 5.5, Jeffamine SD2001 (25-27 %) and 0.1 M sodium malonate, which produced multiple crystal plates (Figure 3.16A), led to single crystals. The additive 1,6-hexanediol promoted the formation of single plates and hexammine cobalt(III) trichloride led to tetragonal crystals (Figure 3.16B).

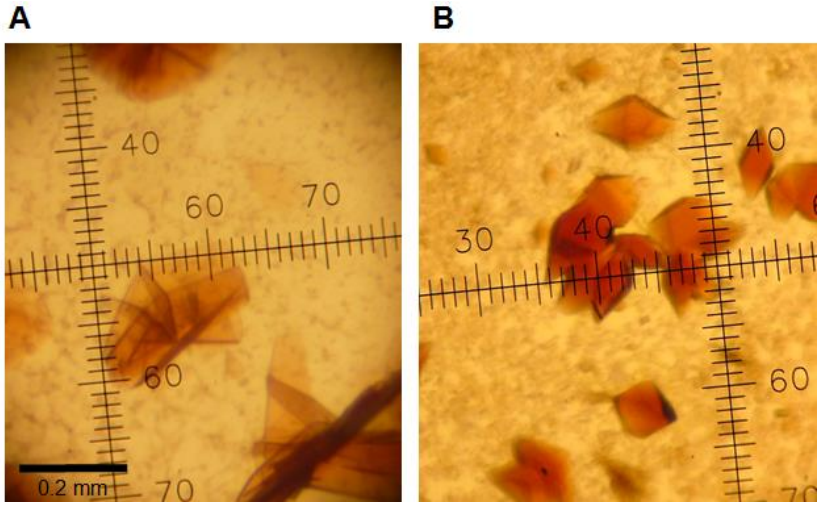

Figure 3.16 – Crystals of *Ng*BCCP obtained by the vapour diffusion (hanging-drop) method at 4 ºC in 0.1 M MES pH 5.5, Jeffamine SD2001 (25-27 %) and 0.1 M sodium malonate, 2 mM $CaCl_2$ without additives (A) and with addition of 0.01 M hexammine cobalt(III) trichloride (B).

Although, these were promising conditions, which were extensively explored in an attempt to optimize and acquire better crystals, all crystals obtained using Jeffamine SD2001 as precipitant were fragile and diffracted poorly. The only other conditions that produced crystals of as-isolated *Ng*BCCP were the ones using 5/4 PO/OH as precipitant, which resulted in small and thin needle crystals that were dependent on protein batch and thus not reproducible.

ii) Mixed-valence *Ng*BCCP

The conditions in which crystals of the as-isolated *Ng*BCCP were obtained, were then used in crystallization trials for the mixed-valence state. In order to have a constant anoxic environment, the drops were prepared inside an anaerobic chamber, in the presence of a reducing agent (sodium ascorbate) and a redox mediator (FMN) with a negative potential (-205 mV at pH 7.0), at the working pH range (pH 5.5 to 6.5). These conditions were essential to avoid *Ng*BCCP oxidation during the incubation period, which would lead to a mixture of oxidation states and consequently different conformations that would be detrimental for the crystallization.

The best crystals were obtained in 0.1 M MES pH 6.0, 30 % 5/4 PO/OH, 2 mM $CaCl_2$, 10 mM sodium ascorbate and 0.2 mM FMN (Figure 3.17).

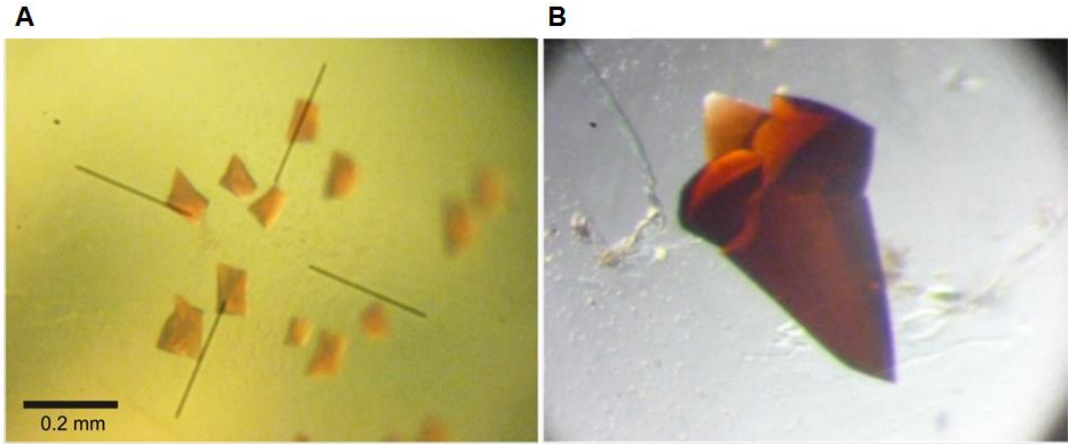

Figure 3.17 – (A) Crystals of *Ng*BCCP obtained by the vapor diffusion (sitting-drop) method at 30 ºC in 0.1 M MES pH 6.0, 30 % 5/4 PO/OH, 2 mM $CaCl_2$, 10 mM sodium ascorbate and 0.2 mM FMN, in a Coy Lab anaerobic chamber (2 % hydrogen, 98 % argon atmosphere). (B) Crystals grow to a maximum size of 0.6 mm after 7 days.

The size of the crystals varied from plate to plate, probably due to small variations in temperature during the preparation of the drops inside the anoxic chamber, prior to their incubation at 30ºC. The smaller crystals appeared in 26 %-30 % 5/4 PO/OH, while the larger crystals only appeared in 30 % 5/4 PO/OH. Some of these crystals were used for data collection, while others were soaked with sodium salts of cyanide, azide and fluoride. Diffraction data was only collected for the crystals soaked with sodium azide since the others did not maintain their shape (cracked or dissolved).

3.2.8.2 Structure analysis of the active NgBCCP

Two structures of *Ng*BCCP in the mixed-valence were solved, one to a final resolution of 1.9 Å acquired in-house (as described in Chapter 2, Section 2.8) and another of 1.4 Å using diffraction data acquired at the synchrotron at SLS (Swiss Light Source). The structures were solved by molecular replacement, using the mixed-valence structure of *P. aeruginosa* BCCP (PDB ID:2VHD) as model (48 % primary sequence identity). A third-structure of the azide-inhibited *Ng*BCCP was solved to a 2.3 Å resolution (data collected at the synchrotron at ESRF, European Synchrotron Radiation Facility). The crystals belong to the $P2_12_12_1$ space group and the *Ng*BCCP dimer constitutes the asymmetric unit. Each monomer has one calcium atom and is composed of two domains of cytochrome fold, each one harbouring a *c*-type heme (E and P heme). The dimer structure is shown in Figure 3.18A as well as its electrostatic surface potential (Figure 3.18A). The C-terminal His-tag is not observed in none of the monomers since it is too dynamic and probably not in the same position within the crystal. The electrostatic surface of *Ng*BCCP is overall negatively charged except at the E heme domain which is more neutral or positively charged.

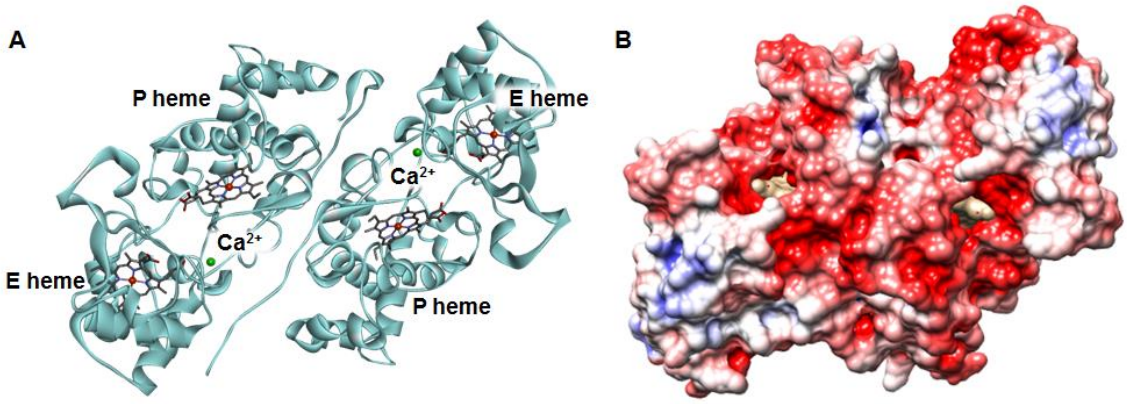

Figure 3.18 – (A) Structure of mixed-valence *Ng*BCCP, homodimer which comprises the asymmetric unit of the crystal and (B) its electrostatic surface potential represented from -5 to 5 KT/e (colored from negative red surface to positive blue surface).

The common features among BCCPs, addressed in the primary sequence analysis are presented in Figure 3.19 (*Ng*BCCP structure numbering) which are: the E and P hemes and their axial ligands, the calcium binding site and the tryptophan between the two heme domains.

The hemes are perpendicular to each other with a Fe-Fe distance of 20.9 Å. E heme is coordinated by the conserved Met280 and His204, and the P heme is coordinated by His59 and a water molecule, as described in other structures of mixed-valence BCCPs [166, 171] (Figure 3.19A). The distance between the oxygen of the water molecule and the Fe of P heme is 2.2 Å. This is in accordance with spectroscopic data for a penta-coordinated P heme, which at cryogenic temperatures has a low-spin EPR signal hexa-coordinated with a water as sixth distal ligand.

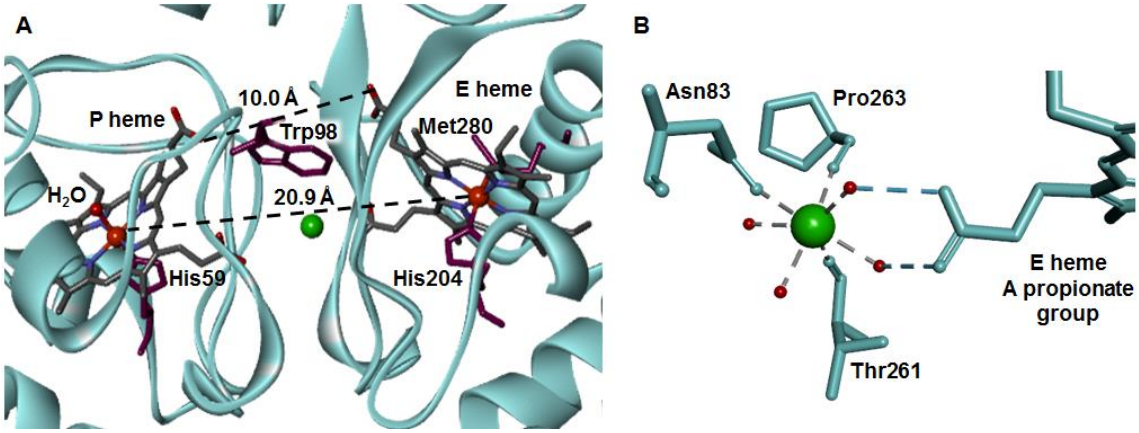

Figure 3.19 – Structure of mixed-valence *Ng*BCCP with the calcium binding site located between the two hemes, a His/Met coordinated E heme and the P heme with a proximal histidine ligand and the distal water molecule (small red sphere). Although the two hemes have a Fe-Fe distance of 20.9 Å, electron transfer is possible due to the tryptophan residue located between their propionate groups. (B) Structure of the calcium binding site, with calcium ion (green sphere) coordinated by the oxygen of four water molecules (small red spheres) and three conserved amino acid residues (Asn83, Thr261 and Pro263). It is in close proximity to the carboxylate group of propionate A from the E heme, which forms hydrogen bonds with two of the waters that coordinate the calcium ion.

The distance between the iron atoms is large (20.9 Å), which according to Marcus theory does not favor electron transfer, as longer distances lead to a decay of the electron transfer rate [244]. However, the distance between the propionate groups of the two hemes is 10.0 Å with the highly conserved tryptophan residue (Trp98) exactly between the two heme groups. This Trp98 is proposed to act as a bridge, enabling electron transfer between the two hemes through electron tunnelling [108, 167, 245].
The calcium is bound to four water molecules and three conserved residues: the amide oxygen of Asn83 and the carbonyls of Thr261 and Pro263 (Figure 3.19B), in a pentagonal bipyramidal arrangement as first described in *P. aeruginosa* BCCP crystallographic structure [108]. The calcium site is in close proximity to the A propionate group from E heme, which coordinates two of the four water molecules.

*Ng*BCCP structure was superimposed with all the available BCCP structures, both in the mixed-valence and oxidized form. Overall the structures are similar, specially the mixed-valence structures, but *P. aeruginosa* BCCP (*Psa*BCCP) in the mixed-valence state (PDB ID: 2VHD) shows the lowest root mean square deviation (RMSD) between 323 Cα, of 0.693 Å (Table 3.4).
Therefore this structure was used to address structural differences between the *Ng*BCCP and *Psa*BCCP (Figure 3.20). In the absence of an oxidized *Ng*BCCP structure, the structure of the oxidized *Psa*BCCP (PDB ID: 1EB7) was used to assess redox related changes.

Table 3.4- Comparison of BCCP structures in the oxidized (Ox) and mixed-valence (MV) forms. RMSD was determined for the aligned Cα atoms of the superimposed structures in SuperPose [191].

Organism, redox state	PDB ID	Resolution (Å)	Cα atoms	RMSD (Å)	Reference
Neisseria gonorrhoeae, MV	-	1.4	-	-	
Pseudomonas aeruginosa, MV	2VHD	2.3	323	0.69	[166]
Pseudomonas aeruginosa, Ox	1EB7	2.4	324	1.27	[108]
Nitrosomonas europaea, Ox	1IQC	1.8	308	0.89	[167]
Paracoccus pantotrophus, MV	2C1V	1.2	335	1.06	[171]
Paracoccus pantotrophus, Ox	2C1U	1.9	322	1.39	[171]
Rhodobacter capsulatus, Ox	1ZZH	2.7	297	1.20	[169]
Geobacter sulfurreducens MacA, MV	4AAM	2.2	313	2.58	[115]
Geobacter sulfurreducens CcpA, Ox	3HQ6	2.0	320	1.88	[132]
Shewanella oneidensis, MV	3O5C	1.8	307	3.63	[147]
Marinobacter hydrocarbonoclasticus, OUT	1RZ5	2.4	309	5.76	[172]
Marinobacter hydrocarbonoclasticus, IN	1RZ6	2.2	303	4.58	[172]

As expected from the small RMSD value, the two mixed-valence structures are identical. The main observable structural differences are the formation of two small helixes (residues 23-26 and 310-313) in *Ng*BCCP structure which are not defined in *Psa*BCCP, and the formation of a shorter helix (123-134) as highlighted in red in Figure 3.20A. These changes occur in non-conserved regions and can therefore be explained by differences in primary sequence, which includes not only the amino acid identity but also single amino acid insertions (Asp122, Ser311 and Ala312) in those *Ng*BCCP regions, identified in the structural alignment. Furthermore, the additional 310-313 helix is located at the dimer interface which explains the dimer interface differences that will be further discussed.

Between the two oxidation states there are major conformational changes that also occur between the two oxidation states of *Psa*BCCP [166], and affect main regions previously described also in *P. pantotrophus* [171], and *N. europaea* [167] BCCPs. These regions are the conserved loops in the *Ng*BCCP C-terminal domain, a 218-246 loop and the residues 282-290 that extend the alpha helix. These residues change dramatically upon reduction of the E heme, which originates further changes in the N-terminal domain (71-118), namely a β-strand between the two heme domains, the alpha helix at the catalytic site (P heme) and the loop region (71-81) that contains the His75. This histidine residue is the P heme distal ligand in the oxidized form and upon reduction it shifts to the dimer interface leaving the catalytic site with an empty coordination for substrate binding. Furthermore, the formation of this loop (71-81) was stabilized by a π-stacking interaction between Gly72 and Trp73 (*Psa*BCCP numbering) of opposite monomers. However, as stated before, this tryptophan residue is not present in *Ng*BCCP and instead there is a Gly77.

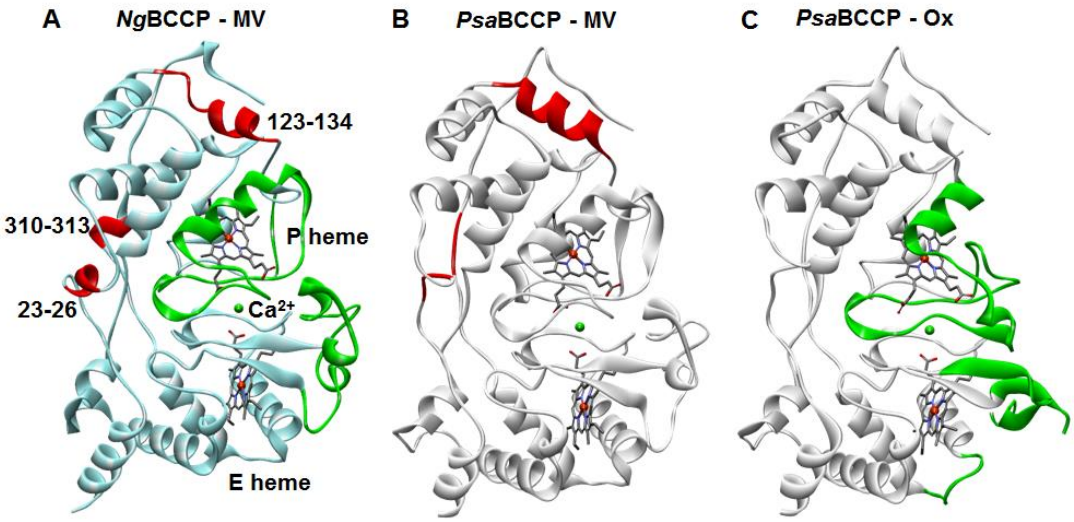

Figure 3.20 – Structure comparison of *Ng*BCCP mixed-valence (MV) form with *Psa*BCCP MV and oxidized (Ox) form. In red is highlighted the structural differences between MV forms, in green the differences between oxidation states.

3.2.8.3 The dimer interface

In *Ng*BCCP increasing ionic strength does not promote dimerization, which led to the previous hypothesis that the dimer interface was less hydrophobic than in other classical BCCPs. Only calcium ions promoted dimerization but at high protein concentrations.

Comparison of the dimer interface surface of *Ng*BCCP, *Psa*BCCP and the *S. oneidensis* BCCP, colored according to hydrophobic and non-hydrophobic residues shown in Figure 3.21, demonstrates that *Ng*BCCP dimer interface is in fact, less hydrophobic.

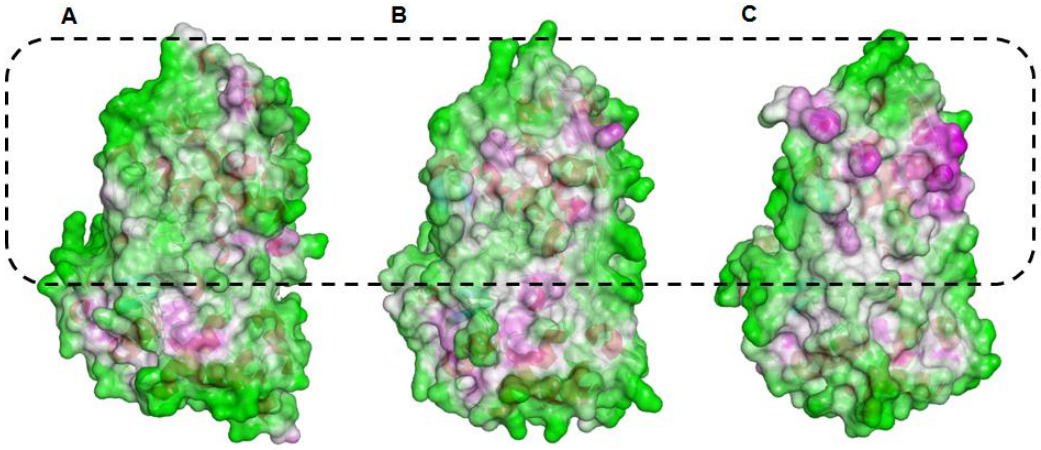

Figure 3.21 – Surface of the mixed-valence tridimensional structures of one monomer of (A) *Ng*BCCP, (B) *P. aeruginosa* BCCP and (C) *S. oneidensis* BCCP colored from non-hydrophobic residues (green) through white, to hydrophobic (magenta). The surface in the dashed black box is the dimer interface region. Figures prepared with PDB ID:2VHD and 3O5C of *P. aeruginosa* and *S. oneidensis* BCCPs, respectively.

In order to understand the differences at the dimer interface that could account for this effect, both *Ng*BCCP and *Psa*BCCP were analysed using the Protein Data Bank Europe Protein Interfaces, Surfaces and Assemblies (PDBePISA) that gives information about which residues compose the interface, the type of interactions formed and its symmetry.

In *Ng*BCCP the number of residues involved in the dimer interface is different between polypeptide chains. In chain A, 52 residues are involved in the interface while in chain B, only 45 residues. These residues constitute an interface surface area of 1714 and 1764 $Å^2$ in chain A and B, respectively, which is similar to the reported 1723 $Å^2$ in *P. pantotrophus* [171]. In the case of *Psa*BCCP the dimer structure is symmetrical, therefore the same number of residues are involved in the dimer interface from both chains (46 residues in each chain). The *Psa*BCCP interface analysed here has a surface area of approximately 1585 $Å^2$.

There is no salt bridge interaction in *Ng*BCCP dimer interface, while in *Psa*BCCP there are 8 interactions. The number of hydrophobic interactions is similar but there are only two residues at the N-terminal domain in *Ng*BCCP, Ala62 and Ala64 in comparison to six in *Psa*BCCP demonstrating that this region is less hydrophobic as predicted.

The other striking difference is in the hydrogen bonds. *Ng*BCCP interface forms 19 hydrogen bond interactions between the two monomers but only two of them are not at the C-terminal end of the protein, Ala62-Leu318 and the A:Met69-B:Asn51 (Figure 3.22). The symmetric corresponding bond A:Asn51-B:Met69 does not occur in the asymmetric unit, due to the loop in the C-terminal end of Chain A which locates B:Met69 closer to A:Pro328 sidechain than to A:Asn51. However, this can be due to crystal packing and location of this loop in the asymmetric unit.

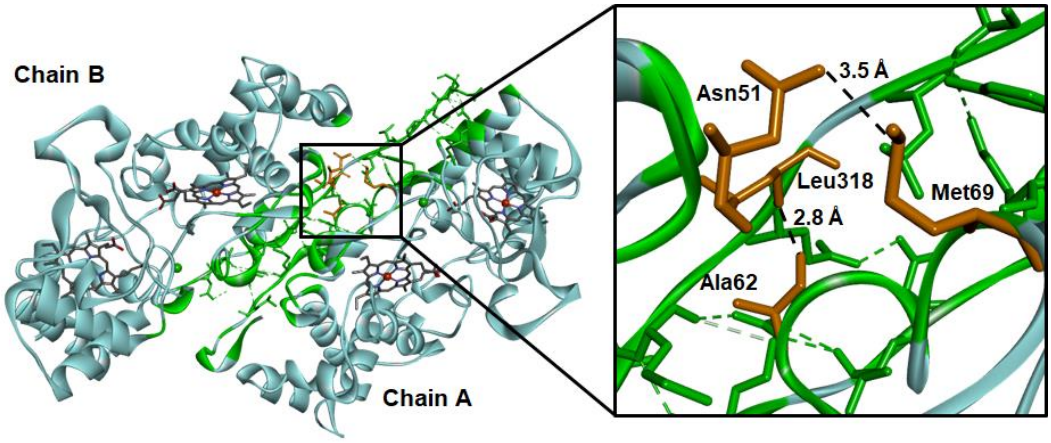

Figure 3.22 – Dimer interface of *Ng*BCCP. The residues involved in the interface according to PDBePISA are highlighted in green. Most interactions occur at the C-terminus of each monomer with the exception of hydrogen bonds Asn51- Met69 and Ala62-Leu318 (zoom view of these residues in orange). Although the C-terminus is along one side of the P domain surface, only these two close interactions involve residues of this domain, the one with larger interface surface.

The 71-81 loops containing the His75 are in close proximity, even though there is no tryptophan residue, with a distance of 4.2 Å between Cα of Gly77 of each monomer. There is no interaction stabilizing this arrangement, unless perhaps the hydrogen bond Asn51-Met69. This contrasts with *Psa*BCCP interface analysis that identified many interactions at the C-terminal end and also several N-terminal residues, such as Asn52, Asn56, Gly58, Lys72 and Trp73 (from the Gly-Trp motif that stabilize this His-loop), covering all the interface surface area.

The additional small helix at the C-terminus (310-313) in the dimer interface is unusual, since in all other BCCPs, this region does not retain any significant secondary structure. As a result, only one of the four residues, Arg313 is able to form hydrogen bond interactions with the opposite monomer.

Furthermore, the Met69 carboxyl group forms a hydrogen bond with Asn83 that coordinates the calcium ion, which suggests that in the absence of calcium ions, small changes in the protein structure will hamper the formation of the dimer or decrease dimer stability.

Moreover, in the oxidized state, this weak dimer interaction and the absence of the loop from the dimer interface, might explain why this form in *Ng*BCCP crystallizes poorly and shows multiplicity even at high protein concentrations with calcium ions. In *P. pantotrophus* BCCP, this loop is

described as being responsible for reducing the area and the hydrophobic character of the dimer interface in the oxidized enzyme [171]

The analysis of the dimer interface suggests that the soluble *Ng*BCCP *in vitro* is not able to form a stable dimer as there is a weaker interaction and a more dynamic monomer/dimer equilibrium. Nevertheless, this enzyme *in vivo* is not free in the periplasm and the N-terminal anchor of each monomer restricts its movements and increases its concentration at the outer membrane. This high local concentration of *Ng*BCCP at the membrane would allow this enzyme to make more successful interactions with closer protein monomers, forming a dimer.

3.2.8.4 The active site

In order to assess the unique spectroscopic features of the P heme, all the active sites from the available BCCP structures were compared and the overall topology remained the same, with at least one oxygen atom (assigned as a water molecule) in the P heme cavity, coordinating the P heme. In *Ng*BCCP structure there are two oxygen atoms assigned to water molecules, 2.6-2.8 Å apart (for chain A and B, respectively, Figure 3.23).

One water molecule (w1) is coordinating the heme and is also within hydrogen bonding distance from Gln108. The other water molecule (w2) is close to the iron (4.1 Å) and to the Glu118 forming a hydrogen bond interaction (2.8 Å/2.7 Å). This arrangement is not unique and it is observed in *P. pantotrophus* (2C1V), *N. europaea* (1IQC) and *S. oneidensis* (3O5C) structures of the active form.

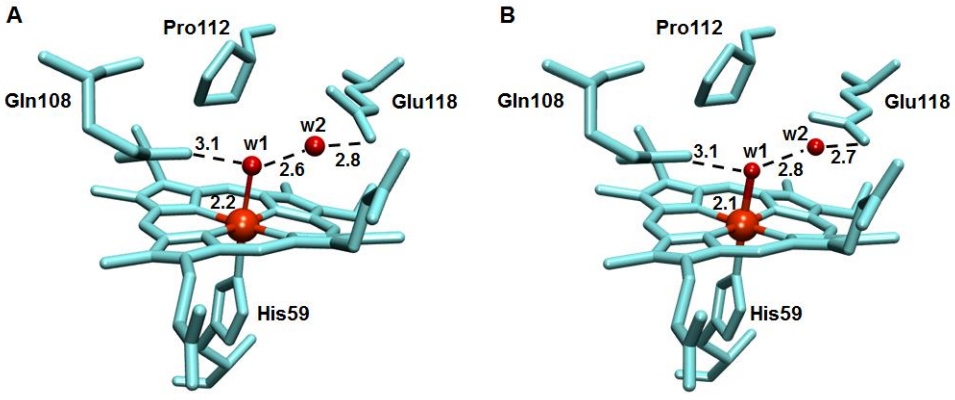

Figure 3.23 – Structure of the P heme active site in (A) chain A and (B) in chain B. There are two water molecules, w1 and w2 (small red spheres representing their oxygen atoms), in the active site coordinated by the conserved Gln108 and Glu118 side-chains.

The cavity residues are conserved in the BCCP family, such as Phe97, Gln108, Pro112, Glu118 and Met119. The conserved glutamate and glutamine residues are proposed to play important roles in the formation and stabilization of the oxoferryl intermediate species, and in particular the glutamate residue, for the cleavage of the hydrogen peroxide O-O bond, as described in the MauG proteins,

which share a similar heme cavity [246-248]. Mutation of any of the two residues results in an inactive enzyme [169].

There is little knowledge regarding the catalytic mechanism of BCCPs and most studies have focused on the catalytic mechanism of eukaryotic CCPs. In *Ng*BCCP the active site topology is different from eukaryotic peroxidases and instead of a histidine there is a glutamate residue, Glu118, which is farther away from w1 (≈ 4 Å) than the histidine (≈ 3.5 Å). Nevertheless, a mechanism similar to the one proposed for eukaryotic CCPs could be perceived. We propose the following mechanism in Figure 3.24, based on our knowledge on BCCPs catalytic intermediates, on the structural data and p*Ka* values determined by kinetic assays, as will be discussed.

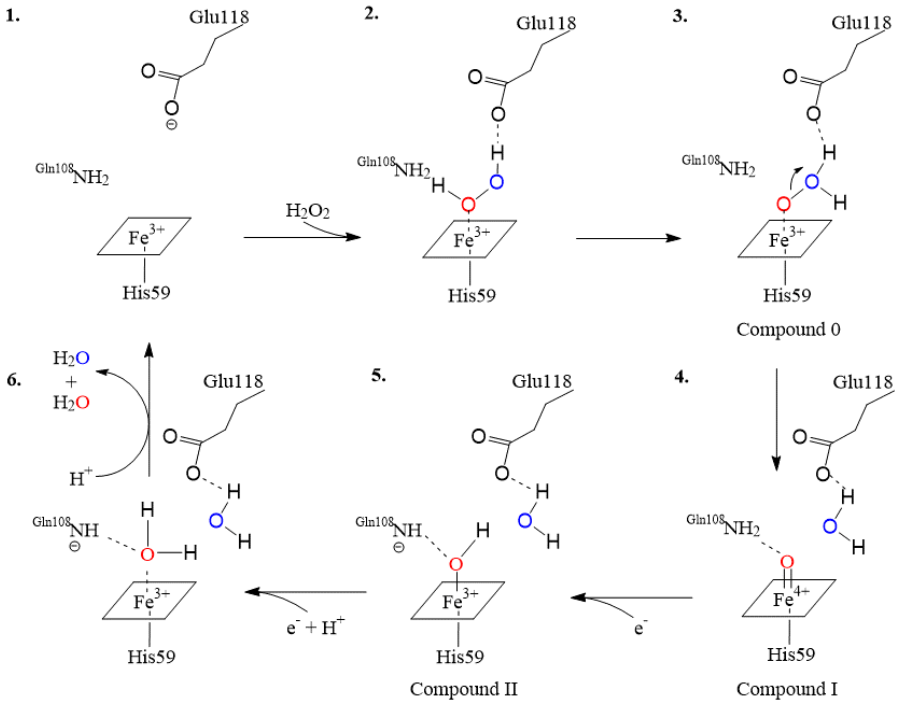

Figure 3.24 – Proposed catalytic mechanism of bacterial peroxidases. (1.) P heme is penta-coordinated and in the presence of hydrogen peroxide (2.), there is formation of a peroxide-bound complex. Glu118 forms a hydrogen bond with one of the oxygens (blue O). (3.) This form, named Compound 0, is followed by the cleavage of O-O bond, releasing one water and forming Compound I (4.). This species is stabilized and can receive protons from Gln108 forming Compound II (5.). Transfer of an additional proton releases a second water molecule (6.).

In this mechanism, Glu118 forms a hydrogen bond with the nearest oxygen atom from the peroxide (in the absence of H_2O_2 for ease of comprehension we refer to w2 in Figure 3.23), helping elongating the O-O bond that leads to bond cleavage. The two protons needed to release the first water molecule are the ones from hydrogen peroxide, with formation of Compound I. The Compound I is a oxoferryl species and the Gln108 (positioned at 3.1 Å from w1) is the most probable proton donor in the reduction of this compound to Compound II due to the short distance between this residue and the

oxygen atom coordinating the P heme Fe atom. Addition of another proton releases a second water molecule.

In fact, the glutamine p*Ka* value ≈ 9 is consistent with the pKa_2 value of 8.4 ± 0.1 determined in the kinetic assays, which would explain the lack of activity at higher pH values where this residue becomes deprotonated.

Glutamate has a p*Ka* value for the side-chain of ≈ 4, however this value can be slightly different inside the heme pocket as it is dependent on the surrounding hydrophobic environment. Calculation of p*Ka* values in other enzyme active sites have shown that the p*Ka* value of a buried glutamate p*Ka* can be 5.5 (in hen egg white lysozyme) or even higher in proteins where it is a proton donor (*e.g. Bacillus licheniformis* α-amylase Glu261 with a calculated p*Ka* >10 [249]) instead of an acid-base catalyst as proposed in this BCCP catalytic mechanism. The lower p*Ka* value estimated for *Ng*BCCP by kinetics was approximately 5.9, suggesting that this value could be assigned to a glutamate that needs to be unprotonated for optimum activity.

As proposed in the schematic mechanism in Figure 3.24, the structural configuration of the mixed-valence *Ng*BCCP active site is similar to the final step of the catalytic cycle, thus and intermediate state of this cycle.

Other intermediates proposed in the catalytic cycle of *P. aeruginosa* [182]and *N. europaea* [134, 135] BCCPs are the protein radicals, namely the tryptophan radical (tryptophan between the two hemes) and the porphyrin radical, respectively. It is not clear their role in the catalytic cycle. It is possible that these protein radicals are essential for fast long range electron transfer between E heme and the P heme.

The horseradish peroxidase (HRP) and ascorbate peroxidase (APX) have similar active sites but with a histidine as acid-base catalyst [250]. Quantum mechanical/molecular mechanical (QM/MM) simulations on HRP suggested a mechanism similar to the one proposed in Figure 3.24, in which the histidine is not protonated and the protons to form the first water molecule are from the hydrogen peroxide. A variation of this mechanism suggests that the O-O cleavage occurs with the assistance of a nearby "catalytic" water molecule [251]. Other features observed in eukaryotic CCPs, such as the movement of heme pocket residues during catalysis, as observed for Arg48 in yeast CCP, which moves towards the oxoferryl species in Compound I structure [183], cannot be assessed without a structure of a BCCP previously incubated with hydrogen peroxide. However, in order to trap this intermediary species and not observe catalysis, this has to be performed with BCCP mutants or with a BCCP as the one from *N. europaea*, which has a penta-coordinated P heme in the full oxidized state.

3.2.8.5 The azide-inhibited NgBCCP

There are no significant structural changes between the active and the azide-inhibited *Ng*BCCP structures, as shown in the superimposed structures of the monomer in Figure 3.25A, and in particular

in the active site (Figure 3.25B). In the inhibited *Ng*BCCP structure, it is clear that the active site is blocked by an azide molecule and water molecules cannot reach the catalytic site (Figure 3.25C). This is the first structure of a BCCP with a ligand in its active site, in this case azide.

There are no significant structural changes in the catalytic site or in protein structure, with a RMSD between all Cα atoms of 0.35 Å, similar to what is observed between the active and azide-inhibited form of cytochrome cd_1 nitrite reductase [252]. The azide molecule interacts directly with the P heme iron, effectively blocking the active site as expected for a competitive inhibitor. It occupies approximately the same positions as the two water molecules in the non-inhibited structure. N_{II} and N_{III} are coordinated by the Glu118 while N_I is coordinated by the ferric heme at 2.5 Å.

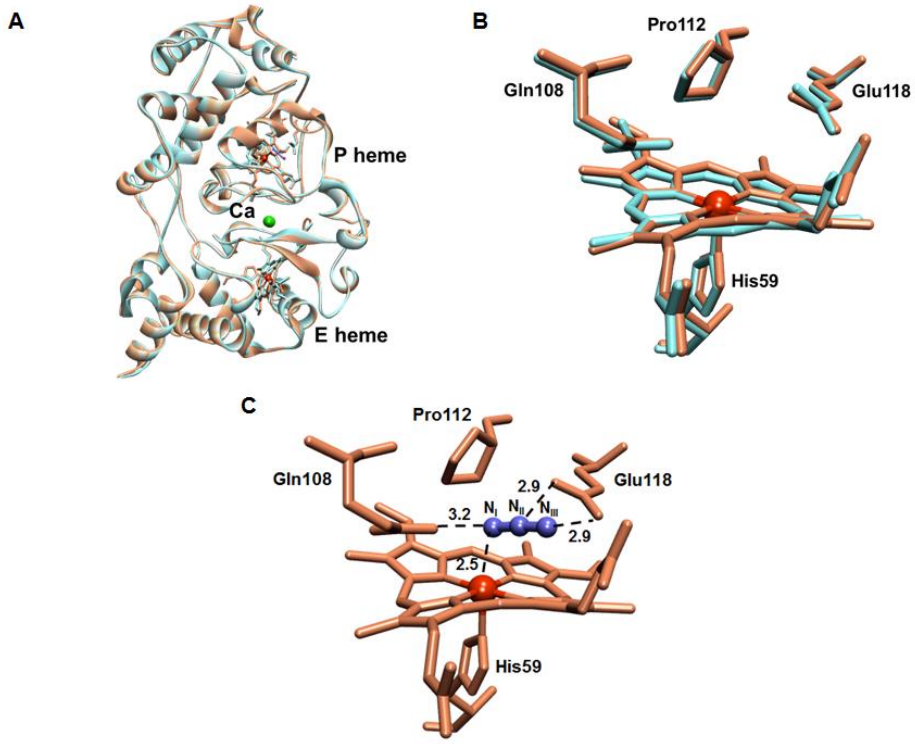

Figure 3.25 – Structure comparison of the *Ng*BCCP active (blue) and azide inhibited (pink) forms. Overall protein structure is conserved (A) as well as the residues in the active site (B). (C) In the the inhibited form there is an azide molecule, coordinated by the conserved Gln108 and Glu118.

In fact, these crystals were acquired at pH 6.0 and, as described previously, azide association constant increases at lower pH (k_{app} of 3.8 mM azide) and as proposed for the yeast azide-inhibited CCP, this can be due to the influence of two ionisable groups [243]. One is azide itself, as HN_3, with a p*Ka* = 4.5 and the other could be the deprotonated form of Glu118, which is coordinating the azide and has a low p*K*a value. Therefore, at lower pH values, hydrogen bonds would stabilize the azide at the catalytic site.

It is necessary to understand how binding of exogenous ligands occurs and which is the protonation state of each key residue in the active site at a given pH value (for instance the pH of human cervix, the primary site of *N. gonorrhoeae* infection in women, which is, on average, 6.8 in the proliferative state and 6.1 in the secretory stage [253]) in order to comprehend how these inhibitors bind and how to make them more effective, with higher affinity. With this knowledge new inhibitors could be envisioned using computational methods and these *Ng*BCCP structures.

3.3 Conclusions

*Ng*BCCP is a highly conserved enzyme in *N. gonorrhoeae* strains, anchored to the outer membrane. In order to further characterize *Ng*BCCP, a recombinant soluble protein was heterologously produced and purified, as a di-heme *c*-type cytochrome. This enzyme, unlike other BCCPs, is a monomer in solution even at high ionic strength. It only dimerizes when its concentration is increased, in the presence of added calcium ions. In fact, this is explained by the *Ng*BCCP dimer interface which has a lower hydrophobic character and a reduced number of interactions in its N-terminal domain. Its location *in vivo*, anchored to the outer-membrane, and the interface properties suggests that the dimer does not need to be as strong as for an enzyme that is freely diffusing in the periplasm. Nevertheless, it shares with the classical bacterial peroxidases a common feature of dimer stabilization by calcium ions.

This calcium site is partially occupied after purification (and its occupancy differs between preparations), as demonstrated by the redox properties of the as-isolated *Ng*BCCP. Calcium site occupancy together with reduction of E heme play a key role in the activation of the enzyme, which becomes more thermostable (with an increase of 9 ºC in the *Tm*). This activation mechanism involves conformational changes that lead to the modification of P heme coordination state, from hexa-coordinated low-spin to penta-coordinated high-spin, as observed in the mixed-valence crystallographic structure, in the spectroscopic data and also reflected in the reduction potentials of both hemes.

One unique spectroscopic feature of *Ng*BCCP P heme, is that it remains partially as a high-spin species at cryogenic temperatures. This reflects changes in the surroundings of the P heme cavity, however, comparison of the available BCCP structures showed no significant differences. A dynamic monomer-dimer equilibrium could cause significant changes at the proximal side of P heme, namely the conserved loop region, carrying the P heme proximal histidine ligand. This loop is not stabilized at the dimer interface by the conserved tryptophan π-stacking motif between monomers, found in other classical BCCPs but absent in *Ng*BCCP.

All the data regarding the calcium effect on dimerization, spectroscopic properties, catalytic activity and stability of *Ng*BCCP, clearly indicate that the activation mechanism involves both the conformational change that leads to the modification of P heme coordination and enzyme dimerization. In the *in vitro* studies, these two events are separated, which might not occur *in vivo* as calcium levels in the periplasm are within micromolar range (in human mucosa calcium levels reach millimolar concentrations) [254, 255] and *Ng*BCCP has a high calcium affinity (K_D of 8.5±0.5 nM). *Ng*BCCP tethering to the outer membrane can foresee a higher local enzyme concentration and thus dimerization, as mentioned.

*Ng*BCCP has a high affinity for its substrate (low K_M), and the optimum conditions are close to the physiological of *N. gonorrhoeae* (pH from 6.0 to 7.5 and a temperature of 37 ºC, as being a human

pathogen) indicating that this enzyme is well adapted to the host environment and therefore can play a determinant role in detoxification of hydrogen peroxide, generated by the host immune system and neighboring lactobacilli, during infection and proliferation. Moreover, we propose that the limiting step in the catalytic cycle is the electron transfer from the E to the P heme and not the formation of the enzyme-substrate complex.

The P heme cavity is accessible to its substrate but also to other exogenous ligands, specifically cyanide which has high affinity (k_{app} = 4 µM) for the active site. The binding of cyanide (*ki* = 0.4 µM), imidazole (*ki* = 41 mM) and azide (*ki* = 9 mM) inhibits the catalytic activity mainly by competitive inhibition, although E heme is also affected at high imidazole concentrations. For the first time it was presented an azide-inhibited BCCP structure that shows that the active site is blocked by the ligand and therefore substrate cannot bind.

Furthermore, the proposed catalytic mechanism based on the proposed catalytic intermediates and on the kinetic data suggests that the two waters in the P heme pocket of *Ng*BCCP structure can be of the intermediate step of the catalytic cycle.

*Ng*BCCP is conserved in *N. gonorrhoeae,* a human pathogenic bacteria, absent in human cells and accessible in the outer membrane, making this enzyme a good candidate for immunization. Further studies with additional exogenous ligands and derivatives of the compounds used in this study should be pursued in order to develop new compounds with higher affinity and specificity.

Chapter 4

LAz, a lipid-modified azurin *Ng*BCCP electron donor

The work presented in this chapter is or will be published in:

"The solution structure of the soluble form of the lipid-modified azurin from *Neisseria gonorrhoeae*, the electron donor of cytochrome *c* peroxidase", by Cláudia S. Nóbrega, Ivo H. Saraiva, Cintia Carreira, Bart Devreese, Manolis Matzapetakis and Sofia R. Pauleta, Biochim. Biophys. Acta. 2016 Feb; 1857(2):169-76. DOI: 10.1016/j.bbabio.2015.11.006.

"Interaction of *Neisseria gonorrhoeae* cytochrome *c* peroxidase with its electron-donor, the lipid-modified azurin", by Cláudia S. Nóbrega and Sofia R. Pauleta. 2017. Manuscript in preparation.

Contributions to Chapter 4:

Bart Devreese performed all the mass spectrometry experiments and the N-terminal sequencing. Sofia R. Pauleta acquired the HSQC NMR spectra of LAz. All the other experiments were performed by Cláudia S. Nóbrega.

4 LAz, a lipid-modified azurin – *Ng*BCCP electron donor

4.1 Introduction

Pathogenic bacteria such as *N. gonorrhoeae* that causes the sexually transmitted disease gonorrhea, are constantly exposed to ROS from various sources and, therefore, have developed numerous defense mechanisms to cope with oxidative stress [220]. These mechanisms are essential to cell survival, given that ROS can damage DNA, proteins and cell membranes. One of such mechanisms includes the bacterial cytochrome *c* peroxidase (*Ng*BCCP) discussed in Chapter 3. These enzymes catalyze the reduction of hydrogen peroxide to water using small electron shuttle proteins of the respiratory chain as electron donors, such as small *c*-type cytochromes [129, 159, 163, 164] or type 1 copper proteins [136, 139, 158, 184, 256, 257] (Figure 4.1).

An example of these electron donors is azurin, a member of a family of copper-containing, water soluble, low molecular weight proteins named cupredoxins, which function as electron shuttles in the electron transfer chain of several microorganisms, such as *P. aeruginosa* (Figure 4.1A) under different growth conditions.

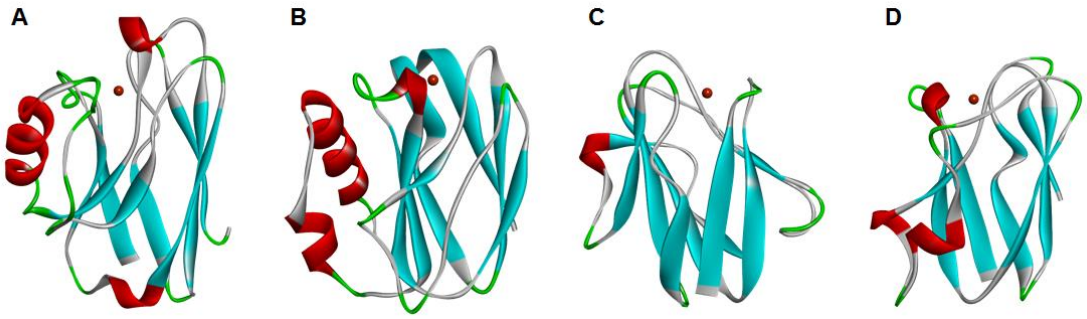

Figure 4.1 – Molecular structures of small type 1 copper proteins such as (A) *P. aeruginosa* azurin, (B) *P. pantotrophus* pseudoazurin, (C) *Paracoccus denitrificans* amicyanin and (D) spinach plastocyanin. Structures are colored according to secondary structure and the copper atom is represented by an orange sphere. Figures were prepared with PDB IDS: 4AZU, 3ERX, 2RAC and 1AG6, respectively.

These proteins have received attention due to their unusual spectroscopy and electronic structure in the oxidized copper(II) form, as well as their ability to transfer electrons rapidly to several enzymes [258, 259].

In cupredoxins, the copper atom adopts a distorted tetrahedral or bipyramidal geometry, with three of the four/five copper coordinating residues located at the C-terminus (Cys, His and Met) and the other(s) at the N-terminus. In the case of azurin, the fifth copper ligand is an oxygen from the carbonyl peptide bond of a glycine that is coordinating the copper atom, making the geometry more bipyramidal [205, 260, 261].

These small copper proteins have a strong absorption band at around 600 nm (with an ε of 3-6 $mM^{-1}.cm^{-1}$), which has been assigned to a SCys-Cu charge transfer band, and a reduction potential higher than the one found in most inorganic copper complexes [262] (Table 4.1).

Table 4.1 – Examples of type 1 copper proteins, their proposed redox partners, wavelength of maximum absorption (λ_{max}), respective molar extinction coefficient (ε) and reduction potentials of the copper centers.

Organism	Protein	Redox Partners	λ_{max} (nm)	ε (mM^{-1} cm^{-1})	Reduction Potential (mV *vs* SHE)	Ref.
Paracoccus denitrificans	amicyanin	methylamine dehydrogenase	595	4.6	+ 294	[263-265]
Achromobacter denitrificans	azurin	cyt c_{551}/nitrite reductase	619	5.1	+ 276	[266, 267]
Achromobacter xylosoxidans	azurin I/II[a]	nitrite reductase	620[a]	6.3/5.7	+ 305[a]	[268]
Alcaligenes faecalis	azurin	aromatic amine dehydrogenase	625	4.0	+ 266	[269, 270]
Pseudomonas aeruginosa	azurin	BCCP/ nitrite reductase	625	3.5	+ 270	[158, 271-273]
Paracoccus pantotrophus	pseudoazurin	BCCP/ nitrite, nitrous oxide and nitric oxide reductases	590	3.0	+ 230	[139, 261, 274]
Alcaligenes faecalis	pseudoazurin	Nitrite reductase	593	5.7	+ 270	[275-277]
Thiobacillus ferrooxidans	rusticyanin	cyt c_4	597	4.3	+ 680/580[b]	[278-280]
Rhus vernicifera	stellacyanin	-	6	4.1	+ 184	[281, 282]
"Spinach"	plastocyanin	photosystem I	600	5.2	+ 370	[283, 284]

[a] *A. xylosoxidans* has two azurins, I and II, with similar λ_{max} and reduction potential.
[b] Measured at pH 3.2 and pH 6.2.

Electron transfer requires specificity in order to avoid promiscuous redox centers but, it also must be quite fast to support the rapid turnover rates needed to complete a catalytic cycle. This interaction can be driven by electrostatic interactions, which depends on the redox pair and bacterial environment. In fact, these transient interactions are proposed to be pre-oriented due to large dipole moments, as observed for two redox shuttles from *P. pantotrophus*, pseudoazurin and cytochrome c_{550} [184]. In these, the positive dipole vectors exit the proteins surface at the point that is proposed to be involved in ET, for instance, at the copper center in cupredoxins or at the heme edge in cytochromes [139]. After collision of the ET complex partners, there is a range of possible conformations that allow lateral fluidity on the surface and for the protein to "probe" the surface. Furthermore, the association between the two proteins that constitute the complex must be weak in

order to quickly dissociate. This is the reason why these proteins have very little structural changes between the oxidized and reduced forms [179, 285].

P. aeruginosa azurin has been shown to be involved in the protection against oxidative stress, since a mutant lacking this protein was shown to be very sensitive to ROS [220, 286]. In *N. gonorrhoeae*, a mutant strain lacking the gene coding for a cupredoxin, the Lipid-modified Azurin (LAz), was found to be much more sensitive to hydrogen peroxide but not to superoxide, unlike the *P. aeruginosa* azurin mutant, resulting in reduced survival in human ectocervical epithelial cells [287].
LAz has a high sequence homology to other copper proteins from the azurin family [288, 289] and it has an unique additional N-terminal region of 39 amino acids that encodes the H.8 epitope (common in *Neisseria* genus), in which there are five imperfect repeats of a sequence rich in alanines (AAEAP) [236, 288] (Figure 4.2). Thus, as explained before for BCCP, LAz is a lipid-modified protein bound to the outer membrane [236] by a palmityl fatty acid at the N-terminus, sharing this cellular location with *Ng*BCCP [287, 288, 290]. In fact, recently it has been shown using antibodies that *N. meningitidis* LAz is located at the outer membrane and that under certain growth conditions it can even be facing the outside of the cell [291].

MKAYLALISAAVIGLAACSQEPAAPAAEATPAGEAPASEAPAAEAAPADAAEAPAAGNCAAT
VESNDNMQFNTKDIQVSKACKEFTITLKHTGTQPKASM**GH**NLVIAKAEDMDGVFKDGVGAAD
TDYVKPDDARVVAHTKLIGGGEESSLTLDPAKLADGDYKFA**C**TFPG**H**GAL**M**NGKVTLVD

Figure 4.2 – LAz primary sequence. The grey sequence consists of the signal peptide recognized and removed by the signal peptidase II (underlined) and the five AAEAP imperfect repeats. The remaining sequence constitutes the globular domain with the five copper binding residues identified (bold and underlined).

The role of this electron shuttle protein is not completely established, since the *Neisseria* genus has an array of periplasmic *c*-type cytochromes with apparent redundancy, shown to have complementary roles as electron shuttles in the respiratory chain of these microorganisms (Figure 4.3). Bacteria from the *Neisseria* genus can grow aerobically and microaerobically, as they present cytochrome cbb_3 oxidases with high affinity for oxygen [292], and can also use nitrite as an alternative electron acceptor, as they present an incomplete denitrification chain, composed by a copper nitrite reductase (AniA) and nitric oxide reductase NorB [293]. In *P. aeruginosa*, the azurin can donate electrons to enzymes of the denitrification pathway and thus, the role for LAz as electron donor to AniA had been proposed, since these two proteins share the same cellular location, as being tethered to the outer membrane [236]. Nevertheless, in the case of *N. gonorrhoeae*, it was shown recently that the membrane bound cytochrome c_5 and CcoP are essential as electrons shuttles to AniA [292]. Therefore, the question remains as to the identity of the redox partner(s) of LAz in *N. gonorrhoeae*.

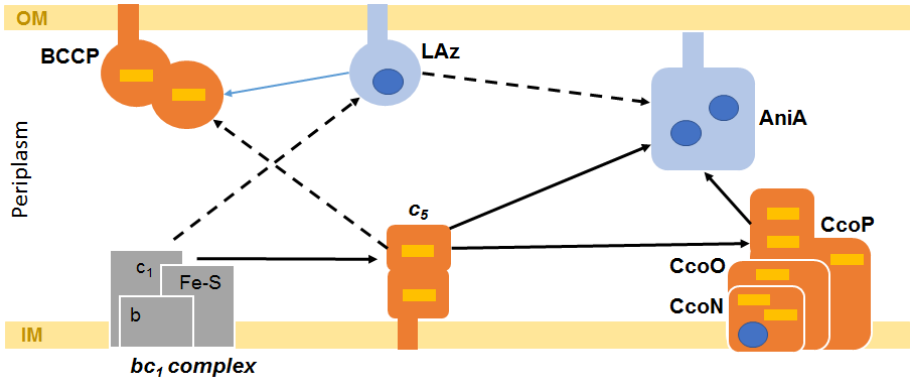

Figure 4.3 – Schematic representation of the electron transfer in *N. gonorrhoeae* and the role of LAz and other electron donors/acceptors. The arrows represent electron transfer. Solid arrows are proven and dashed arrows are proposed electron transfers. The electron transfer between LAz and *Ng*BCCP as a blue arrow, will be characterized in this chapter. OM – Outer membrane; IM – Inner membrane.

The structure of LAz incorporating Zn instead of Cu was determined by X-ray at 1.9 Å resolution (PDB ID: 3AY2). Recently, the solution structure of LAz with Cu was solved using NMR [205] (Figure 4.4A). LAz has an elongated *β*-barrel formed by eight *β*-strands that compose two antiparallel *β*-sheets arranged in the Greek key motif with one main alpha helix after *β*4 (the helix comprises residues 58-68 in LAz structure), and belongs to the azurin family (given its copper center and topology, Figure 4.4). Furthermore, LAz reduction potential was determined to be 277 ± 5 mV, at pH 7.0 [205], which is similar to the reduction potential of other cupredoxins (Table 4.1).

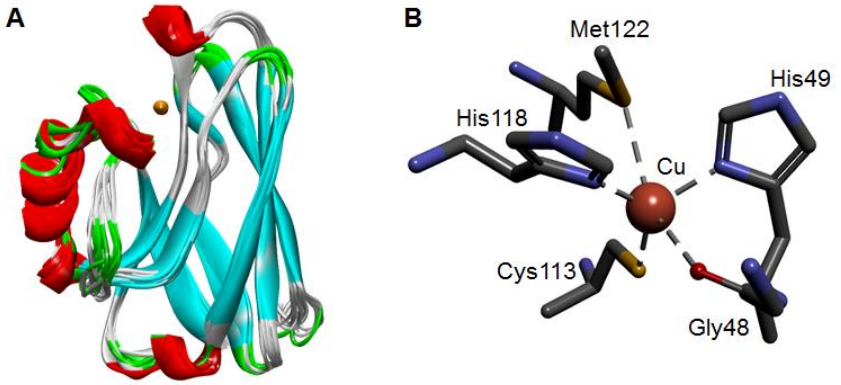

Figure 4.4 – (A) LAz soluble structure determined by NMR and (B) detailed structure of the copper center. The ensemble of ten NMR structures is colored by secondary structure with an elongated *β*-barrel formed by eight *β*-strands (in blue) that compose two antiparallel *β*-sheets, and one main alpha helix (red). The type 1 copper center responsible for its spectroscopic properties, comprises a copper atom (orange sphere) coordinated by the side chains of His49, Cys113, His118, Met122 and the oxygen of the peptide bond from Gly48. Figures prepared with PDB ID: 2N0M.

Previous kinetic studies with small redox proteins and BCCPs estimated turnover values (k_{cat}/[electron donor]) in the $\mu M^{-1}\ s^{-1}$ range as observed in various redox pairs, such as *S. oneidensis* BCCP/cytochrome c_5 ($18\ \mu M^{-1}\ s^{-1}$ [131]) and *R. capsulatus* BCCP/ cytochrome c_2 ($2\ \mu M^{-1}.s^{-1}$ [145]). These

rates are dependent on donor identity, binding orientation, ionic strength and even pH (in *P. pantotrophus* this rate is independent from pH value from 5 to 9 [136]).

This work will focus on LAz as the potential physiological electron donor of *Ng*BCCP. The biochemical properties of a recombinant *N. gonorrhoeae* LAz will be determined, as well as the kinetic parameters of the LAz/*Ng*BCCP redox pair to better understand the role of this cupredoxin in the oxidative stress defense mechanism. The nature of this interaction will be addressed by ITC, NMR and molecular docking simulations, revealing a weak transient interaction and some of the many challenges in studying transient electron transfer complexes.

4.2 Results and discussion

4.2.1 Biochemical characterization of *N. gonorrhoeae* LAz

N. gonorrhoeae and other neisserial species have in their periplasmatic space proteins that are bound to the membrane by a lipid-modified residue followed by a linker region and finally the globular domain [236]. LAz, like *Ng*BCCP, is one of these membrane-bound proteins, with a linker region (H.8 epitope) and a conserved globular domain. Similar to *Ng*BCCP in Chapter 3, a recombinant LAz construct was heterologously produced in *E. coli* without the N-terminal H.8 epitope. A 14 kDa protein with a theoretical pI of 5.2 was successfully purified with a high yield of 50 mg and 20 mg of protein per liter of LB and M9 media, respectively. The profile of the pure sample SDS-PAGE, showed either one or two bands with similar molecular weights, depending on protein preparation (Figure 4.5A). Mass spectrometry identified these two different protein populations with the molecular mass of 13631 ± 5 Da and 15736 ± 5 Da. The first value is in accordance with the expected value for LAz of 13633.3 Da after removal of the signal peptide. The second corresponds to a less abundant population of LAz with the unprocessed signal peptide.

Since the first construct prepared for heterologous expression had a signal peptide from *P. pantrotrophus* pseudoazurin, a different construct was prepared using the *E. coli* signal peptide (PelB) however, the result was the same, independently of the construct used for protein production, there were always two different protein populations which varied in proportion.

The purest fraction was obtained from M9 media periplasmic extract with a purity ratio (A_{625nm}/A_{278nm}) of approximately 1.0 (Figure 4.5B). The amount of copper ions was determined to be 0.79 ± 0.04 Cu per polypeptide chain, which is consistent with one copper atom per polypeptide chain, as seen in other cupredoxins.

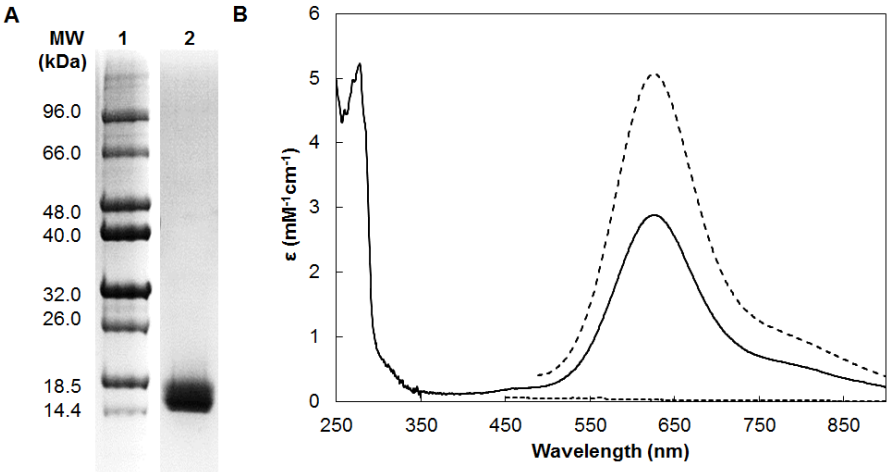

Figure 4.5 – (A) SDS-PAGE of the purified of LAz (lane 2) in a 15 % Tris-Tricine gel stained with Coomassie Blue. Lane 1 is the protein marker. (B) UV-visible absorption spectra of LAz, in 20 mM phosphate buffer pH 7.0, as-isolated (solid line), fully oxidized with potassium ferricyanide (dashed line) and fully reduced with sodium dithionite (dotted line).

The copper center is responsible for LAz unique spectroscopic properties, common to other known cupredoxins. In the visible spectra of the oxidized LAz there is a strong absorption band at 625 nm (Figure 4.5B) that is responsible for its characteristic blue color. As-isolated LAz is usually in a mixture of oxidation states, the reduced protein is colorless and has no visible spectrum, and thus addition of ferricyanide increases the visible absorption spectrum.

The copper atom is coordinated by five residues, Gly48 (the carbonyl O), His49 (Nδ1), Cys113 (Sγ), His118 (Nδ1) and Met122 (Sδ), in a pseudotrigonal bipyramidal geometry [205] similar to what is found in other azurins [294-296]. The intense band is due to a low-energy π ligand-to-metal charge transfer between Cys-S and Cu^{II} ($d_{x^2-y^2}$), as described for plastocyanin (at ~ 600 nm) [283, 297]. The molar extinction coefficient for the fully oxidized LAz, at 625 nm, based on the copper quantification, is 5.1 $mM^{-1}cm^{-1}$. This value is similar to the one found for other azurins, such as the ones of *P. aeruginosa* azurin (ε_{625nm} = 3.5 $mM^{-1}cm^{-1}$ [271]) and *Achromobacter denitrificans* azurin (ε_{619nm} = 5.1 $mM^{-1}cm^{-1}$ [267]) (more examples can be found in Table 4.1).

LAz molecular weight in solution was determined by size-exclusion chromatography in 50 mM Tris-HCl, pH 7.6, in the presence (Figure 4.6) or absence of 150 mM NaCl. In solution, LAz has an apparent molecular weight of 21 ± 2 kDa with 150 mM NaCl and of 25 ± 2 kDa in its absence.

LAz molecular mass determined by mass spectrometry was 13.6 and 15.7 kDa (a mixture of that seems to be of 1:1). Thus, the higher molecular weight of 21 and 25 kDa could suggest that in solution LAz exhibits a monomer-dimer equilibrium. However, LAz NMR data is consistent with a monomeric species [205]. In fact, looking at the solution structure represented in Figure 4.4A, it becomes clear that LAz has an elongated β-barrel. The non-spheric shape and thus higher Stokes volume explains the higher molecular weight observed in solution.

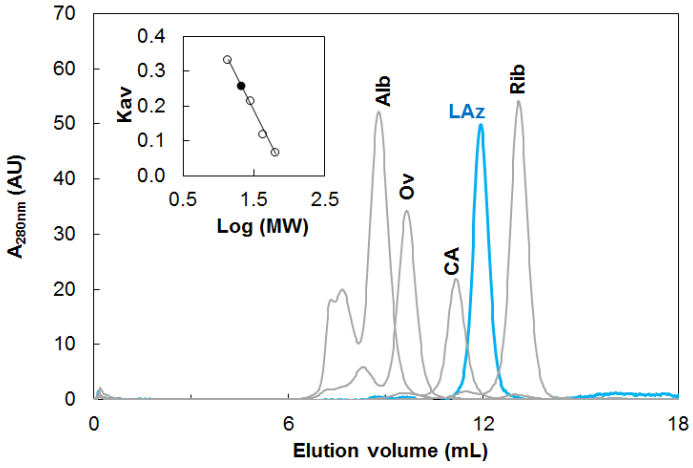

Figure 4.6 – Molecular size-exclusion chromatography of LAz in 50 mM Tris-HCl pH 7.6 and 150 mM NaCl (21 kDa, blue line). In grey are the elution profiles of standards proteins used to estimate the apparent molecular weight: Albumin (Alb, 65 kDa), Ovalbumin (Ov, 44 kDa), Carbonic Anhydrase (CA, 29 kDa) and Ribonuclease A (Rib, 13.7 kDa).

4.2.2 *Ng*BCCP steady-state kinetics with LAz as electron donor

The LAz role as *Ng*BCCP ET partner was assessed in a preliminary test with periplasmatic extract from *E. coli* BL21 (DE3) cells, overexpressing *Ng*BCCP. Two small electron shuttle proteins were used as electron donors, LAz and horse heart cytochrome *c*, in an assay in which instead of pure enzyme, the periplasmic extract of *E. coli* cells producing *Ng*BCCP was used (Figure 4.7).

LAz incubated with 0.02 µg and 0.004 µg of periplasmic extract, after addition of 100 µM H_2O_2 showed oxidation rates of 0.86 ± 0.08 and 0.12 ± 0.01 µM LAz.s^{-1}, respectively. The periplasmatic extract lacking *Ng*BCCP showed no LAz oxidation when adding hydrogen peroxide, which indicates that LAz is oxidized specifically by *Ng*BCCP. This was the first indication that LAz was an efficient electron donor for this enzyme.

When the horse heart cytochrome *c* was used as electron donor with the highest amount of periplasmic extract containing *Ng*BCCP (0.02 µg protein), the initial oxidation rate was only 0.02 ± 0.01 µM cyt *c*.s^{-1}. This shows that horse heart cytochrome *c* is less efficient than LAz and a poor electron donor to *Ng*BCCP.

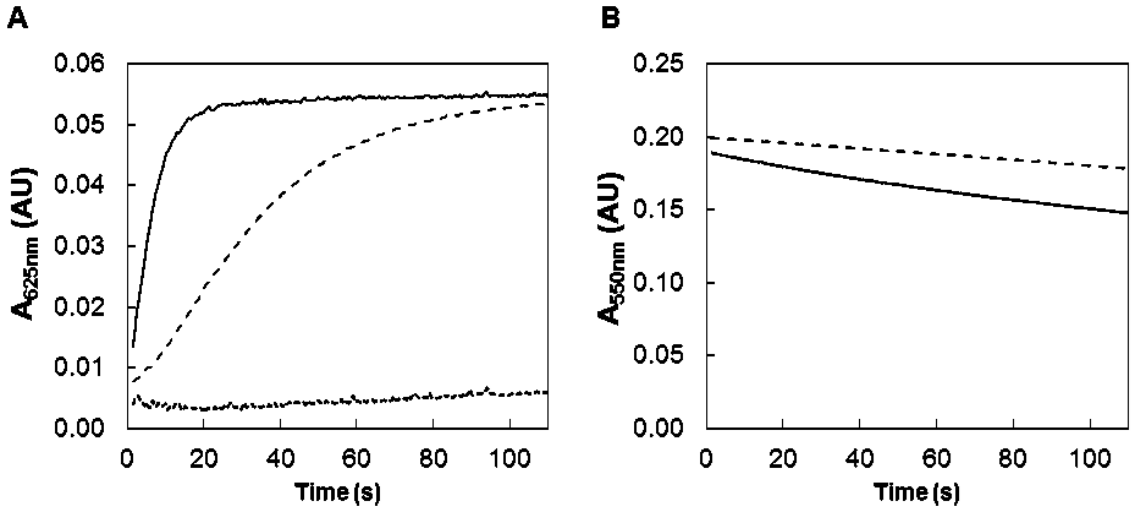

Figure 4.7 – Kinetic traces of the periplasmic extract of *E. coli*/pEC86/pET22*Ng*BCCP with 10 µM reduced LAz (A) or horse heart cytochrome *c* (B) as electron donors, after addition of 100 µM H_2O_2 (time 0 s), in 10 mM MES pH 6.0, 10 mM NaCl and 1 mM $CaCl_2$. The oxidation rates were estimated in the presence of 0.02 µg protein (solid line) and 0.004 µg protein (dashed line). A control with a periplasmic extract of *E. coli*/pEC86/pET22b (not producing enzyme) was performed with 0.02 µg protein and LAz (dotted line).

In Chapter 3 it was shown that *Ng*BCCP has peroxidase activity with $ABTS^{2-}$ as electron donor, and that to reach maximum activity it needs reductive activation in the presence of calcium ions. Here it was tested whether LAz was able to activate the peroxidase and how fast this process is (Figure 4.8A). Without pre-incubation with LAz (0 min), *Ng*BCCP has approximately half-maximum activity and after 10 min of incubation, it reached maximum activity. The respective kinetic traces are represented in Figure 4.8B.

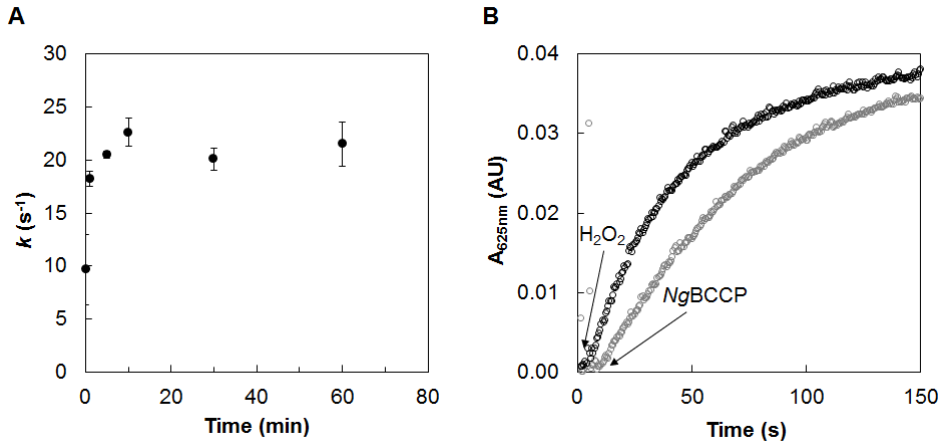

Figure 4.8 – (A) *Ng*BCCP activation by incubation with fully reduced 9 µM LAz over time . (B) The kinetic traces show LAz oxidation followed at A_{625nm} for *Ng*BCCP incubated for 0 min (grey circles, only in this condition *Ng*BCCP was added after H_2O_2) and 10 min (black circles). Without any previous activation (0 min) the turnover rate is 10 ± 3 s^{-1} and it reaches maximum activity after a 10 min incubation (23 ± 1 s^{-1}).

Therefore LAz is capable of activating *Ng*BCCP and of maintaining the catalytic cycle of this enzyme. In fact, the reduction potential of LAz (277 ± 5 mV, at pH 7.0 [205]) is close to the one of E heme of BCCP (+ 310 ± 10 mV, at pH 7.5), and this experiment shows that it can donate electrons to the E heme activating the enzyme.

In order to assess the role of calcium ions in the *Ng*BCCP catalytic activity with LAz as electron donor, the assays were performed in the presence or absence of excess calcium ions and the initial oxidation rates were 0.329 ± 0.004 µM LAz.s^{-1} and 0.085 ± 0.003 µM LAz.s^{-1}, respectively.

Therefore, calcium ions are needed in the assay in order to reach maximum activity. This could be an indication that formation of a productive ET complex is dependent on calcium ions, probably due to a simplification of the *Ng*BCCP solution states (as described in Chapter 3). This was not observed with $ABTS^{2-}$ as electron donor, possibly because it was in saturating concentrations and it was able to give electrons directly to P heme, unlike LAz.

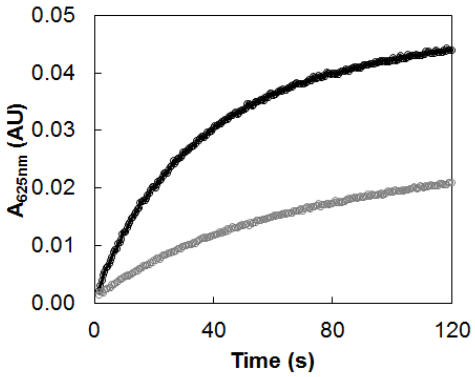

Figure 4.9 – The kinetic traces of *Ng*BCCP activity with 10 µM LAz and 100 µM H_2O_2 in 10 mM MES pH 6.0. LAz oxidation was followed at A_{625nm} in the presence (black circles) and absence (grey circles) of 2 mM $CaCl_2$ in the assay. The initial rates determined were 0.329 ± 0.004 µM LAz.s^{-1} and 0.085 ± 0.003 µM LAz.s^{1}, respectively. Time zero was adjusted to the time pre-activated *Ng*BCCP was added.

Further analysis of the catalytic activity of the LAz/*Ng*BCCP pair was performed to determine its dependence on substrate concentration, pH, temperature and ionic strength.

The kinetic parameters for the pre-activated *Ng*BCCP catalytic activity with LAz as electron donor were a K_M = 0.4 ± 0.2 µM H_2O_2 and a turnover number of 39 ± 0.03 s^{-1}, at pH 6.0 and at 25 ºC, by simulating the data with a Michaelis-Menten. (Figure 4.10A). Compared to $ABTS^{2-}$ the K_M decreased about one order of magnitude (from 4 to 0.4 µM H_2O_2), which shows the high affinity of *Ng*BCCP for hydrogen peroxide, but the turnover number is lower. LAz is not used in the assay at saturating concentrations as occurred with $ABTS^{2-}$ and the same occurs for other reported kinetic studies of BCCPs. Therefore, in order to compare the kinetic parameters with other BCCPs, the turnover number was corrected to the electron donor concentration, k_{cat}/[ED].

This comparison is valid since the amount of electron donor used in the assays is typically much lower than the expected electron donor K_M value (60 µM cytochrome c_2 from *R. capsulatus* [145] and approximately 70 µM pseudoazurin from *P. pantotrophus* [139]). At 25 ºC, pH 6.0, the k_{cat}/[LAz] = 3.9 $\mu M^{-1}.s^{-1}$, which is in the same order of magnitude as the one determined for BCCP /cytochrome c_2 in *R. capsulatus* (2 $\mu M^{-1}.s^{-1}$) [145].

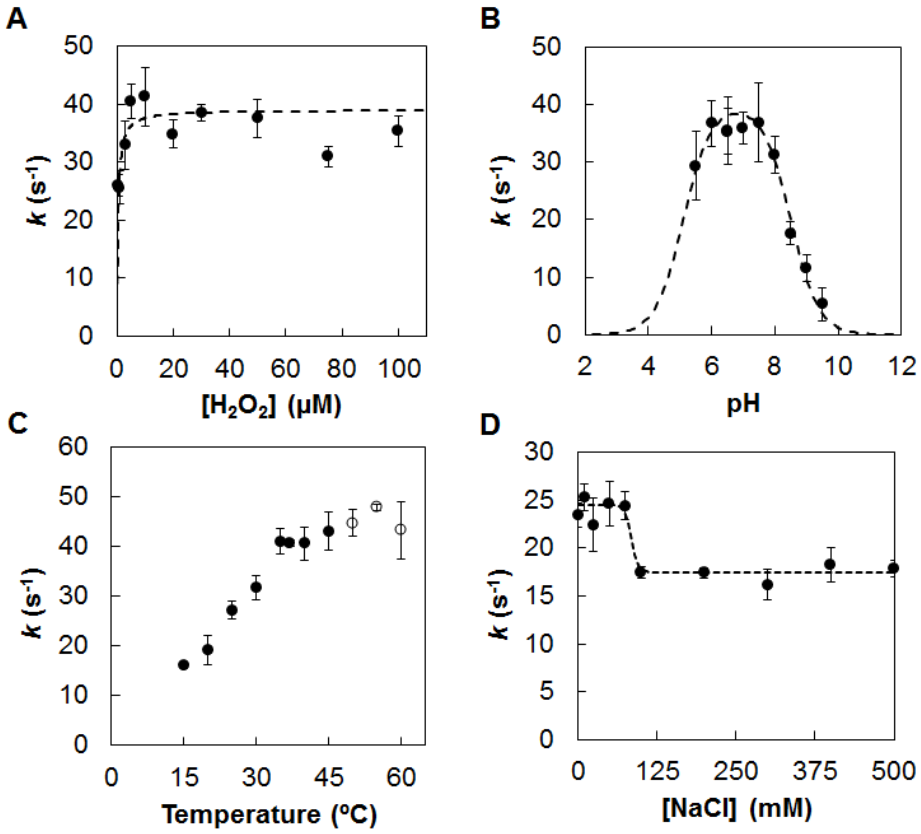

Figure 4.10 – Steady-state kinetics using LAz as electron donor. Catalytic activity of pre-activated *Ng*BCCP as a function of substrate concentration (A), pH (B), temperature (C) and ionic strengh (D). The open circles in (C) are experimental points where the reaction is not complete due to protein denaturation. The dashed lines represent the simulated data using the equations in Chapter 2, Materials and Methods (see Section 2.6.2).

Regarding the pH dependence (Figure 4.10B), the catalytic activity was simulated with a bell-shaped curve with a maximum at pH 6.8, and with a pKa_1 = 5.1 ± 0.1 and a pKa_2 = 8.5 ± 0.1, similar to what was observed with $ABTS^{2-}$ (5.9 ± 0.1 and 8.4 ± 0.1, respectively). pH values below 5.5 were not tested as LAz is not stable. Nevertheless, the apparent pKa_1 value is lower than the one determined with $ABTS^{2-}$ as electrons donor, and this is probably due to the fact that $ABTS^{2-}$ is unable to maintain the enzyme active at pH 6.0, while the reaction with LAz is complete at this pH value (similar rates are shown for pH values from 6.0 to 7.5) and LAz is completely oxidized by *Ng*BCCP at the end of the assay. Therefore, as the p*Ka* values reported for LAz/*Ng*BCCP pair are similar to the ones reported for the $ABTS^{2-}$/*Ng*BCCP pair, they might reflect changes on the protonation/deprotonation of key residues in the peroxidase, rather than in the electron donor.

As for the temperature dependence, the peroxidase activity increases with temperature, up to 37 ºC (the human body temperature, similar rates from 35 to 45 ºC) after which it apparently still increases but the assays are incomplete, as LAz is not completely oxidized (Figure 4.10C). This is attributed to denaturation and therefore, inactivation of *Ng*BCCP at temperatures > 50 ºC, as the mixed-valence *Ng*BCCP has a *Tm* of 55.6 ºC, as determined in Chapter 3. LAz *Tm* was not determined however, the copper atom is not lost at the end of the assay (estimated from the absorbance at A_{625nm}), which indicates that LAz did not denaturate.

When varying the ionic strength, LAz oxidation rates decrease 29 % with NaCl concentrations ≥ 100 mM (Figure 4.10D). At lower and higher concentrations there is a plateau with no significant increase or decrease in activity. Ionic strength variation affects protein-protein interaction, mainly the rate of association and dissociation of the protein pair, which allows the characterization of the nature of the complex interaction.

In an electrostatic driven protein-protein interactions, the dependence of rate constant on ionic strength is explained by an increasing or decreasing monotonic function, as described by Watkins et al. parallel plate model [298]. This effect is due to charged residues distributed in the proteins interface regions. For instance, higher ionic strength decreases the rate constant between proteins of opposite charge due to shielding of the charged groups of each protein. In some cases, both an increase and decrease of the rate constant are observed at lower ionic strengths, forming a curve with an optimum ionic strength. This effect is attributed to formation of a strong complex at lower ionic strengths but in a conformation that is not productive [298].

There is no effect on LAz/*Ng*BCCP turnover, as it is stable above 100 mM NaCl, therefore we can conclude that this interaction is not driven by electrostatic forces but mostly of hydrophobic nature, which are not affected by changes in ionic strength. This was also observed for *M. hydrocarbonoclasticus* cytochrome c_{552}/BCCP pair, as catalytic activity remained unaltered up to 600 mM NaCl [130].

The small decrease in catalytic activity between 80 and 100 mM NaCl can be explained by formation of a more productive complex at lower ionic strength, possibly due to changes in the proteins solvation shell. The majority of specific interfaces are "dry" but transient interfaces tend to be rich in water molecules ("wet") [285, 299]. Although hydrophobic interfaces are characterized by a more complete desolvation, in some cases, the water molecules at the interface form water-mediated polar interactions that may contribute to the stability of the complex [299]. Additionally, changes in the surface solvation might hinder the lateral mobility of the two proteins.

Furthermore, hydrophobic effects are favored at higher temperatures [300] therefore, *N. gonorrhoeae* as an obligate pathogenic bacteria, is also adapted to an environment with a temperature of 37 ºC, at which catalytic activity is optimal (higher temperatures lead to higher catalytic activity). The location of the native complex at the outer membrane might subject LAz/*Ng*BCCP to significant changes in ionic strength. The hydrophobic nature will allow this complex to retain high turnover numbers independently of changes in the environment, at physiological pH and temperature.

Analysis of the kinetic parameters suggests that the LAz/*Ng*BCCP ET pair is more efficient than the $ABTS^{2-}$/*Ng*BCCP pair, with a lower K_M value of 0.4 µM H_2O_2. The turnover numbers were high despite the fact that we used non-saturating LAz concentrations and that ET is dependent of site recognition, in contrast to $ABTS^{2-}$, a small molecule at saturating conditions that might donate electrons directly to P heme and does not require site recognition.

4.2.3 Inhibition of the *Ng*BCCP catalytic activity with LAz as electron donor

In the previous chapter it was assessed the inhibition of *Ng*BCCP catalytic activity by exogenous ligands. An azide-inhibited *Ng*BCCP structure was determined where the active site was blocked by an azide molecule and therefore, the substrate was not able to access P heme. Here, it was determined the effect of azide on the catalytic activity with LAz as electron donor, at pH 6.0 and 7.5 (Figure 4.11). Inhibition parameters were not defined since LAz is not at saturating concentrations.

Addition of potassium ferrycianide to the assay fully oxidizes LAz as observed by the increase in absorption at 625 nm, which shows that the presence of increasing concentrations of sodium azide does not affect the stability of the copper center. Therefore, azide inhibition can be attributed solely to its binding to the P heme, the catalytic site, and it does not affect LAz center though we cannot rule out that it interferes with LAz binding. Since uncompetitive inhibition is observed at much higher azide concentrations (which would affect E heme and then ET to P heme) it is unlikely that LAz binding is greatly affected.

The kinetic traces show that lower concentrations of azide are needed to inhibit *Ng*BCCP catalytic activity at pH 6.0, than at pH 7.5. At pH 6.0 the peroxidase activity is almost completely abolished with 2.5 mM azide, while at pH 7.5 a concentration above 40 mM azide is required. As described in Chapter 3, at higher pH values the binding affinity of azide decreases and the *ki* constant increases.

At pH 6.0, it was observed that azide has a higher affinity for the catalytic site of *Ng*BCCP however, at this pH value $ABTS^{2-}$ is not capable of maintaining *Ng*BCCP active, so it was not possible to assess the effect of azide on the catalytic activity between pH 6.0 and pH 7.5. Using LAz as electron donor it was possible to compare the behavior at these two pH values and it is clear that the lower concentrations required to inhibit the catalytic activity at lower pH agree with a higher affinity of azide to P heme, as indicated by the estimation of the k_{app} values in Chapter 3: 3.8 mM and 41 mM azide for pH 6.0 and 7.5, respectively. In fact, with LAz as electron donor it is observed that concentrations below this k_{app} values significantly inhibited the catalytic activity, either due to the use of non-saturating concentrations of reduced LAz or to azide effectively blocking the active site at lower concentrations, which indicates a lower competitive inhibition contant (concentration required to produce half maximum inhibition).

These results emphasize the importance of the pH value in inhibition studies as it is expected an acidic environment in the periplasm of *N. gonorrhoeae* cells, such as the one in the human cervix (6.8 in the proliferative state and 6.1 in the secretory stage [253]). The lower pH does not inhibit the catalytic activity of the *Ng*BCCP/LAz pair, but it might increase the affinity of the inhibitor, as observed for sodium azide.

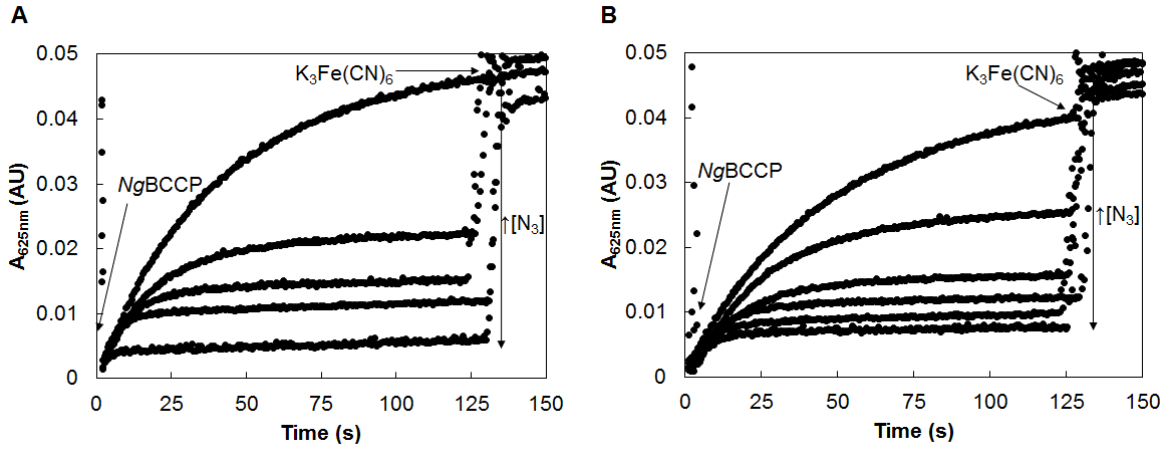

Figure 4.11 – Kinetic traces of 10 µM LAz oxidation by *Ng*BCCP in the presence of 100 µM H_2O_2 at (A) pH 6.0 and (B) pH 7.5, with incresasing concentrations of sodium azide (A: 0, 0.2, 0.5, 1 and 2.5 mM azide; B: 0, 5, 10, 20, 30 and 40 mM azide). As sodium azide concentrations increase, there is a decrease in LAz oxidation rates. Addition of potassium ferrycyanide at the end of the assay fully oxidizes LAz showing that the copper center was not lost. Time was adjusted to the addition of pre-activated *Ng*BCCP, as time 0 s.

4.2.4 Preliminary calorimetric studies – *Ng*BCCP and LAz interaction

Isothermal titration calorimetry (ITC) was used to determine the thermodynamic parameters of LAz binding to *Ng*BCCP. A concentrated LAz solution (0.75-1.5 mM) was titrated into the cell solution containing *Ng*BCCP (20-30 µM). Preliminary results showed better titration curves at 35 ºC (compared to 15 and 25 ºC) with sodium phosphate buffer, pH 7.0, however this buffer is

incompatible with the presence of calcium ions (2 mM $CaCl_2$), needed for complete dimerization of *Ng*BCCP (Chapter 3), as it precipitates as calcium phosphate. Other buffers were tested, such as 10 mM HEPES pH 7.5, 10 mM MES pH 6.0 and 10 mM cacodylate pH 6.0, containing 2 mM $CaCl_2$. The best results were then obtained with 10 mM MES, pH 6.0, 2 mM $CaCl_2$ and are presented in Figure 4.12.

The titration curve is not complete as there is no initial plateau. Nevertheless, this data gave an estimate of the order of magnitude of the entalphy change (ΔH), entropy change (ΔS), equilibrium dissociation constant (K_D) and stoichiometry (n). The binding of LAz to *Ng*BCCP is an exothermic process (negative ΔH of - 1.6 kJ.mol^{-1}), like yeast CCP/cytochrome *c* binding [301], although the enthalpy and entropy changes (ΔS of 0.09 kJ.mol^{-1}K^{-1}) observed are quite small. The K_D estimated from the titration curve was approximately 10 µM, which indicates a weak affinity typical for transient complexes, such as ET complexes.

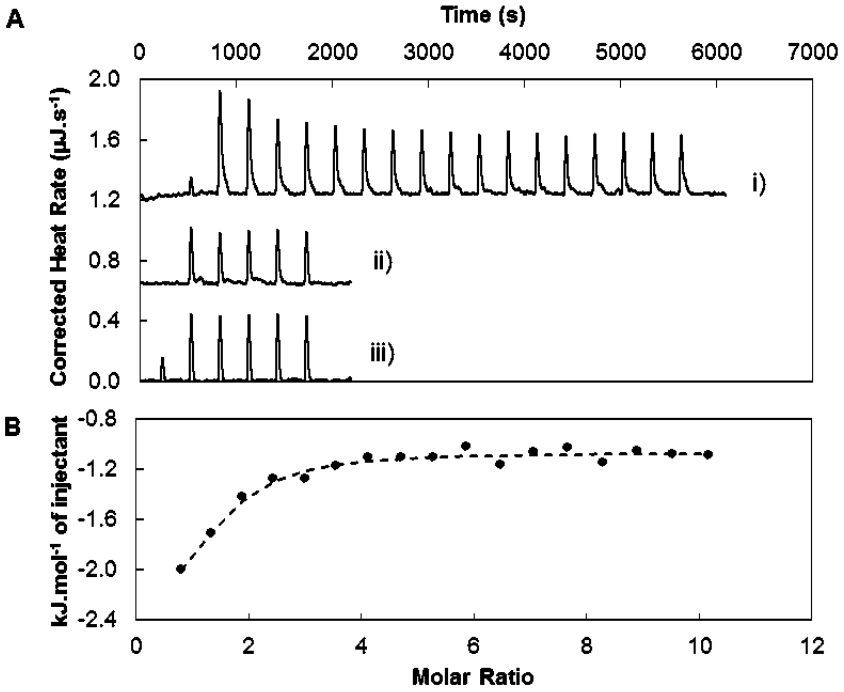

Figure 4.12 – (A) Isothermal titration calorimetry of the binding of LAz to *Ng*BCCP equilibrated in 10 mM MES pH 6.0, 2 mM $CaCl_2$. i) A 1.4 mM LAz solution was titrated into a 30 µM *Ng*BCCP solution. Controls for the heat of dilution were performed: ii) LAz solution titrated into the equilibration buffer and iii) equilibration buffer titrated into the final mixture of LAz and *Ng*BCCP. (B) The heat change of the results obtained in panel (A) for experiment i). The best fit is represented by the black dashed-line that was corrected for the heat of dilution.

Given the low ΔH, higher concentrations of *Ng*BCCP would be needed in order to obtain a complete titration curve and to properly estimate the stoichiometry (which was approximately 1 in these preliminary assays), for a binding equilibrium with a K_D in this order of magnitude.

The concentration of *Ng*BCCP in the assay was increased to 60 µM, but the enzyme precipitated probably due to a combination of factors, such as high protein concentrations, temperature and high stirring rates during the assay. In these experiments, the heat of dilution increased and the interaction effect was less pronounced most likely due to protein aggregation.

A different technique was tested, the microscale thermophoresis, that uses smaller amounts of the target protein. Microscale thermophoresis is based on the molecules diffusion upon heating to estimate the affinity constant. In this technique nanomolar amounts of fluorescent labeled (NT.647) *Ng*BCCP were incubated with various concentrations of LAz.

This presented a challenge since at high LAz concentrations (up to 750 µM) the sample is more viscous, while at lower LAz concentrations *Ng*BCCP adheres to the capillary walls. All these issues were improved by testing different types of capillaries or by using additives (for instance 0.05 % Tween) but still the viscosity of the solution at high LAz concentrations (needed to determine relatively high K_D values) appears to be one of the major problems, not allowing correct measurements of the fluorescence change. Therefore, the binding could not be analyzed by microscale thermophoresis due to changes in the initial fluorescence intensity, given by the labeled *Ng*BCCP whose concentration is maintained constant in all capillaries. Nevertheless, the raw fluorescence changes indicating a possible "quenching" effect due to binding, could be fitted to a dissociation constant between 1-10 µM, a value that is of the same order of magnitude as the one determined by ITC.

Overall these techniques suggested that this complex has low affinity, with a dissociation constant in the micromolar range (1-10 µM). Values in this range have been reported for other transient ET complex interactions, such as the two transient complexes in *P. pantotrophus*: BCCP/cytochrome c_{550} (K_D of 2.8 µM [163]) and BCCP/pseudoazurin (K_D of 16.4 µM [184]).

The conditions needed to correctly determine the affinity and thermodynamic parameters using ITC or microscale electrophoresis have some issues, such as solution viscosity or protein precipitation. In alternative this interaction could be studied using fluorescence-based binding assays.

4.2.5 *Ng*BCCP and LAz complex - Interface mapping

In order to further characterize the LAz/*Ng*BCCP ET complex and to obtain a model structure of this complex, we performed NMR titration and docking simulations.

There are not many techniques that can elucidate the atomic structure of a protein complex. NMR titration spectroscopy was used to detect small perturbations (chemical shifts) in the nuclei of the residues involved in the contact interface, given that the resonances of LAz have been previously assigned.

In addition, molecular docking simulations were used to predict the model structures of the LAz/*Ng*BCCP complex. The results obtained will be presented and discussed in the following section.

4.2.5.1 Heteronuclear NMR titration and surface analysis

The $^{1}H^{15}N$ HSQC spectrum of reduced LAz was previously assigned [208] and the solution structure determined by NMR [205]. In order to determine which LAz residues are affected by the binding of *Ng*BCCP, three independent samples were prepared with a LAz:*Ng*BCCP ratio of 1:0, 1:1 and 1:2. In these samples LAz was reduced with sodium ascorbate. Under these conditions *Ng*BCCP is in the mixed-valence state, with a paramagnetic ferric P heme. This could cause paramagnetic relaxation enhancement of the spins in proximity to the P heme. However, it is expected that LAz interacts with the surface surrounding the E heme, which is located at a distance > 20 Å from the P heme. E heme in the mixed-valence *Ng*BCCP is reduced and diamagnetic therefore, these paramagnetic relaxation enhancement effects are not expected to be observed.

Figure 4.13 shows the chemical shift variation of LAz resonances upon *Ng*BCCP binding in a 1:1 and 1:2 ratio. The residues affected in the titration were divided into three groups according to their combined proton and nitrogen chemical shifts variation: $\Delta\delta_{HN} \geq 0.025$ ppm, in red; $\Delta\delta_{HN}$ between 0.015-0.025 ppm in pink; $\Delta\delta_{HN}$ between 0.005-0.015 ppm in grey. The highest chemical shift observed was 0.06 ppm and this indicates that the binding occurs in a fast exchange regime in the NMR timescale.

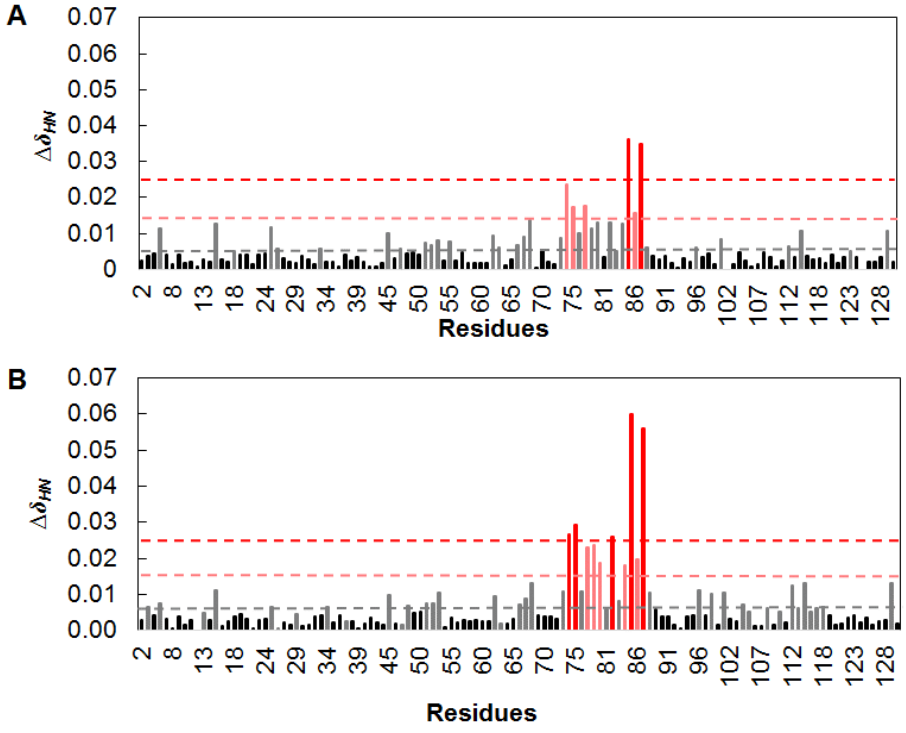

Figure 4.13 – Chemical shift variation of LAz resonances upon *Ng*BCCP binding in a 1:1 (A) and 1:2 (B) ratio. The shifts were categorized into three groups: $\Delta\delta_{HN} \geq 0.025$ ppm, in red; $\Delta\delta_{HN}$ between 0.015-0.025 ppm in pink; $\Delta\delta_{HN}$ between 0.005-0.015 ppm in grey. LAz has four proline residues which do not appear in the HSQC spectra.

In fact, these chemical shifts are relatively small in comparison with what is observed for other transient ET complexes, for instance for *Phormidium laminosum* plastocyanin/cytochrome *f* pair the largest shifts are 0.5–1.0 ppm [302], and for the yeast CCP/cytochrome *c* pair the largest shifts are between 0.05–0.30 ppm [303].

The higher chemical shifts in the 1:2 ratio compared to the 1:1 ratio, can be explained by the binding equilibrium. Considering a K_D of 10 μM, as estimated in the ITC experiments, in the 1:1 ratio, only 73 % of LAz molecules are bound to *Ng*BCCP, while in a 1:2 ratio it would be about 92 % of LAz molecules. Although this is an estimative, the changes observed between the two samples agree with such an equilibrium constant in the micromolar range.

The two residues that experience the highest chemical shifts are His85 and Lys87 (red group in Figure 4.13). The NH of these residues is shown in the overlaid ^{1}H-^{15}N heteronuclear NMR spectra of the three titration samples presented in Figure 4.14. This demonstrates the small magnitude of these chemical shifts and that chemical shifts of other residues ($\Delta\delta_{HN}$ < 0.03 ppm) are not has perceptible in the NMR spectra, such as the one observed in Asp78, also present in Figure 4.14.

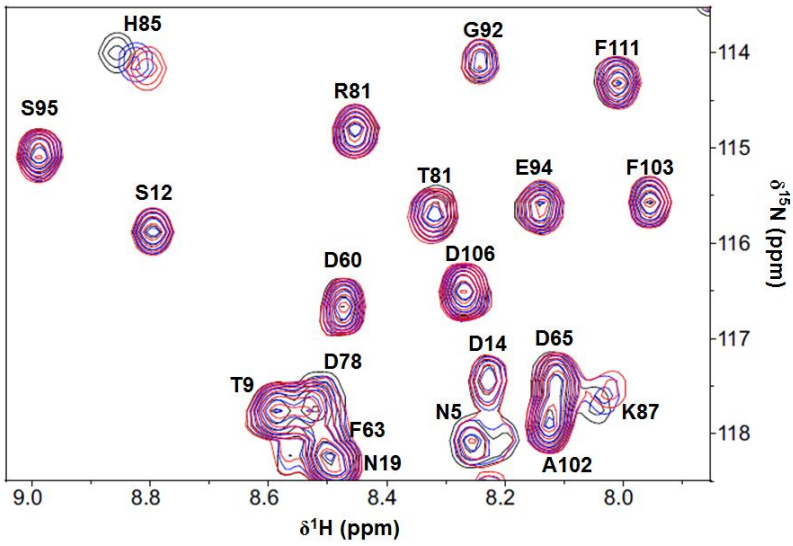

Figure 4.14 – Overlay of the spectral region of the ^{1}H-^{15}N heteronuclear NMR spectra of free LAz (black) and after addition of one (blue) or two (red) equivalents of *Ng*BCCP. The NH resonance of three of the residues that experience the high chemical shifts are present in this region.

When mapping these residues onto LAz surface (Figure 4.15) it is clear that the main affected region comprises the residues 74 to 87, which is a loop region followed by *β*5 (Groups in 1:2 ratio: $\Delta\delta_{HN} \geq$ 0.025 ppm: Tyr74, Val75, Val82, His85 and Lys87 in red; 0.015>$\Delta\delta_{HN}$ >0.025 ppm: Asp78, Asp79, Ala80, Ala84 and Thr86 in pink).

Three of the residues coordinating the copper center, Gly58, Cys113 and His118, are included in the group with the lowest chemical shift (0.005>$\Delta\delta_{HN}$ >0.015 ppm, in grey).

This result was not the expected one because in other studies with type 1 copper proteins, the interface involves residues surrounding the copper center. For instance in pseudoazurin, the most affected residues belong to a hydrophobic patch surrounded by a ring of lysines around the copper center [139]. A closer look at LAz solution structure shows that this loop in solution is slightly apart from the *β*-barrel, forming a "cavity" behind the loop. This suggested that this loop might have some liberty to move and addition of *Ng*BCCP to the solution caused significant perturbations in this loop. Therefore this changes might not be directly related to formation of the complex.

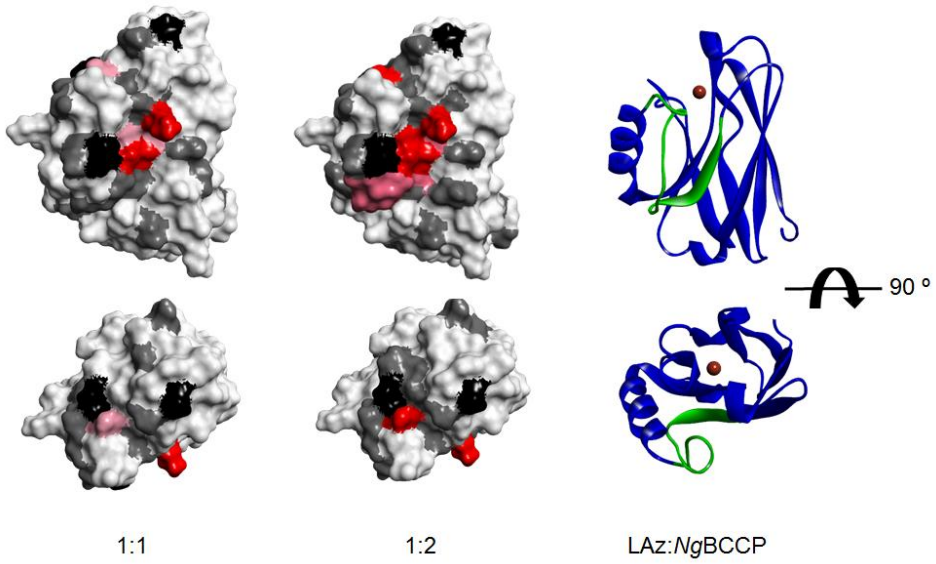

Figure 4.15 – Mapping of the chemical shifts in Figure 4.13 onto the surface of LAz according to the same color code: $\Delta\delta_{HN} \geq 0.025$ ppm, in red; $\Delta\delta_{HN}$ between 0.015-0.025 ppm in pink; $\Delta\delta_{HN}$ between 0.005-0.015 ppm in grey. Proline residues are colored in black. The surface and respective structure are represented from a "side view" of LAz *β*-barrel with the copper center (orange sphere) on top, and a "top view" facing the copper atom. The residues with larger shifts are distributed along a loop region and a *β*-strand (*β*5), highlighted in green in the LAz structure.

The electrostatic surface potential and hydrophobic surface of both molecules were analyzed in order to assess the nature of the small chemical shifts (grey surface) and whether they might be involved in formation of the complex. The residues located in hydrophobic patches on LAz surface experienced smaller shifts (Figure 4.16), on one side of the copper site (at His118) and at the N-terminal end. This hydrophobic patch surrounding the histidine residue that coordinates the copper atom, has been proposed to be involved in complex formation of *A. xylosoxidans* azurin and the partner nitrite reductase [296].

LAz has an overall negative/neutral surface (red to white surface), though there is a small positive patch due to three surface lysines (Figure 4.16). LAz has a total of 12 lysine residues (plus 1 arginine) evenly distributed over the non-hydrophobic surface and balanced by negatively charged aspartate (15) and glutamate (5) residues, which are also distributed around the surface. Thus, there is no

specific charged patch as the one observed in *P. pantotrophus* pseudoazurin, which has a positively charged ring of lysines surrounding the hydrophobic patch at the copper site.

In fact, this charge distribution in pseudoazurin creates a large dipole moment with the vector centered at the center of mass and leaving the protein through the His81, the exposed residue that coordinates the copper atom. Analysis of the dipole moment of azurins, pseudoazurin and LAz shows that the azurins have a smaller dipole vector compared to pseudoazurin (Table 4.2). In LAz, the dipole vector is centered at its center of mass and passes through Met122 that coordinates the copper atom (Figure 4.16C).

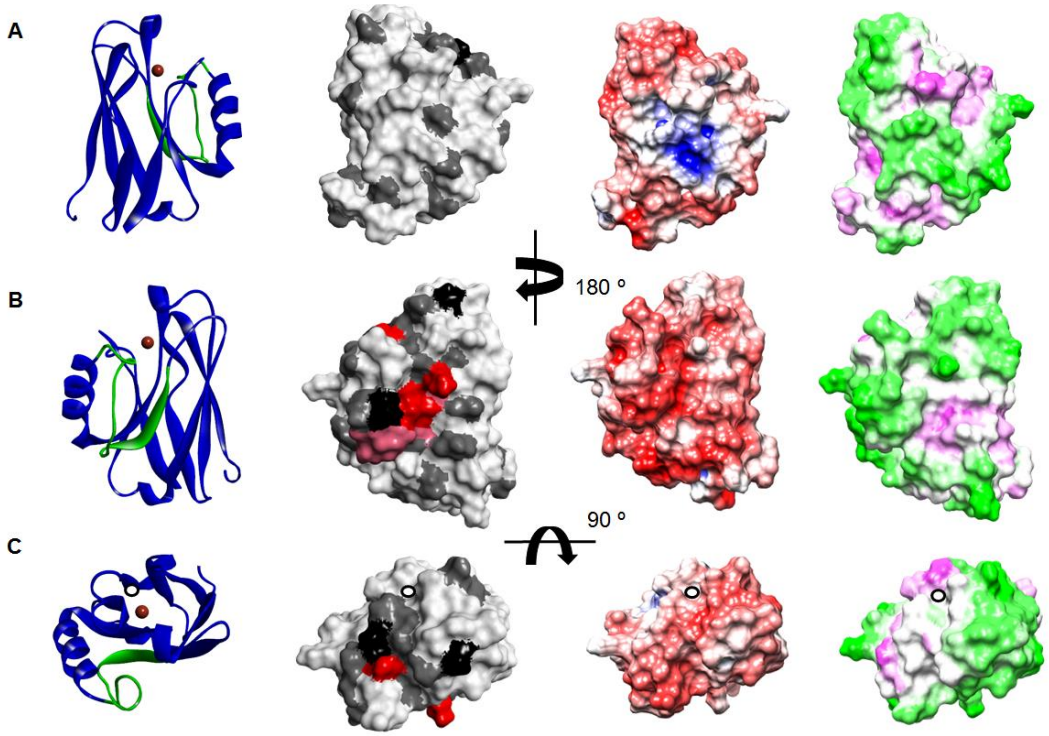

Figure 4.16 – Electrostatic and hydrophobic surface of LAz represented from a: (A) "back", (B) "front" and (C) "top view". From left to right: the ribbon structural representation of the proteins, the NMR chemical shift mapping, electrostatic surface and hydrophobic surface. The electrostatic surface potential is represented from -5 to 5 KT/e (colored from negative red surface to positive blue surface). The black circle in LAz "top view"(C) indicates the exit site of the dipole moment vector by Met122, which coordinates the copper atom. The hydrophobic surface is colored from non-hydrophobic residues (green) to hydrophobic residues (mangenta). These images were prepared in Discovery Studio except the electrostatic surface, which was rendered in Chimera.

In *Ng*BCCP, the surface surrounding the E heme is also hydrophobic (Figure 4.17B) and the remaining surface is non-hydrophobic, as seen in the dimer (Figure 4.17A). This agrees with the proposal by Crowley and Carrondo that ET complexes typically have a hydrophobic surface surrounding their redox centers [304], which promotes electron transfer. This also agrees with the kinetic data and the previous conclusion that the complex formation between LAz and *Ng*BCCP has a hydrophobic nature.

Table 4.2 – Dipole moments for LAz and other type 1 copper proteins.

Organism	Protein	PDB	Redox state	Net charge[a]	Dipole moment (Debye)
Neisseria gonorrhoeae	Lipid-modified Azurin	2N0M	reduced	- 4	174
			oxidized	- 3	217
Pseudomonas aeruginosa	Azurin	4AZU	reduced	- 2	118
			oxidized	- 1	135
Achromobacter xylosoxidans	Azurin I	1RKR	reduced	0	138
			oxidized	+ 1	183
Paracoccus pantrotrophus	Pseudoazurin	3ERX	reduced	- 4	918
			oxidized	- 3	970

[a] Net charge determined for the structure with a copper atom with +1 or +2 oxidation states, respectively.

*Ng*BCCP surface is negatively charged (Figure 4.17A) therefore, the positive dipole vector faces the copper center towards *Ng*BCCP surface. This is similar to what was previously observed for both cytochrome c_{550} and pseudoazurin from *P. pantotrophus*, which have very large dipole moments with positive vectors that exit the protein surface precisely at the ET interface [139]. Similarly, LAz dipole moment might be essential for the pre-orientation of these two proteins, in order to form an "encounter complex" and productive interactions.

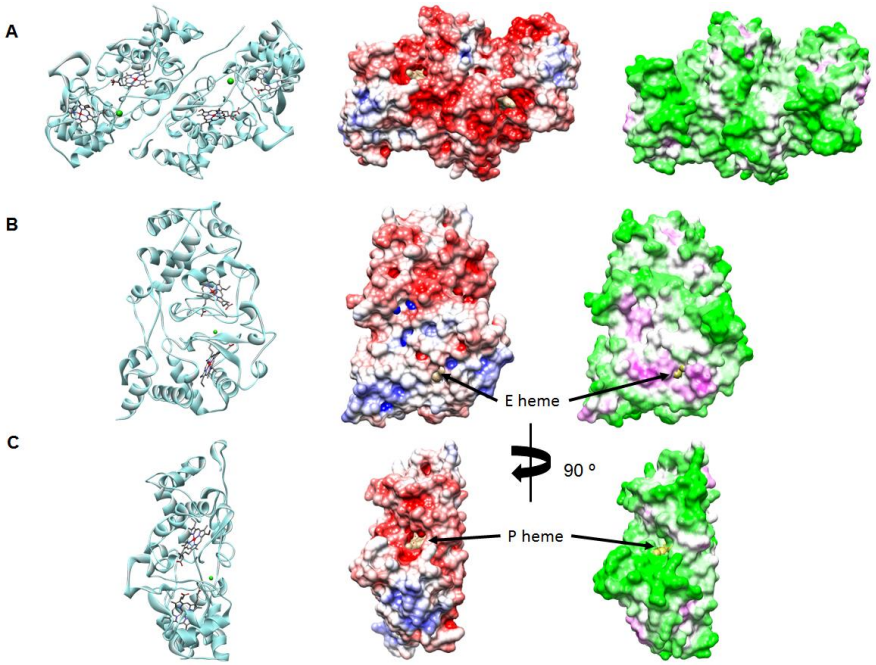

Figure 4.17 – Electrostatic and hydrophobic surface of *Ng*BCCP dimer (A) and monomer in the mixed-valence state (B, C). From left to right: the ribbon structural representation of the proteins, electrostatic surface and hydrophobic surface. The electrostatic surface potential is represented from -5 to 5 KT/e (colored from negative red surface to positive blue surface). The hydrophobic surface is colored from non-hydrophobic residues (green) to hydrophobic residues (mangenta). The open surface to the E and P hemes cavities is marked with black arrows. These images were prepared in Discovery Studio except the electrostatic surface which was rendered in Chimera.

The NMR data and protein surface analysis further supports the model in which the formation of the LAz/*Ng*BCCP complex is governed by weak hydrophobic effects, directing LAz to the E heme, with a dipole moment which might grant the necessary pre-orientation to the two proteins.

Furthermore, small chemical shifts were observed in a few resonances that indicate that this ET complex has a transient nature and since a loop region is being affected, it became difficult to correctly assign the interface region. The smallest shifts are spread around LAz surface, suggesting that this protein might be "probing" different conformations, in contrast to single-orientation complexes. A similar conclusion was taken from the NMR study of bovine myoglobin and cytochrome b_5 which showed, as well, small shifts that were associated to a "dynamic ensemble of orientations" due to constant diffusion over the surface of the other protein [303].

Nevertheless, in LAz/*Ng*BCCP native forms this might not occur because the linker region, between the lipid-modified residues that anchors the protein to the membrane and the globular domain, restricts the number of possible conformations of the complex. Therefore, the inability to diffuse freely and the hydrophobic character might be sufficient for formation of a productive ET complex.

4.2.5.2 Molecular Docking simulation of LAz/NgBCCP complex – Two strategies

The docking of LAz to *Ng*BCCP was performed using two different docking algorithms, ZDOCK [211, 305] and BiGGER [210]. ZDOCK is a rigid-body docking program that uses electrostatics, shape complementarity and statistical potential terms for scoring. BiGGER performs a "soft" dock of the two molecules and scores based on surface contact area. The final solutions are scored according to side-chains contacts and electrostatics, which are incorporated in a Global score.

Additional docking restrains can be added in both programs, for instance from NMR experiments. The residues affected in the NMR titration are unlikely to belong to a productive ET complex, therefore the docking simulations were performed without NMR restrains in order to evaluate the predicted interface region of both proteins and whether these conformations could lead to a successful ET complex.

Docking was performed using both the monomer and dimer of *Ng*BCCP in the mixed-valence state as target and the first NMR model of LAz (PDB ID: 2N0M) was used as probe. In both docking approaches, many unproductive solutions were obtained when using the monomer, most located at the dimer interface. This was probably due to the hydrophobic character of this surface. Thus, analysis was restricted to the *Ng*BCCP dimer.

***i)* ZDOCK docking algorithm**

Using ZDOCK server, the top 500 models locate LAz mainly around *Ng*BCCP E domain and a few solutions around the dimer interface. The top 100 solutions are presented in Figure 4.18A. The distance between the copper and the iron from E heme in both monomers was monitored. In 71 of

the top 100 models, this distance was smaller than 20 Å (maximum distance that enables electron transfer [245]).

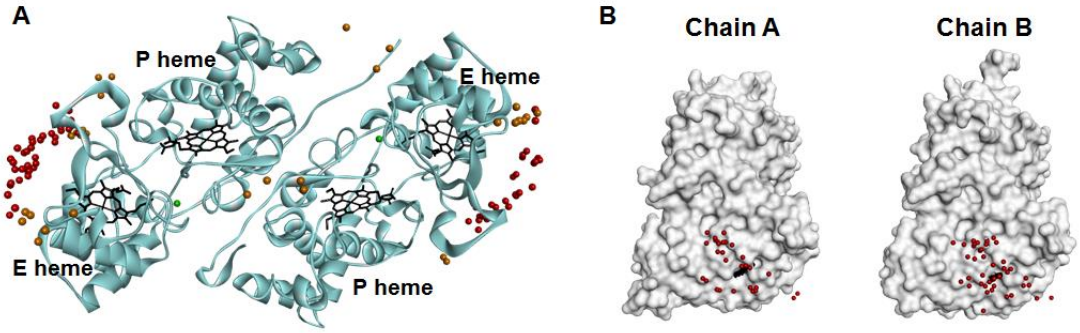

Figure 4.18 – Docking of LAz in *Ng*BCCP dimer using ZDOCK algorithm. (A) The top 100 solutions are represented by LAz's copper atom position (orange/red spheres). The copper atoms within a distance of 20 Å from the E heme iron center are in red. (B) It is presented the distribution of these solutions in each monomer (chain A and B).

The five models with highest score were included in this group and are presented in Figure 4.19 and the statistics for the protein-protein interface are listed in Table 4.3, which will be further discussed.

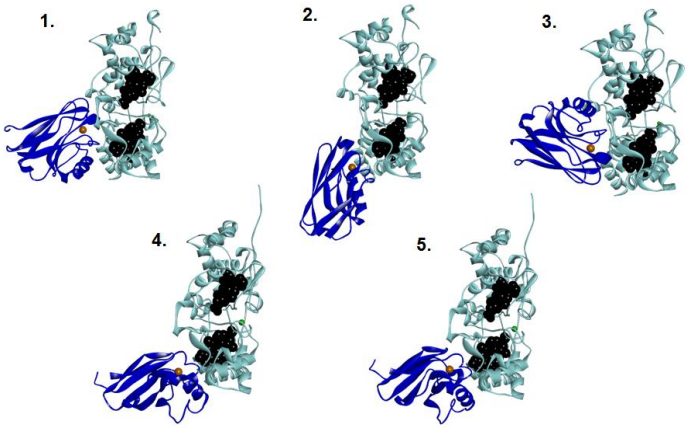

Figure 4.19 – The five docking solutions with highest score obtained by ZDOCK. Only the monomer is represented and the hemes and copper atom are represented as large black and orange spheres, respectively.

ii) BiGGER docking algorithm

In the second docking approach the BiGGER docking algorithm was used. A soft-docking was performed and 5000 models were selected from all the possible configurations generated by rotating LAz around the surface of *Ng*BCCP. The 5000 models were analyzed according to the global rank or individual ranks. The top 500 solutions for global score (Figure 4.20A) are distributed around the dimer interface and some are located around the E domain or between E and P domains, similarly to the top 500 solutions given by ZDOCK.

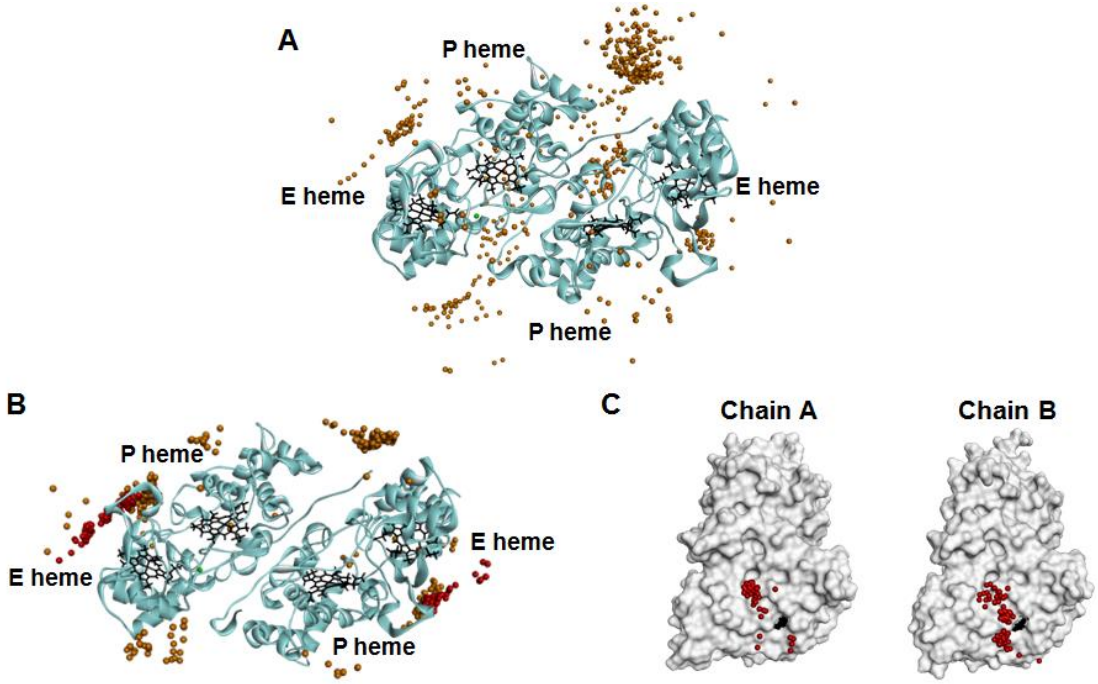

Figure 4.20 – Docking of LAz in *Ng*BCCP dimer using BiGGER algorithm. The top 500 solutions according to (A) global and (B) hydrophobic scores are represented by LAz's copper atom position (orange/red spheres). In (B) the copper atoms within a distance of 20 Å from the E heme iron center (148 solutions) are in red. (C) It is presented the distribution of these top 148 solutions surrounding each monomer (chain A and B).

Looking separately at the electrostatic and hydrophobic scores, the best solutions for the first score locate LAz around the dimer interface while the top 500 solutions for the second score more than half (311) locate LAz near the E heme (Figure 4.20B).

As mentioned, this interaction has a hydrophobic character and in fact, the hydrophobic score seems to have selected some of the most plausible candidates. An additional score was implemented according to the distance between the cofactors (from the copper atom to the iron in the E heme of both monomers). From the top 500 solutions, 148 are within 20 Å distance and can be seen marked in red (red spheres in Figure 4.20B,C).

The monomers surface is not completely symmetrical and due to the 15 º rotation and translation search around the dimer, most of these solutions are near E heme from chain B. From these top hydrophobic score solutions, the ones with the highest global score were clustered into six groups with slightly different conformations. Figure 4.21 shows the models with highest global score of each cluster. Models 1, 2, 3 and 5 are similar, with the alpha helix towards the P domain, while in models 4 and 6, the alpha helix is in the opposite side.

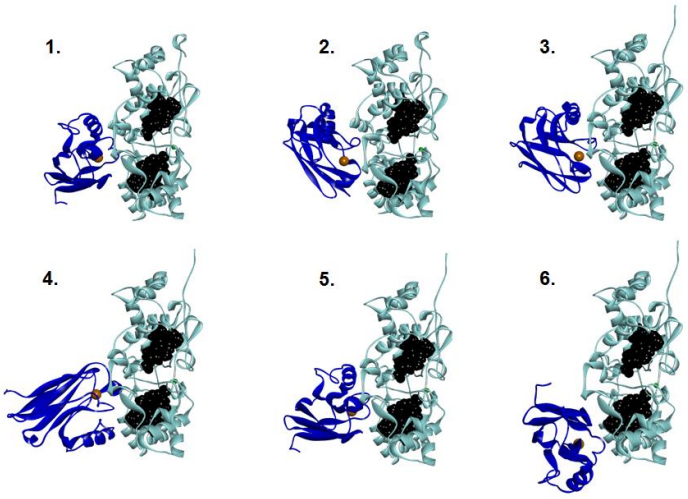

Figure 4.21 – The six docking solutions using BiGGER algorithm, representing clusters of high global and hydrophobic scores. The hemes and copper atom are represented as large black and orange spheres, respectively.

iii) Docking solutions and protein-protein interface analysis

Overall both docking strategies gave similar results and have distinct advantages. ZDOCK rigid-body docking found good candidates in the top models without using any restrain, probably because upon binding there is no change in conformation. BiGGER soft-dock was used as opposed to a hard-dock, to account for possible changes in side-chains upon binding but this can also generate many unproductive conformations. One advantage of BiGGER is that it allows to look separately at each score and to validate the docking solutions according to previous information on the system, such as the hydrophobic character.

Geometrical and physicochemical properties of the protein-protein interface were determined for each model and are presented in Table 4.3. Transient protein-protein interfaces are characterized by small interface contact areas (change in accessible surface area, ΔASA; <1500 Å^2) [306, 307], small conformational changes upon binding (NMR data supports this) which translates in a higher gap volume index (determined as a measure of complementarity), helix and turns as secondary structure features at the interface [285], hydrogen bonds and salt bridges [307, 308].

The interface contact area of all the models agrees with a highly transient complex (822-1040 Å^2) and the gap volume index is ~ 3 Å, which is consistent with other docking studies of transient protein-protein complexes [307-309]. An exception was found for BiGGER model 2, which shows a larger gap volume index (4.8 Å) and also has the highest Fe-Cu distance, which indicates a lower complementarity between LAz and *Ng*BCCP. A negative solvation free energy gain (Δ^iG) upon formation of the interface indicates that the interface is hydrophobic, as previously proposed. This is further supported by the proportion of apolar residues in the interface (~ 60%). This is less hydrophobic than what is observed for instance in the N_2OR/cytochrome c_{552} redox pair, which showed a higher percentage of apolar residues (80%) [309], and therefore a stronger hydrophobic effect.

Table 4.3 – Geometrical and physicochemical characteristics of the top five and six models for ZDOCK and BiGGER docking algorithms, respectively.

ZDOCK

Model	Score	Fe-Cu distance (Å)	ΔASA (Å^2)	Gap volume index (Å)	Δ^iG[a] (kcal/mol)	Apolar residues (%)	H-bonds /Salt Bridge
1	1111.891	17.3	945.2	2.7	-8.8	62.0	13/1
2	1040.71	15.9	863.7	2.5	-7.3	61.0	6/1
3	1032.133	16.7	1040.8	2.9	-8.6	64.0	4/1
4	987.716	15.3	783.9	2.9	-10.5	64.0	7/0
5	967.957	14.9	804.8	3.1	-11.3	60.0	4/0

BiGGER

Model	Global Score	Hydro. Score[b]	Fe-Cu distance (Å)	ΔASA (Å^2)	Gap volume index (Å)	Δ^iG[a] (kcal/mol)	Apolar residues (%)	H-bonds /Salt Bridges
1	4.23	-4.88	18.3	994.8	3.0	-7.3	58.0	4/1
2	4.48	-5.07	19.7	863.2	4.8	-5.0	59.0	4/2
3	5.22	-6.96	19.6	924.3	3.7	-7.1	61.0	8/0
4	5.79	-4.82	18.3	826.8	3.1	-7.7	61.0	9/0
5	2.72	-7.14	17.6	877.3	3.4	-7.6	60.0	5/2
6	2.2	-6.01	19.0	822.5	3.3	-4.5	56.0	7/0

[a] Δ^iG - Solvation energy gain; [b] Hydrophobic score

Although the models show small differences, the interface surface regions are common. The interface involves small helices and loop sections surrounding the copper center, where it was predicted a number of possible hydrogen bonds and salt-bridge interactions for each model that could stabilize this complex (few interactions suggest weak binding [304]). However, these predictions do not consider packing of the side-chains upon binding because these models use the conformation of the side-chains in the structures initially provided for the molecular docking simulations.

Nevertheless, when comparing the list of residues proposed for those interactions with the list of NMR chemical shifts many are in common, such as: Asn13, Asn15, Ala15, Val67, Gly68, Tyr74, Gly117 and His118. The most striking residue in this list is the Tyr74, which belongs to the group of residues with the largest chemical shifts), and also His118 that coordinates the copper atom, both located at the hydrophobic patch surrounding the copper center (Figure 4.22A).

An average map of interface residues using all eleven best docking solutions was made to compare with the NMR interface map (Figure 4.22B). In the NMR surface map, the proposed interface region, comprises a group of residues that suffered small chemical shifts surrounding the copper center, centered at Tyr74 (in red) and Pro116 (not observed in the HSQC spectra and colored in black).

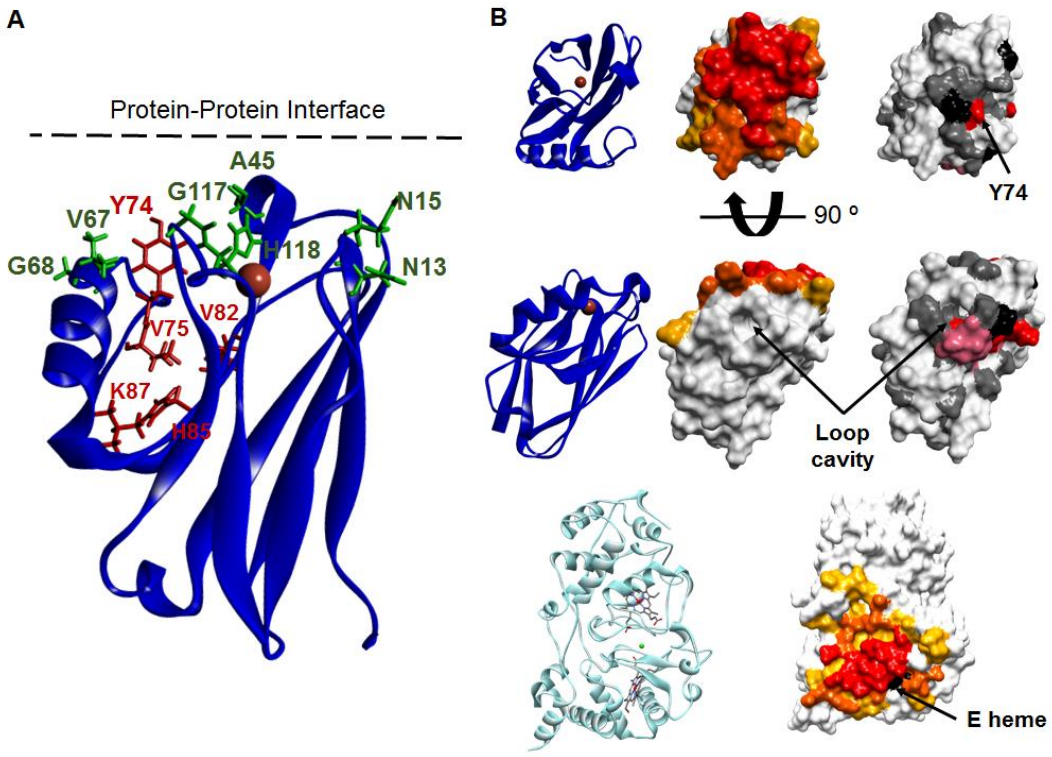

Figure 4.22 – Protein-protein interface surface in the docking models and comparison to the NMR data. (A) Several residues slightly shifted in the NMR spectrum (in green) are located at the proposed protein-protein interface and might be involved in hydrogen bonds across the interface. The residues with larger chemical shifts are located in the loop region (in red) and one, Tyr74, is also at the interface. (B) The protein-protein interface surface of LAz and *Ng*BCCP was colored according to the frequency of the surface residue in the top eleven models previously described (>75% models, red; 50 - 75% models, orange; 25 - 50% models, yellow). Comparison with the NMR surface map shows that the "top side" of LAz matching the docking surface, is affected with Tyr74 close to its center, while the loop region is away from the interface surface.

These residues could be part of the protein-protein interface region in LAz, which is dynamic as observed by the small chemical shifts. Furthermore, Tyr74 OH group is exposed at the surface and could be involved in hydrogen bonding upon binding. A closer look at LAz solution structure shows that changes in this Tyr74 might cause a series of indirect changes in the loop region, observed in the NMR titration, due to a network of hydrogen bonds and hydrophobic interactions between those residues (Val75, Val82, His85, Lys87), that would be perturbed, such as Val75-His85 π-alkyl interaction and His85-Asp79 H-bond.

The top models of each docking method were analyzed using PATHWAYS in order to address a potential electron transfer pathways between the two proteins. The one that predicted the highest ET rate was model 4 from ZDOCK, probably due to the shortest Fe-Cu distance.

Figure 4.23 shows the electron transfer pathway from the copper site to E heme and then to P heme through the conserved Trp98. The best path in all models analyzed had in common two residues from LAz, His118 and Gly117, which were in the group of residues with the smallest shifts in the NMR experiment.

In model 4 (ZDOCK), ET occurs between Gly117 and the E heme, to its iron atom. In other type 1 copper proteins, the equivalent residue of His118 (in *P. pantotrophus* pseudoazurin, His81 [184] and in *P. aeruginosa* azurin, His117 [310]) has also been proposed as the exit point of electrons. Therefore, although there are slightly small differences in orientation, all the best docking solutions position these two residues in close proximity to the E heme.

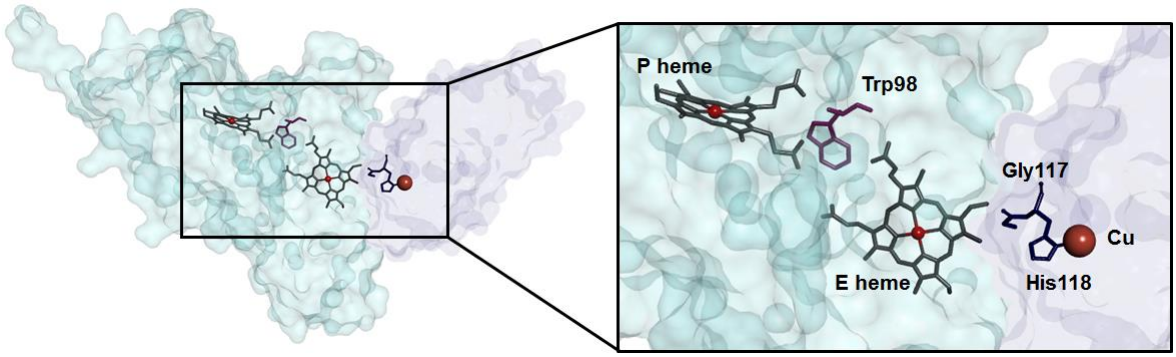

Figure 4.23 – The electron transfer pathway, based on the docking models, starts in the copper atom, passes through His118 and then Gly117 in LAz (purple), directly to the E heme in *Ng*BCCP (blue).

Thus, it is proposed that these models represent the probable conformation of the LAz/*Ng*BCCP electron transfer complex, though in reality there are probably several dynamic conformations. Additional studies to optimize the NMR experiments could be pursued in order to unambiguously identify the LAz surface that contacts with *Ng*BCCP upon formation of the complex. Another informative technique could be paramagnetic relaxation enhancement NMR spectroscopy as this would allow to detect intermediate conformations, as performed with the yeast CCP/cytochrome *c* complex [311, 312].

4.3 Conclusions

LAz and *Ng*BCCP are two lipid associated proteins from the pathogenic bacteria *N. gonorrhoeae*, attached to the outer membrane with the globular domain located in the periplasm. In order to characterize LAz, a soluble recombinant protein consisting of the globular domain was heterougously produced and purified, in a similar strategy as *Ng*BCCP. LAz is a monomer in solution, it has the spectroscopic properties of a type 1 copper protein, with one copper atom per protein, and it is the physiological electron donor of *Ng*BCCP.

The LAz/*Ng*BCCP pair showed high catalytic activity and a lower K_M value than $ABTS^{2-}$/*Ng*BCCP pair. Optimum activity was achieved at higher temperatures (37 ºC) and at pH 6.0 to 7.5, conditions close to the physiological ones for *N. gonorrhoeae*. Steady-state kinetics at various ionic strengths showed that this interaction has a hydrophobic character. Therefore, not only *Ng*BCCP but the pair is adapted to the host environment.

The low affinity and the transient nature of electron transfer complexes limits, to some extent, the approaches that can be used to study them. Calorimetric assays suggested that this complex was transient with a K_D in the micromolar range. NMR data further supported this as the chemical shifts observed upon binding were quite small. Analysis became more challenging as a loop region in LAz structure was the most affected in this interaction, as this region is not near the copper center, which is essential for successful ET between the two proteins.

The combined NMR, docking and surface analysis suggested that the hydrophobic patch surrounding the copper center is most likely the interface region and that a key tyrosine residue at this interface (Tyr74) can be responsible for the loop changes, an indirect effect due to an intricate network of interactions between the loop residues. This interaction positions another key residue from LAz in close proximity to E heme, the His118, essential for electron transfer.

The data therefore supports the three important steps in the complex formation, common to many other ET complexes: i) LAz pre-orientation due to its positive dipole vector, with exit point at Met122 that directs the copper center towards *Ng*BCCP surface; ii) a binding step, which includes a “probing” process or lateral mobility around the protein, ruled by water-mediated polar interactions and weak hydrophobic effects; iii) and finally quick dissociation is possible also due to the weak hydrophobic nature, which allows the high turnover observed in the steady-state kinetics.

The affinity constant and thermodynamic properties of this transient complex remain to be determined.

Chapter 5

Biochemical characterization of YhjA a trihemic enzyme with quinol peroxidase activity *in vitro* from *Escherichia coli*

The work presented in this chapter will be published in:

"YhjA - an *Escherichia coli* trihemic enzyme with quinol peroxidase activity", by Cláudia S. Nóbrega, Bart Devreese and Sofia R. Pauleta, 2017. Manuscript in preparation.

Contributions to Chapter 5:

Bart Devreese performed all the mass spectrometry experiments. Sofia R. Pauleta acquired and analyzed the ^{1}H NMR spectra of NT domain. All the other experimental studies were performed by Cláudia S. Nóbrega.

5 Biochemical characterization of YhjA, a trihemic enzyme with quinol peroxidase activity *in vitro* from *Escherichia coli*

5.1 Introduction

Microorganisms have developed several strategies to detoxify ROS, such as hydrogen peroxide, which enable them to survive in oxygenated environments. Peroxidases and catalases are specialized enzymes that are required by any cell or organism to maintain the concentration of hydrogen peroxides below toxic levels. The enzymatic reaction of catalase is the disproportionation of hydrogen peroxide, while peroxidases catalyze the reduction of H_2O_2 by using different reduced compounds (organic molecules or small proteins, as electron donors). These later enzymes are considered the primary scavengers of H_2O_2 in the cell, which is usually present in the low micromolar range. In *E. coli*, the most efficient peroxidase is the alkyl hydroperoxide reductase (Ahp [88]), and at high concentrations of hydrogen peroxide catalases, KatG [34] and KatE [84], play an important additional role. The contribution of these three enzymes for rapid scavenging of H_2O_2 was in fact confirmed in a triple mutant that showed no scavenging activity [88]. All of these enzymes are located in the cytoplasm and have different affinities to hydrogen peroxide, typically peroxidases, such as Ahp have a K_M value in the micromolar range (*E. coli* Ahp becomes saturated at < 20 µM, K_M value not reported [88]), while KatG and KatE show a much higher K_M of 5.9 mM [34] and 20 mM [313], respectively. Although, in *E. coli* these three enzymes are the most relevant *in vivo*, there are other enzymes with known peroxidase activity that add complexity to the H_2O_2 scavenging system. These enzymes are the thiol peroxidase (Tpx [314]), bacterioferritin comigratory protein (Bcp [90]) and glutathione peroxidase homologue (BtuE [101]), with YhjA being included in this group of enzymes. YhjA is annotated as a putative cytochrome *c* peroxidase whose peroxidase activity has not yet been clearly demonstrated.

Most of the studies on YhjA have been at the genomic level, in which it was shown that the promoter region of *yhjA* has a FNR and a OxyR binding sites [123], suggesting that its expression would be higher under anaerobic conditions [315] and respond to oxidative and/or nitrosative stress [57, 316]. In fact, it was demonstrated that *yhjA* promoter shows higher *lacZ* expression under oxygen limited conditions [123]. This lead apparently to a controversy since YhjA would only be present in limited oxygen environments and oxidative stress derives from oxygen species. However, this is not a unique trait of YhjA. In dihemic bacterial cytochrome *c* peroxidases (BCCP), such as *N. gonorrhoeae* BCCP, the gene expression is also regulated by FNR [228], activated at low oxygen tensions, when the efficiency of the electron transfer pathway for oxidative phosphorylation is low, and thus leakage of electrons to the quinol pool leads to the formation of reactive oxygen species.

The analysis of YhjA primary sequence indicates the presence of three heme-binding motifs (-CXXCH-), and its C-terminal domain, containing two heme domains, is homologous to the well

characterized classical dihemic bacterial peroxidases, such as the ones found in *P. aeruginosa* [317] and *P. pantotrophus* [137], as well as in many other bacterial species [22] (Chapter 1).

Trihemic BCCPs have been poorly studied, with homologues only described in *A. actinomycetemcomitans* [149-151], *Z. mobilis* [153] and *Leptospirillum spp.* [318], although the homologous gene is found in known pathogenic bacteria [22]. In an iron-oxidizing acidophilic bacterium, such as *Leptospirillum* spp., the trihemic BCCP gene (*yhjA*) is part of a "*ccp* operon" constituted by *yhjA*, *ahpC* and *perR*, all related to the oxidative stress defense mechanism. According to the authors, this operon is unique to *Leptospirillum* spp. and the encoded BCCP (named CcP) is essential to defend the microorganisms against exogenous H_2O_2 sources and in the early steps of colonization and biofilm formation on metal sulfides [318]. In the case of *Z. mobilis* (PerC) and *A. actinomycetemcomitans* (QPO) trihemic BCCPs a quinol peroxidase activity has been assigned. Furthermore, in *A. actinomycetemcomitans* a null QPO mutant showed higher sensitivity towards H_2O_2 and a lower growth rate under aerobic conditions [150]. In the case of *Z. mobilis*, it was initially suggested that PerC was involved in an aerobic respiratory pathway that seemed incomplete as it lacked a terminal oxidase [319], but later it was recognized its role in the membranes as a quinol peroxidase [153].

The pool of quinones is formed by diffusible quinone molecules which are confined to the lipid phase of the inner membrane. This pool is involved in a series of electron transfer reactions with membrane associated enzymes, such as it is proposed for the quinol peroxidases.

Quinones are redox active compounds that can release or uptake two electrons and two protons forming an intermediate semiquinone species. The balance of these quinones affects not only the associated redox reactions but also membrane fluidity. This depends greatly on the type of membranes, metabolic phase and the organism [320].

Ubiquinone, menaquinone and demethylmenaquinone are three types of quinones that can be found in *E. coli* membranes (Figure 5.1), in different proportions, dependent on the electron acceptors (oxygen, nitrate, fumarate or DMSO) and on the carbon source (addition of glucose for instance) [321].

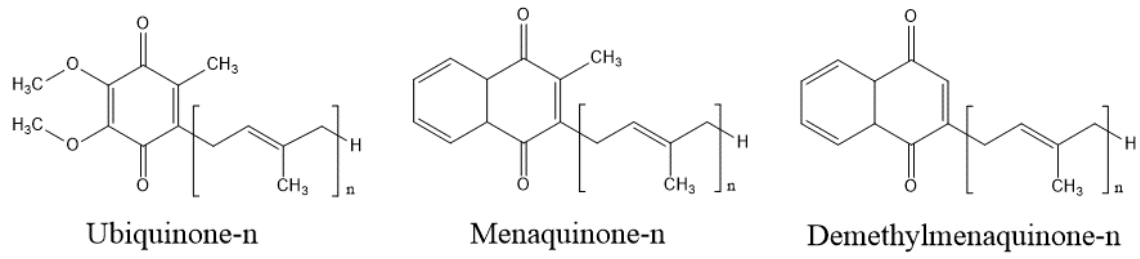

Figure 5.1 – Molecular structures of quinones that can be found in *E. coli* cell membranes. Ubiquinone belongs to the benzoquinone family and it is the major quinone under aerobic conditions. Menaquinone and demethylmenaquinone belong to the naphtoquinone family and are mainly present in the membranes under anaerobic conditions.

Under anaerobic conditions the pool of quinones in *E. coli* is mainly constituted by naphthoquinones: demethylmenaquinone and menaquinone [321] (DMQ/ MQH_2 $E^{o\prime}$ = +40 mV and MQ/MQH_2; $E^{o\prime}$ = −74 mV, respectively [322]). Demethylmenaquinone levels are the highest (approximately 70 % of the pool of quinones) under anaerobic conditions with nitrate as acceptor and in this condition no ubiquinone (UQ/UQH_2; $E^{o\prime}$ = +100 mV [322]) was identified. Menaquinone is produced under anaerobic conditions and its levels are higher (75 %) with fumarate or DMSO as electron acceptors. Ubiquinone is most abundant in *E. coli* membranes under aerobic conditions accounting for more than 60 % of the quinones, using glucose as carbon source. Under anaerobic conditions using fumarate or DMSO as electron donor, ubiquinone constitutes only 10% of the quinone content [321]. These values are presented as an example of the changes that occur in the pool of quinones in response to the electron acceptor in the medium.

The high sequence homology between YhjA from *E. coli* and homologous enzymes from *Salmonella typhimurium* and *Yersinia pestis* [22] points to the importance in understanding the role of this group of enzymes, as well as its enzymatic mechanism, as they can play important roles as virulence trait or as a therapeutic target.

In this work, it was addressed the *yhjA* gene expression dependency on growth stage, oxygen and respiratory pathway, as well as the biochemical characterization of the recombinant YhjA trihemic enzyme. The YhjA N-terminal domain, a new domain only found in trihemic BCCPs, was characterized for the first time and the nature of its distal axial ligand elucidated. Steady-state kinetics was performed in order to identify the potential physiological electron donor and kinetic parameters. These results aim to understand YhjA catalytic mechanism and its contribution to *E. coli* outstanding resilience towards oxidative stress.

5.2 Results and Discussion

5.2.1 Heterologous production and characterization of recombinant YhjA and subdomains

Analysis of the primary sequence of YhjA (Figure 5.2) indicates that the distinct features found in other dihemic BCCPs are conserved: calcium binding residues, E heme methionine axial ligand, the two heme binding motives (CXXCH) in the C-terminal (CT) domain, the tryptophan that mediates electron transfer between E and P hemes and the glutamine and glutamate residues proposed to be involved in the catalytic cycle of classical BCCPs. The main differences reside in the absence of the P heme axial ligand and the heme located in the additional N-terminal (NT) domain. Relative to the distal P heme axial ligand, instead of a histidine residue (His87 and His59 in *P. pantotrophus* and *N. europaea*, respectively) YhjA has Val227. In none of the trihemic BCCPs there is a substitute histidine residue for this axial ligand, suggesting that the active site in this class of enzymes is always available for substrate binding, as previously observed in the dihemic *N. europeae* BCCP [167]. In the case of the NT heme, there are two possible distal axial ligands, Met125 or His134 (according to *E. coli* numbering), both conserved in all trihemic BCCPs. The identity of the distal axial ligand will be further discussed and identified in the following sections (Section 5.2.3, Figure 5.5).

Another unique feature of the trihemic enzymes is the fact that these enzymes are membrane bound (typically BCCPs are soluble enzymes but there are exceptions as explained in Chapter 1, Section 1.3.3). In the case of *E. coli* BCCP, one transmembrane helix was predicted by TMHMM 2.0 [189] that includes residues Ile7 to Asp29. Single transmembrane helices are often signal peptides but analysis of the N-terminus sequence does not predict a signal peptidase cutting site. All these residues in the N-terminal domain until Ala41, are absent in the recombinant YhjA so that a soluble version of the protein can be produced and purified.

Analysis of the N-terminal primary sequence in *A. actinomycetemcomitans* trihemic peroxidase also predicted a transmembrane helix (comprising residues 4 to 26) and in fact, the N-terminus of the native protein was sequenced, showing a correspondence with the first residues of the primary sequence, which excludes the possibility of a signal peptide [149].

In order to address YhjA peroxidase activity *in vitro*, as well as to characterize the different domains of this enzyme, three constructs were prepared with a C-terminal HisTag, YhjA_6His, NT domain and CT domain, and one construct of YhjA with a N-terminal StrepII-tag.

YhjA_6His (produced without the transmembrane domain, as a soluble form) was purified with a yield of 1.3 mg of pure protein per liter of medium and it has an apparent molecular mass of a 45 ± 2 kDa monomer in solution (Figure A1.1 in Annex 1) with 3.1 ± 0.3 hemes per protein, determined by the pyridine hemochrome assay.

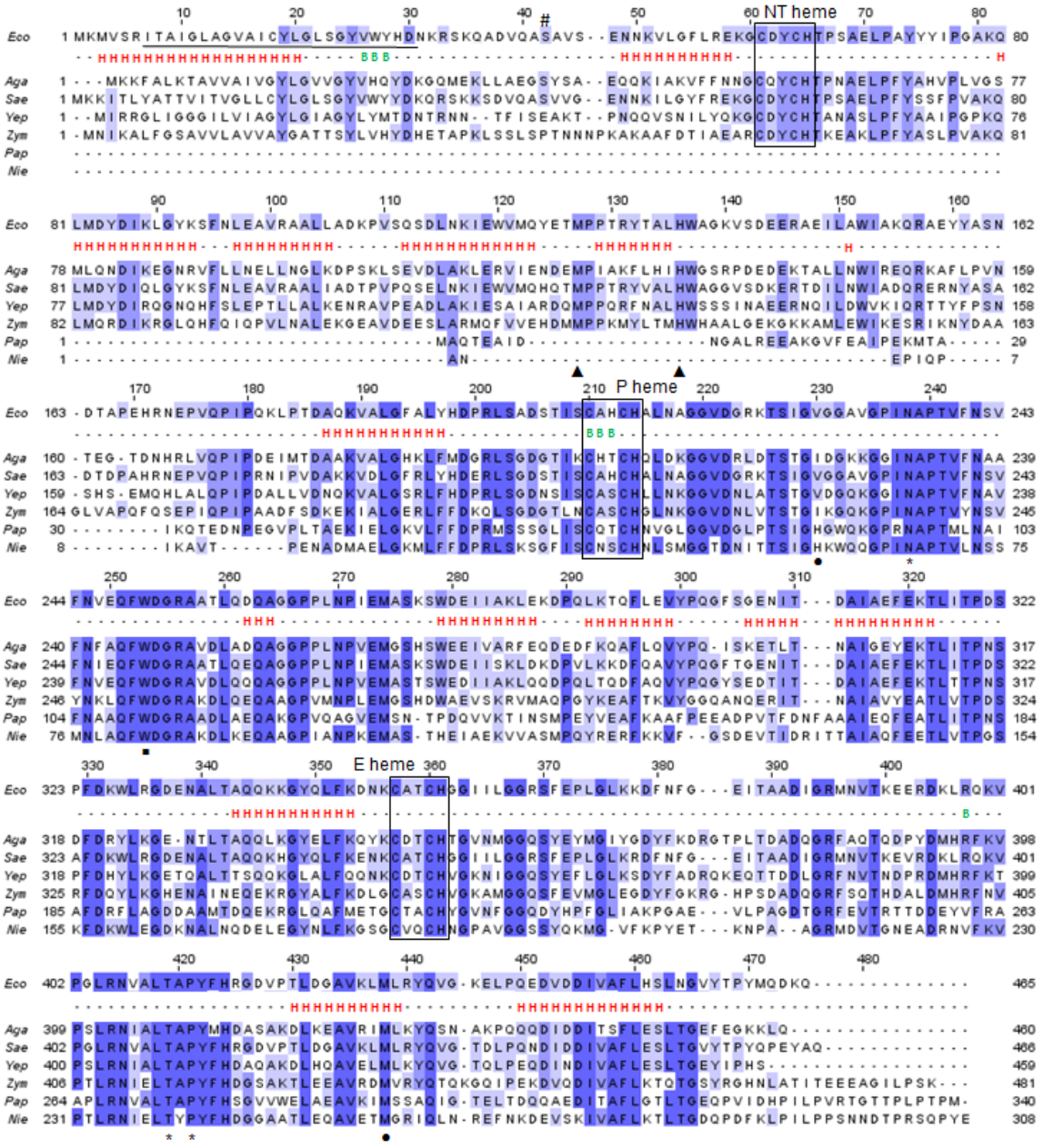

Figure 5.2 – Multiple primary sequence alignment of trihemic and dihemic bacterial cytochrome *c* peroxidases and secondary structure consensus prediction of YhjA using Jpred 4 (H - helix, B - *β*-sheet). *E. coli* (Eco; GI: 586681), *A. actinomycetemcomitans* (Aga; GI: 122703614), *S. enterica* (Sae; GI: 380465268), *Y. pestis* (Yep; GI: 913031110), *Z. mobilis* (Zym; GI: 395396769), *P. pantotrophus* (Pap; GI: 916812477) and *N. europaea* (Nie; GI: 30180613). The coloring is in accordance with percentage of identity at each position, from darker color box (100 % identity) to white box (≤ 20 % identity). The sequences are sorted by pairwise identity to YhjA from *E. coli*. The underlined residues are the transmembrane helix. Some residues are marked as: (#) the first residue in the soluble recombinant YhjA, (●) axial ligands of E and P heme (the latest a histidine only present in dihemic BCCP), (*) calcium binding residues, (■) tryptophan residue between heme domains and (▲) the proposed axial ligands for N heme.

Mass spectrometry further confirmed that there were three covalently bound hemes (50081.4 ± 5 Da). However, a preliminary kinetic characterization soon showed that its catalytic activity was poor as it

was necessary millimolar concentrations of H_2O_2 to observe any activity (using $ABTS^{2-}$ as a synthetic electron donor) and this enzyme did not saturate with substrate (concentrations up to 26 mM H_2O_2 were tested). We hypothesized whether the C-terminal His-tag could be interfering with the protein catalytic site since histidines can interact with hemes as axial ligands.

In order to rule out this hypothesis, a new construct was produced with a different tag, a N-terminal StrepII-tag that could be removed by a TEV protease, which proved to be a better approach than the previous one. This new recombinant YhjA_Strep (from now on, just YhjA) was fully characterized and it will be described in the following sections. For most of the assays the tag was not removed except for comparison of catalytic activity (Section 5.2.6) and determination of apparent molecular mass.

YhjA is a 51 kDa periplasmic soluble protein, with a theoretical pI of 5.6, which was purified with a yield of 0.7 mg of pure protein per liter of growth medium and a heme/protein ratio of 3.0 ± 0.1. The molecular mass given by ESI-MS was 51070 ± 10 Da, which corresponded to the mass of the polypeptide chain of YhjA with 3 *c*-type hemes attached (50956 Da) and without the first amino acid residue, the N-terminal methionine, probably due to signal peptide processing, and the addition of one HEPES molecule from the buffer. The heme/protein ratio, as well as the molecular mass determined by mass spectrometry are in agreement with YhjA having three covalently bound hemes.

NT domain (N-terminal domain) was purified with an average yield of 1 mg of pure protein per liter and a 0.7 ± 0.1 heme/protein ratio. The molecular mass of 14769.5 ± 5 Da agrees with one covalently bound heme to the polypeptide chain, and shows that NT domain is approximately one third of YhjA.

The CT domain, containing the two C-terminal *c*-type heme binding domains and comprising two thirds of YhjA polypeptide chain, showed to be a challenge to be properly produced and purified. CT domain production showed a smaller yield of approximately 0.3 mg of pure protein per liter of growth medium, and the molecular mass by mass spectrometry was 33731.95 ± 5 Da, which corresponds to the mass of the polypeptide chain without any covalently bound heme. A low heme *c* content (0.2 ± 0.1 heme/protein) in the final protein could indicate that there is a small amount of holoprotein but essentially indicates that the CT domain is mainly produced in the apo-form. A new construct of the CT domain with a N-terminal StrepII-tag was prepared, and the production of this protein had also a small yield and it was mainly produced in the apo-form, as from the previous construct.

Overall, even though the yield for YhjA and NT domain was low, these proteins were successfully produced and purified, enabling their biochemical characterization.

5.2.2 Biochemical characterization – Solution states of YhjA and its domains

The molecular weight of the proteins in solution was determined by size-exclusion chromatography. YhjA behaves as a monomer of 44 ± 2 kDa (without tag 40 ± 2 kDa), behavior that is not affected

by the presence or absence of calcium ions (2 mM $CaCl_2$: 42 ± 2 kDa, 2 mM EGTA: 43 ± 2 kDa) or by high ionic strength (I = 550 mM; 40 ± 2 kDa) (Figure 5.3A). The CT and NT domains are also monomers in solution with 41 ± 2 kDa and 10 ± 2 kDa, respectively. The similar molecular weight for YhjA and CT domain suggests that in YhjA the domains are not linearly organized giving an apparently lower molecular weight Figure 5.4B.

Differential scanning calorimetry (DSC) was used in order to assess the solution states of YhjA, at pH 7.5. The thermogram for YhjA, shown in Figure 5.3B, comprises two overlapping endothermic transitions, with *Tm* values of 48.1 ± 0.2 ºC and 52.09 ± 0.03 ºC and a total calorimetric enthalpy (ΔH_{cal}) of 630 ± 2 kJ.mol^{-1}, consistent with a monomeric species in solution. These two events can be interpreted as being two unfolding intermediates or the unfolding of two independent domains. The first transition corresponds to one third of the protein sample with a van't Hoff enthalpy of ΔHv_1 = 530 ± 5 kJ.mol^{-1}, while the second transition accounts for the remaining two thirds of protein sample and has a ΔHv_2 = 653 ± 5 kJ.mol^{-1}. This later transition has a *Tm* and van't Hoff enthalpy values similar to the single transition observed for *P. pantotrophus* BCCP [163] (52.1ºC and ΔHv=777 kJ.mol^{-1}) and *Ng*BCCP in Chapter 3 (46.9 ºC and ΔHv = 752.0 kJ.mol^{-1}), at pH 7.5 in the presence of excess calcium ions.

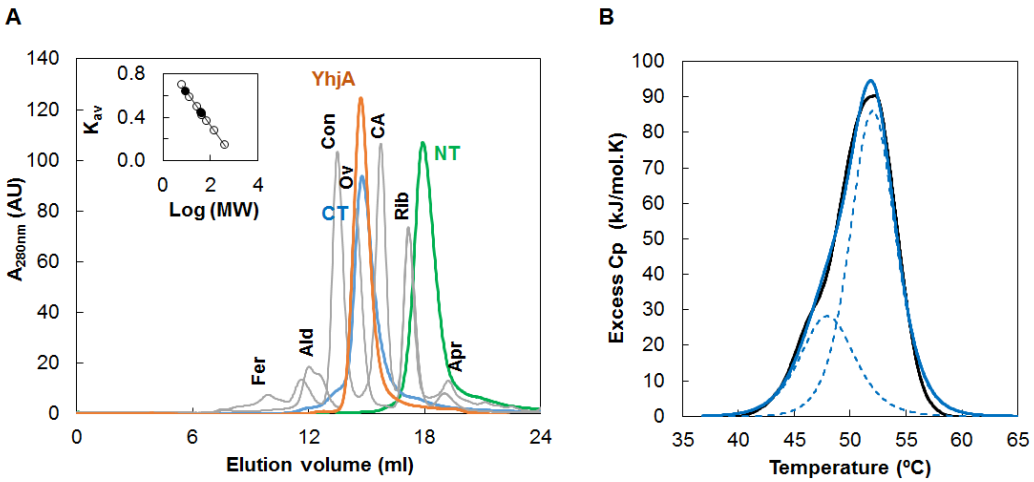

Figure 5.3 – (A) Elution profile of the size-exclusion chromatography of YhjA (orange line), CT domain (blue line) and NT domain (green line). In grey are the elution profiles of the standard proteins used to estimate the apparent molecular weight of the proteins: Ferritin (Fer, 440 kDa), Aldolase (Ald, 158 kDa), Conalbumin (Con, 75 kDa), Ovalbumin (Ov, 44 kDa), Carbonic Anhydrase (CA, 29 kDa), Ribonuclease A (Rib, 13.7 kDa) and Aprotinin (Apr, 6.5 kDa). (B) Differential scanning calorimetry of YhjA at pH 7.5 in the presence of calcium ions (black line). The thermograms were baseline corrected and normalized for protein concentration. The simulation fitting the data is represented by a blue solid line which is the sum of the two independent models (blue dashed-lines).

Considering the domain organization of YhjA the first event can correspond to the unfolding of the NT domain, as it is about one third of the protein (15 kDa out of total 51 kDa). The second transition can be assigned to the other two thirds of the protein, the CT domain that is homologous to the

classical BCCPs (Figure 5.4A). These separate transitions can reflect different hydrophobicity and flexibility of the NT domain in comparison to the other two domains which act as a single entity. The independence of domain unfolding in a multi-domain protein has also been observed in the thermogram of streptokinase, a three domain protein [323].

In fact, prediction of YhjA secondary structure in Figure 5.2 suggests that there are no structural features (helices or sheets) between the NT and CT domains (residues 150-183), which can confer some degree of flexibility between these two main domains. Given this and the size-exclusion chromatography results it can be proposed that the three domains are not linearly organized, and that the N-terminal domain folds towards the CT domain, giving a more globular shape to the protein. Since in the classical BCCPs the N-terminus is a small helix located at the side of the E heme domain [108], it can be postulated that the NT domain is closer to this domain (Figure 5.4B).

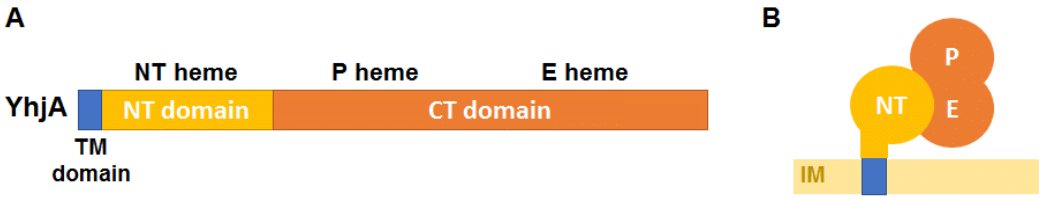

Figure 5.4 – Schematic representation of (A) YhjA domains and localization of the hemes in each domain, and (B) the proposed fold of YhjA domains when bound to the inner membrane (IM) in the periplasmatic space.

Furthermore, the classical BCCPs are either dimers or in a monomer/dimer equilibrium dependent on the presence of calcium ions and high ionic strength [129, 163]. On the contrary, YhjA behaves as a monomer and DSC data is also consistent with a monomeric solution state.

5.2.3 Spectroscopic characterization of the N-terminal domain

YhjA has three heme binding domains, the CT domain comprising two hemes, E heme and P heme, and the new NT domain with a third heme binding motif, which increases the complexity of the YhjA spectroscopic data and its analysis. Therefore, in order to study this enzyme and to be able to correctly assign the spectroscopic features of each of the 3 hemes, we have spectroscopically characterized the NT domain.

The UV-visible spectrum of the as-isolated NT domain (Figure 5.5A) has a 695 nm absorption band which has been attributed to a methionine axial ligand [38]. The ^{1}H NMR spectrum of the reduced NT domain (Figure 5.5B) also confirms the presence of a methionine ligand, with the observation of the methyl of the methionine down shifted to high field. The as-isolated NT domain EPR spectrum (Figure 5.5C) has a single low-spin signal with $g_z = 2.83$ and $g_y = 2.38$. The third component of the signal, according to the equation for low-spin hemes $g_z^2 + g_y^2 + g_x^2 = 16$ [42], should have a $g_x \approx 1.52$ but it is too weak and broad to be observed.

Therefore, we postulate that the additional N-terminal heme in YhjA is His/Met coordinated, with the axial methionine ligand being the conserved Met125. The spectroscopic data shows that the NT heme is low-spin as expected for a hexa-coordinated heme.

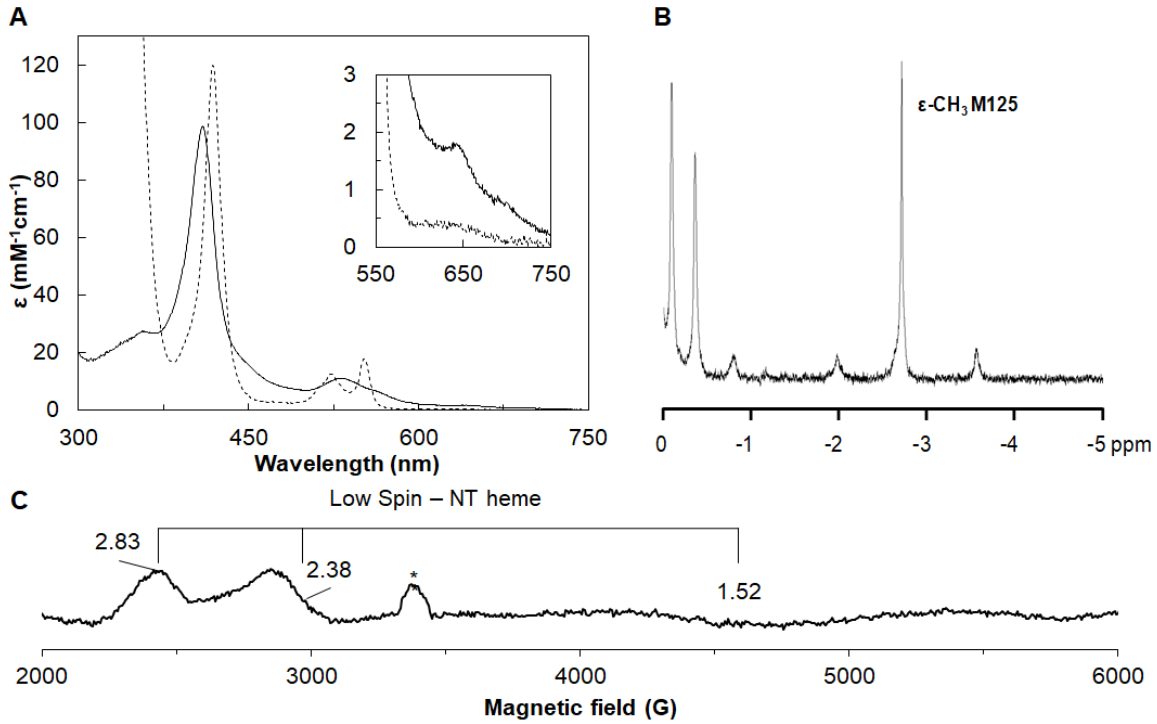

Figure 5.5 – Spectroscopic properties of NT domain. (A) UV-visible absorption spectra of NT domain in the as-isolated state (solid line) and dithionite reduced (grey line), in 10 mM HEPES, pH 7.5. The inset shows the 550-750 nm region of the visible spectra. (B) ^{1}H NMR spectrum of reduced NT domain, showing the methyl of methionine heme ligand down shifted to high field. Spectrum was acquired on a 600 MHz Avance III NMR spectrometer equipped with a cryoprobe, at 298 K in 20 mM phosphate buffer, pH 7.0. (C) X-band EPR spectrum of 0.2 mM as-isolated NT domain in 10 mM HEPES pH 7.5. The asterisk marks a paramagnetic contaminant from the cavity. All spectroscopic features agree with a methionine residue as axial ligand.

5.2.4 Spectroscopic characterization of YhjA

The as-isolated YhjA UV-visible spectrum (Figure 5.6) has the typical features of a *c*-type cytochrome absorption spectrum. The Soret band at 407 nm (extinction coefficient of 287 ± 5 $mM^{-1}.cm^{-1}$) indicates that all three hemes are oxidized, and features at 360 nm and 620 nm are characteristic of the presence of high-spin hemes.

At 695 nm, there is a weak band in the as-isolated spectrum, which also appears in the visible spectrum of the NT domain and has been attributed to a Met axial ligand [38]. Although E heme is His/Met coordinated, in the classical BCCPs this band is usually not observed, as it was shown that the Met axial ligand of E heme is weakly bound to the heme iron, resulting in a high/low-spin equilibrium at room temperature [160]. Therefore, this band is assigned to the His/Met coordinated NT heme.

Upon reduction with Asc/DAD, there is a shift of the Soret band to 419 nm and the appearance of α- and β-bands at 553 nm and 524 nm, respectively, consequence of the reduction of E and NT hemes (both His/Met coordinated and with a positive reduction potential, as it will be discussed in Section 5.2.5). In this spectrum, it is still observed a Soret band of an oxidized heme, as a shoulder at 407 nm, corresponding to the oxidized P heme. The high-spin absorption band at 620 nm decreases in intensity and is assigned to the high-spin P heme (Figure 5.6).

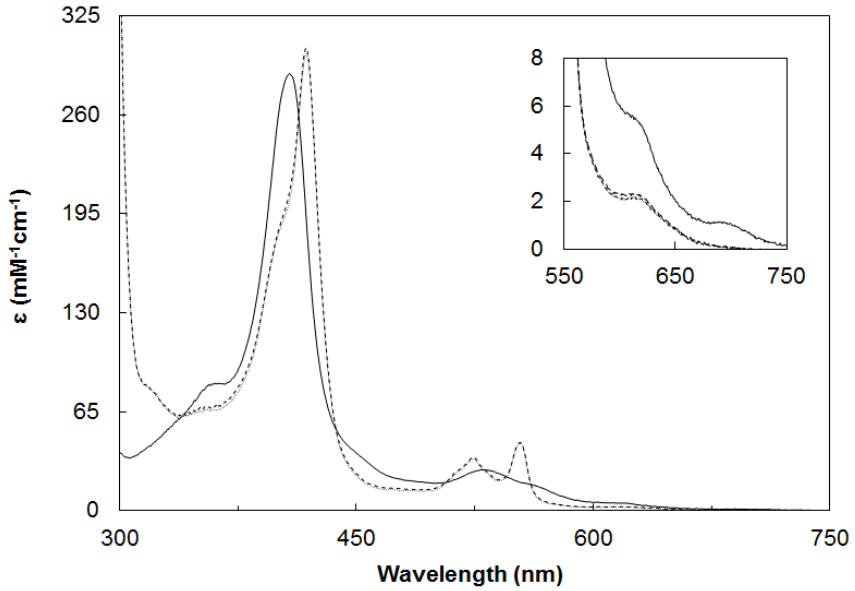

Figure 5.6 – UV-visible absorption spectra of YhjA, in 10 mM HEPES pH 7.5, as-isolated (solid line), in the mixed-valence state (dashed line) and in the mixed-valence state incubated with calcium for 10 min (dotted line). The inset shows the high-spin region of the visible spectra.

The effect of calcium ions in the visible spectrum of the mixed-valence YhjA (with E and NT hemes reduced and P heme oxidized) was studied using two approaches: (i) addition of $CaCl_2$ (Figure 5.6) and (ii) observing the changes over time by incubating the enzyme with 1 mM EGTA (Figure 5.7).

i) Upon addition of calcium ions, it was only observed a small increase in the absorption band at 620 nm, which is attributed to the high-spin of P heme;

ii) After the addition of EGTA, which specifically chelates calcium ions, there is a decrease in intensity of the absorption bands at 360 and 620 nm, which is consistent with the loss of high-spin species and formation of a low-spin species. This is explained considering that the high-spin form of P heme is calcium-dependent but in the as-isolated YhjA the calcium site is sufficiently filled for P heme to remain high-spin (this site has a high affinity to calcium). However, the nature of the ligand that forms the low-spin species in the calcium depleted enzyme remains to be determined, as trihemic BCCPs lack the conserved distal histidine heme ligand in their primary sequence.

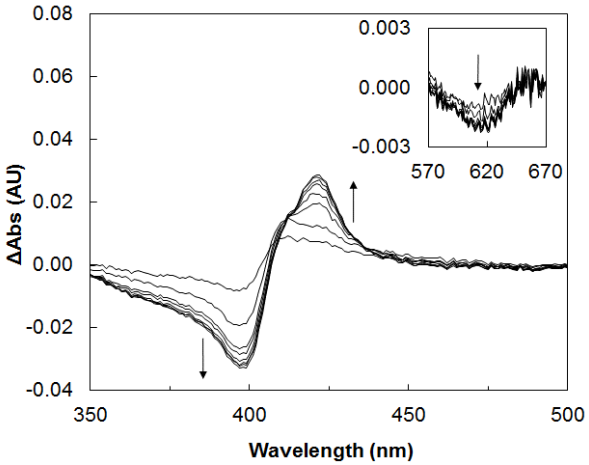

Figure 5.7 – Difference absorption spectra of YhjA in the mixed-valence state, in 10 mM HEPES pH 7.5, upon addition of 1 mM EGTA. The inset shows difference at the high-spin region of the visible spectra. Arrows indicate the direction of changes in the spectra that were acquired over time (0.5, 1.5, 2.5, 5.0, 7.5, 10 and 15 min), as calcium ions were being chelated by EGTA.

The effect of hydrogen peroxide in the spectrum of the as-isolated YhjA was also studied since the P heme is high-spin and available for binding of exogenous ligands. It was observed a shift in the maximum of the Soret absorption band from 407 to 410 nm, accompanied by a decrease in the high-spin absorption bands at 360 nm and 620 nm (Figure 5.8). Such a shift in the Soret band was also reported in a similar experiment for *P. aeruginosa* BCCP H71G mutant that, like YhjA, lacks the P heme distal histidine ligand and therefore in the oxidized-form is penta-coordinated [182]. The Soret shift in the oxidized *P. aeruginosa* BCCP mutant was associated to the formation of an intermediate species at the P heme, the oxo-ferryl (compound I), followed by formation of a radical species.

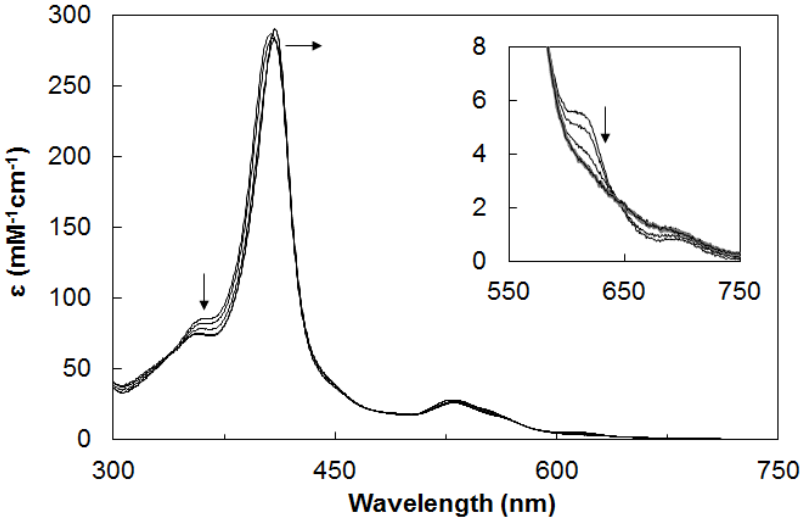

Figure 5.8 – UV-visible absorption spectra of the as-isolated YhjA in the presence of six equivalents of H_2O_2, in 10 mM HEPES pH 7.5. It is observed a shift of the Soret band from 407 to 410 nm and a decrease in the high-spin absorption bands at 360 nm and 620 nm as shown in the inset. The spectra were recorded at 0, 1, 3, 5 and 10 min after addition of H_2O_2.

In other peroxidases, similar changes in the spectra were associated with formation of a tryptophan [181, 324] or porphyrin [325, 326] radical. Formation of a porphyrin radical is characterized by a decrease in absorption of the Soret band [327], while the shift in the Soret band was associated with formation of compound II and a tryptophan radical in a horseradish cytochrome *c* peroxidase mutant [181]. In YhjA, the conserved tryptophan between the E and P hemes is a possible candidate for the radical species, since it could be oxidized by the oxo-ferryl species, as suggested by Hsiao *et al.* in the study on *P. aeruginosa* BCCP [182].

In conclusion, the UV-visible spectra of YhjA suggest that the P heme is penta-coordinated in the oxidized form, forming an intermediate state in the presence of hydrogen peroxide, which involves the formation of a protein radical species. Without further studies this radical remains unidentified.

Furthermore, the P heme high-spin penta-coordinated state seems to be dependent on calcium ions, as removal of calcium ions by EGTA, led to the observation of a low-spin species, possibly due to protein conformational changes that affect P heme coordination, becoming hexa-coordinated. Since there is no distal histidine ligand another residue might be fulfilling this role, possibly a residue from the P heme cavity. However, without a structure of YhjA it is not clear which residue could be responsible for this spin change.

YhjA was further characterized by EPR spectroscopy. The EPR spectra of the oxidized and mixed-valence state of YhjA are shown in Figure 5.9, with the respective simulations. In the oxidized state, there are two main low spin signals (Figure 5.9A): One low-spin signal with $g_z = 3.1$, was attributed to E heme since after only 1 min of incubation with Asc/DAD it partially disappears (disappears completely after 60 min; Figure 5.9B,C). Similar signals, described as Highly Axial Low Spin (HALS) signals, have been found in other *c*-type cytochromes including BCCPs (low-spin E heme signal) from *S. oneidensis* and *P. stutzeri* [40, 129, 131], even though these type of signals have a $g_{max} \geq 3.2$.

This E heme low-spin signal is similar to the ones observed in *N. europaea* cytochrome c_{552} N64Δ mutant [40], with a broad g_y component, which in the spectra from Figure 5.9A is overlapped with the signals from NT and P hemes and was estimated to have a $g \sim 2.25$. The third component of the signal, should have a $g_x \approx 1.1$ but it is too weak to be observed.

As shown in Figure 5.5C, NT heme EPR spectrum has a low-spin signal with $g_z = 2.83$, $g_y = 2.38$ and $g_x \approx 1.52$. Therefore, the second low-spin signal in the as-isolated YhjA with the same *g* values was assigned to both NT and P hemes (two overlapping signals, the relative spin intensity values are in Table 5.1)

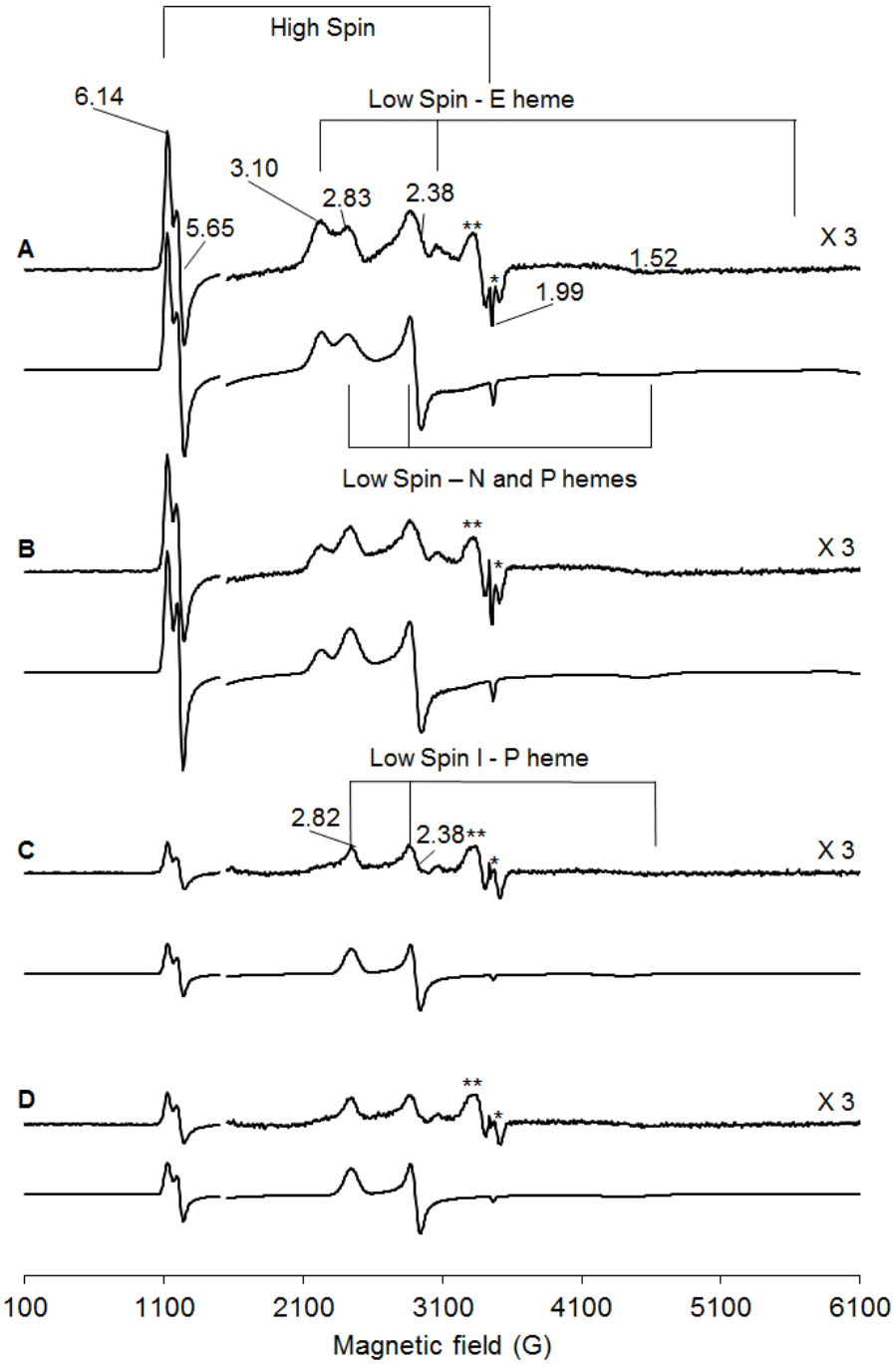

Figure 5.9 – X-band EPR spectra of YhjA and respective simulated data below, in different oxidation states and effect of calcium ions. (A) 0.3 mM YhjA in the oxidized form, (B) after 1 min incubation with Asc/DAD, (C) after 60 min incubation with Asc/DAD and (D) after 30 min incubation with 2 mM $CaCl_2$ after reduction with Asc/DAD. The asterisk (*) marks a radical signal the double asterisk (**) a signal that was not assigned, both present in all spectra. The low-spin region of the spectra was amplified 3 times.

In the mixed-valence state of YhjA (Figure 5.9C), E and NT hemes are reduced and diamagnetic, therefore the observed low-spin signal corresponds to the P heme in the oxidized state. Furthermore, the *g* values of the P heme do not change significantly (g_z = 2.82 and g_y = 2.38) between the two oxidation states of the enzyme. In the classical BCCPs, the *g* values for the hexa-coordinated P heme

are approximately g_z = 3.00 and g_y = 2.27 (in *P. aeruginosa* BCCP [166]) and shift to 2.86 and 2.36, respectively, in the presence of calcium ions, as P heme becomes penta-coordinated and high-spin. This low-spin EPR signal has been attributed to P heme being coordinated by a water molecule, as observed in the X-ray structures of classical mixed-valence BCCPs [167]. Although a water molecule is considered a weak ligand, the binding to P heme at cryogenic temperatures originates spectroscopic properties of a low-spin heme attributed to the higher energy of the Fe-water coordination [171], as discussed in Chapter 3. In the case of YhjA, the P heme *g* values are similar to those of a low-spin P heme with a water molecule as sixth distal ligand, regardless of the oxidation state of the enzyme. This agrees with the visible spectra and analysis of the primary sequence, which indicated that this heme is high-spin penta-coordinated even in the fully oxidized state.

Table 5.1 – Relative amount of spin signal calculated by integration of the simulated high/low-spin signals of each acquired spectrum.

Heme Spin Signal	**Relative amount of spin signal (%)**			
	As-isolated	**Ascorbate 1 min**	**Ascorbate 60 min**	**Ascorbate + Calcium**
High-Spin	28	32	33	37
Low-Spin - E heme	41	24	-	-
Low-spin - NT/P hemes	31	44	67	63

The UV-visible spectra at room temperature showed features of high-spin hemes, which are also present in the EPR spectra at cryogenic temperatures. The EPR spectrum of as-isolated YhjA has a strong high-spin signal with *g* values of 6.14, 5.65 and 1.99, which were assigned to E and P hemes, since NT heme is low-spin at cryogenic temperatures as shown in Figure 5.5C. This signal decreases after 60 min incubation with Asc/DAD, indicating that E heme is contributing to the high-spin component of the as-isolated YhjA EPR spectra. The high-spin signal in the mixed-valence YhjA spectrum is assigned to P heme, which has approximately a 30 % high-spin and 70 % low-spin signal components (Table 5.1). Calcium addition to the mixed-valence YhjA (Figure 5.9D) slightly increases this high-spin signal, in accordance with the changes observed in the P heme absorption features in the same conditions.

Finally, there is a small signal of a radical with a *g* value of ~2, derived from the protein sample, which is present in all the spectra regardless of the condition and redox state, overlapping with the high-spin signal (as a note, this radical signal is considerably smaller relative to the other signals). As the protein sample was not pre-incubated with any compound and the YhjA structure remains unknown, it is not possible to assign this radical signal. Another additional signal with *g* value of 2.04, remains practically unaltered in all spectra and it could not be assigned as there is no heme EPR signal with such a large component at this value and no other signals could be paired with this value. It is not possible to assign this signal to either a radical or to another species at this time.

Overall the spectroscopic characterization of YhjA and NT domain revealed unique traits of these trihemic enzymes. The characterization of NT domain enabled the assignment of the heme distal axial ligand to Met125 and simplified the analysis of the YhjA spectroscopic data. The spectroscopic properties of the C-terminal domain have similar features to the classical BCCPs, specifically with the one isolated from *N. europaea*, which is the only classical BCCP up-to-date, shown to have a penta-coordinated P heme in both the oxidized state and in the mixed-valence state [126].

The EPR spectra of a trihemic BCCP was presented for the first time, showing unique features of the catalytic site (P heme). In YhjA EPR spectra at cryogenic temperatures, the P heme has two distinct states: a high-spin penta-coordinated state and a low-spin hexa-coordinated state with a water molecule as sixth ligand, as described for *Ng*BCCP in Chapter 3.

The rhombicity of the high-spin P heme signal in the mixed-valence YhjA spectrum, can be due to the presence of one or more weak ligands at cryogenic temperatures. Such an effect was demonstrated by comparison of EPR spectra and crystal structure of a MauG P107S mutant to the wild-type [328]. In this mutant changed the heme cavity structure (structurally equivalent to P heme) and the heme became coordinated by a weak ligand, the Glu113 side-chain (in YhjA could be equivalent to Glu270). The axial high-spin signal observed in the WT became rhombic in the MauG P107S mutant. Changes in the YhjA P heme cavity residues might have a similar effect on the EPR spectrum.

Overall, the P heme cavity residues such as Gln260 and Glu270, proposed to be involved in the catalytic activity, are conserved in all BCCPs. Another conserved residue at the cavity is Pro264 (equivalent to the mutated Pro107 in MauG) which is followed by a conserved Pro265-Leu266 motif unique to the trihemic enzymes with the exception of *Z. mobilis* (Figure 5.2). A larger multiple primary sequence alignment of 12 trihemic BCCPs (data not shown) identified this motif in 8 sequences, which comprise the four sequences in Figure 5.2 and the ones from *Lawsonia intracellularis*, *Pasteurella multocida*, *Shigella flexneri* and *Citrobacter farmer* identified in a BLAST search. Considering that the tridimensional structure of the C-terminal domain of trihemic and classical BCCPs might be similar, these residues would be in close proximity to the catalytic cavity and, as in the MauG mutant, they could change the structure of the distal pocket and contribute to some of the P heme spectroscopic features.

5.2.5 Redox titration – Reduction potential of YhjA hemes

As stated before, the CT domain of YhjA is homologous to the classical BCCPs, thus it is expected to have a high and a low potential heme, while the redox properties of the additional NT domain were not known. The reduction potential of each YhjA heme was determined by potentiometric titrations at pH 7.5 (Figure 5.10A), and the values, estimated using the Nernst equation considering three independent redox centers, are listed in Table 5.2.

Table 5.2 – Reduction potential of each YhjA heme in the reductive and oxidative titration, at pH 7.5 in the presence of 2 mM $CaCl_2$.

	Reduction potentials (mV)		
Direction	**P Heme**	**N Heme**	**E Heme**
Oxidation	- 190 ± 10	140 ± 10	220 ± 10
Reduction	- 150 ± 10	125 ± 10	200 ± 10

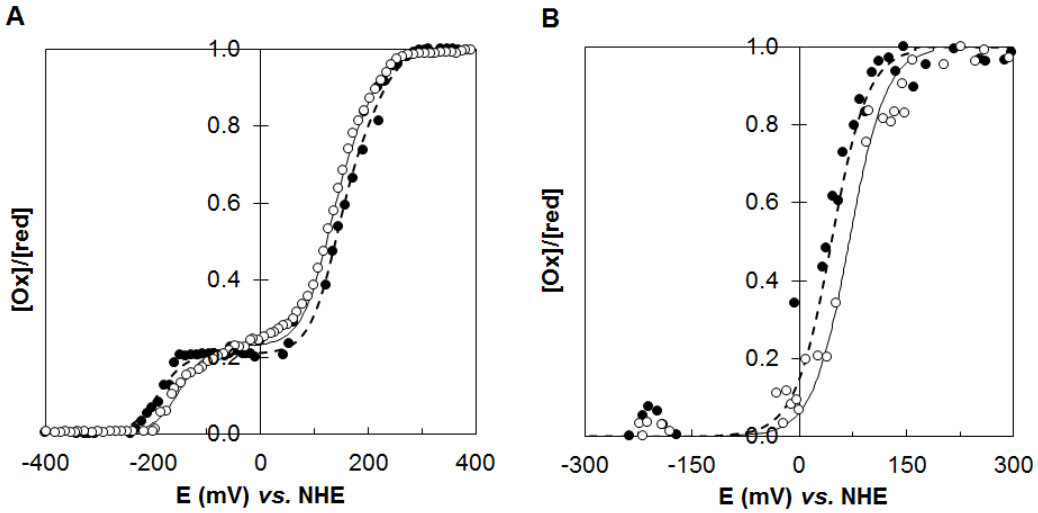

Figure 5.10 – Potentiometric titration of (A) YhjA and (B) NT at pH 7.5 in the presence of 2 mM $CaCl_2$. The reductive titration is represented by open circles and the oxidative titration by closed circles. The lines represent the simulation of the potentiometric curve using the reduction potentials listed in Table 5.2 for YhjA and with a reduction potential of + 55 ± 10 mV for the NT domain.

The reduction potential of the isolated NT domain was determined to be + 55 ± 10 mV (Figure 5.10B). The comparison between the usual reduction potentials of the two hemes in the classical BCCPs with the ones obtained, led us to assign the reduction potential of this heme in the full length YhjA to + 133 ± 10 mV. The difference between these two values is likely due to changes in protein conformation and solvent exposure of the NT heme. NT heme is expected to be less solvent exposed in the full length enzyme due to contact between the two main domains of YhjA. This reduction potential is within the expected range for a His/Met coordinated *c*-type heme [32].

The reduction potentials of the three hemes are more negative than the ones determined for *A. actinomycetemcomitans* QPO, + 67 (P), + 156 (NT) and + 290 mV (E), at pH 7.5 [151]. The P heme has a negative reduction potential in YhjA, as found in classical BCCPs (the reduction potentials of classical BCCPs are listed in Table 1.1 in Chapter 1), while in this other enzyme it was determined to be positive. The differences in the catalytic cavity of the two enzymes or the positive reduction potential might be due to the presence of detergent (0.5 % SM-1200) in their assays, which could slightly affect the protein folding and consequently its redox properties.

5.2.6 Catalytic mechanism – Steady-state kinetics

The spectroscopic data suggested that YhjA does not need reductive activation since its P heme is high-spin and penta-coordinated in the oxidized state and it is able to bind its substrate, hydrogen peroxide. This fact was corroborated by the preliminary kinetic data with $ABTS^{2-}$ as electron donor (Figure 5.11), which showed identical initial rates for the oxidized and mixed-valence state of the enzyme with calcium ions. The calcium dependence of the catalytic activity was assessed for the oxidized form, and without addition of calcium ions to the assay, the initial rates slightly decreased from 0.121 ± 0.001 µM $ABTS^{2-}.s^{-1}$ to 0.115 ± 0.002 µM $ABTS^{2-}.s^{-1}$. Thus, YhjA does not require reductive activation but calcium ions are needed to attain maximum peroxidase activity (unlike *A. actinomycetemcomitans* QPO, which also does not need reductive activation but its activity was not affected by calcium ions removal with EGTA [149]).

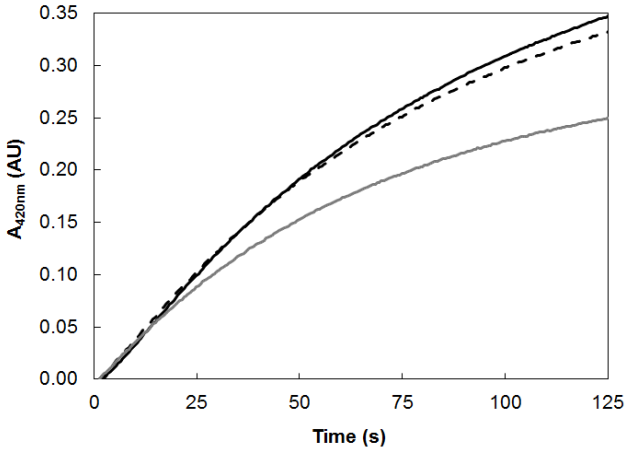

Figure 5.11 – Kinetic traces of re-oxidation of $ABTS^{2-}$ in the presence of 1 mM H_2O_2 upon addition of YhjA in the mixed-valence state (full line) and in as-isolated state (dashed line), in 10 mM HEPES, 10 mM NaCl, 1 mM $CaCl_2$ at pH 7.5 and 25 ºC. In the assays using the as-isolated YhjA without calcium being present in the assay buffer, the initial rates decrease (solid grey line). Mixed-valence YhjA was prepared by incubating a stock solution of as-isolated enzyme in 10 mM HEPES pH 7.5, 10 mM NaCl, 2 mM $CaCl_2$, 0.2 mM sodium ascorbate and 5 µM DAD for 60 min at room temperature. Time zero was adjusted to the time YhjA was added.

In addition, the kinetic assays showed that YhjA with and without Strep-tag had similar initial rates for YhjA peroxidase activity, demonstrating that the Strep-tag does not interfere with the catalytic activity (data not show). Furthermore, mixed-valence YhjA does not catalyze hydroperoxides since with 0.1 and 1 mM cumene hydroperoxide or *tert*-butyl peroxide there was no apparent activity using 3 mM $ABTS^{2-}$, as electron donor.

In order to characterize the peroxidase activity of YhjA, four electron donors were tested: $ABTS^{2-}$, hydroquinone, duroquinol and menadiol (Figure 5.12), and the respective kinetic parameters for YhjA activity were determined at 25 ºC, pH 7.5 (Table 5.3 and Figure 5.13).

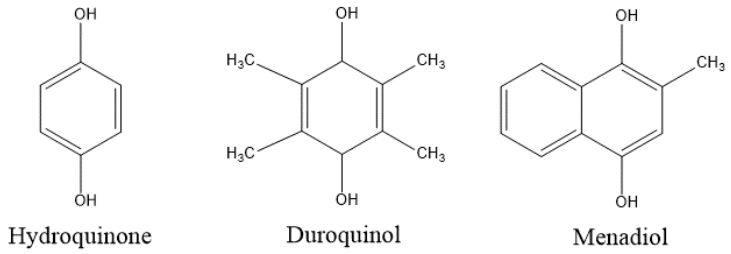

Figure 5.12 – Chemical structures of the quinols used in this work: hydroquinone and duroquinol, from the benzoquinone family and menadiol, from the naphtoquinone family.

$ABTS^{2-}$ is an artificial electron donor that has been used as an alternative electron source for classical bacterial peroxidases when the physiological electron donor is unknown [115, 132]. Although the turnover number obtained is high, the K_M for $ABTS^{2-}$ is also the highest (3.7 ± 0.9 mM H_2O_2) found for the compounds under study, making it the most inefficient electron donor tested with the lowest specificity constant (k_{cat}/K_M). Nevertheless, it is not as low as determined for the previous construct (YhjA_6His) that had a K_M of 17 ± 5 mM H_2O_2, which proved that this construct had an effect on the catalytic activity and it was not in the native form. This is an example of one of the possible problems of heterologous protein production, in the absence of a native protein for comparison.

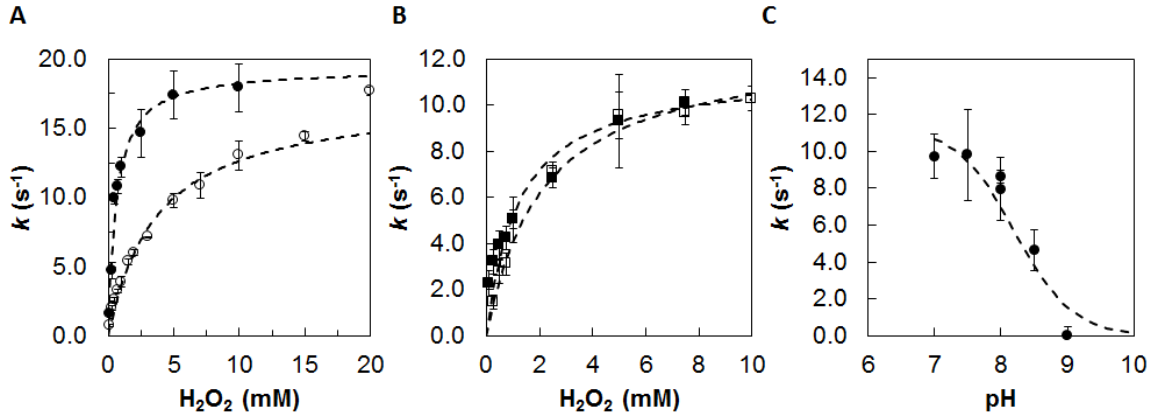

Figure 5.13 – Steady-state kinetics of YhjA peroxidase activity using $ABTS^{2-}$ (A, open circles), hydroquinone (A, closed circles), menadiol (B, open squares) and duroquinol (B, closed squares). The pH effect on YhjA catalytic activity was assessed with hydroquinone (C). The dashed lines represent the simulated data using the equations 2.7 and 2.16 from Chapter 2. The results are represented as mean of three replicates and the parameters used in the simulation are the ones listed in the text and in Table 5.3. YhjA used in the kinetic assays was in the as-isolated state.

Table 5.3 – Kinetic parameters obtained for reduction of hydrogen peroxide by YhjA using different electron donors. All the kinetic parameters were obtained by fitting the kinetic data to a Michaelis-Menten (Equation 2.7 in Chapter 2).

Electron donor	k_{cat} **(s^{-1})**	K_M **(mM)**	k_{cat}/K_M **($mM^{-1}.s^{-1}$)**
$ABTS^{2-}$	17 ± 2	3.7 ± 0.9	4.7 ± 0.3
Hydroquinone	19 ± 2	0.6 ± 0.2	32.2 ± 0.3
Duroquinol	12 ± 2	1.2 ± 0.5	9.6 ± 0.4
Menadiol	13 ± 2	1.8 ± 0.5	7.1 ± 0.3

Hydroquinone is the best electron donor with a K_M of 0.6 ± 0.2 mM H_2O_2 and a turnover number of 19 ± 2 s^{-1}, resulting in a specificity constant of 32.2 ± 0.3 $mM^{-1}.s^{-1}$. This turnover number is similar to $ABTS^{2-}$, k_{cat} = 17 ± 2 s^{-1} and comparable with the turnover number of *G. sulferreducens* classical BCCP (15.5 s^{-1}) [132].

The turnover numbers of duroquinol and menadiol are lower and have similar k_{cat} = 12 ± 2 s^{-1} and 13 ± 2 s^{-1}, respectively, but the apparent K_M is lower for duroquinol, which results in an apparent higher specificity. Comparing the oxidation profile of duroquinol with the one of menadiol and hydroquinone, it is clear that the reaction stops after approximately 75 seconds (Figure 5.14) even at lower hydrogen peroxide concentrations (1 mM, a concentration that is not expected to inhibit or damage the enzyme). Thus, only menadiol and hydroquinone are capable of transferring electrons efficiently to YhjA, maintaining the enzyme in an active state.

The reason why hydroquinone performs better than duroquinol, even though both are ubiquinol analogues (benzoquinone family) is probably due to its simplicity and lack of ring substituents (Figure 5.12), such as the four methyl groups in duroquinol ($E^{o\prime}$ = + 35 mV, pH 7.0 [207]) and ubiquinol ($E^{o\prime}$ = + 100 mV, pH 7.0 [322]), which translates in hydroquinone having a higher reduction potential ($E^{o\prime}$ = + 280 mV, pH 7.0 [329]). Menadiol is a menaquinol analogue (naphtoquinone family), which has a single methyl group, like menaquinol, and a negative reduction potential ($E^{o\prime}$ = - 1 mV, pH 7.0 [207]). The lack of additional ring substituents in menadiol seems to be essential for enzyme specificity and turnover.

Compared to classical BCCPs, which have K_M values in the micromolar range, YhjA is a poor *in vitro* peroxidase. However, both K_M values and specificity constants are comparable to the quinol peroxidase activity of cytochrome *bd*, a terminal oxidase in *E. coli*, which has a K_M of 7 mM and k_{cat}/K_M = 15 $mM^{-1}.s^{-1}$ [330] for the reduction of hydrogen peroxide. Furthermore, the transmembranar helix is not present in this construct, which might influence the YhjA K_M value.

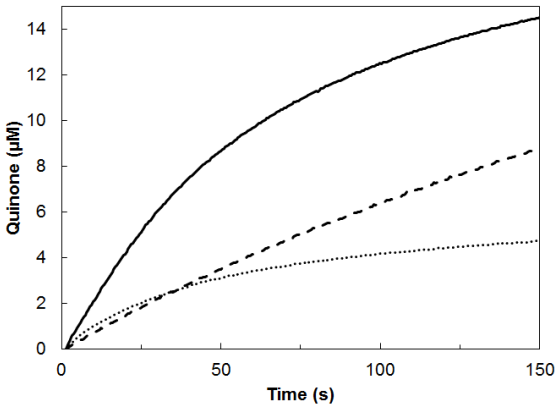

Figure 5.14 – Kinetic traces of re-oxidation of different quinols in the presence of 1 mM hydrogen peroxide upon addition of as-isolated YhjA. Electron donors: hydroquinone (solid line), menadiol (dashed line) and duroquinol (dotted line). The traces were corrected for the autoxidation rates of the respective quinol. Assays were performed in 10 mM HEPES pH 7.5, 10 mM NaCl, 1 mM $CaCl_2$, at 25ºC. Time zero was adjusted to the time YhjA was added.

The pH dependence of the peroxidase activity of YhjA was assessed using hydroquinone as electron donor (Figure 5.13C) from pH 5.5 to pH 9.0. YhjA is not stable at lower pH values (5.5 - 6.5) as it precipitated. The curve was simulated with a p*Ka* of 8.2 ± 0.1 and a maximum activity at pH 7.0. A similar p*Ka* value has been observed in the classical BCCPs, and thus might be attributed to the same residue, the conserved glutamine in the catalytic center, as discussed in Chapter 3.

Steady-state kinetics show that YhjA displays quinol peroxidase activity (QPO) *in vitro* like other trihemic bacterial peroxidases [149, 153]. This enzyme was fully active in the oxidized state, as spectroscopic data predicted, and this trait is a common feature of trihemic bacterial peroxidases as they lack the conserved distal histidine heme ligand in their primary sequence.

YhjA can use quinol as an electron source and of the quinones tested, hydroquinone has proven to be the best electron donor, though it still has a high K_M value. However, quinones, such as hydroquinone, are not found in *E. coli* quinol pool. YhjA is probably able to use it due to its simple structure and higher reduction potential allowing electron transfer, independently of the quinol-binding site selectivity and possibly donating electrons directly to the E heme. There are no consensus quinone binding sites but analysis of the quinone/quinol binding pockets of other enzymes from *E. coli*, such as fumarate reductase [331], cytochrome bo_3 [332] and succinate dehydrogenase [333], show that residues like aspartate, histidine and tyrosine (among other residues such as cysteine, arginine and glutamate) play a role in affinity and semiquinone stability and are usually located in transmembranar regions. In the YhjA predicted transmembrane helix there are two tyrosines (Tyr19 and Tyr25) and an aspartate residue (Asp30), conserved in all trihemic sequences in the alignment in Figure 5.2, and additionally a cysteine and a histidine residues which could be involved in quinone binding. The enzyme used in these assays was a soluble form, therefore these residues located close or in the membrane region are absent, explaining the lower turnover numbers for duroquinol and menadiol.

Duroquinol proved to be an inefficient electron donor while menadiol, a menaquinol analogue, does not inhibit the reaction and therefore, the physiological electron donor of YhjA is proposed to be menaquinol, as expected for an enzyme proposed to be expressed under oxygen limited conditions [123]. An alternative electron donor could be a periplasmatic membrane-bound cytochrome *c*, NapC, however in *E. coli* this protein delivers electrons to nitrate reductase and it is co-regulated with that particular enzyme [45]. Therefore, NapC would only be available when nitrate is present in the medium. In fact, it is more likely that YhjA evolved to specifically accept electrons from a quinol, mainly menaquinol, as the main quinones present under anaerobic conditions are the naphthoquinones: demethylmenaquinone and menaquinone [321].

Moreover, it was reported that *E. coli* cells overexpressing a recombinant YhjA, did not present QPO activity using ubiquinol-1 as electron donor [151]. YhjA has low affinity for hydrogen peroxide and used a menaquinol analogue as electron donor, which would explain why QPO activity was

undetected in this previous study in an *E. coli* strain overexpressing recombinant YhjA, as conditions were not ideal. This study was performed under aerobic conditions (in these conditions membranes lack menaquinol), with low amounts of hydrogen peroxide (80 µM H_2O_2) and a benzoquinone as electron donor (ubiquinol-1) [151].

All the data suggest that the YhjA catalytic mechanism might be similar to the one of classical bacterial peroxidases, as the E and P heme domains are conserved, as well as the tryptophan residue between the two hemes, and it would involve an intermediary oxo-ferryl compound with consequent formation of a radical species. The NT heme positive reduction potential and its proximity to the quinol pool make it the likely electron acceptor, and donor to the E heme. In fact, the most recent work with *A. actinomycetemcomitans* QPO shows that a quinol molecule reduces both NT and E hemes and that the catalytic activity occurs through a Ping-Pong Bi Bi mechanism [152]. Further aspects regarding electron transfer pathway and the identity of the radical species are still unclear and structural data is required to clarify it.

5.2.7 *yhjA* gene expression and regulation

E. coli is a model organism for Gram-negative bacteria and has been used to study oxidative stress, with a large number of data concerning gene expression and regulation being gathered for this bacterium. Here, the gene expression levels of *yhjA* encoding a putative bacterial cytochrome *c* peroxidase were assessed by *q*PCR and the data compared with the results of the various microarray experiments described in the literature. The oxygen dependence and also the influence of the two alternative respiratory pathways (using fumarate *vs.* nitrate as terminal electron acceptors under anaerobic conditions) in *yhjA* expression were assessed (Figure 5.15).

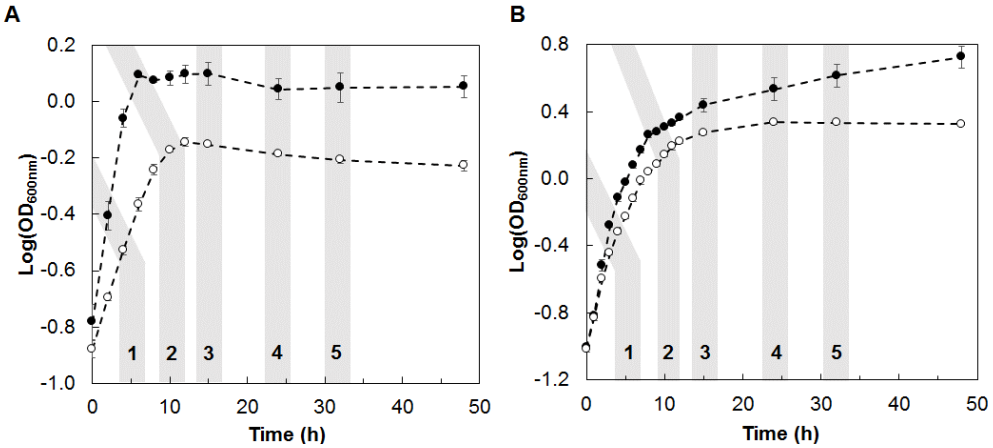

Figure 5.15 – Growth curves of *E. coli* K-12 grown in modified M9 media (A) under anaerobic conditions supplemented with fumarate (open circles) or nitrate (closed circles) as final electron acceptors and (B) under aerobic (closed circles) or microaerophilic conditions (open circles). The grey areas correspond to the growth stages analyzed by *q*PCR: 1 – Mid exponential; 2 – Late exponential; 3 – Early stationary; 4 – Stationary (24 h) and 5 – Stationary (32 h). This is an average representation of the growth curves of three biological replicates and the error bars are the standard deviation.

Besides *yhjA*, the genes *fnr*, *oxyR*, *ahpC*, *katE* and *katG*, as oxidative stress related genes, were also measured throughout the distinct growth phases and growth conditions to assess their role in comparison to *yhjA*.

The *q*PCR results show that *yhjA* has a 15-fold higher expression under anaerobic conditions than under aerobic conditions, with fumarate as electron acceptor in the mid exponential and late stationary phases (Figure 5.16A).

Moreover, under aerobic conditions it was observed a small increase in *yhjA* expression when entering the stationary phase (late exponential phase). Nevertheless, in this growth phase *yhjA* expression levels are about 5-fold higher under anaerobic conditions, than under aerobic conditions and 4-fold higher than under microaerophilic conditions (see relative gene expression valus in Annex 1, Figure A1.2). This confirmed previous studies in which a *yhjA* promoter showed higher *lacZ* expression under oxygen limited conditions [123].

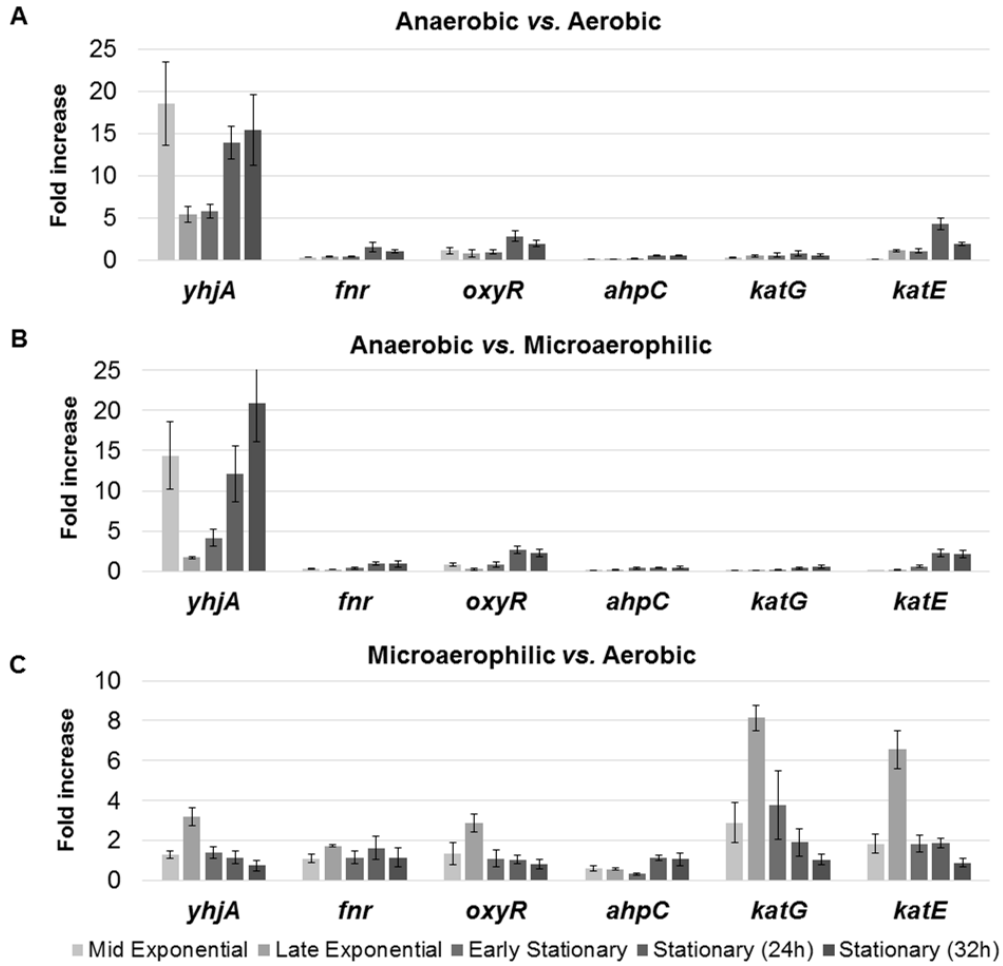

Figure 5.16 – Relative gene expression fold increase in *E. coli* K-12 under (A) anaerobic growth (fumarate as electron acceptor) *versus* aerobic growth, (B) anaerobic growth *versus* microaerophilic growth, and (C) microaerophilic growth *versus* aerobic growth. Data is shown as the ratio of the mean relative expressions, based on three biological replicates. In (A) and (B) the major differences observed between growth stages for *yhjA* are due to variation of the normalized gene expression value in aerobic and microaerophilic conditions (1.4-6.6) while in anaerobiosis the value is more constant (on average 35).

As *yhjA* is mainly anaerobically expressed, it was evaluated how the respiratory pathway affects its expression and also the expression of the other genes. Figure 5.17 shows the relative gene expression pattern under anaerobic conditions, using fumarate or nitrate as electron acceptors. The analysis of this data indicates that under anaerobic conditions, *yhjA* is expressed at similar levels regardless of the electron acceptor.

Similarly to what was observed for fumarate supplemented media, in the stationary phase of nitrate supplemented media the gene expression is higher. This is in agreement with Ito *et al*. microarray data [334], that included *yhjA* in those studies, although the comparison was between planktonic cells in the exponential and stationary phases, grown under aerobic conditions.

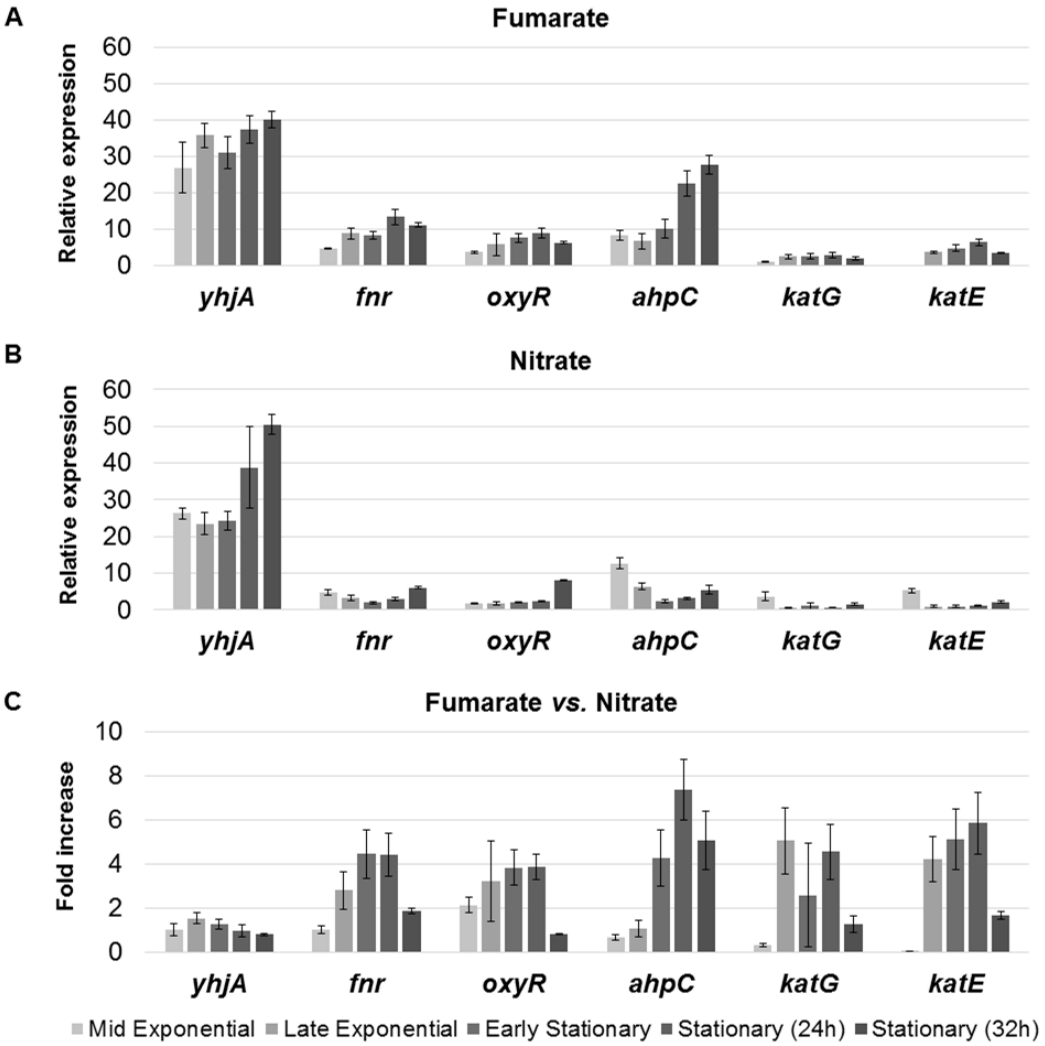

Figure 5.17 – Relative gene expression of oxidative stress related genes in *E. coli* K-12 during growth under anaerobic conditions with either fumarate (A) or nitrate (B) as electron acceptor. (C) Fold change of gene expression between anaerobic growths with fumarate *versus* nitrate, as terminal electron acceptor. The gene expression of each gene was normalized to the *16SrRNA* to account for variations in each point taken from each growth. Data is shown as the mean relative expression based on three biological replicates.

The general expression pattern of the remaining genes is similar within the same media. When comparing fumarate *versus* nitrate (Figure 5.17C) it is clear that the major differences are in the other genes rather than in *yhjA*, and mainly when the cells enter the stationary phase. In fact, there is a higher expression in *fnr, oxyR, ahpC, katE* and *katG* (4-7 fold increase) for cells grown with fumarate. However, between anaerobic and aerobic conditions, in fumarate supplemented media those genes are actually being repressed (fold increase <1, such as *fnr* and *ahpC*) or expressed at similar levels (fold increase 1-2, *oxyR, katG* and *katE*).

The major difference between fumarate and nitrate is the energy yield of these alternative respiratory pathways. Nitrate is more favorable energetically, which explains the higher growth rate in nitrate than in fumarate [321] (Figure 5.15). Therefore, it was expected that not only the overall respiratory pathway changed but the overall catabolism as well, which might affect the gene expression profile. Nevertheless, the expression levels of *yhjA* remained unchanged probably because its main regulator is FNR, as explained in Chapter 1 when addressing *yhjA* promoter region (even if *fnr* expression levels under aerobic conditions are slightly higher compared with anaerobic conditions, FNR is only active under anoxic conditions [117]).

Between aerobic and microaerophilic conditions it is clear that *katG* is induced in the exponential phase (Figure 5.16B), while *katE* is induced in the late exponential phase, before entering the stationary phase, which is consistent with this gene being regulated by RpoS, a stationary phase sigma factor [335]. The gene *katE* is repressed under anaerobic conditions as shown for nitrate supplemented media (Figure 5.17C). This is in agreement with Constantinidou *et al*. microarray [336] using fumarate or nitrate as electron acceptor and glycerol as carbon source, in similar conditions to our assay, in which it was observed that *yhjA* and *katG* were activated and *katE* repressed. Kang *et al*. [337] did a similar analysis at the beginning of the exponential phase ($O.D._{600nm}$ of 0.1 to 0.2), using glucose (0.1 %) as carbon source. Their work agrees with *ahpC, katE* and *fnr* being repressed and *katG* overexpressed under anaerobic conditions. OxyR was overexpressed as well, however in the present work no samples were taken so early in the exponential phase and it was not observed a significant *oxyR* overexpression in the exponential phase.

In sum, our data agrees with the literature and regarding *yhjA* expression levels, these are higher under anaerobic conditions. However, the increase in the stationary phase was not expected as this gene is not regulated by RpoS. Gel retardation assays showed that FNR and OxyR are able to bind at the same time to *yhjA* promoter region but OxyR could bind in the absence of FNR and vice-versa [123]. Thus, it is possible that as described by Dukan and Nyström [338] under aerobic and microaerophilic conditions, as cells are entering stasis in the late exponential phase/early stationary phase, there is a slow increase in ROS and a stasis-induced expression of OxyR-dependent genes, such as *yhjA*. Therefore, as cells enter the stationary phase, *yhjA* expression levels in aerated environments decrease, not only because *oxyR* expression is repressed by RpoS [339] but also due to a

decrease in ROS as a result from the expression of large number of oxidative stress defenses induced by OxyR and RpoS.

However, this does not explain the higher *yhjA* expression levels under anaerobic conditions, in particular in the stationary phase of cells grown in nitrate supplemented media, since in fumarate supplemented media the expression levels are maintained more or less similar throughout the five growth stages. Since the cells were grown under anaerobic conditions, OxyR is not exposed to ROS and can only be activated by nitrosative stress [57], which occurs in nitrate supplemented media [340]. In fact, it is not clear in which conditions OxyR binds *yhjA* promoter. Partridge *et al.* suggested that *yhjA* promoter region resembled the one from OxyR-activated promoters (from oxidative stress induced genes), lacking an additional ATAGnT element, and that the fourth OxyR contact point did not resemble ATAGnT and AnCTAT. It was also proposed that OxyR was essential for expression since mutation of the OxyR binding site in the promoter region decreased the promoter expression under oxygen limited conditions [123]. It is possible that OxyR is able to bind and together with FNR enhance gene expression, however our results show that gene expression is primarily induced by FNR due to a higher gene expression in all growth stages under anaerobic conditions, in the absence of oxidative stress. Without further information, we cannot exclude that *yhjA* gene expression can be induced by OxyR activated through oxidative and/or nitrosative stress. In fact, this has been demonstrated in other OxyR regulated promotors, as both S-oxidized or S-nytrosylated OxyR are able to activate a *katG* promoter *in vitro* [340], although our data shows no effect on *kat*G expression.

5.2.8 YhjA physiological role

In order to evaluate the physiological role of YhjA *in vivo* we determined the cells viability for a wild type (WT) *E. coli* K-12 strain and a *yhjA* null mutant strain, when exposed to oxidative stress reagents, such as hydrogen peroxide, cumene hydroperoxide and *tert*-butyl peroxide (Figure 5.18).

Both strains have similar resistance to *tert*-butyl peroxide however, for hydrogen peroxide, there is a tendency for lower survival in the *yhjA* null mutant strain, although with a great error between replicates. This mutant is also more sensitive to cumene hydroperoxide than the WT. This seemed to indicate that YhjA had some peroxidatic activity *in vivo*, but as previously described, a recombinant YhjA did not catalyze cumene hydroperoxide *in vitro*.

Since *E. coli* has several scavenging enzymes that deal with peroxide related stress it was necessary to use high concentrations of hydrogen peroxide, far from physiological, in order to see a difference between the two strains. Cumene hydroperoxide is a membrane soluble peroxide that causes peroxidation of the membrane lipids, which results in decreased membrane fluidity [94]. Catalases and Ahp are located in the cytoplasm and they are not able to answer this type of oxidative stress. Typically this role belongs to a family of peroxiredoxins that detoxify *tert*-butyl peroxide and cumene hydroperoxide, but not H_2O_2, such as the organic hydroperoxide resistance protein Ohr [341].

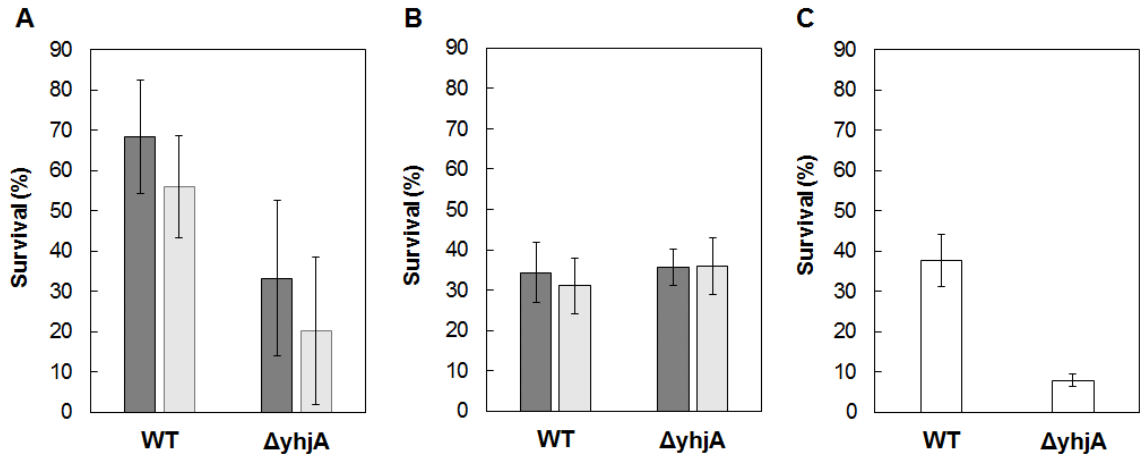

Figure 5.18 – Decreased survival of *E. coli* K-12 wild type (WT) and the *yhjA* null mutant (Δ*yhjA*) strains after 30 min of oxidative stress imposed by (A) hydrogen peroxide, (B) *tert*-butyl peroxide (25 mM in dark grey, 50 mM in light grey bars) or (C) 1 mM cumene hydroperoxide (white bars). Survival is expressed as the percentage of c.f.u. obtained for a non-treated control. The error bars are the standard deviation of three independent experiments.

The disc diffusion method was used to determine if the *yhjA* null mutant displayed higher sensitivity to oxidative stress caused by discs saturated in various concentrations of H_2O_2 or cumene hydroperoxide. The assay was inconclusive for hydrogen peroxide because *E. coli* K-12 was able to withstand all the concentrations used (up to 100 mM) as this bacterium is highly resilient to hydrogen peroxide due to the catalases and Ahp.

The WT strain is slightly more sensitive to cumene hydroperoxide in both aerobic and anaerobic conditions (Figure 5.19). This difference is not significant and adding to the previous result it seems that YhjA does not play a direct role in detoxifying cumene hydroperoxide. A similar experiment with WT strain and QPO null mutant strain from *A. actinomycetemcomitans*, also did not show any difference when incubated with *tert*-butyl peroxide or cumene hydroperoxide [150].

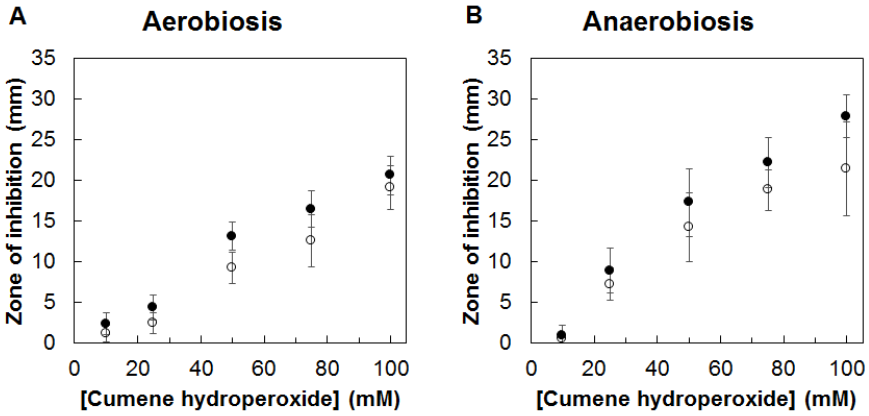

Figure 5.19 – Comparison of inhibition zone diamater of *E. coli* K-12 wild type (closed circles) and Δ*yhjA* (open circles) strains when exposed to various concentrations of cumene hydroperoxide in aerobic or anaerobic environment. The error bars represent the standard deviation for three independent assays.

The small differences observed between the two strains might be due to the presence/absence of this membrane bound enzyme that affected to some extent the membrane integrity, fluidity and sensitivity when exposed to cumene hydroperoxide in liquid/solid media. However, it is clear that both strains are more sensitive to hydroperoxide stress under anaerobic conditions. This further supports that YhjA is not involved in the defense against hydroperoxides as proposed for other *E. coli* peroxidases such as BCP and Tpx, as it is expected to be more abundant in those conditions from the *q*PCR data. Since YhjA is a membrane bound protein and the recombinant YhjA has quinol peroxidase activity *in vitro*, the activity of membranes from *E. coli* K-12 WT strain was compared with the one from the *yhjA* null mutant strain, grown under the same conditions. It was observed that addition of hydroquinone increases the reduction rate of 0.1 mM H_2O_2 by both membrane samples but there is no significant difference in QPO activity between the two (Figure 5.20).

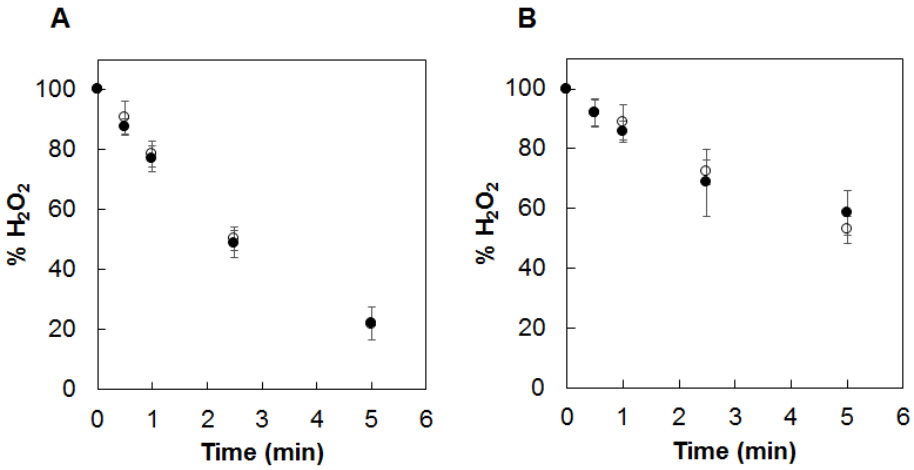

Figure 5.20 – Peroxidase activity of 10 µg of cell membranes from *E. coli* K-12 wild-type (closed circles) and Δ*yhjA* knockout mutant (open circles) cells, grown anaerobically and collected in the stationary phase (16 h). The assay was performed in 100 mM Tris-HCl, pH 7.6 and 2 mM $CaCl_2$ in the presence (A) or absence (B) of 100 µM hydroquinone. The error bars represent the standard deviation of three replicates.

This observation did not change with higher concentration of hydrogen peroxide (0.5 mM). The lack of *in vivo* quinol peroxidase activity in YhjA is thus attributed to its lower turnover number in comparison to cytochrome *bd* [330], a terminal oxidase that, as described previously, is the only other *E. coli* enzyme described up-to-date with QPO activity under anaerobic conditions.

All the results agree with an anaerobically expressed enzyme, that reduces hydrogen peroxide but not hydroperoxides. However, in anaerobic environments, the main ROS sources are exogenous (other microorganisms or host defenses).

A possible role for YhjA is as a defense mechanism against aeration, that is, when cells growing under anaerobic conditions are transiently exposed to oxygen, as represented in Figure 5.21. Upon exposure to oxygen, significant amounts of hydrogen peroxide are produced endogenously by various flavoenzymes, such as the aspartate oxidase (NadB) and the fumarate reductase (Frd, with a

subunit homologous to NadB) [342, 343]. The autoxidation of the quinol pool is also an additional source of ROS, specifically menaquinol autoxidation, which is synthesized mainly under anaerobic conditions [344]. A membrane bound quinol peroxidase, such as YhjA would prove to be advantageous in this scenario because not only it would defend the cell against hydrogen peroxide, as it would use the quinol pool avoiding higher levels of quinol autoxidation.

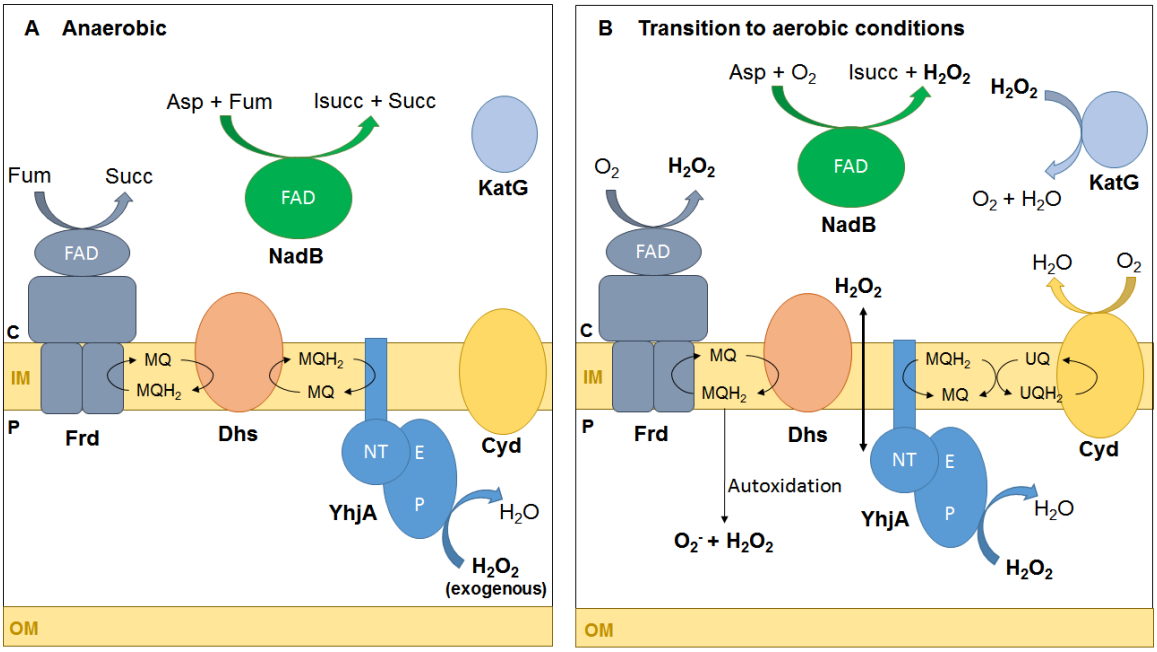

Figure 5.21 – Proposed model for YhjA role in *E. coli* when transitioning from an anaerobic to an aerobic environment. (A) Under anaerobic conditions flavoenzymes, such as aspartate oxidase (NadB, oxidizes aspartate, Asp, to iminosuccinate, Isucc) and fumarate reductase (Frd) reduce fumarate (Fum) to succinate (Succ). Frd, YhjA and other membrane associated reductases, use the reductive power of the quinol pool which is regenerated by dehydrogenases (Dhs). (B) When cells are first exposed to low oxygen tensions, as the fumarate levels decrease, Frd and NadB become significant sources of H_2O_2. The autoxidation of the menaquinol (MQH_2) also contributes to the increase of ROS. This effect is reduced by cytochrome terminal oxidases, such as cytochrome bd (Cyd) that act as electron sinks as it reduces O_2 to H_2O. As anaerobically expressed enzymes, KatG and YhjA are the first hydrogen peroxide scavengers. Other significant H_2O_2 sources upon aeration are still not well characterized. C – cytoplasm; P – periplasm; IM – Inner membrane; OM – Outer membrane.

Other defenses for higher concentrations of H_2O_2 would consist of the cytoplasmic KatG, which is expressed anaerobically. Meanwhile, as oxygen levels increase, additional defenses would be produced, such as Ahp that would be derepressed as confirmed by our *q*PCR data.

Overall this shows that *E. coli* defense system seems to be well adapted to rapid changes in environmental oxygen tensions and that YhjA would play an essential role as a periplasmatic peroxidase and initial defense mechanism.

5.3 Conclusions

Trihemic BCCPs constitute a subgroup of bacterial peroxidases that has not been explored extensively up-to-date. This study presents for the first time a biochemically characterization of the trihemic bacterial peroxidase YhjA, one of the enzymes from the large array of hydrogen peroxide scavengers in the *E. coli* oxidative stress system.

This enzyme is a membrane bound protein and its gene expression was analyzed in response to several factors: oxygen levels, respiratory pathway and growth stage. The *q*PCR data showed that *yhjA* is expressed in the absence of oxygen with increased fold in the stationary phase, consistent with its regulation by FNR and possibly OxyR, due to nitrosative stress, although this hypothesis has yet to be explored. The expression levels were independent of the electron acceptor used in the media (fumarate/nitrate), even though this changes *E. coli* overall metabolism. The other genes related to oxidative stress, *fnr, oxyR, katG, katE* and *ahpC*, were analyzed for comparison of the transcription data and overall the results agreed with the ones from the literature.

The as-isolated recombinant YhjA is monomeric and has unique spectroscopic features not found in the classical BCCPs, with its peroxidatic heme being penta-coordinated. It does not require reductive activation for full activity and ability to bind the substrate, although it still needs calcium ions. The enzyme has quinol peroxidase activity with millimolar concentrations of hydrogen peroxide using hydroquinone and menadiol as electron donors. Since duroquinol, an ubiquinol analogue, is not an efficient electron donor and hydroquinone is absent from *E. coli* membranes, we suggest that menaquinol is its physiological electron donor. A YhjA structure will be needed to further study and comprehend the catalytic mechanism, quinol binding site and the catalytic cavity, which will contribute to the understanding of its spectroscopic properties. It should be noted that this construct lacks some of the N-terminus residues proposed to be necessary for quinol binding site in the membrane bound protein. Therefore this enzyme might be slightly different from the native form. Production of the native YhjA has been attempted without success [149], but it should be pursued in the future in order to address these issues.

YhjA *in vivo*, shows no clear peroxidase activity as a mutant strain lacking this enzyme showed no significant difference from the wild type when exposed to ROS. This shows how difficult it can be to correlate the data obtained *in vitro* to the *in vivo* data. This has been a challenge for Tpx, Bcp and BtuE peroxidases from *E. coli* and also proves to be a challenge for YhjA. *E. coli* is a highly resilient microorganism that is unable to cope with hydrogen peroxide without the catalases and Ahp. However, all these enzymes have been conserved through evolution which indicates that they do play a role in *E. coli* homeostasis and physiology.

As previously stated YhjA plays a role in anaerobiosis, unlike in *A. actinomycetemcomitans* where a QPO null mutant exhibited an oxidative stress sensitive phenotype under aerobic conditions [150]. Therefore, although these two proteins have resemblances, evolution has given them two different

roles, which may be related to the fact that these organisms colonize distinct habitats and are exposed to different conditions and oxidative stress environments. Unlike strict anaerobes, *E. coli*, a facultative anaerobe, colonizes diverse habitats that are susceptible to encounter oxygen sources, such as the human gastrointestinal system. These ubiquitous bacteria have evolved in order to be able to cope with oxidative stress when faced with oxygenated environments or when pathogenic strains are targeted by the immune system oxidative burst. These few anaerobic defenses, which include YhjA, might be sufficient as a first response against these threats, while additional defenses are produced through O_2/ROS-induced pathways.

Chapter 6

Conclusions and Future Perspectives

6 Conclusions and Future Perspectives

6.1 Conclusions

This thesis presents the characterization of the bacterial peroxidases from the human pathogen *N. gonorrhoeae* and from *E. coli*. The study of these enzymes offers some new insights on their biochemical properties, the activation and catalytic mechanisms, the role played by the calcium ions on activation and their physiological role.

In Chapter 3, it was performed a biochemical and structural characterization of the globular domain of *Ng*BCCP. *Ng*BCCP shares many of the properties of classical BCCPs, such as dimer stabilization by calcium ions, the requirement of reductive activation for maximum activity and a high affinity for hydrogen peroxide.

*Ng*BCCP has a high affinity for calcium ions however, it only forms a dimer in the presence of excess calcium ions in solution and at higher protein concentrations (> 10 μM). This enzyme is a monomer *in vitro* even at high ionic strength. This was attributed to a dynamic monomer-dimer equilibrium, due to a less hydrophobic dimer interface and to the absence of the "Trp-Gly" π-stacking interaction between opposite monomers that stabilizes the loop with the P heme distal histidine ligand at the interface, in the mixed-valence state. It was hypothesized that the *Ng*BCCP location, anchored to the outer membrane by a lipid-modified residue, and thus not able to diffuse freely in the periplasm, will increase the local concentration of these proteins and favor *Ng*BCCP dimer formation *in vivo*.

The spectroscopic properties of *Ng*BCCP were identical to other classical BCCPs. However, the mixed-valence *Ng*BCCP EPR spectrum presented one distinct feature, a unique high-spin signal attributed to P heme at cryogenic temperatures, which is not observed in classical BCCPs, although in the mixed-valence state, the P heme is high-spin penta-coordinated at room temperature. In other mixed-valence BCCPs it was observed a low-spin P heme signal at cryogenic temperatures, which has been attributed to a water molecule as the sixth axial ligand in substitution of the distal histidine ligand, as observed in the X-ray structures of these enzymes. In the mixed-valence *Ng*BCCP structure, the P heme catalytic site is identical to other mixed-valence BCCPs structures thus, the high-spin signal was attributed to the differences in the dimer interface (in the concentrations used the protein is expected to be a dimer).

This enzyme is conserved in *N. gonorrhoeae* and it is absent from human cells, making it a good candidate as a therapeutic target. The spectroscopic and kinetic studies in the presence of inhibitors presented in this chapter identified a few exogenous ligands that inhibit the *Ng*BCCP catalytic activity and, for the first time, it was determined the structure of an azide-inhibited BCCP. Nevertheless, the identification of additional exogenous ligands should be pursued in order to develop new compounds with higher affinity and specificity, which are non-toxic to humans.

In Chapter 4, it was performed a biochemical characterization of LAz from *N. gonorrhoeae* and determined its role as *Ng*BCCP physiological electron donor. The *Ng*BCCP/LAz ET pair was characterized and a model of the ET complex was created by using docking simulations. It is clear that *Ng*BCCP/LAz ET pair is adapted to the host environment, with maximum activity at pH and temperature values close to the physiological ones. Analysis of the surface and kinetic properties showed that this ET complex has a hydrophobic nature. LAz /NgBCCP interaction is dynamic, with a predicted dissociation constant in the micromolar range, forming a weak transient complex. Nevertheless, the expected higher concentration of these two proteins at the outer membrane due to their membrane attachement, should facilitate the formation of a productive complex. This trait, common to many proteins of the *Neisseria* genus (for instance AniA and Lip), seems to be directly connected to some of their distinct biochemical properties, as originally hypothesized in the objectives of this thesis.

The docking model of the complex suggested that the His118 that coordinates LAz copper atom, at the center of the hydrophobic patch surrounding the copper center, is involved in the electron transfer to the E heme of *Ng*BCCP.

Overall, the data presented in Chapter 4 supports the three important steps in the complex formation, common to many other ET complexes: i) pre-orientation due to a positive dipolar vector; ii) a binding step, which includes lateral mobility around the protein, ruled by weak hydrophobic effects; iii) and quick dissociation. The study of this ET complex presented a few challenges regarding the techniques used in this thesis and therefore new techniques and approaches should be considered in order to further characterize this protein complex.

In Chapter 5, it was presented a biochemical characterization of YhjA, a trihemic peroxidase from *E. coli* with three heme binding domains: two heme-binding domains in the C-terminal domain homologous to the classical BCCPs and a N-terminal domain with a single heme-binding domain.

In pathogenic bacteria the role of bacterial peroxidases is attributed to a defense mechanism against the host or other microorganisms during proliferation and infection, as proposed for *Ng*BCCP. In *E. coli*, an ubiquitous bacteria, this may be one of the possible roles of YhjA during an opportunistic infection however, as *yhjA* is overexpressed under anaerobic conditions, it was proposed a different role for this enzyme, as an oxidative stress defense mechanism when transitioning from anaerobic to aerobic conditions, which could be essential in habitats such as the gastrointestinal tract. Furthermore, YhjA is also present in other pathogenic bacteria such as *Salmonella* and *Yersinia* sp.

The spectroscopic characterization of the N-terminal domain was crucial to correctly characterize and assign the spectroscopic features of YhjA. For the first time it was identified the distal axial ligand of the N-terminal heme, the conserved Met125. Moreover, the mixed-valence YhjA EPR spectrum shows a high-spin signal assigned to the P heme, as observed for *Ng*BCCP. YhjA does not form a dimer as *Ng*BCCP and its P heme is always penta-coordinated regardless of the oxidation

state, as it has no distal histidine ligand in its primary sequence. Thus, the explanation proposed for this high-spin signal in *Ng*BCCP was not applicable to YhjA and possibly this feature is due to conformational changes in the P heme pocket. Therefore, the nature of this high-spin signal, as well as of the other unidentified signals in the EPR spectra, may be determined when a YhjA structure is available.

Steady-state kinetic assays showed that compared to dihemic BCCPS, YhjA is a poor peroxidase with K_M values in the millimolar range. YhjA has quinol peroxidase activity *in vitro*, and it was proposed that menaquinol, a quinol present in the *E. coli* inner membrane under anaerobic conditions, might be the physiological electron donor. The quinol is able to reduce the NT heme (+ 133 mV) and the E heme (+ 300 mV), as in the proposed mechanism of *A. actinomycetemcomitans* QPO [152].

Furthermore, the YhjA catalytic mechanism at the catalytic site was proposed to be similar to the one discussed for dihemic bacterial peroxidases in Chapter 3, due to the conserved primary sequence of the C-terminal domain. In YhjA and *Ng*BCCP the catalytic site residues are conserved, such as the glutamine and glutamate residues (Gln260/Glu270 and Gln164/Glu174, numbering of the native primary sequence of YhjA and *Ng*BCCP, respectively) proposed to play a key role in the catalytic mechanism. Furthermore, these two bacterial peroxidases share a p*Ka* value (p*Ka* of approximately 8.4) that we tentatively assigned to this conserved glutamine, as this residue is in close proximity to the iron atom of the P heme and it needs to be protonated in order to stabilize the Compound I, an intermediary species of the catalytic cycle, and possibly to donate one proton required for the reduction of Compound I to water, as in the proposed catalytic mechanism.

Additionally, it was identified a protein radical in the visible spectrum of as-isolated YhjA incubated with hydrogen peroxide, possibly from the conserved tryptophan between E and P domains, similar to what was previously described for the *P. aeruginosa* BCCP H71G mutant. This was an indication that the trihemic and dihemic peroxidases catalytic mechanism might be more similar than what might have been originally anticipated.

Therefore, the similar catalytic intermediates and the conserved primary sequence of the YhjA C-terminal domain suggest that the structural conformation of this domain will be similar to *Ng*BCCP and other dihemic BCCPs. The electron transfer pathway between the quinol and the E heme has still to be determined.

6.2 Future Perspectives

The *Ng*BCCP inhibition studies presented in this thesis were a first approach in order to identify inhibiting compounds of this enzyme. A systematic study with different inhibitors and conditions that mimic the physiological ones regarding pH value, ionic strength and temperature, should be useful not only to understand the inhibition mechanism.

Regarding the characterization of *Ng*BCCP/LAz ET pair, as stated in Chapter 4, the affinity constant and thermodynamic properties of this transient complex remain to be determined. Other experiments using surface plasmon resonance or fluorescence assays could be envisioned to determine the affinity constant. Paramagnetic relaxation enhancement NMR spectroscopy could be used in order to clearly identify the protein-protein interface by NMR, as it provides information on minor intermediary encounter species, such as the ones in weak transient complexes that form a "dynamic ensemble of orientations".

Regarding YhjA, new studies are needed in order to understand its role in a bacterium with a complex and highly diverse oxidative stress defense mechanism, as *E. coli*. In order to address the role of YhjA as a quinol peroxidase in the inner membranes, under anaerobic conditions, other *E. coli* K-12 mutant strains should be used for comparison to the WT, such as a *cyd* (cytochrome *bd*) null mutant and a double *yhjA* and *cyd* mutant, as cytochrome *bd* also has significant quinol peroxidase activity. Furthermore different quinol substrates should be tested, to address quinol specificity.

Regarding the quinol specificity, it is necessary to produce and purify the native, membrane bound YhjA, in order to determine the role of the transmembrane helix in the quinol peroxidase activity and to identify the quinol binding site residues. The latter would require extensive site-directed mutagenesis or a structure of the enzyme bounded to the physiological electron donor, which might be challenging due to the small yields (having as reference the yield of the recombinant YhjA reported in Chapter 5). Nevertheless, the recombinant YhjA used in this thesis is a good model for additional studies on the formation of catalytic intermediary species, either by EPR or electrochemistry, as in the oxidized YhjA there is no catalytic turnover.

Finally, in the future it would be essential to determine the YhjA structure by X-ray crystallography, as there is no available structure of a trihemic BCCP and some of the spectroscopic properties might be explained by its structural features. The determination of the crystallization conditions would allow to trap and identify intermediary species of the catalytic cycle by incubating YhjA crystals with hydrogen peroxide prior to cryo-cooling.

References

References

[1] Rich, P. R. (2003) The molecular machinery of Keilin's respiratory chain, *Biochem. Soc. Trans. 31*, 1095-1105.

[2] Reedy, C. J., and Gibney, B. R. (2004) Heme protein assemblies, *Chem. Rev. 104*, 617-649.

[3] Liu, J., Chakraborty, S., Hosseinzadeh, P., Yu, Y., Tian, S., Petrik, I., Bhagi, A., and Lu, Y. (2014) Metalloproteins containing cytochrome, iron-sulfur, or copper redox centers, *Chem. Rev. 114*, 4366-4469.

[4] Denisov, I. G., Makris, T. M., Sligar, S. G., and Schlichting, I. (2005) Structure and chemistry of cytochrome P450, *Chem. Rev. 105*, 2253-2277.

[5] Rodgers, K. R. (1999) Heme-based sensors in biological systems, *Curr. Opin. Chem. Biol. 3*, 158-167.

[6] Jiang, X., and Wang, X. (2004) Cytochrome *c*-mediated apoptosis, *Annu. Rev. Biochem. 73*, 87-106.

[7] Collman, J. P., Boulatov, R., Sunderland, C. J., and Fu, L. (2004) Functional analogues of cytochrome *c* oxidase, myoglobin, and hemoglobin, *Chem. Rev. 104*, 561-588.

[8] Berry, E. A., and Trumpower, B. L. (1987) Simultaneous determination of hemes *a*, *b*, and *c* from pyridine hemochrome spectra, *Anal. Biochem. 161*, 1-15.

[9] Smith, L. J. a. K. A. a. T. J. M. (2010) Heme proteins-diversity in structural characteristics, function, and folding., *Proteins 78*, 2349--2368.

[10] Brown, K. R., Allan, B. M., Do, P., and Hegg, E. L. (2002) Identification of novel hemes generated by heme A synthase: evidence for two successive monooxygenase reactions, *Biochemistry 41*, 10906-10913.

[11] Bowman, S. E., and Bren, K. L. (2008) The chemistry and biochemistry of heme *c*: functional bases for covalent attachment, *Nat. Prod. Rep. 25*, 1118-1130.

[12] Hederstedt, L. (2012) Heme A biosynthesis, *Biochim. Biophys. Acta 1817*, 920-927.

[13] Bali, S., Lawrence, A. D., Lobo, S. A., Saraiva, L. M., Golding, B. T., Palmer, D. J., Howard, M. J., Ferguson, S. J., and Warren, M. J. (2011) Molecular hijacking of siroheme for the synthesis of heme and d_1 heme, *Proc. Natl. Acad. Sci. U.S.A. 108*, 18260-18265.

[14] Sanders, C., Turkarslan, S., Lee, D. W., and Daldal, F. (2010) Cytochrome *c* biogenesis: the Ccm system, *Trends Microbiol. 18*, 266-274.

[15] Martinez, S. E., Huang, D., Ponomarev, M., Cramer, W. A., and Smith, J. L. (1996) The heme redox center of chloroplast cytochrome *f* is linked to a buried five-water chain, *Protein Sci. 5*, 1081-1092.

[16] Jüngst, A., Wakabayashi, S., Matsubara, H., and Zumft, W. G. (1991) The nirSTBM region coding for cytochrome cd_1-dependent nitrite respiration of Pseudomonas stutzeri consists of a cluster of mono-, di-, and tetraheme proteins, *FEBS Lett. 279*, 205-209.

[17] Jentzen, W., Ma, J. G., and Shelnutt, J. A. (1998) Conservation of the conformation of the porphyrin macrocycle in hemoproteins, *Biophys. J. 74*, 753-763.

[18] Hartshorne, R. S., Kern, M., Meyer, B., Clarke, T. A., Karas, M., Richardson, D. J., and Simon, J. (2007) A dedicated haem lyase is required for the maturation of a novel bacterial cytochrome *c* with unconventional covalent haem binding, *Mol. Microbiol. 64*, 1049-1060.

[19] Eaves, D. J., Grove, J., Staudenmann, W., James, P., Poole, R. K., White, S. A., Griffiths, I., and Cole, J. A. (1998) Involvement of products of the *nrf*EFG genes in the covalent attachment of haem *c* to a novel cysteine-lysine motif in the cytochrome c_{552} nitrite reductase from *Escherichia coli*, *Mol. Microbiol. 28*, 205-216.

[20] Einsle, O., Messerschmidt, A., Stach, P., Bourenkov, G. P., Bartunik, H. D., Huber, R., and Kroneck, P. M. (1999) Structure of cytochrome *c* nitrite reductase, *Nature 400*, 476-480.

[21] Weiss, R., Gold, A., and Terner, J. (2006) Cytochromes *c*': biological models for the S = 3/2, 5/2 spin-state admixture?, *Chem. Rev. 106*, 2550-2579.

[22] Atack, J. M., and Kelly, D. J. (2007) Structure, mechanism and physiological roles of bacterial cytochrome *c* peroxidases, *Adv. Microb. Physiol. 52*, 73-106.

[23] Fülöp, V., Moir, J. W., Ferguson, S. J., and Hajdu, J. (1995) The anatomy of a bifunctional enzyme: structural basis for reduction of oxygen to water and synthesis of nitric oxide by cytochrome cd_1, *Cell 81*, 369-377.

[24] Watmough, N. J., Cheesman, M. R., Butler, C. S., Little, R. H., Greenwood, C., and Thomson, A. J. (1998) The dinuclear center of cytochrome bo_3 from Escherichia coli, *J. Bioenerg. Biomembr. 30*, 55-62.

[25] Scheller, F. W., Yarman, A., Bachmann, T., Hirsch, T., Kubick, S., Renneberg, R., Schumacher, S., Wollenberger, U., Teller, C., and Bier, F. F. (2014) Future of biosensors: a personal view, *Adv. Biochem. Eng. Biotechnol. 140*, 1-28.

[26] Price, C. E., and Driessen, A. J. (2010) Biogenesis of membrane bound respiratory complexes in *Escherichia coli*, *Biochim. Biophys. Acta 1803*, 748-766.
[27] Clarke, T. A., Mills, P. C., Poock, S. R., Butt, J. N., Cheesman, M. R., Cole, J. A., Hinton, J. C., Hemmings, A. M., Kemp, G., Söderberg, C. A., Spiro, S., Van Wonderen, J., and Richardson, D. J. (2008) Escherichia coli cytochrome *c* nitrite reductase NrfA, *Methods Enzymol. 437*, 63-77.
[28] Pokkuluri, P. R., Londer, Y. Y., Duke, N. E., Pessanha, M., Yang, X., Orshonsky, V., Orshonsky, L., Erickson, J., Zagyanskiy, Y., Salgueiro, C. A., and Schiffer, M. (2011) Structure of a novel dodecaheme cytochrome *c* from *Geobacter sulfurreducens* reveals an extended 12 nm protein with interacting hemes, *J. Struct. Biol. 174*, 223-233.
[29] Ambler, R. P. (1991) Sequence variability in bacterial cytochromes *c*, *Biochim. Biophys. Acta 1058*, 42-47.
[30] Bertini, I., Cavallaro, G., and Rosato, A. (2006) Cytochrome *c*: occurrence and functions, *Chem. Rev. 106*, 90-115.
[31] Matias, P. M., Coelho, A. V., Valente, F. M., Plácido, D., LeGall, J., Xavier, A. V., Pereira, I. A., and Carrondo, M. A. (2002) Sulfate respiration in Desulfovibrio vulgaris Hildenborough. Structure of the 16-heme cytochrome *c* HmcA AT 2.5-A resolution and a view of its role in transmembrane electron transfer, *J. Biol. Chem. 277*, 47907-47916.
[32] Zheng, Z., and Gunner, M. R. (2009) Analysis of the electrochemistry of hemes with E(m)s spanning 800 mV, *Proteins 75*, 719-734.
[33] Moore, G. R., and Pettigrew, G. W. (1990) *Cytochromes c - Evolutionary, Structural and Physicochemical aspects*.
[34] Hillar, A., Peters, B., Pauls, R., Loboda, A., Zhang, H., Mauk, A. G., and Loewen, P. C. (2000) Modulation of the activities of catalase-peroxidase HPI of *Escherichia coli* by site-directed mutagenesis, *Biochemistry 39*, 5868-5875.
[35] Greenwood, C., Foote, N., Gadsby, P. M. A., and Thomson, A. J. (1988) A di-haem cytochrome *c* peroxidase (*Pseudomonas aeruginosa*): its activation and catalytic cycle, *Chem. Scripta 28A*, 79-84.
[36] Eaton, W. A., and Charney, E. (1969) Near-infrared absorption and circular dichroism spectra of ferrocytochrome *c*: *d-d* transitions, *J. Chem. Phys. 51*, 4502-4505.
[37] Rich, P. R., Moody, A. J., and Ingledew, W. J. (1992) Detection of a near infra-red absorption band of ferrohaem a_3 in cytochrome *c* oxidase, *FEBS Lett. 305*, 171-173.
[38] Shechter, E., and Saludjian, P. (1967) Conformation of ferricytochrome *c*. IV. Relationship between optical absorption and protein conformation, *Biopolymers 5*, 788-790.
[39] Smulevich, G. (1998) Understanding heme cavity structure of peroxidases: comparison of electronic absorption and resonance Raman spectra with crystallographic results, *Biospectroscopy 4*, S3-17.
[40] Zoppellaro, G., Bren, K. L., Ensign, A. A., Harbitz, E., Kaur, R., Hersleth, H. P., Ryde, U., Hederstedt, L., and Andersson, K. K. (2009) Review: studies of ferric heme proteins with highly anisotropic/highly axial low spin (S = 1/2) electron paramagnetic resonance signals with bis-histidine and histidine-methionine axial iron coordination, *Biopolymers 91*, 1064-1082.
[41] Taylor, C. P. (1977) The EPR of low spin heme complexes. Relation of the t_2g hole model to the directional properties of the *g* tensor, and a new method for calculating the ligand field parameters, *Biochim. Biophys. Acta 491*, 137-148.
[42] de Vries, S., and Albracht, S. P. (1979) Intensity of highly anisotropic low-spin heme EPR signals, *Biochim. Biophys. Acta 546*, 334-340.
[43] Peisach, J., and Mims, W. B. (1973) Linear electric field-induced shifts in electron paramagnetic resonance: a new method for study of the ligands of cytochrome P-450, *Proc. Natl. Acad. Sci. U.S.A. 70*, 2979-2982.
[44] Cabiscol, E., Tamarit, J., and Ros, J. (2000) Oxidative stress in bacteria and protein damage by reactive oxygen species, *Int. Microbiol. 3*, 3-8.
[45] Mishra, S., and Imlay, J. (2012) Why do bacteria use so many enzymes to scavenge hydrogen peroxide?, *Arch. Biochem. Biophys. 525*, 145-160.
[46] Naqui, A., Chance, B., and Cadenas, E. (1986) Reactive oxygen intermediates in biochemistry, *Annu. Rev. Biochem. 55*, 137-166.
[47] Massey, V., Strickland, S., Mayhew, S. G., Howell, L. G., Engel, P. C., Matthews, R. G., Schuman, M., and Sullivan, P. A. (1969) The production of superoxide anion radicals in the reaction of reduced flavins and flavoproteins with molecular oxygen, *Biochem. Biophys. Res. Commun. 36*, 891-897.
[48] Stohs, S. J., and Bagchi, D. (1995) Oxidative mechanisms in the toxicity of metal ions, *Free Radic. Biol. Med. 18*, 321-336.
[49] Bolton, J. L. (2002) Quinoids, quinoid radicals, and phenoxyl radicals formed from estrogens and antiestrogens, *Toxicology 177*, 55-65.

[50] Seaver, L. C., and Imlay, J. A. (2004) Are respiratory enzymes the primary sources of intracellular hydrogen peroxide?, *J. Biol. Chem. 279*, 48742-48750.
[51] Imlay, J. A. (2003) Pathways of oxidative damage, *Annu. Rev. Microbiol. 57*, 395-418.
[52] Apel, K., and Hirt, H. (2004) Reactive oxygen species: metabolism, oxidative stress, and signal transduction, *Annu. Rev. Plant. Biol. 55*, 373-399.
[53] Chiang, S. M., and Schellhorn, H. E. (2012) Regulators of oxidative stress response genes in *Escherichia coli* and their functional conservation in bacteria, *Arch. Biochem. Biophys. 525*, 161-169.
[54] Michán, C., Manchado, M., Dorado, G., and Pueyo, C. (1999) In vivo transcription of the *Escherichia coli* oxyR regulon as a function of growth phase and in response to oxidative stress, *J. Bacteriol. 181*, 2759-2764.
[55] Zheng, M., Wang, X., Templeton, L. J., Smulski, D. R., LaRossa, R. A., and Storz, G. (2001) DNA microarray-mediated transcriptional profiling of the *Escherichia coli* response to hydrogen peroxide, *J. Bacteriol. 183*, 4562-4570.
[56] Zheng, M., Aslund, F., and Storz, G. (1998) Activation of the OxyR transcription factor by reversible disulfide bond formation, *Science 279*, 1718-1721.
[57] Hausladen, A., Privalle, C. T., Keng, T., DeAngelo, J., and Stamler, J. S. (1996) Nitrosative stress: activation of the transcription factor OxyR, *Cell 86*, 719-729.
[58] Kim, S. O., Merchant, K., Nudelman, R., Beyer, W. F., Keng, T., DeAngelo, J., Hausladen, A., and Stamler, J. S. (2002) OxyR: a molecular code for redox-related signaling, *Cell 109*, 383-396.
[59] Herbig, A. F., and Helmann, J. D. (2001) Roles of metal ions and hydrogen peroxide in modulating the interaction of the *Bacillus subtilis* PerR peroxide regulon repressor with operator DNA, *Mol Microbiol 41*, 849-859.
[60] Lee, J. W., and Helmann, J. D. (2006) The PerR transcription factor senses H_2O_2 by metal-catalysed histidine oxidation, *Nature 440*, 363-367.
[61] Sethu, R., Gouré, E., Signor, L., Caux-Thang, C., Clémancey, M., Duarte, V., and Latour, J. M. (2016) Reaction of PerR with Molecular Oxygen May Assist H_2O_2 Sensing in Anaerobes, *ACS Chem. Biol. 11*, 1438-1444.
[62] Hassett, D. J., Charniga, L., Bean, K., Ohman, D. E., and Cohen, M. S. (1992) Response of *Pseudomonas aeruginosa* to pyocyanin: mechanisms of resistance, antioxidant defenses, and demonstration of a manganese-cofactored superoxide dismutase, *Infect. Immun. 60*, 328-336.
[63] Tsaneva, I. R., and Weiss, B. (1990) *sox*R, a locus governing a superoxide response regulon in *Escherichia coli* K-12, *J. Bacteriol. 172*, 4197-4205.
[64] Greenberg, J. T., Monach, P., Chou, J. H., Josephy, P. D., and Demple, B. (1990) Positive control of a global antioxidant defense regulon activated by superoxide-generating agents in *Escherichia coli*, *Proc. Natl. Acad. Sci. U.S.A. 87*, 6181-6185.
[65] Gaudu, P., Dubrac, S., and Touati, D. (2000) Activation of SoxR by overproduction of desulfoferrodoxin: multiple ways to induce the *soxRS* regulon, *J. Bacteriol. 182*, 1761-1763.
[66] Pomposiello, P. J., Bennik, M. H., and Demple, B. (2001) Genome-wide transcriptional profiling of the *Escherichia coli* responses to superoxide stress and sodium salicylate, *J. Bacteriol. 183*, 3890-3902.
[67] Kobayashi, K., and Tagawa, S. (2004) Activation of SoxR-dependent transcription in *Pseudomonas aeruginosa*, *J. Biochem. 136*, 607-615.
[68] Palma, M., Zurita, J., Ferreras, J. A., Worgall, S., Larone, D. H., Shi, L., Campagne, F., and Quadri, L. E. (2005) *Pseudomonas aeruginosa* SoxR does not conform to the archetypal paradigm for SoxR-dependent regulation of the bacterial oxidative stress adaptive response, *Infect. Immun. 73*, 2958-2966.
[69] Lynch, M., and Kuramitsu, H. (2000) Expression and role of superoxide dismutases (SOD) in pathogenic bacteria, *Microbes Infect. 2*, 1245-1255.
[70] Gort, A. S., Ferber, D. M., and Imlay, J. A. (1999) The regulation and role of the periplasmic copper, zinc superoxide dismutase of *Escherichia coli*, *Mol. Microbiol. 32*, 179-191.
[71] Niederhoffer, E. C., Naranjo, C. M., Bradley, K. L., and Fee, J. A. (1990) Control of *Escherichia coli* superoxide dismutase (*sodA* and *sodB*) genes by the ferric uptake regulation (fur) locus, *J. Bacteriol. 172*, 1930-1938.
[72] Massé, E., and Gottesman, S. (2002) A small RNA regulates the expression of genes involved in iron metabolism in *Escherichia coli*, *Proc. Natl. Acad. Sci. U.S.A. 99*, 4620-4625.
[73] Compan, I., and Touati, D. (1993) Interaction of six global transcription regulators in expression of manganese superoxide dismutase in *Escherichia coli* K-12, *J. Bacteriol. 175*, 1687-1696.
[74] Kroll, J. S., Langford, P. R., Wilks, K. E., and Keil, A. D. (1995) Bacterial [Cu,Zn]-superoxide dismutase: phylogenetically distinct from the eukaryotic enzyme, and not so rare after all!, *Microbiology 141 (9)*, 2271-2279.

[75] Wilks, K. E., Dunn, K. L., Farrant, J. L., Reddin, K. M., Gorringe, A. R., Langford, P. R., and Kroll, J. S. (1998) Periplasmic superoxide dismutase in meningococcal pathogenicity, *Infect. Immun. 66*, 213-217.

[76] Battistoni, A., Donnarumma, G., Greco, R., Valenti, P., and Rotilio, G. (1998) Overexpression of a hydrogen peroxide-resistant periplasmic Cu,Zn superoxide dismutase protects *Escherichia coli* from macrophage killing, *Biochem. Biophys. Res. Commun. 243*, 804-807.

[77] Farr, S. B., D'Ari, R., and Touati, D. (1986) Oxygen-dependent mutagenesis in *Escherichia coli* lacking superoxide dismutase, *Proc. Natl. Acad. Sci. U.S.A. 83*, 8268-8272.

[78] Imlay, J. A., and Fridovich, I. (1991) Assay of metabolic superoxide production in *Escherichia coli*, *J. Biol. Chem. 266*, 6957-6965.

[79] Kono, Y., and Fridovich, I. (1983) Isolation and characterization of the pseudocatalase of *Lactobacillus plantarum*, *J. Biol. Chem. 258*, 6015-6019.

[80] Zamocky, M., Furtmüller, P. G., and Obinger, C. (2008) Evolution of catalases from bacteria to humans, *Antioxid. Redox Signal. 10*, 1527-1548.

[81] Hillar, A., and Nicholls, P. (1992) A mechanism for NADPH inhibition of catalase compound II formation, *FEBS Lett. 314*, 179-182.

[82] Chelikani, P., Fita, I., and Loewen, P. C. (2004) Diversity of structures and properties among catalases, *Cell Mol. Life Sci. 61*, 192-208.

[83] Horsburgh, M. J., Ingham, E., and Foster, S. J. (2001) In *Staphylococcus aureus*, fur is an interactive regulator with PerR, contributes to virulence, and Is necessary for oxidative stress resistance through positive regulation of catalase and iron homeostasis, *J. Bacteriol. 183*, 468-475.

[84] Schellhorn, H. E., and Hassan, H. M. (1988) Transcriptional regulation of *katE* in *Escherichia coli* K-12, *J. Bacteriol. 170*, 4286-4292.

[85] Brunder, W., Schmidt, H., and Karch, H. (1996) KatP, a novel catalase-peroxidase encoded by the large plasmid of enterohaemorrhagic *Escherichia coli* O157:H7, *Microbiology 142 (Pt 11)*, 3305-3315.

[86] Poole, L. B. (2005) Bacterial defenses against oxidants: mechanistic features of cysteine-based peroxidases and their flavoprotein reductases, *Arch. Biochem. Biophys. 433*, 240-254.

[87] Poole, L. B., Reynolds, C. M., Wood, Z. A., Karplus, P. A., Ellis, H. R., and Li Calzi, M. (2000) AhpF and other NADH:peroxiredoxin oxidoreductases, homologues of low Mr thioredoxin reductase, *Eur. J. Biochem. 267*, 6126-6133.

[88] Seaver, L. C., and Imlay, J. A. (2001) Alkyl hydroperoxide reductase is the primary scavenger of endogenous hydrogen peroxide in *Escherichia coli*, *J. Bacteriol. 183*, 7173-7181.

[89] Reeves, S. A., Parsonage, D., Nelson, K. J., and Poole, L. B. (2011) Kinetic and thermodynamic features reveal that *Escherichia coli* BCP is an unusually versatile peroxiredoxin, *Biochemistry 50*, 8970-8981.

[90] Jeong, W., Cha, M. K., and Kim, I. H. (2000) Thioredoxin-dependent hydroperoxide peroxidase activity of bacterioferritin comigratory protein (BCP) as a new member of the thiol-specific antioxidant protein (TSA)/Alkyl hydroperoxide peroxidase C (AhpC) family, *J. Biol. Chem. 275*, 2924-2930.

[91] Atack, J. M., Harvey, P., Jones, M. A., and Kelly, D. J. (2008) The *Campylobacter jejuni* thiol peroxidases Tpx and Bcp both contribute to aerotolerance and peroxide-mediated stress resistance but have distinct substrate specificities, *J. Bacteriol. 190*, 5279-5290.

[92] Wang, G., Olczak, A. A., Walton, J. P., and Maier, R. J. (2005) Contribution of the *Helicobacter pylori* thiol peroxidase bacterioferritin comigratory protein to oxidative stress resistance and host colonization, *Infect. Immun. 73*, 378-384.

[93] Tao, K. (2008) Subcellular localization and in vivo oxidation-reduction kinetics of thiol peroxidase in *Escherichia coli*, *FEMS Microbiol. Lett. 289*, 41-45.

[94] Cha, M. K., Kim, W. C., Lim, C. J., Kim, K., and Kim, I. H. (2004) *Escherichia coli* periplasmic thiol peroxidase acts as lipid hydroperoxide peroxidase and the principal antioxidative function during anaerobic growth, *J. Biol. Chem. 279*, 8769-8778.

[95] Rhee, S. G., Chae, H. Z., and Kim, K. (2005) Peroxiredoxins: a historical overview and speculative preview of novel mechanisms and emerging concepts in cell signaling, *Free Radic. Biol. Med. 38*, 1543-1552.

[96] Chae, H. Z., Chung, S. J., and Rhee, S. G. (1994) Thioredoxin-dependent peroxide reductase from yeast, *J. Biol. Chem. 269*, 27670-27678.

[97] Master, S. S., Springer, B., Sander, P., Boettger, E. C., Deretic, V., and Timmins, G. S. (2002) Oxidative stress response genes in *Mycobacterium tuberculosis*: role of ahpC in resistance to peroxynitrite and stage-specific survival in macrophages, *Microbiology 148*, 3139-3144.

[98] Pérez, J. M., Arenas, F. A., Pradenas, G. A., Sandoval, J. M., and Vásquez, C. C. (2008) *Escherichia coli* YqhD exhibits aldehyde reductase activity and protects from the harmful effect of lipid peroxidation-derived aldehydes, *J. Biol. Chem. 283*, 7346-7353.

[99] Nichols, D. S. (2003) Prokaryotes and the input of polyunsaturated fatty acids to the marine food web, *FEMS Microbiol. Lett. 219*, 1-7.
[100] Flohe, L., Günzler, W. A., and Schock, H. H. (1973) Glutathione peroxidase: a selenoenzyme, *FEBS Lett. 32*, 132-134.
[101] Arenas, F. A., Covarrubias, P. C., Sandoval, J. M., Pérez-Donoso, J. M., Imlay, J. A., and Vásquez, C. C. (2011) The *Escherichia coli* BtuE protein functions as a resistance determinant against reactive oxygen species, *PLoS One 6*, e15979.
[102] Ohdate, T., Kita, K., and Inoue, Y. (2010) Kinetics and redox regulation of Gpx1, an atypical 2-Cys peroxiredoxin, in *Saccharomyces cerevisiae*, *FEMS Yeast Res. 10*, 787-790.
[103] La Carbona, S., Sauvageot, N., Giard, J. C., Benachour, A., Posteraro, B., Auffray, Y., Sanguinetti, M., and Hartke, A. (2007) Comparative study of the physiological roles of three peroxidases (NADH peroxidase, Alkyl hydroperoxide reductase and Thiol peroxidase) in oxidative stress response, survival inside macrophages and virulence of *Enterococcus faecalis*, *Mol. Microbiol. 66*, 1148-1163.
[104] LeGall, J., Prickril, B. C., Moura, I., Xavier, A. V., Moura, J. J., and Huynh, B. H. (1988) Isolation and characterization of rubrerythrin, a non-heme iron protein from *Desulfovibrio vulgaris* that contains rubredoxin centers and a hemerythrin-like binuclear iron cluster, *Biochemistry 27*, 1636-1642.
[105] Riebe, O., Fischer, R. J., Wampler, D. A., Kurtz, D. M., and Bahl, H. (2009) Pathway for H_2O_2 and O_2 detoxification in Clostridium acetobutylicum, *Microbiology 155*, 16-24.
[106] Weinberg, M. V., Jenney, F. E., Cui, X., and Adams, M. W. (2004) Rubrerythrin from the hyperthermophilic archaeon *Pyrococcus furiosus* is a rubredoxin-dependent, iron-containing peroxidase, *J. Bacteriol. 186*, 7888-7895.
[107] Goodhew, C. F., Wilson, I. B., Hunter, D. J., and Pettigrew, G. W. (1990) The cellular location and specificity of bacterial cytochrome *c* peroxidases, *Biochem. J. 271*, 707-712.
[108] Fülöp, V., Ridout, C. J., Greenwood, C., and Hajdu, J. (1995) Crystal structure of the di-haem cytochrome *c* peroxidase from *Pseudomonas aeruginosa*, *Structure 3*, 1225-1233.
[109] Erman, J. E., and Vitello, L. B. (2002) Yeast cytochrome *c* peroxidase: mechanistic studies via protein engineering, *Biochim. Biophys. Acta 1597*, 193-220.
[110] Payne, T. M., Yee, E. F., Dzikovski, B., and Crane, B. R. (2016) Constraints on the Radical Cation Center of Cytochrome *c* Peroxidase for Electron Transfer from Cytochrome *c*, *Biochemistry 55*, 4807-4822.
[111] Veitch, N. C. (2004) Horseradish peroxidase: a modern view of a classic enzyme, *Phytochemistry 65*, 249-259.
[112] Grigorenko, V. G., Andreeva, I. P., Rubtsova, M. Y., and Egorov, A. M. (2015) Recombinant horseradish peroxidase: production and analytical applications, *Biochemistry (Mosc) 80*, 408-416.
[113] Dietz, K. J. (2016) Thiol-Based Peroxidases and Ascorbate Peroxidases: Why Plants Rely on Multiple Peroxidase Systems in the Photosynthesizing Chloroplast?, *Mol. Cells 39*, 20-25.
[114] Falade, A. O., Nwodo, U. U., Iweriebor, B. C., Green, E., Mabinya, L. V., and Okoh, A. I. (2017) Lignin peroxidase functionalities and prospective applications, *MicrobiologyOpen 6*.
[115] Seidel, J., Hoffmann, M., Ellis, K. E., Seidel, A., Spatzal, T., Gerhardt, S., Elliott, S. J., and Einsle, O. (2012) MacA is a second cytochrome *c* peroxidase of *Geobacter sulfurreducens*, *Biochemistry 51*, 2747-2756.
[116] Bingham-Ramos, L. K., and Hendrixson, D. R. (2008) Characterization of two putative cytochrome *c* peroxidases of *Campylobacter jejuni* involved in promoting commensal colonization of poultry, *Infect. Immun. 76*, 1105-1114.
[117] Spiro, S., and Guest, J. R. (1990) FNR and its role in oxygen-regulated gene expression in *Escherichia coli*, *FEMS Microbiol. Rev. 6*, 399-428.
[118] Turner, S., Reid, E., Smith, H., and Cole, J. (2003) A novel cytochrome *c* peroxidase from *Neisseria gonorrhoeae*: a lipoprotein from a Gram-negative bacterium, *Biochem. J. 373*, 865-873.
[119] Lissenden, S., Mohan, S., Overton, T., Regan, T., Crooke, H., Cardinale, J. A., Householder, T. C., Adams, P., O'Conner, C. D., Clark, V. L., Smith, H., and Cole, J. A. (2000) Identification of transcription activators that regulate gonococcal adaptation from aerobic to anaerobic or oxygen-limited growth, *Mol. Microbiol. 37*, 839-855.
[120] Van Spanning, R. J., De Boer, A. P., Reijnders, W. N., Westerhoff, H. V., Stouthamer, A. H., and Van Der Oost, J. (1997) FnrP and NNR of *Paracoccus denitrificans* are both members of the FNR family of transcriptional activators but have distinct roles in respiratory adaptation in response to oxygen limitation, *Mol. Microbiol. 23*, 893-907.
[121] Vollack, K. U., Härtig, E., Körner, H., and Zumft, W. G. (1999) Multiple transcription factors of the FNR family in denitrifying *Pseudomonas stutzeri*: characterization of four *fnr*-like genes, regulatory responses and cognate metabolic processes, *Mol. Microbiol. 31*, 1681-1694.

[122] Li, N., Luo, Q., Jiang, Y., Wu, G., and Gao, H. (2014) Managing oxidative stresses in *Shewanella oneidensis*: intertwined roles of the OxyR and OhrR regulons, *Environ. Microbiol. 16*, 1821-1834.

[123] Partridge, J. D., Poole, R. K., and Green, J. (2007) The *Escherichia coli* yhjA gene, encoding a predicted cytochrome *c* peroxidase, is regulated by FNR and OxyR, *Microbiology 153*, 1499-1507.

[124] Soininen, R., and Ellfolk, N. (1972) *Pseudomonas* cytochrome *c* peroxidase. IV. Some kinetic properties of the peroxidation reaction, and enzymatic determination of the extinction coefficients of *Pseudomonas* cytochrome *c*-551 and azurin, *Acta Chem. Scand. 26*, 861-872.

[125] Soininen, R., and Ellfolk, N. (1973) *Pseudomonas* cytochrome c peroxidase. V. Absorption spectra of the enzyme and of its compounds with ligands. Inhibition of the enzyme by cyanide and azide, *Acta Chem. Scand. 27*, 35-46.

[126] Arciero, D. M., and Hooper, A. B. (1994) A di-heme cytochrome *c* peroxidase from *Nitrosomonas europaea* catalytically active in both the oxidized and half-reduced states, *J. Biol. Chem. 269*, 11878-11886.

[127] De Smet, L., Pettigrew, G. W., and Van Beeumen, J. J. (2001) Cloning, overproduction and characterization of cytochrome *c* peroxidase from the purple phototrophic bacterium *Rhodobacter capsulatus*, *Eur. J. Biochem. 268*, 6559-6568.

[128] Zahn, J. A., Arciero, D. M., Hooper, A. B., Coats, J. R., and DiSpirito, A. A. (1997) Cytochrome *c* peroxidase from *Methylococcus capsulatus* Bath, *Arch. Microbiol. 168*, 362-372.

[129] Timóteo, C. G., Tavares, P., Goodhew, C. F., Duarte, L. C., Jumel, K., Gírio, F. M., Harding, S., Pettigrew, G. W., and Moura, I. (2003) Ca^{2+} and the bacterial peroxidases: the cytochrome *c* peroxidase from *Pseudomonas stutzeri*, *J. Biol. Inorg. Chem. 8*, 29-37.

[130] Alves, T., Besson, S., Duarte, L. C., Pettigrew, G. W., Girio, F. M., Devreese, B., Vandenberghe, I., Van Beeumen, J., Fauque, G., and Moura, I. (1999) A cytochrome *c* peroxidase from *Pseudomonas nautica* 617 active at high ionic strength: expression, purification and characterization, *Biochim. Biophys. Acta 1434*, 248-259.

[131] Pulcu, G. S., Frato, K. E., Gupta, R., Hsu, H. R., Levine, G. A., Hendrich, M. P., and Elliott, S. J. (2012) The diheme cytochrome *c* peroxidase from *Shewanella oneidensis* requires reductive activation, *Biochemistry 51*, 974-985.

[132] Hoffmann, M., Seidel, J., and Einsle, O. (2009) CcpA from *Geobacter sulfurreducens* is a basic di-heme cytochrome *c* peroxidase, *J. Mol. Biol. 393*, 951-965.

[133] Ellis, K. E., Seidel, J., Einsle, O., and Elliott, S. J. (2011) *Geobacter sulfurreducens* cytochrome *c* peroxidases: electrochemical classification of catalytic mechanisms, *Biochemistry 50*, 4513-4520.

[134] Bradley, A. L., Chobot, S. E., Arciero, D. M., Hooper, A. B., and Elliott, S. J. (2004) A distinctive electrocatalytic response from the cytochrome *c* peroxidase of *Nitrosomonas europaea*, *J. Biol. Chem. 279*, 13297-13300.

[135] Elliott, S. J., Bradley, A. L., Arciero, D. M., and Hooper, A. B. (2007) Protonation and inhibition of *Nitrosomonas europaea* cytochrome *c* peroxidase observed with protein film voltammetry, *J. Inorg. Biochem. 101*, 173-179.

[136] Paes de Sousa, P. M., Pauleta, S. R., Gonçalves, M. L., Pettigrew, G. W., Moura, I., Dos Santos, M. M., and Moura, J. J. (2007) Mediated catalysis of *Paracoccus pantotrophus* cytochrome *c* peroxidase by *P. pantotrophus* pseudoazurin: kinetics of intermolecular electron transfer, *J. Biol. Inorg. Chem. 12*, 691-698.

[137] Gilmour, R., Goodhew, C. F., Pettigrew, G. W., Prazeres, S., Moura, I., and Moura, J. J. (1993) Spectroscopic characterization of cytochrome *c* peroxidase from *Paracoccus denitrificans*, *Biochem. J. 294 (Pt 3)*, 745-752.

[138] Gilmour, R., Goodhew, C. F., Pettigrew, G. W., Prazeres, S., Moura, J. J., and Moura, I. (1994) The kinetics of the oxidation of cytochrome *c* by *Paracoccus* cytochrome c peroxidase, *Biochem. J. 300 (Pt 3)*, 907-914.

[139] Pauleta, S. R., Guerlesquin, F., Goodhew, C. F., Devreese, B., Van Beeumen, J., Pereira, A. S., Moura, I., and Pettigrew, G. W. (2004) *Paracoccus pantotrophus* pseudoazurin is an electron donor to cytochrome *c* peroxidase, *Biochemistry 43*, 11214-11225.

[140] Ellfolk, N., Rönnberg, M., Aasa, R., Andréasson, L. E., and Vänngård, T. (1983) Properties and function of the two hemes in *Pseudomonas* cytochrome *c* peroxidase, *Biochim. Biophys. Acta 743*, 23-30.

[141] Foote, N., Turner, R., Brittain, T., and Greenwood, C. (1992) A quantitative model for the mechanism of action of the cytochrome *c* peroxidase of *Pseudomonas aeruginosa*, *Biochem. J. 283*, 839-843.

[142] Rönnberg, M., and Ellfolk, N. (1975) *Pseudomonas* cytochrome *c* peroxidase XI. Kinetics of the peroxidatic oxidation of Pseudomonas respiratory chain components, *Acta Chem. Scand. B 29*, 719-727.

[143] Rönnberg, M., Ellfolk, N., and Dunford, H. B. (1984) The formation of the primary hydrogen peroxide compound (compound I) of *Pseudomonas* cytochrome *c* peroxidase as a function of pH, *Acta Chem. Scand. B 38*, 79-83.

[144] Becker, C. F., Watmough, N. J., and Elliott, S. J. (2009) Electrochemical evidence for multiple peroxidatic heme states of the diheme cytochrome *c* peroxidase of *Pseudomonas aeruginosa*, *Biochemistry 48*, 87-95.

[145] Hu, W., De Smet, L., Van Driessche, G., Bartsch, R. G., Meyer, T. E., Cusanovich, M. A., and Van Beeumen, J. (1998) Characterization of cytochrome *c*-556 from the purple phototrophic bacterium *Rhodobacter capsulatus* as a cytochrome-*c* peroxidase, *Eur. J. Biochem. 258*, 29-36.

[146] Frato, K. E., Walsh, K. A., and Elliott, S. J. (2016) Functionally Distinct Bacterial Cytochrome *c* Peroxidases Proceed through a Common (Electro)catalytic Intermediate, *Biochemistry 55*, 125-132.

[147] Schütz, B., Seidel, J., Sturm, G., Einsle, O., and Gescher, J. (2011) Investigation of the electron transport chain to and the catalytic activity of the diheme cytochrome *c* peroxidase CcpA of *Shewanella oneidensis*, *Appl. Environ. Microbiol. 77*, 6172-6180.

[148] McClure, R., Nudel, K., Massari, P., Tjaden, B., Su, X., Rice, P. A., and Genco, C. A. (2015) The Gonococcal Transcriptome during Infection of the Lower Genital Tract in Women, *PLoS One 10*, e0133982.

[149] Yamada, H., Takashima, E., and Konishi, K. (2007) Molecular characterization of the membrane-bound quinol peroxidase functionally connected to the respiratory chain, *FEBS J. 274*, 853-866.

[150] Takashima, E., and Konishi, K. (2008) Characterization of a quinol peroxidase mutant in *Aggregatibacter actinomycetemcomitans*, *FEMS Microbiol. Lett. 286*, 66-70.

[151] Takashima, E., Yamada, H., Yamashita, T., Matsushita, K., and Konishi, K. (2010) Recombinant expression and redox properties of triheme *c* membrane-bound quinol peroxidase, *FEMS Microbiol. Lett. 302*, 52-57.

[152] Abe, T., Kawarai, T., Takahashi, Y., and Konishi, K. (2017) Enzymatic kinetics of the quinol peroxidase of an aggressive periodontopathic bacterium, *J. Biochem.*

[153] Balodite, E., Strazdina, I., Galinina, N., McLean, S., Rutkis, R., Poole, R. K., and Kalnenieks, U. (2014) Structure of the *Zymomonas mobilis* respiratory chain: oxygen affinity of electron transport and the role of cytochrome *c* peroxidase, *Microbiology 160*, 2045-2052.

[154] Wang, Y., Graichen, M. E., Liu, A., Pearson, A. R., Wilmot, C. M., and Davidson, V. L. (2003) MauG, a novel diheme protein required for tryptophan tryptophylquinone biogenesis, *Biochemistry 42*, 7318-7325.

[155] Wang, Y., Li, X., Jones, L. H., Pearson, A. R., Wilmot, C. M., and Davidson, V. L. (2005) MauG-dependent in vitro biosynthesis of tryptophan tryptophylquinone in methylamine dehydrogenase, *J. Am. Chem. Soc. 127*, 8258-8259.

[156] Braaz, R., Armbruster, W., and Jendrossek, D. (2005) Heme-dependent rubber oxygenase RoxA of *Xanthomonas* sp. cleaves the carbon backbone of poly(cis-1,4-Isoprene) by a dioxygenase mechanism, *Appl. Environ. Microbiol. 71*, 2473-2478.

[157] Seidel, J., Schmitt, G., Hoffmann, M., Jendrossek, D., and Einsle, O. (2013) Structure of the processive rubber oxygenase RoxA from *Xanthomonas* sp., *Proc. Natl. Acad. Sci. U.S.A. 110*, 13833-13838.

[158] Ronnberg, M., Araiso, T., Ellfolk, N., and Dunford, H. B. (1981) The reaction between reduced azurin and oxidized cytochrome *c* peroxidase from *Pseudomonas aeruginosa*, *J. Biol. Chem. 256*, 2471-2474.

[159] Pettigrew, G. W., Prazeres, S., Costa, C., Palma, N., Krippahl, L., Moura, I., and Moura, J. J. (1999) The structure of an electron transfer complex containing a cytochrome *c* and a peroxidase, *J. Biol. Chem. 274*, 11383-11389.

[160] Foote, N., Peterson, J., Gadsby, P. M., Greenwood, C., and Thomson, A. J. (1984) A study of the oxidized form of *Pseudomonas aeruginosa* cytochrome *c*-551 peroxidase with the use of magnetic circular dichroism, *Biochem. J. 223*, 369-378.

[161] Foote, N., Peterson, J., Gadsby, P. M., Greenwood, C., and Thomson, A. J. (1985) Redox-linked spin-state changes in the di-haem cytochrome *c*-551 peroxidase from *Pseudomonas aeruginosa*, *Biochem. J. 230*, 227-237.

[162] Gilmour, R., Prazeres, S., McGinnity, D. F., Goodhew, C. F., Moura, J. J., Moura, I., and Pettigrew, G. W. (1995) The affinity and specificity of Ca(2+)-binding sites of cytochrome-*c* peroxidase from *Paracoccus denitrificans*, *Eur. J. Biochem. 234*, 878-886.

[163] Pettigrew, G. W., Goodhew, C. F., Cooper, A., Nutley, M., Jumel, K., and Harding, S. E. (2003) The electron transfer complexes of cytochrome *c* peroxidase from *Paracoccus denitrificans*, *Biochemistry 42*, 2046-2055.

[164] Pettigrew, G. W., Pauleta, S. R., Goodhew, C. F., Cooper, A., Nutley, M., Jumel, K., Harding, S. E., Costa, C., Krippahl, L., Moura, I., and Moura, J. (2003) Electron transfer complexes of cytochrome *c*

peroxidase from *Paracoccus denitrificans* containing more than one cytochrome, *Biochemistry 42*, 11968-11981.

[165] Paes de Sousa, P. M., Rodrigues, D., Timóteo, C. G., Simões Gonçalves, M. L., Pettigrew, G. W., Moura, I., Moura, J. J., and Correia dos Santos, M. M. (2011) Analysis of the activation mechanism of *Pseudomonas stutzeri* cytochrome *c* peroxidase through an electron transfer chain, *J. Biol. Inorg. Chem. 16*, 881-888.

[166] Echalier, A., Brittain, T., Wright, J., Boycheva, S., Mortuza, G. B., Fülöp, V., and Watmough, N. J. (2008) Redox-linked structural changes associated with the formation of a catalytically competent form of the diheme cytochrome c peroxidase from *Pseudomonas aeruginosa*, *Biochemistry 47*, 1947-1956.

[167] Shimizu, H., Schuller, D. J., Lanzilotta, W. N., Sundaramoorthy, M., Arciero, D. M., Hooper, A. B., and Poulos, T. L. (2001) Crystal structure of *Nitrosomonas europaea* cytochrome *c* peroxidase and the structural basis for ligand switching in bacterial di-heme peroxidases, *Biochemistry 40*, 13483-13490.

[168] De Smet, L., Leys, D., and Van Beeumen, J. J. (2002) Crystallization and preliminary X-ray diffraction analysis of cytochrome c peroxidase from the purple phototrophic bacterium *Rhodobacter capsulatus*, *Acta Crystallogr. D Biol. Crystallogr. 58*, 522-523.

[169] De Smet, L., Savvides, S. N., Van Horen, E., Pettigrew, G., and Van Beeumen, J. J. (2006) Structural and mutagenesis studies on the cytochrome *c* peroxidase from *Rhodobacter capsulatus* provide new insights into structure-function relationships of bacterial di-heme peroxidases, *J. Biol. Chem. 281*, 4371-4379.

[170] Lee, Y., Boycheva, S., Brittain, T., and Boyd, P. D. (2007) Intramolecular electron transfer in the dihaem cytochrome *c* peroxidase of *Pseudomonas aeruginosa*, *Chembiochem 8*, 1440-1446.

[171] Echalier, A., Goodhew, C. F., Pettigrew, G. W., and Fülöp, V. (2006) Activation and catalysis of the di-heme cytochrome *c* peroxidase from *Paracoccus pantotrophus*, *Structure 14*, 107-117.

[172] Dias, J. M., Alves, T., Bonifácio, C., Pereira, A. S., Trincão, J., Bourgeois, D., Moura, I., and Romão, M. J. (2004) Structural basis for the mechanism of Ca(2+) activation of the di-heme cytochrome *c* peroxidase from *Pseudomonas nautica* 617, *Structure 12*, 961-973.

[173] Prazeres, S., Moura, I., Moura, J. J. G., Gilmour, R., Goodhew, C. F., and Pettigrew, G. W. (1993) Control of the spin state of the peroxidatic haem by calcium ions in cytochrome *c* peroxidase from *Paracoccus denitrificans*: A 1H NMR study, *Magn. Reson. Chem. 31*, 68-72.

[174] Prazeres, S., Moura, J. J., Moura, I., Gilmour, R., Goodhew, C. F., Pettigrew, G. W., Ravi, N., and Huynh, B. H. (1995) Mössbauer characterization of *Paracoccus denitrificans* cytochrome *c* peroxidase. Further evidence for redox and calcium binding-induced heme-heme interaction, *J. Biol. Chem. 270*, 24264-24269.

[175] Pauleta, S. R., Lu, Y., Goodhew, C. F., Moura, I., Pettigrew, G. W., and Shelnutt, J. A. (2001) Calcium-dependent conformation of a heme and fingerprint peptide of the diheme cytochrome *c* peroxidase from *Paracoccus pantotrophus*, *Biochemistry 40*, 6570-6579.

[176] Pauleta, S. R., Lu, Y., Goodhew, C. F., Moura, I., Pettigrew, G. W., and Shelnutt, J. A. (2008) Calcium-dependent heme structure in the reduced forms of the bacterial cytochrome *c* peroxidase from *Paracoccus pantotrophus*, *Biochemistry 47*, 5841-5850.

[177] Rönnberg, M., Osterlund, K., and Ellfolk, N. (1980) Resonance Raman spectra of Pseudomonas cytochrome *c* peroxidase, *Biochim. Biophys. Acta 626*, 23-30.

[178] Ellis, K. E., Frato, K. E., and Elliott, S. J. (2012) Impact of quaternary structure upon bacterial cytochrome *c* peroxidases: does homodimerization matter?, *Biochemistry 51*, 10008-10016.

[179] Pettigrew, G. W., Echalier, A., and Pauleta, S. R. (2006) Structure and mechanism in the bacterial dihaem cytochrome *c* peroxidases, *J. Inorg. Biochem. 100*, 551-567.

[180] Rönnberg, M., Lambeir, A. M., Ellfolk, N., and Dunford, H. B. (1985) A rapid-scan spectrometric and stopped-flow study of compound I and compound II of *Pseudomonas* cytochrome *c* peroxidase, *Arch. Biochem. Biophys. 236*, 714-719.

[181] Morimoto, A., Tanaka, M., Takahashi, S., Ishimori, K., Hori, H., and Morishima, I. (1998) Detection of a tryptophan radical as an intermediate species in the reaction of horseradish peroxidase mutant (Phe-221 --> Trp) and hydrogen peroxide, *J. Biol. Chem. 273*, 14753-14760.

[182] Hsiao, H. C., Boycheva, S., Watmough, N. J., and Brittain, T. (2007) Activation of the cytochrome *c* peroxidase of *Pseudomonas aeruginosa*. The role of a heme-linked protein loop: a mutagenesis study, *J. Inorg. Biochem. 101*, 1133-1139.

[183] Casadei, C. M., Gumiero, A., Metcalfe, C. L., Murphy, E. J., Basran, J., Concilio, M. G., Teixeira, S. C., Schrader, T. E., Fielding, A. J., Ostermann, A., Blakeley, M. P., Raven, E. L., and Moody, P. C. (2014) Heme enzymes. Neutron cryo-crystallography captures the protonation state of ferryl heme in a peroxidase, *Science 345*, 193-197.

[184] Pauleta, S. R., Cooper, A., Nutley, M., Errington, N., Harding, S., Guerlesquin, F., Goodhew, C. F., Moura, I., Moura, J. J., and Pettigrew, G. W. (2004) A copper protein and a cytochrome bind at the same site on bacterial cytochrome *c* peroxidase, *Biochemistry 43*, 14566-14576.

[185] Koh, M., Meyer, T. E., De Smet, L., Van Beeumen, J. J., and Cusanovich, M. A. (2003) Characterization of the interaction of *Rhodobacter capsulatus* cytochrome *c* peroxidase with charge reversal mutants of cytochrome *c*(2), *Arch. Biochem. Biophys. 410*, 230-237.

[186] Tamura, K., Stecher, G., Peterson, D., Filipski, A., and Kumar, S. (2013) MEGA6: Molecular Evolutionary Genetics Analysis version 6.0, *Mol. Biol. Evol. 30*, 2725-2729.

[187] Thompson, J. D., Higgins, D. G., and Gibson, T. J. (1994) CLUSTAL W: improving the sensitivity of progressive multiple sequence alignment through sequence weighting, position-specific gap penalties and weight matrix choice, *Nucleic Acids Res. 22*, 4673-4680.

[188] Drozdetskiy, A., Cole, C., Procter, J., and Barton, G. J. (2015) JPred4: a protein secondary structure prediction server, *Nucleic Acids Res. 43*, W389-394.

[189] Sonnhammer, E. L., von Heijne, G., and Krogh, A. (1998) A hidden Markov model for predicting transmembrane helices in protein sequences, *Proc. Int. Conf. Intell. Syst. Mol. Biol. 6*, 175-182.

[190] Waterhouse, A. M., Procter, J. B., Martin, D. M., Clamp, M., and Barton, G. J. (2009) Jalview Version 2 - a multiple sequence alignment editor and analysis workbench, *Bioinformatics 25*, 1189-1191.

[191] Maiti, R., Van Domselaar, G. H., Zhang, H., and Wishart, D. S. (2004) SuperPose: a simple server for sophisticated structural superposition, *Nucleic Acids Res. 32*, W590-594.

[192] Krissinel, E., and Henrick, K. (2007) Inference of macromolecular assemblies from crystalline state, *J. Mol. Biol. 372*, 774-797.

[193] Baker, N. A., Sept, D., Joseph, S., Holst, M. J., and McCammon, J. A. (2001) Electrostatics of nanosystems: application to microtubules and the ribosome, *Proc. Natl. Acad. Sci. U.S.A. 98*, 10037-10041.

[194] Lotan, I., and Head-Gordon, T. (2006) An Analytical Electrostatic Model for Salt Screened Interactions between Multiple Proteins, *J. Chem. Theory. Comput. 2*, 541-555.

[195] Dolinsky, T. J., Nielsen, J. E., McCammon, J. A., and Baker, N. A. (2004) PDB2PQR: an automated pipeline for the setup of Poisson-Boltzmann electrostatics calculations, *Nucleic Acids Res. 32*, W665-667.

[196] Arslan, E., Schulz, H., Zufferey, R., Kunzler, P., and Thony-Meyer, L. (1998) Overproduction of the Bradyrhizobium japonicum c-type cytochrome subunits of the cbb_3 oxidase in *Escherichia coli*, *Biochem. Biophys. Res. Commun. 251*, 744-747.

[197] Fernandes, A. P., Couto, I., Morgado, L., Londer, Y. Y., and Salgueiro, C. A. (2008) Isotopic labeling of *c*-type multiheme cytochromes overexpressed in *E. coli*, *Protein Expr. Purif. 59*, 182-188.

[198] Tropea, J. E., Cherry, S., and Waugh, D. S. (2009) Expression and purification of soluble His(6)-tagged TEV protease, *Methods Mol. Biol. 498*, 297-307.

[199] Ohnishi, S. T., and Barr, J. K. (1978) A simplified method of quantitating protein using the biuret and phenol reagents, *Anal. Biochem. 86*, 193-200.

[200] Hanna, P. M., Tamilarasan, R., and McMillin, D. R. (1988) Cu(I) analysis of blue copper proteins, *Biochem. J. 256*, 1001-1004.

[201] Dutton, P. L. (1978) Redox potentiometry: determination of midpoint potentials of oxidation-reduction components of biological electron-transfer systems, *Methods Enzymol. 54*, 411-435.

[202] Childs, R. E., and Bardsley, W. G. (1975) The steady-state kinetics of peroxidase with 2,2'-azino-di-(3-ethyl-benzthiazoline-6-sulphonic acid) as chromogen, *Biochem. J. 145*, 93-103.

[203] Alberty, R. A., and Bloomfield, V. (1963) Multiple Intermedates in Steady State Enzyme Kinetics. V. Effect of pH on the rate of a simple enzymatic reaction, *J. Biol. Chem. 238*, 2804-2810.

[204] Taylor, J. R. (1997) *An introduction to error analysis: The study of uncertainties in physical measurements*, 2nd ed., University Science Books, Sausalito, United States.

[205] Nóbrega, C. S., Saraiva, I. H., Carreira, C., Devreese, B., Matzapetakis, M., and Pauleta, S. R. (2016) The solution structure of the soluble form of the lipid-modified azurin from *Neisseria gonorrhoeae*, the electron donor of cytochrome c peroxidase, *Biochim. Biophys. Acta 1857*, 169-176.

[206] Childs, R. E., and Bardsley, W. G. (1975) The steady-state kinetics of peroxidase with 2,2'-azino-di-(3-ethyl-benzthiazoline-6-sulphonic acid) as chromogen, *Biochem J 145*, 93-103.

[207] Giordani, R., and Buc, J. (2004) Evidence for two different electron transfer pathways in the same enzyme, nitrate reductase A from *Escherichia coli*, *Eur. J. Biochem. 271*, 2400-2407.

[208] Nóbrega, C. S., Matzapetakis, M., and Pauleta, S. R. (2012) ^{1}H, ^{13}C and ^{15}N resonance assignment of the soluble form of the lipid-modified Azurin from *Neisseria gonorrhoeae*, *Biomol. NMR Assign. 7*, 311-314.

[209] Garrett, D. S., Seok, Y. J., Peterkofsky, A., Clore, G. M., and Gronenborn, A. M. (1997) Identification by NMR of the binding surface for the histidine-containing phosphocarrier protein HPr on the N-terminal domain of enzyme I of the *Escherichia coli* phosphotransferase system, *Biochemistry 36*, 4393-4398.

[210] Palma, P. N., Krippahl, L., Wampler, J. E., and Moura, J. J. (2000) BiGGER: a new (soft) docking algorithm for predicting protein interactions, *Proteins 39*, 372-384.

[211] Pierce, B. G., Wiehe, K., Hwang, H., Kim, B. H., Vreven, T., and Weng, Z. (2014) ZDOCK server: interactive docking prediction of protein-protein complexes and symmetric multimers, *Bioinformatics 30*, 1771-1773.

[212] Mintseris, J., Pierce, B., Wiehe, K., Anderson, R., Chen, R., and Weng, Z. (2007) Integrating statistical pair potentials into protein complex prediction, *Proteins 69*, 511-520.

[213] Regan, J. J., Risser, S. M., Beratan, D. N., and Onuchic, J. N. (1993) Protein electron transport: single versus multiple pathways, *J. Phys. Chem. 97*, 13083-13088.

[214] Betts, J. N., Beratan, D. N., and Onuchic, J. N. (1992) Mapping electron tunneling pathways: an algorithm that finds the 'minimum length'/maximum coupling pathway between electron donors and acceptors in proteins, *J. Am. Chem. Soc. 114*, 4043-4046.

[215] Baba, T., Ara, T., Hasegawa, M., Takai, Y., Okumura, Y., Baba, M., Datsenko, K. A., Tomita, M., Wanner, B. L., and Mori, H. (2006) Construction of *Escherichia coli* K-12 in-frame, single-gene knockout mutants: the Keio collection, *Mol. Syst. Biol. 2*, 2006.0008.

[216] Zinkevich, V., and Beech, I. B. (2000) Screening of sulfate-reducing bacteria in colonoscopy samples from healthy and colitic human gut mucosa, *FEMS Microbiol. Ecol. 34*, 147-155.

[217] Thornton, B., and Basu, C. (2011) Real-time PCR (*q*PCR) primer design using free online software, *Biochem Mol. Biol. Educ. 39*, 145-154.

[218] Naumann, M., Rudel, T., and Meyer, T. F. (1999) Host cell interactions and signalling with *Neisseria gonorrhoeae*, *Curr. Opin. Microbiol. 2*, 62-70.

[219] Gerbase, A. C., Rowley, J. T., Heymann, D. H., Berkley, S. F., and Piot, P. (1998) Global prevalence and incidence estimates of selected curable STDs, *Sex Transm. Infect. 74 Suppl 1*, S12-16.

[220] Seib, K. L., Wu, H.-J., Kidd, S. P., Apicella, M. A., Jennings, M. P., and McEwan, A. G. (2006) Defenses against oxidative stress in *Neisseria gonorrhoeae*: a system tailored for a challenging environment., *Microbiol. Mol. Biol. Rev. 70*, 344-361.

[221] Archibald, F. S., and Duong, M. N. (1986) Superoxide dismutase and oxygen toxicity defenses in the genus *Neisseria*, *Infect. Immun. 51*, 631-641.

[222] Johnson, S. R., Steiner, B. M., Cruce, D. D., Perkins, G. H., and Arko, R. J. (1993) Characterization of a catalase-deficient strain of *Neisseria gonorrhoeae*: evidence for the significance of catalase in the biology of N. gonorrhoeae, *Infect. Immun. 61*, 1232-1238.

[223] Chen, C. Y., and Morse, S. A. (1999) *Neisseria gonorrhoeae* bacterioferritin: structural heterogeneity, involvement in iron storage and protection against oxidative stress, *Microbiology 145 (Pt 10)*, 2967-2975.

[224] Skaar, E. P., Tobiason, D. M., Quick, J., Judd, R. C., Weissbach, H., Etienne, F., Brot, N., and Seifert, H. S. (2002) The outer membrane localization of the *Neisseria gonorrhoeae* MsrA/B is involved in survival against reactive oxygen species, *Proc. Natl. Acad. Sci. U. S. A. 99*, 10108-10113.

[225] Seib, K. L., Jennings, M. P., and McEwan, A. G. (2003) A Sco homologue plays a role in defence against oxidative stress in pathogenic *Neisseria*, *FEBS Lett. 546*, 411-415.

[226] Seib, K. L., Wu, H.-J., Srikhanta, Y. N., Edwards, J. L., Falsetta, M. L., Hamilton, A. J., Maguire, T. L., Grimmond, S. M., Apicella, M. A., McEwan, A. G., and Jennings, M. P. (2007) Characterization of the OxyR regulon of *Neisseria gonorrhoeae*., *Mol. Microbiol. 63*, 54-68.

[227] Turner, S., Reid, E., Smith, H., and Cole, J. (2003) A novel cytochrome *c* peroxidase from *Neisseria gonorrhoeae*: a lipoprotein from a Gram-negative bacterium, *Biochem. J. 373*, 865-873.

[228] Whitehead, R. N., Overton, T. W., Snyder, L. A., McGowan, S. J., Smith, H., Cole, J. A., and Saunders, N. J. (2007) The small FNR regulon of *Neisseria gonorrhoeae*: comparison with the larger Escherichia coli FNR regulon and interaction with the NarQ-NarP regulon, *BMC Genomics 8*, 35.

[229] Seib, K. L., Tseng, H.-J., McEwan, A. G., Apicella, M. A., and Jennings, M. P. (2004) Defenses against oxidative stress in *Neisseria gonorrhoeae* and *Neisseria meningitidis*: distinctive systems for different lifestyles., *J. Infect. Dis. 190*, 136-147.

[230] Dumortier, C., Meyer, T. E., and Cusanovich, M. A. (1999) Protein dynamics: imidazole binding to class I *C*-type cytochromes, *Arch. Biochem. Biophys. 371*, 142-148.

[231] Viola, F., Aime, S., Coletta, M., Desideri, A., Fasano, M., Paoletti, S., Tarricone, C., and Ascenzi, P. (1996) Azide, cyanide, fluoride, imidazole and pyridine binding to ferric and ferrous native horse

heart cytochrome *c* and to its carboxymethylated derivative: a comparative study, *J. Inorg. Biochem. 62*, 213-222.
[232] Ikeda-Saito, M., and Iizuka, T. (1975) Studies on the heme environment of horse heart ferric cytochrome *c*. Azide and imidazole complexes of ferric cytochrome *c*, *Biochim. Biophys. Acta 393*, 335-342.
[233] Marri, P. R., Paniscus, M., Weyand, N. J., Rendón, M. A., Calton, C. M., Hernández, D. R., Higashi, D. L., Sodergren, E., Weinstock, G. M., Rounsley, S. D., and So, M. (2010) Genome sequencing reveals widespread virulence gene exchange among human *Neisseria* species, *PLoS One 5*, e11835.
[234] Roach, D. J., Burton, J. N., Lee, C., Stackhouse, B., Butler-Wu, S. M., Cookson, B. T., Shendure, J., and Salipante, S. J. (2015) A Year of Infection in the Intensive Care Unit: Prospective Whole Genome Sequencing of Bacterial Clinical Isolates Reveals Cryptic Transmissions and Novel Microbiota, *PLoS Genet. 11*, e1005413.
[235] Sankaran, K., and Wu, H. C. (1994) Lipid modification of bacterial prolipoprotein. Transfer of diacylglyceryl moiety from phosphatidylglycerol, *J. Biol. Chem. 269*, 19701-19706.
[236] Li, X., Parker, S., Deeudom, M., and Moir, J. W. (2011) Tied down: tethering redox proteins to the outer membrane in *Neisseria* and other genera, *Biochem. Soc. Trans. 39*, 1895-1899.
[237] Protasevich, I., Ranjbar, B., Lobachov, V., Makarov, A., Gilli, R., Briand, C., Lafitte, D., and Haiech, J. (1997) Conformation and thermal denaturation of apocalmodulin: role of electrostatic mutations, *Biochemistry 36*, 2017-2024.
[238] Ellfolk, N., Rönnberg, M., Aasa, R., Andréasson, L. E., and Vänngård, T. (1984) Anion binding to resting and half-reduced *Pseudomonas* cytochrome *c* peroxidase, *Biochim. Biophys. Acta 784*, 62-67.
[239] Kokhan, O., Shinkarev, V. P., and Wraight, C. A. (2010) Binding of imidazole to the heme of cytochrome c_1 and inhibition of the bc_1 complex from *Rhodobacter sphaeroides*: II. Kinetics and mechanism of binding, *J. Biol. Chem. 285*, 22522-22531.
[240] Dixon, M. (1953) The determination of enzyme inhibitor constants, *Biochem. J. 55*, 170-171.
[241] Cornish-Bowden, A. (1974) A simple graphical method for determining the inhibition constants of mixed, uncompetitive and non-competitive inhibitors, *Biochem. J. 137*, 143-144.
[242] Chen, Y. R., Deterding, L. J., Tomer, K. B., and Mason, R. P. (2000) Nature of the inhibition of horseradish peroxidase and mitochondrial cytochrome *c* oxidase by cyanyl radical, *Biochemistry 39*, 4415-4422.
[243] Jacobson, T., Williamson, J., Wasilewski, A., Felesik, J., Vitello, L. B., and Erman, J. E. (2004) Azide binding to yeast cytochrome *c* peroxidase and horse metmyoglobin: comparative thermodynamic investigation using isothermal titration calorimetry, *Arch. Biochem. Biophys. 422*, 125-136.
[244] Marcus, R. A., and Sutin, N. (1985) Electron transfers in chemistry and biology, *Biochimica et Biophysica Acta (BBA) - Reviews on Bioenergetics 811*, 265-322.
[245] Winkler, J. R. (2000) Electron tunneling pathways in proteins, *Curr. Opin. Chem. Biol. 4*, 192-198.
[246] Geng, J., Huo, L., and Liu, A. (2017) Heterolytic O-O bond cleavage: Functional role of Glu113 during bis-Fe(IV) formation in MauG, *J. Inorg. Biochem. 167*, 60-67.
[247] Abu Tarboush, N., Yukl, E. T., Shin, S., Feng, M., Wilmot, C. M., and Davidson, V. L. (2013) Carboxyl group of Glu113 is required for stabilization of the diferrous and bis-Fe(IV) states of MauG, *Biochemistry 52*, 6358-6367.
[248] Shin, S., Yukl, E. T., Sehanobish, E., Wilmot, C. M., and Davidson, V. L. (2014) Site-directed mutagenesis of Gln103 reveals the influence of this residue on the redox properties and stability of MauG, *Biochemistry 53*, 1342-1349.
[249] Nielsen, J. E., and McCammon, J. A. (2003) Calculating pKa values in enzyme active sites, *Protein Sci. 12*, 1894-1901.
[250] Gumiero, A., Metcalfe, C. L., Pearson, A. R., Raven, E. L., and Moody, P. C. (2011) Nature of the ferryl heme in compounds I and II, *J. Biol. Chem. 286*, 1260-1268.
[251] Vidossich, P., and Magistrato, A. (2014) QM/MM molecular dynamics studies of metal binding proteins, *Biomolecules 4*, 616-645.
[252] Polyakov, K. M., Boyko, K. M., Tikhonova, T. V., Slutsky, A., Antipov, A. N., Zvyagilskaya, R. A., Popov, A. N., Bourenkov, G. P., Lamzin, V. S., and Popov, V. O. (2009) High-resolution structural analysis of a novel octaheme cytochrome *c* nitrite reductase from the haloalkaliphilic bacterium Thioalkalivibrio nitratireducens, *J. Mol. Biol. 389*, 846-862.
[253] Singer, A. (1975) The uterine cervix from adolescence to the menopause, *Br. J. Obstet. Gynaecol. 82*, 81-99.
[254] Dominguez, D. C. (2004) Calcium signalling in bacteria, *Mol. Microbiol. 54*, 291-297.
[255] Rosch, J. W., Sublett, J., Gao, G., Wang, Y. D., and Tuomanen, E. I. (2008) Calcium efflux is essential for bacterial survival in the eukaryotic host, *Mol. Microbiol. 70*, 435-444.

[256] Foote, N., Turner, R., Brittain, T., and Greenwood, C. (1992) A quantitative model for the mechanism of action of the cytochrome *c* peroxidase of *Pseudomonas aeruginosa*, *Biochem. J. 283 (Pt 3)*, 839-843.

[257] Brittain, T., and Greenwood, C. (1992) Complex formation between the copper protein, azurin and the cytochrome *c* peroxidase of *Pseudomonas aeruginosa*, *J. Inorg. Biochem. 48*, 71-77.

[258] McLaughlin, M. P., Retegan, M., Bill, E., Payne, T. M., Shafaat, H. S., Peña, S., Sudhamsu, J., Ensign, A. A., Crane, B. R., Neese, F., and Holland, P. L. (2012) Azurin as a protein scaffold for a low-coordinate nonheme iron site with a small-molecule binding pocket, *J. Am. Chem. Soc. 134*, 19746-19757.

[259] Zaballa, M. E., Abriata, L. A., Donaire, A., and Vila, A. J. (2012) Flexibility of the metal-binding region in apo-cupredoxins, *Proc. Natl. Acad. Sci. U.S.A. 109*, 9254-9259.

[260] Hashimoto, W., Ochiai, A., Hong, C. S., Murata, K., and Chakrabarty, A. M. (2015) Structural studies on Laz, a promiscuous anticancer Neisserial protein, *Bioengineered 6*, 141-148.

[261] Najmudin, S., Pauleta, S. R., Moura, I., and Romão, M. J. (2010) The 1.4 Å resolution structure of *Paracoccus pantotrophus* pseudoazurin, *Acta Crystallogr. Sect. F: Struct. Biol. Cryst. Commun. 66*, 627-635.

[262] Solomon, E. I., and Lowery, M. D. (1993) Electronic structure contributions to function in bioinorganic chemistry, *Science 259*, 1575-1581.

[263] Davidson, V. L. (2008) Protein control of true, gated, and coupled electron transfer reactions, *Acc. Chem. Res. 41*, 730-738.

[264] Gray, K. A., Knaff, D. B., Husain, M., and Davidson, V. L. (1986) Measurement of the oxidation-reduction potentials of amicyanin and *c*-type cytochromes from *Paracoccus denitrificans*, *FEBS Lett. 207*, 239-242.

[265] Husain, M., and Davidson, V. L. (1985) An inducible periplasmic blue copper protein from *Paracoccus denitrificans*. Purification, properties, and physiological role, *J. Biol. Chem. 260*, 14626-14629.

[266] Pérez-Henarejos, S. A., Alcaraz, L. A., and Donaire, A. (2015) Blue Copper Proteins: A rigid machine for efficient electron transfer, a flexible device for metal uptake, *Arch. Biochem. Biophys. 584*, 134-148.

[267] Ainscough, E. W., Bingham, A. G., Brodie, A. M., Ellis, W. R., Gray, H. B., Loehr, T. M., Plowman, J. E., Norris, G. E., and Baker, E. N. (1987) Spectrochemical studies on the blue copper protein azurin from *Alcaligenes denitrificans*, *Biochemistry 26*, 71-82.

[268] Dodd, F. E., Hasnain, S. S., Hunter, W. N., Abraham, Z. H., Debenham, M., Kanzler, H., Eldridge, M., Eady, R. R., Ambler, R. P., and Smith, B. E. (1995) Evidence for two distinct azurins in *Alcaligenes xylosoxidans* (NCIMB 11015): potential electron donors to nitrite reductase, *Biochemistry 34*, 10180-10186.

[269] Sukumar, N., Chen, Z. W., Ferrari, D., Merli, A., Rossi, G. L., Bellamy, H. D., Chistoserdov, A., Davidson, V. L., and Mathews, F. S. (2006) Crystal structure of an electron transfer complex between aromatic amine dehydrogenase and azurin from *Alcaligenes faecalis*, *Biochemistry 45*, 13500-13510.

[270] Rosen, P., Segal, M., and Pecht, I. (1981) Electron transfer between azurin from *Alcaligenes faecalis* and cytochrome c_{551} from *Pseudomonas aeruginosa*, *Eur. J. Biochem. 120*, 339-344.

[271] Brill, A. S., Bryce, G. F., and Maria, H. J. (1968) Optical and magnetic properties of *Pseudomonas* azurins, *Biochim. Biophys. Acta 154*, 342-351.

[272] Hirst, J., and Armstrong, F. A. (1998) Fast-scan cyclic voltammetry of protein films on pyrolytic graphite edge electrodes: characteristics of electron exchange, *Anal. Chem. 70*, 5062-5071.

[273] Silvestrini, M. C., Colosimo, A., Brunori, M., Walsh, T. A., Barber, D., and Greenwood, C. (1979) A re-evaluation of some basic structural and functional properties of *Pseudomonas* cytochrome oxidase, *Biochem. J. 183*, 701-709.

[274] Chan, C., Willis, A. C., Robinson, C. V., Aplin, R. T., Radford, S. E., and Ferguson, S. J. (1995) The complete amino acid sequence confirms the presence of pseudoazurin in *Thiosphaera pantotropha*, *Biochem. J. 308 (Pt 2)*, 585-590.

[275] Libeu, C. A., Kukimoto, M., Nishiyama, M., Horinouchi, S., and Adman, E. T. (1997) Site-directed mutants of pseudoazurin: explanation of increased redox potentials from X-ray structures and from calculation of redox potential differences, *Biochemistry 36*, 13160-13179.

[276] Nishiyama, M., Suzuki, J., Ohnuki, T., Chang, H. C., Horinouchi, S., Turley, S., Adman, E. T., and Beppu, T. (1992) Site-directed mutagenesis of pseudoazurin from *Alcatigenes faecalis* S-6; Pro80Ala mutant exhibits marked increase in reduction potential, *Protein Eng. Des. Sel. 5*, 177-184.

[277] Kakutani, T., Watanabe, H., Arima, K., and Beppu, T. (1981) A Blue Protein as an Inactivating Factor for Nitrite Reductase from *Alcaligenes faecalis* Strain S-6, *J. Biochem. 89*, 463-472.

[278] Ingledew, W. J., and Cobley, J. G. (1980) A potentiometric and kinetic study on the respiratory chain of ferrous-iron-grown *Thiobacillus ferrooxidans*, *Biochim. Biophys. Acta 590*, 141-158.
[279] Hall, J. F., Kanbi, L. D., Strange, R. W., and Hasnain, S. S. (1999) Role of the axial ligand in type 1 Cu centers studied by point mutations of met148 in rusticyanin, *Biochemistry 38*, 12675-12680.
[280] Nunzi, F., Woudstra, M., Campèse, D., Bonicel, J., Morin, D., and Bruschi, M. (1993) Amino-acid sequence of rusticyanin from *Thiobacillus ferrooxidans* and its comparison with other blue copper proteins, *Biochim. Biophys. Acta 1162*, 28-34.
[281] Sailasuta, N., Anson, F. C., and Gray, H. B. (1979) Studies of the thermodynamics of electron transfer reactions of blue copper proteins, *J. Am. Chem. Soc. 101*, 455-458.
[282] Malmström, B. G., Reinhammar, B., and Vänngård, T. (1970) The state of copper in stellacyanin and laccase from the lacquer tree *Rhus vernicifera*, *Biochim. Biophys. Acta 205*, 48-57.
[283] Gewirth, A. A., and Solomon, E. I. (1988) Electronic structure of plastocyanin: excited state spectral features, *J. Am. Chem. Soc. 110*, 3811-3819.
[284] Katoh, S., Shiratori, I., and Takamiya, A. (1962) Purification and some properties of spinach plastocyanin, *J. Biochem. 51*, 32-40.
[285] Acuner Ozbabacan, S. E., Engin, H. B., Gursoy, A., and Keskin, O. (2011) Transient protein-protein interactions, *Protein Eng. Des. Sel. 24*, 635-648.
[286] Chaudhari, A., Fialho, A. M., Ratner, D., Gupta, P., Hong, C. S., Kahali, S., Yamada, T., Haldar, K., Murphy, S., Cho, W., Chauhan, V. S., Das Gupta, T. K., and Chakrabarty, A. M. (2006) Azurin, *Plasmodium falciparum* malaria and HIV/AIDS: inhibition of parasitic and viral growth by Azurin, *Cell Cycle 5*, 1642-1648.
[287] Wu, H. J., Seib, K. L., Edwards, J. L., Apicella, M. A., McEwan, A. G., and Jennings, M. P. (2005) Azurin of pathogenic *Neisseria* spp. is involved in defense against hydrogen peroxide and survival within cervical epithelial cells, *Infect. Immun. 73*, 8444-8448.
[288] Woods, J. P., Dempsey, J. F., Kawula, T. H., Barritt, D. S., and Cannon, J. G. (1989) Characterization of the neisserial lipid-modified azurin bearing the H.8 epitope, *Mol. Microbiol. 3*, 583-591.
[289] Gotschlich, E. C., and Seiff, M. E. (1987) Identification and Gene Structure of an Azurin-Like Protein with a Lipoprotein Signal Peptide in *Neisseria gonorrhoeae*, *Fems Microbiol. Lett. 43*, 253-255
[290] Cannon, J. G. (1989) Conserved lipoproteins of pathogenic *Neisseria* species bearing the H.8 epitope: lipid-modified azurin and H.8 outer membrane protein, *Clin. Microbiol. Rev. 2 Suppl*, S1-4.
[291] Deeudom, M., Huston, W., and Moir, J. W. (2015) Lipid-modified azurin of *Neisseria meningitidis* is a copper protein localized on the outer membrane surface and not regulated by FNR, *Antonie Van Leeuwenhoek 107*, 1107-1116.
[292] Aas, F. E., Li, X., Edwards, J., Hongrø Solbakken, M., Deeudom, M., Vik, Å., Moir, J., Koomey, M., and Aspholm, M. (2015) Cytochrome *c*-based domain modularity governs genus-level diversification of electron transfer to dissimilatory nitrite reduction, *Environ. Microbiol. 17*, 2114-2132.
[293] Barth, K. R., Isabella, V. M., and Clark, V. L. (2009) Biochemical and genomic analysis of the denitrification pathway within the genus *Neisseria*, *Microbiology 155*, 4093-4103.
[294] Nar, H., Messerschmidt, A., Huber, R., van de Kamp, M., and Canters, G. W. (1991) Crystal structure analysis of oxidized *Pseudomonas aeruginosa* azurin at pH 5.5 and pH 9.0. A pH-induced conformational transition involves a peptide bond flip, *J. Mol. Biol. 221*, 765-772.
[295] Adman, E. T. (1991) Copper protein structures, *Adv. Protein. Chem. 42*, 145-197.
[296] Paraskevopoulos, K., Sundararajan, M., Surendran, R., Hough, M. A., Eady, R. R., Hillier, I. H., and Hasnain, S. S. (2006) Active site structures and the redox properties of blue copper proteins: atomic resolution structure of azurin II and electronic structure calculations of azurin, plastocyanin and stellacyanin, *Dalton Trans.*, 3067-3076.
[297] Solomon, E. I., and Hadt, R. G. (2011) Recent advances in understanding blue copper proteins, *Coordination Chemistry Reviews 255*, 774-789.
[298] Watkins, J. A., Cusanovich, M. A., Meyer, T. E., and Tollin, G. (1994) A "parallel plate" electrostatic model for bimolecular rate constants applied to electron transfer proteins, *Protein Sci. 3*, 2104-2114.
[299] Rodier, F., Bahadur, R. P., Chakrabarti, P., and Janin, J. (2005) Hydration of protein-protein interfaces, *Proteins 60*, 36-45.
[300] van Dijk, E., Hoogeveen, A., and Abeln, S. (2015) The hydrophobic temperature dependence of amino acids directly calculated from protein structures, *PLoS Comput. Biol. 11*, e1004277.
[301] Wang, X., and Pielak, G. J. (1999) Equilibrium thermodynamics of a physiologically-relevant heme-protein complex, *Biochemistry 38*, 16876-16881.
[302] Crowley, P. B., Otting, G., Schlarb-Ridley, B. G., Canters, G. W., and Ubbink, M. (2001) Hydrophobic interactions in a cyanobacterial plastocyanin-cytochrome *f* complex, *J. Am. Chem. Soc. 123*, 10444-10453.

[303] Worrall, J. A., Liu, Y., Crowley, P. B., Nocek, J. M., Hoffman, B. M., and Ubbink, M. (2002) Myoglobin and cytochrome b_5: a nuclear magnetic resonance study of a highly dynamic protein complex, *Biochemistry 41*, 11721-11730.

[304] Crowley, P. B., and Carrondo, M. A. (2004) The architecture of the binding site in redox protein complexes: implications for fast dissociation, *Proteins 55*, 603-612.

[305] Pierce, B. G., Hourai, Y., and Weng, Z. (2011) Accelerating protein docking in ZDOCK using an advanced 3D convolution library, *PLoS One 6*, e24657.

[306] Jones, S., and Thornton, J. M. (1996) Principles of protein-protein interactions, *Proc. Natl. Acad. Sci. U.S.A. 93*, 13-20.

[307] Lo Conte, L., Chothia, C., and Janin, J. (1999) The atomic structure of protein-protein recognition sites, *J. Mol. Biol. 285*, 2177-2198.

[308] Nooren, I. M., and Thornton, J. M. (2003) Structural characterisation and functional significance of transient protein-protein interactions, *J. Mol. Biol. 325*, 991-1018.

[309] Dell'acqua, S., Pauleta, S. R., Monzani, E., Pereira, A. S., Casella, L., Moura, J. J., and Moura, I. (2008) Electron transfer complex between nitrous oxide reductase and cytochrome c_{552} from *Pseudomonas nautica*: kinetic, nuclear magnetic resonance, and docking studies, *Biochemistry 47*, 10852-10862.

[310] Gorren, A. C., den Blaauwen, T., Canters, G. W., Hopper, D. J., and Duine, J. A. (1996) The role of His117 in the redox reactions of azurin from *Pseudomonas aeruginosa*, *FEBS Lett. 381*, 140-142.

[311] Volkov, A. N. (2015) Structure and Function of Transient Encounters of Redox Proteins, *Acc. Chem. Res. 48*, 3036-3043.

[312] Bashir, Q., Volkov, A. N., Ullmann, G. M., and Ubbink, M. (2010) Visualization of the encounter ensemble of the transient electron transfer complex of cytochrome *c* and cytochrome *c* peroxidase, *J. Am. Chem. Soc. 132*, 241-247.

[313] Obinger, C., Maj, M., Nicholls, P., and Loewen, P. (1997) Activity, peroxide compound formation, and heme d synthesis in *Escherichia coli* HPII catalase, *Arch. Biochem. Biophys. 342*, 58-67.

[314] Baker, L. M., and Poole, L. B. (2003) Catalytic mechanism of thiol peroxidase from *Escherichia coli*. Sulfenic acid formation and overoxidation of essential CYS61, *J. Biol. Chem. 278*, 9203-9211.

[315] Unden, G., Achebach, S., Holighaus, G., Tran, H. G., Wackwitz, B., and Zeuner, Y. (2002) Control of FNR function of *Escherichia coli* by O_2 and reducing conditions, *J. Mol. Microbiol. Biotechnol. 4*, 263-268.

[316] Christman, M. F., Storz, G., and Ames, B. N. (1989) OxyR, a positive regulator of hydrogen peroxide-inducible genes in *Escherichia coli* and *Salmonella typhimurium*, is homologous to a family of bacterial regulatory proteins, *Proc. Natl. Acad. Sci. U.S.A. 86*, 3484-3488.

[317] Foote, N., Thompson, A. C., Barber, D., and Greenwood, C. (1983) *Pseudomonas* cytochrome c_{551} peroxidase. A purification procedure and study of CO-binding kinetics, *Biochem. J. 209*, 701-707.

[318] Zapata, C., Paillavil, B., Chávez, R., Álamos, P., and Levicán, G. (2017) Cytochrome *c* peroxidase (CcP) is a molecular determinant of the oxidative stress response in the extreme acidophilic *Leptospirillum* sp. CF-1, *FEMS Microbiol. Ecol. 93*.

[319] Charoensuk, K., Irie, A., Lertwattanasakul, N., Sootsuwan, K., Thanonkeo, P., and Yamada, M. (2011) Physiological importance of cytochrome *c* peroxidase in ethanologenic thermotolerant *Zymomonas mobilis*, *J. Mol. Microbiol. Biotechnol. 20*, 70-82.

[320] Sarewicz, M., and Osyczka, A. (2015) Electronic connection between the quinone and cytochrome *c* redox pools and its role in regulation of mitochondrial electron transport and redox signaling, *Physiol. Rev. 95*, 219-243.

[321] Unden, G., and Bongaerts, J. (1997) Alternative respiratory pathways of *Escherichia coli*: energetics and transcriptional regulation in response to electron acceptors, *Biochim. Biophys. Acta 1320*, 217-234.

[322] Alvarez, A. F., Rodriguez, C., and Georgellis, D. (2013) Ubiquinone and menaquinone electron carriers represent the yin and yang in the redox regulation of the ArcB sensor kinase, *J. Bacteriol. 195*, 3054-3061.

[323] Azuaga, A. I., Dobson, C. M., Mateo, P. L., and Conejero-Lara, F. (2002) Unfolding and aggregation during the thermal denaturation of streptokinase, *Eur. J. Biochem. 269*, 4121-4133.

[324] Hiner, A. N., Martínez, J. I., Arnao, M. B., Acosta, M., Turner, D. D., Lloyd Raven, E., and Rodríguez-López, J. N. (2001) Detection of a tryptophan radical in the reaction of ascorbate peroxidase with hydrogen peroxide, *Eur. J. Biochem. 268*, 3091-3098.

[325] Pan, Z., Zhang, R., and Newcomb, M. (2006) Kinetic studies of reactions of iron(IV)-oxo porphyrin radical cations with organic reductants, *J. Inorg. Biochem. 100*, 524-532.

[326] Erman, J. E., and Yonetani, T. (1975) A kinetic study of the endogenous reduction of the oxidized sites in the primary cytochrome *c* peroxidase-hydrogen peroxide compound, *Biochim. Biophys. Acta 393*, 350-357.

[327] Erman, J. E., Vitello, L. B., Mauro, J. M., and Kraut, J. (1989) Detection of an oxyferryl porphyrin pi-cation-radical intermediate in the reaction between hydrogen peroxide and a mutant yeast cytochrome *c* peroxidase. Evidence for tryptophan-191 involvement in the radical site of compound I, *Biochemistry 28*, 7992-7995.

[328] Feng, M., Jensen, L. M., Yukl, E. T., Wei, X., Liu, A., Wilmot, C. M., and Davidson, V. L. (2012) Proline 107 is a major determinant in maintaining the structure of the distal pocket and reactivity of the high-spin heme of MauG, *Biochemistry 51*, 1598-1606.

[329] Nivinskas, H., Staskeviciene, S., Sarlauskas, J., Koder, R. L., Miller, A. F., and Cenas, N. (2002) Two-electron reduction of quinones by *Enterobacter cloacae* NAD(P)H:nitroreductase: quantitative structure-activity relationships, *Arch. Biochem. Biophys. 403*, 249-258.

[330] Al-Attar, S., Yu, Y., Pinkse, M., Hoeser, J., Friedrich, T., Bald, D., and de Vries, S. (2016) Cytochrome *bd* Displays Significant Quinol Peroxidase Activity, *Sci. Rep. 6*, 27631.

[331] Iverson, T. M., Luna-Chavez, C., Croal, L. R., Cecchini, G., and Rees, D. C. (2002) Crystallographic studies of the *Escherichia coli* quinol-fumarate reductase with inhibitors bound to the quinol-binding site, *J. Biol. Chem. 277*, 16124-16130.

[332] Hellwig, P., Yano, T., Ohnishi, T., and Gennis, R. B. (2002) Identification of the residues involved in stabilization of the semiquinone radical in the high-affinity ubiquinone binding site in cytochrome *bo*(3) from *Escherichia coli* by site-directed mutagenesis and EPR spectroscopy, *Biochemistry 41*, 10675-10679.

[333] Tran, Q. M., Rothery, R. A., Maklashina, E., Cecchini, G., and Weiner, J. H. (2006) The quinone binding site in *Escherichia coli* succinate dehydrogenase is required for electron transfer to the heme *b*, *J. Biol. Chem. 281*, 32310-32317.

[334] Ito, A., May, T., Kawata, K., and Okabe, S. (2008) Significance of rpoS during maturation of *Escherichia coli* biofilms, *Biotechnol. Bioeng. 99*, 1462-1471.

[335] Vijayakumar, S. R., Kirchhof, M. G., Patten, C. L., and Schellhorn, H. E. (2004) RpoS-regulated genes of *Escherichia coli* identified by random lacZ fusion mutagenesis, *J. Bacteriol. 186*, 8499-8507.

[336] Constantinidou, C., Hobman, J. L., Griffiths, L., Patel, M. D., Penn, C. W., Cole, J. A., and Overton, T. W. (2006) A reassessment of the FNR regulon and transcriptomic analysis of the effects of nitrate, nitrite, NarXL, and NarQP as *Escherichia coli* K12 adapts from aerobic to anaerobic growth, *J. Biol. Chem. 281*, 4802-4815.

[337] Kang, Y., Weber, K. D., Qiu, Y., Kiley, P. J., and Blattner, F. R. (2005) Genome-wide expression analysis indicates that FNR of *Escherichia coli* K-12 regulates a large number of genes of unknown function, *J. Bacteriol. 187*, 1135-1160.

[338] Dukan, S., and Nyström, T. (1999) Oxidative stress defense and deterioration of growth-arrested *Escherichia coli* cells, *J. Biol. Chem. 274*, 26027-26032.

[339] González-Flecha, B., and Demple, B. (1997) Transcriptional regulation of the *Escherichia coli* oxyR gene as a function of cell growth, *J. Bacteriol. 179*, 6181-6186.

[340] Seth, D., Hausladen, A., Wang, Y. J., and Stamler, J. S. (2012) Endogenous protein S-Nitrosylation in *E. coli*: regulation by OxyR, *Science 336*, 470-473.

[341] Cussiol, J. R., Alves, S. V., de Oliveira, M. A., and Netto, L. E. (2003) Organic hydroperoxide resistance gene encodes a thiol-dependent peroxidase, *J. Biol. Chem. 278*, 11570-11578.

[342] Korshunov, S., and Imlay, J. A. (2010) Two sources of endogenous hydrogen peroxide in *Escherichia coli*, *Mol. Microbiol. 75*, 1389-1401.

[343] Messner, K. R., and Imlay, J. A. (2002) Mechanism of superoxide and hydrogen peroxide formation by fumarate reductase, succinate dehydrogenase, and aspartate oxidase, *J. Biol. Chem. 277*, 42563-42571.

[344] Korshunov, S., and Imlay, J. A. (2006) Detection and quantification of superoxide formed within the periplasm of *Escherichia coli*, *J. Bacteriol. 188*, 6326-6334.

Annex 1

Annex 1

In Chapter 5 it is presented the biochemical and spectroscopic characterization of a recombinant YhjA with a N-terminal StrepII-tag. Previously, a different construct with a C-terminal His-tag (YhjA_6His) had been produced, purified and characterized.

This Annex 1 is a summary of the results obtained for YhjA_6His, which are presented in Figure A1.1. In Figure A1.1A it shows that this protein has a molecular weight in solution of 45 kDa, which is similar to the one of StrepII_YhjA. However, YhjA_6His does not present the high-spin signal in the UV-visible and EPR spectra (Figure A1.1B, C). In Figure A1.1D, steady-state kinetics of YhjA_6His with $ABTS^{2-}$ as electron donor show that it does not saturate with high concentrations of hydrogen peroxide (26 mM H_2O_2). These results demonstrated that this construct was not in the native form and this had an effect on the catalytic activity.

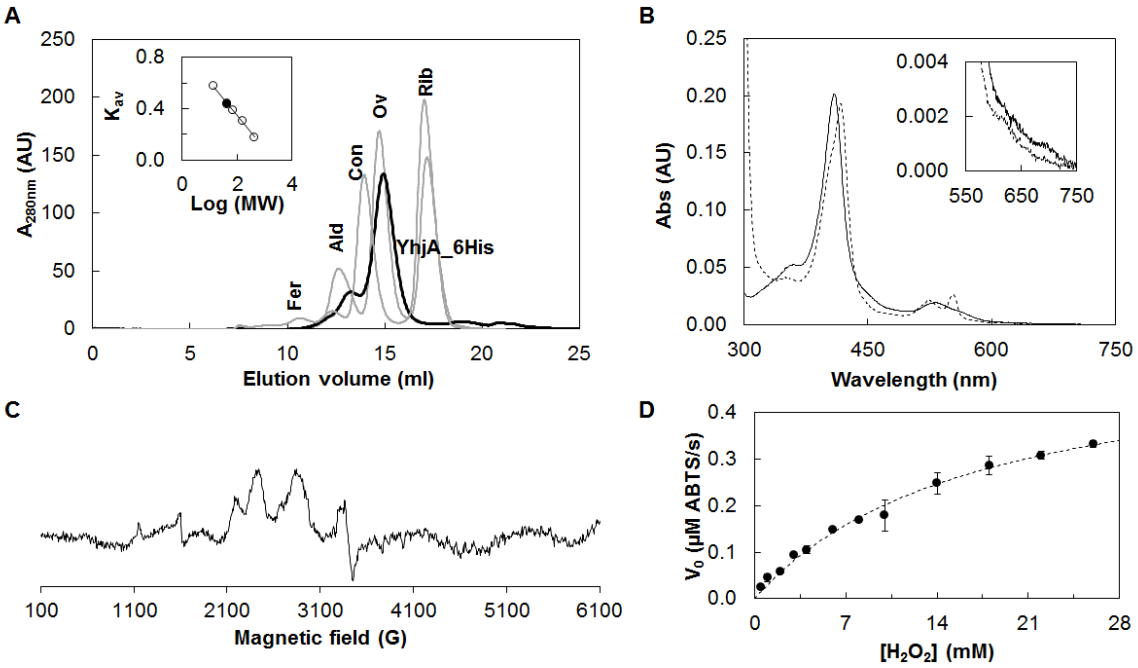

Figure A1.1– Biochemical characterization of YhjA_6His (data not shown in Chapter 5). (A) Elution profile of the size-exclusion chromatography of YhjA_6His (45 kDa; black line). In grey are the elution profiles of the standard proteins: Ferritin (Fer, 440 kDa), Aldolase (Ald, 158 kDa), Conalbumin (Con, 75 kDa), Ovalbumin (Ov, 44 kDa), Ribonuclease A (Rib, 13.7 kDa). (B) UV-visible spectra of YhjA_6His in the as-isolated state (solid line) and in the mixed-valence state, reduced with Asc/DAD (dashed line). (C) EPR spectrum of the as-isolated enzyme acquired as described in Chapter 2, Section 2.6.2.2. (D) Steady-state kinetics of YhjA_6His peroxidase activity using 3 mM $ABTS^{2-}$ as electron donor. The data was simulated with a Michaelis-Menten (dashed line) as described in Chapter 2, Section 2.7 with a K_M of 17 mM H_2O_2 of and V_{max} of 0.55 µM $ABTS^{2-}.s^{-1}$.

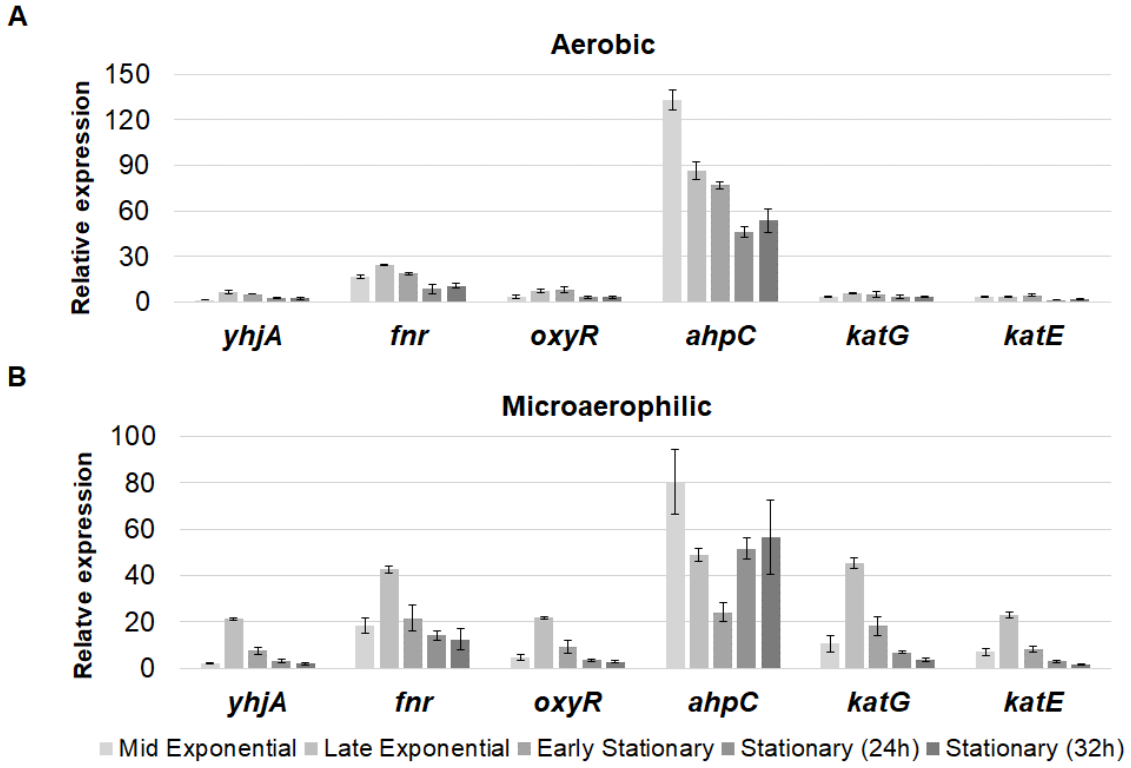

Figure A1.2 – Relative gene expression of oxidative stress related genes in *E. coli* K-12 during growth under aerobic (A) and microaerophilic (B) conditions. The gene expression of each gene was normalized to the *16SrRNA* to account for variations in each point taken from each growth. Data is shown as the mean relative expression based on three biological replicates.